SANDIA REPORT
SAND2021-14614
Printed November 2021

Sandia National Laboratories

Gen 3 Particle Pilot Plant (G3P3) – High-Temperature Particle System for Concentrating Solar Power (Phases 1 and 2)

Clifford K. Ho
Jeremy Sment
Kevin Albrecht
Brantley Mills
Nathan Schroeder
Hendrick Laubscher
Luis F. Gonzalez-Portillo[1]
Cara Libby[2]
John Pye[3]
Phillippe Gunawan Gan[3]
Ye Wang[3]

With contributions from:
[1]Universidad Politécnica de Madrid, [2]Electric Power Research Institute, Georgia Institute of Technology, King Saud University, CSIRO, [3]Australian National University, U. Adelaide, PROMES-CNRS, DLR, Bridgers & Paxton, Bohannan Huston, Solar Dynamics, Carbo Ceramics, Solex Thermal Science, Vacuum Process Engineering, Allied Mineral Products, Matrix PDM, Saudi Electricity Company, and University of Texas at Austin

Prepared by
Sandia National Laboratories
Albuquerque, New Mexico
87185 and Livermore,
California 94550

Issued by Sandia National Laboratories, operated for the United States Department of Energy by National Technology & Engineering Solutions of Sandia, LLC.

Available to DOE and DOE contractors from
U.S. Department of Energy
Office of Scientific and Technical Information
P.O. Box 62
Oak Ridge, TN 37831

Telephone: (865) 576-8401
Facsimile: (865) 576-5728
E-Mail: reports@osti.gov
Online ordering: http://www.osti.gov/scitech

Available to the public from
U.S. Department of Commerce
National Technical Information Service
5301 Shawnee Rd
Alexandria, VA 22312

Telephone: (800) 553-6847
Facsimile: (703) 605-6900
E-Mail: orders@ntis.gov
Online order: https://classic.ntis.gov/help/order-methods/

ABSTRACT

The U.S. Department of Energy Solar Energy Technologies Office initiated the Generation 3 Concentrating Solar Power (CSP) program to achieve higher operating temperatures (>700 °C) to enable next-generation CSP high-temperature power cycles such as the supercritical CO_2 (sCO2) Brayton Cycle. Three teams were selected to pursue high-temperature gas, liquid, and solid pathways for the heat-transfer media. Phases 1 and 2, which lasted from 2018 – 2020, consisted of design, modeling, and testing activities to further de-risk each of the technologies and develop a design for construction, commissioning, and operation of a pilot-scale facility in Phase 3 (2021 – 2024).

This report summarizes the activities in Phases 1 and 2 for the solid-particle pathway led by Sandia National Laboratories. In Phases 1 and 2, Sandia successfully de-risked key elements of the proposed Gen 3 Particle Pilot Plant (G3P3) by improving the design, operation, and performance of key particle component technologies including the receiver, storage bins, particle-to-sCO2 heat exchanger, particle lift, and data acquisition and controls. Modeling and testing of critical components have led to optimized designs that meet desired performance metrics. Detailed drawings, piping and instrumentation diagrams, and process flow diagrams were generated for the integrated system, and structural analyses of the assembled tower structure were performed to demonstrate compliance with relevant codes and standards. Instrumentation and control systems of key subsystems were also demonstrated. Together with Bridgers & Paxton, Bohannan Huston, and Sandia Facilities, we have completed a 100% G3P3 tower design package with stamped engineering drawings suitable for construction bid in Phase 3.

ACKNOWLEDGEMENTS

The authors thank the technologists and staff at the National Solar Thermal Test Facility (NSTTF) at Sandia NM for their significant contributions to the testing described in this report. We also thank the researchers and staff at the following institutions who have provided critical input into the G3P3 design and performance (citations and links to many of their contributions referenced in this report are provided in the relevant sections): Electric Power Research Institute, Georgia Institute of Technology, King Saud University, CSIRO, Australian National University, U. Adelaide, PROMES-CNRS, DLR, Bridgers & Paxton, Bohannan Huston, Solar Dynamics, Carbo Ceramics, Solex Thermal Science, Vacuum Process Engineering, Allied Mineral Products, Matrix PDM, Saudi Electricity Company, Universidad Politécnica de Madrid, and University of Texas at Austin.

This work is funded in part or whole by the U.S. Department of Energy Solar Energy Technologies Office under Award Number 34211. This report was prepared as an account of work sponsored by an agency of the United States Government. Neither the United States Government nor any agency thereof, nor any of their employees, makes any warranty, express or implied, or assumes any legal liability or responsibility for the accuracy, completeness, or usefulness of any information, apparatus, product, or process disclosed, or represents that its use would not infringe privately owned rights. Reference herein to any specific commercial product, process, or service by trade name, trademark, manufacturer, or otherwise does not necessarily constitute or imply its endorsement, recommendation, or favoring by the United States Government or any agency thereof. The views and opinions of authors expressed herein do not necessarily state or reflect those of the United States Government or any agency thereof.

CONTENTS

LIST OF FIGURES

LIST OF TABLES

This page left blank

EXECUTIVE SUMMARY

In Phases 1 and 2, we successfully de-risked key elements of the proposed Gen 3 Particle Pilot Plant (G3P3) by improving the design, operation and performance of key particle component technologies. Modeling and testing of critical components have led to optimized designs that meet desired performance metrics. Detailed drawings, piping and instrumentation diagrams, and process flow diagrams were generated for the integrated system, and structural analyses of the assembled tower structure were performed to demonstrate compliance with relevant codes and standards. Instrumentation and control systems of key subsystems were also demonstrated.

Together with Bridgers & Paxton, Bohannan Huston, and Sandia Facilities, we have completed a 100% G3P3 tower design package with signed and sealed engineering drawings suitable for construction bid in Phase 3. The G3P3 continuation application also addresses all five Phase 3 downselection criteria as summarized below.

1. Phases 1 and 2 Risk Reduction

1.1. Particle Receiver

- Advective heat losses were found to be the primary loss mechanisms in reducing thermal efficiencies in previous free-falling particle receiver designs
- Seven new features (hood, quartz aperture covers, active airflow, multistage release, reduced volume receiver, SNOUT, and chimney) were simulated and/or tested in Phase 1 to reduce heat loss, mitigate wind impacts, reduce particle emissions, and minimize damage from high fluxes. Of these, three features (multistage release, reduced volume, SNOUT) were shown to have significant impact (increasing receiver efficiency by over 10 percentage points in some cases) and are being implemented in the G3P3-USA receiver design.
- Rigorous optimization was applied to a 2 MW_t G3P3-USA receiver geometry; simulated efficiencies are expected to approach ~85 - 90%.
- Over 250 hours of on-sun and ground-based testing were performed in Phase 2 to investigate multistage release, reduced volume receiver, and automated particle flow control (PID) to regulate the particle outlet temperature.
    - Measured receiver efficiencies achieved up to ~90%, but low irradiance, non-uniform particle flow, and cold advection/wind can significantly lower efficiencies; G3P3 design expected to mitigate adverse effects.
    - PID controls were effective at maintaining particle outlet temperatures up to ~780 °C.
    - Multi-stage release was effective at cooling backwall temperatures.
    - Reduced cavity volume was effective at reducing advective heat loss.
    - Emission of particle dust was below EPA and NIOSH standards.
- 100 MW_e three-receiver tower design was simulated with good wind resilience and efficiencies (> ~80%).

1.2. Particle Storage

- Flat-bottomed G3P3 storage bins were designed to induce funnel flow, reducing wall erosion and heat loss via stagnant self-insulating particles.

- Small-scale tests were performed to validate particle flow and heat-transfer models.
- Pre-cast refractory liner materials were tested for erosion and thermal expansion; shotcrete application methods were investigated and tested.
- Methods for reducing temperature of concrete slab were investigated.
- Tower-integrated and ground-based storage bins designs were evaluated for commercial systems with capacities from 10 - 100 MW_e with consideration of heat loss (<1%) and the structural limitations of tower-integrated systems in regions with high seismicity.

1.3. Particle Heat Exchanger

- Simulations and testing of 100 kW_t SuNLaMP HX and shell-and-tube KSU heat exchanger provided lessons learned and informed design of G3P3 HX.
- Shell-and-plate G3P3 HX design with integral headers, closer plate spacing (~3 mm), and counterflow design was simulated to yield >300 – 400 W/m^2-K with <2% (500 kPa) pressure drop.
- Subscale (20 kW_t) prototype was manufactured from stainless steel with novel design features to understand manufacturing steps and verify performance.
- Subscale prototype was tested up to 500 °C at 17 MPa, which yielded overall heat transfer coefficients of >300 W/m^2-K and pressure drop <7 kPa (0.04%).
- Particle flow testing was performed at 650 °C with varying plate spacing (1.5 – 6 mm) and demonstrated reliable and uniform particle flow in narrow vertical channels at operating temperature.
- Bonding, brazing, and chemical etching of IN740H was conducted, but bond strength has not yet met ASME code requirement. Parallel efforts provided the bond, braze, and etch development for constructing the heat exchanger from IN617 and HR230.
- sCO2 corrosion of 800H was larger than expected; corrosion testing is being planned for 800H, 740H, IN617, and/or HR230.

1.4. Particle Lift

- Bucket elevator was designed and selected for G3P3-USA due to excessive costs for small-scale skip hoist; skip hoist will be implemented for G3P3-KSA.
- Heat loss from the G3P3 bucket elevator was modeled, and insulation was designed to minimize heat losses and particle temperature drops to < 3 °C.
- Transient heat loss, costs, and designs were evaluated for 100 MW_e commercial-scale skip hoist.

1.5. Particles

- CARBO HSP 40/70 selected for G3P3-USA based on demonstrated solar absorptance, durability, and flowability at high temperatures.
- CARBO HSP 40/70 particles were exposed to 10,000 irradiance cycles reaching 1000°C per cycle which resulted in a 1% decrease in absorptivity. Particles held at a constant temperature of 800°C for 400 hours also resulted in a 1% decrease in absorptivity.
- Particle flow processes and alternative low-cost particles were evaluated.

- Impact of particle properties on LCOE and other solar thermal applications were evaluated.

2. Phase 3 Management, Design, and Construction Basis

- Project Execution Plan was completed to manage Phase 3 scope, schedule, and budget as detailed in MS Project file.
- G3P3 equipment list, costs, timeline, process flow diagrams, P&ID, and engineering drawings were completed.
- G3P3 tower design and drawings were signed/sealed by Bridgers & Paxton/ Bohannan Huston and reviewed by SNL Facilities (ready for construction bid).

3. Technoeconomic Analyses and Market Adoption Study

- LCOE Analysis
    - EES model of 100 MW_e system were developed to evaluate sensitivity of LCOE to key component costs and processes. Probabilistic analyses showed up to 85% probability of real LCOE ≤ $0.06/kWh using published cost and performance models.
    - SolarTherm/Modelica model developed to evaluate transients and alternative component designs to optimize system performance, achieve LCOE <$0.06/kWh, and evaluate optimal dispatch strategy for peaker plants.
    - Alternative particle-based CSP systems evaluated by partners (DLR's centrifugal particle receiver and CNRS-PROMES's fluidized particle receiver) were independently estimated to yield LCOE < $0.06/$kWh_e$.
- Market Adoption Study
    - Key differentiators for particle-based vs. alternative Gen3 systems were identified and implemented in market adoption study.
    - EPRI and SolarDynamics performed production-cost modeling to evaluate market opportunities for particle systems around the world.
    - G3P3-KSA has teamed with Saudi Electricity Company for direct path to commercialization; Heliogen expressed interest in collaborating on G3P3-USA to investigate alternative particle technologies.

4. Phase 3 Test Matrix and Risk Reduction

- Phase 3 test plan and risk register were completed; scope, schedule, and cost were detailed in MS Project file.
- Test matrix includes detailed plan for de-risking integrated particle-based system and components through commissioning, start-up, shut-down, storage, off-design operation, emergency operations, and performance testing.

5. Risks of Scaling Up to 100 MWe

- Risks of scaling G3P3 to 100 MW_e commercial system were compiled with associated mitigation measures in ^risk register.

- Commercial-scale design and associated risks and mitigation opportunities were developed based on discussions with industry and commercial vendors.

The G3P3 project was selected for both internal and external quality-assurance audits at Sandia in 2019, and the management and practices of the G3P3 project were found to be in compliance with ISO-9001 standards, with several noteworthy practices being called out as "best practices" for the Labs to follow.

All output from this work, including those from external partners, are summarized in the Conclusions (Section 4).

1. BACKGROUND

Particle receivers are being pursued to enable higher temperatures (>700 °C) with direct storage for next-generation dispatchable concentrating solar power (CSP) plants, process heating, thermochemistry, and solar fuels production [1]. Unlike conventional CSP receivers that use fluids flowing through tubes, the proposed particle-receiver system uses solid particles (ceramic or sand) that are heated directly as they fall through a beam of concentrated sunlight. Because the solar energy is directly absorbed by the particles, the flux limitations associated with tubular receivers are mitigated, enabling higher concentration ratios. Once heated, the particles are stored in an insulated bin before passing through a particle-to-working-fluid heat exchanger to power a high-efficiency Brayton cycle (e.g., supercritical CO_2 (sCO2) or air). The cooled particles are collected and then lifted back to the top of the receiver. Aside from the particle lift, the entire process is based on gravity-driven flow of the particles through each component, which can reduce parasitic power consumption and failure points.

Sandia successfully developed and demonstrated a 1 MW_t high-temperature directly irradiated falling particle receiver system that achieved particle temperatures over 700 °C with continuous recirculation [2, 3]. Key findings from those studies indicated that direct irradiance of falling particles enabled very high heating rates (up to several hundred degrees Celsius over ~ 1 – 2 m of drop height with ~1 – 7 kg/s and up to 1000 kW/m^2), but additional methods to reduce heat losses (convective and radiative) and particle losses were needed to increase receiver thermal efficiencies and reduce costs. A key partner, King Saud University (KSU), has also tested a complete falling particle-based CSP system at the 300 kW_t scale [4]. Other particle receiver designs besides direct irradiance free-falling receivers have been considered by researchers, including obstructed flow [2, 5], centrifugal [6, 7], flow in tubes with or without fluidization [8-10], and multi-pass recirculation [11, 12].

Until now, DOE SETO funding has focused primarily on component-level research that developed new particle-receiver designs, process and performance models, and small-scale proof-of-concept demonstrations. However, integration with other required subsystems such as storage, heat exchangers, and particle-lift systems remains to be demonstrated at larger scales and for significant durations. The next step (and the purpose of the Gen 3 program) is to move towards demonstration of larger-scale integrated particle-based systems and address risks associated with receiver thermal efficiency, particle heat exchanger performance and cost, minimization of heat loss, durability, reliability, and particle attrition and conveyance.

2. OBJECTIVES

The objective of this work was to first mitigate key risks associated with the particle-based CSP system through focused R&D efforts (Phases 1 and 2), and then design, construct, and operate a multi-MW_t falling particle receiver system that can operate for thousands of hours, provide 6 hours of energy storage, and heat a working fluid (e.g., sCO2 or air) to ≥ 700 °C (Phase 3) (Figure 1). This first-of-a-kind Gen 3 Particle Pilot Plant (G3P3) will be developed through coordinated efforts with leading international researchers who are also investigating particle-based systems to accelerate deployment and commercialization. This report provides a summary of the activities during Phases 1 and 2 (2018 – 2020). Appendix A provides administrative data regarding the G3P3 project during Phases 1 and 2 of the DOE CSP Gen 3 program.

To increase our chances of success, we plan to develop two G3P3 systems in parallel: (1) a G3P3-USA system deployed at Sandia's National Solar Thermal Test Facility (NSTTF), and (2) a G3P3-KSA system deployed in the Kingdom of Saudi Arabia with support from Saudi Electricity Company (SEC). Both systems will feature vertically integrated thermal components that meet the desired Gen 3 metrics. Key attributes of G3P3-USA and G3P3-KSA are summarized in Table 1, and success factors for each component and the overall G3P3 system are shown in Table 2.

We believe the development of two G3P3 systems that investigate variations of key components (e.g., receiver, heat exchanger, lift, working fluid) will further reduce risks and provide opportunities for increased operational experience. In addition, partnering with SEC, which is interested in developing particle-based CSP plants in Saudi Arabia and the Middle East, provides a direct path towards commercialization.

The focus of this application is on G3P3-USA. Per DOE instruction, G3P3-KSA is described in a separate report. The G3P3-USA system will consist of a ~2 MW_t particle receiver situated on top of a tower to heat the particles from ~600 °C to nearly 800 °C in a single pass. The particles will be collected in an insulated high-temperature particle storage tank capable of holding ~160,000 kg (~160 tons) of particles for 6 hours of storage before being passed through a 1 MW_t particle-to-working-fluid heat exchanger. The heat exchanger will be connected to a flow system capable of providing pressurized sCO2 that will be heated from ~550 °C to ≥700 °C. The particles are then collected in a "low-temperature" insulated storage bin, and a high-efficiency insulated particle lift system will carry the particles (~580 – 615 °C) back to the top of the receiver. A control system will maintain a constant working-fluid outlet temperature, even with varying inlet conditions (e.g., particle and working-fluid inlet temperatures, mass flow rates).

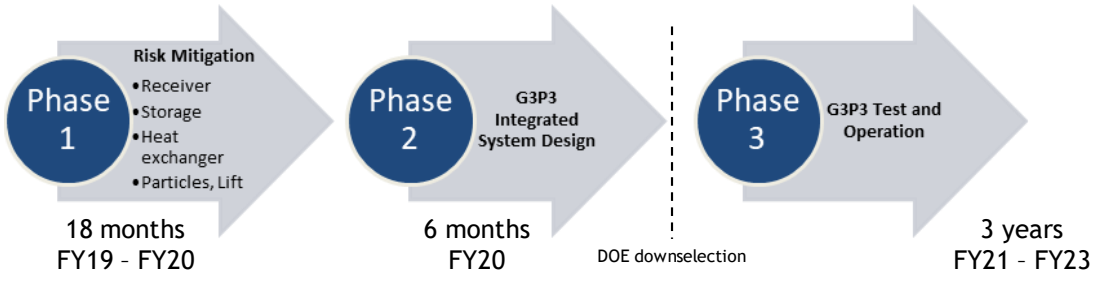

Figure 1. Project phases for the proposed Gen 3 Particle Pilot Plants (G3P3). Phase 2 was extended to ~9 months due to the COVID-19 pandemic, which will extend Phase 3.

Table 1. Comparison of system designs for G3P3-USA and G3P3-KSA.

Parameter	G3P3-USA	G3P3-KSA
Receiver thermal power	~2 MW_t	6 – 7 MW_t
Solar multiple	~2	~2
Particles	CARBO HSP 40/70 ceramic beads	CARBO for G3P3-KSA; still evaluating silica sand for larger systems
Receiver	Falling particles with SNOUT and StAIR; single slide gate	Obstructed flow with inclined back; Multiple slide gates (5) to match flux
Heat exchanger	1 MW_t duty; Moving packed bed; particle flow in shell; 20-25 MPa sCO2 flow in plates	~3 MW_t duty; Moving packed bed; particle flow in tubes; air flow in shell with air pressure up to 4 bar (Aurelia A1300)
Particle Lift	Bucket elevator	Skip hoist
Power block	~1 MW_t sCO2 flow loop	1.3 MW_e Air Brayton turbine/generator (Auerlia A1300)
Tower structure	Open	Enclosed

Table 2. Summary of target performance metrics for each component and the overall G3P3 system. Cost targets are for the commercial scale (~100 MW_e).

Component	Target Metrics	Basis
Particles	Cost ≤ $1/kg Attrition ≤ 0.001% of flow	• Cost target based on price competitiveness with molten salts • Attrition target related to cost metrics for storage and LCOE
Receiver	Thermal duty: ≥ 2 MW_t Cost ≤ $150/$kW_t$ Thermal eff. ≥ ~80 - 85% (pilot), 85-90% (commercial) T_{out} ≥ 775 °C $\dot{m}$ ≥ 5 kg/s	• Thermal duty meets FOA goals and matches capability at NSTTF • Cost and outlet temperature meet SETO CSP goals • Recent simulations show that a commercial receiver efficiency of 85-90% can still yield $0.06/$kWh_e$; pilot-scale efficiency scales down with receiver size [13] • Mass flow based on required thermal duty
Thermal Storage	T_{out} ≥ 765 °C Capacity ≥ 6 MWh_t Cost ≤ $15/$kWh_t$	• Particle temperature based on heat-exchanger approach temperature of 50 °C and desired sCO2 outlet T ≥ 715 °C • Capacity and duration meets 6 hours of storage (deferred 10 hours) for 1 MW_t heat exchanger per FOA
Heat Exchanger	Particle mass flow ≥ 5 kg/s U ≥ 300 W/m^2-K $T_{sCO2,out}$ ≥ 715 °C	• Mass flow rate enables ≥ 1 MW_t as required by FOA • Overall heat transfer coefficient (U) and temperature targets designed to meet cost and performance requirements [14]
Particle Lift	Mass flow rate ≥ 5 kg/s Lift efficiency ≥ 50% (commercial) T_{max} ~600 °C	• Mass flow rate enables ≥ 1 MW_t • Lift efficiency required to reduce particle attrition and parasitics; can be achieved with preliminary design of hoist system [15] • Temperature of “cold” particles will be up to ~600 °C
System	LCOE ≤ $0.06/kWh	• From FOA for 100 MW_e system

3. PROJECT RESULTS AND DISCUSSION / DOWNSELECTION CRITERIA

The following sections describe the Phase 1 and Phase 2 activities and accomplishments organized according to the five Phase 3 downselection criteria: 1) Phases 1 and 2 Risk Reduction, 2) Phase 3 Management, Design, and Construction Basis, 3) Technoeconomic Analyses and Market Adoption Study, 4) Phase 3 Test Matrix and Risk Reduction, and 5) Risks of Scaling Up to 100 MW_e. Progress on associated milestones is summarized in Appendix B.

3.1. Phases 1 and 2 Risk Reduction

Activities were performed in Phases 1 and 2 to reduce risks and costs, improve designs, and increase performance in the following key G3P3 system components: (1) receiver, (2) storage, (3) heat exchanger, (4) lift, and (5) particles. A risk register was created as a tool for organizing and managing the de-risking tasks performed by all G3P3 partners. The risk register was developed and organized as follows:

1. An Ishikawa cause and effect analysis (fishbone diagram) was created to identify modes through which G3P3 would fail to be built or tested (Figure 2). The failure modes were organized into 7 categories: receiver, storage, heat exchange, cooling system (sCO2 loop or air), particle lift, particle selection, and system integration (including both technical and programmatic).
2. Each failure mode was evaluated in individual and group sessions to identify all potential root causes or risks. The risks were then organized into the risk register by component or category and given a mitigation task with metrics (sample excerpt shown in Figure 3).
3. Using quantitative and qualitative analytic hierarchical processes, each risk was rated and ranked based on impact to the successful demonstration of the pilot system and probability of occurrence. This process is very similar to the FMEA except these risks related to failing to meet technical performance metrics of the 1 MW system rather than impacts to environmental safety and hazards.
4. An allocation of the total budget and schedule was allotted to each technical risk in the register along with an assigned owner at Sandia or one of 16 external partners to execute the risk mitigation task.
5. Team leads reported on progress made on the de-risking activities in terms of % complete which was used to calculate the earned value relative to the schedule and budget allocation.

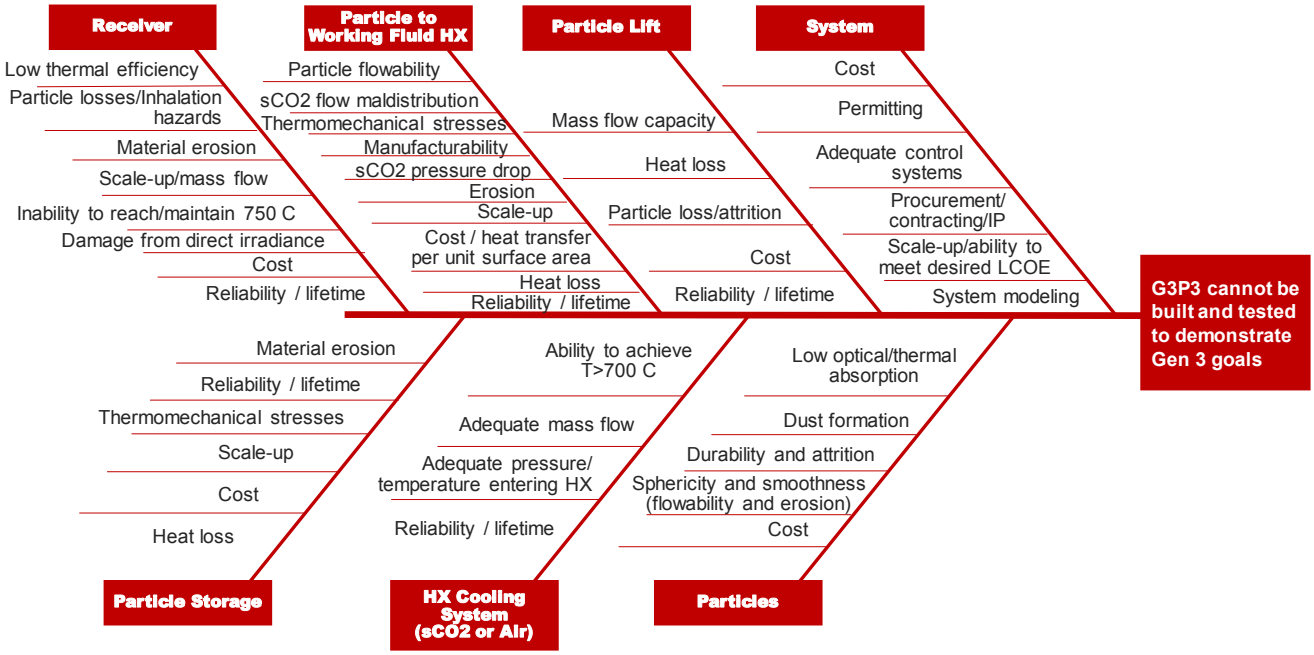

Figure 2. Ishikawa cause-and-effect analysis (fishbone diagram) showing key components and risks for G3P3.

Risk Identification (Focus on Phases 1 and 2)				Risk Analysis			Risk Monitoring and Mitigation					
Task ID	Category or Component	Subcategory	Risk or Potential Outcome	Impact	Probability	Matrix Score (1 - 25)	Risk Mitigation Task and Metrics	Owner	Due Date in Months	Percent Complete	Budget (DOE)	Earned Value
2.1	Receiver	Low thermal efficiency	Convective losses through open aperture as a function of wind direction and speed	High	High	16.00	Simulate or test mitigation measures (aperture covering, multistage release, air recirculation) to demonstrate reduced convective losses. Characterize impact of wind direction and speed on thermal efficiency with reduced variability in thermal efficiency due to wind. Demonstrate ability to predict heat (and subsequently) power generation.	Sandia	18	95%	$800,000	$760,000
2.1	Receiver	Low thermal efficiency	Heat transfer to the particles is too low, or heat losses (including egress) are too high	Moderate	Moderate	9.00	Develop better understanding of heat transfer to allow CFD models for optimising heat transfer and minimising heat egress	Adelaide	18	80%	$57,092	$442,349
2.4	Receiver	Low thermal efficiency	Receiver thermal efficiency is too low relative to desired 90% metric	High	Low	8.00	Propose solution to reach the 90% receiver thermal efficiency target and develop a simulation model of the solution	CNRS-PROMES	18	40%	70000	$28,000
2.1	Receiver	Low thermal efficiency	Receiver thermal efficiency overpredicted by multiphase CFD simulations	Moderate	Moderate	9.00	Emphasis on model validation using Sandia/CSIRO test results Comparison of modelling results using different techniques (Eulerian vs. Lagrangian)	ANU	18	70%	65348	$121,572

Figure 3. Excerpt from G3P3 risk register showing example tasks related to the fishbone diagram.

3.1.1. G3P3 Receiver Risk-Reduction R&D

In Phases 1 and 2, both numerical simulations and experimental test campaigns were performed to reduce risks associated with the particle receiver, which included low receiver efficiency, particle loss, material damage, and scalability. Alternative receiver designs were considered (falling particles, centrifugal, fluidized), and the falling particle receiver (FPR) design was selected as the baseline for G3P3 based on its demonstrated on-sun performance, low complexity, low cost, and other factors detailed in the evaluation results from a 14-person technical advisory committee (TAC) using an analytic hierarchy process to rate 10 factors including cost, reliability, efficiency, and scalability (Milestone 2.9 and 8.4). Appendix C provides additional details of the receiver down-selection process using the Analytic Hierarchy Process (AHP). The sections below therefore focus on the falling particle receiver tasks and findings.

3.1.1.1. Receiver Design Evolution

The evolution of the G3P3 FPR design from the existing FPR at the National Solar Thermal Test Facility (NSTTF) is described here. While the existing FPR successfully demonstrated the ability to achieve high particle temperatures, further changes were desired to improve the receiver thermal efficiency and reduce the sensitivity to wind. The G3P3 receiver design has seen considerable design improvements since the project's onset and the design evolution is depicted graphically in Figure 4. The annualized thermal efficiency of the G3P3 FPR has been numerically shown to be 83.6% with 1,216 available hours for testing subject to anticipated environmental conditions at the NSTTF in Albuquerque, NM.

R&D efforts began with lessons learned from past receiver designs and testing. Five potential design concepts were identified and analyzed in Phase 1 to address low receiver efficiency and wind sensitivity. These concepts included: the integration of a hood or tunnel, quartz half-shell aperture coverings, active air flow, cavity optimization, and a multistage receiver design. Each of these design concepts is briefly discussed below including a determination of their efficacy for use in the G3P3 FPR design. From the results of these design studies, two parallel paths were then pursued: an optimized receiver geometry (referred to as a reduced volume receiver or RVR) with an integrated tunnel (referred to as a solar nod optimized unobstructed tunnel or SNOUT) and a multistage receiver concept (referred to as the staggered angle iron receiver of StAIR).

The RVR with SNOUT served as the baseline conceptual design for the G3P3 FPR going forward into Phase 2. Further geometric optimizations were numerically explored, and additional features were investigated numerically and in testing. Geometric optimizations in the SNOUT shape, aperture size, and cavity dimensions improved compatibility with the NSTTF heliostat field and lowered anticipated wall temperatures inside the cavity and SNOUT. The additional features that were considered included an integrated receiver "chimney" and "wind relief" features on the exterior of the spillage board to further minimize the effects of wind. While these features were numerically shown to improve the overall performance of the FPR, the added complexity of integration with the G3P3 outweighed the performance improvement and were therefore excluded from the final design.

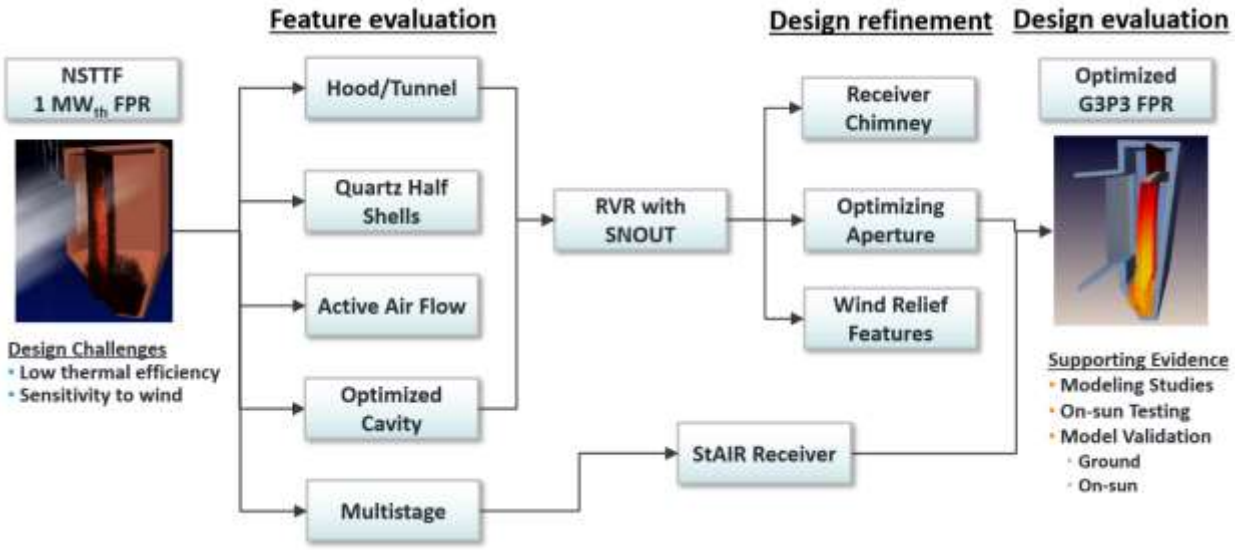

Figure 4. Design Evolution for the G3P3 FPR

Extensive "ground-based" and "on-sun" testing was conducted at the NSTTF on the final features to be integrated with the G3P3 FPR. These test campaigns were designed to experimentally evaluate each of the planned features for the G3P3 design and collect validation data that would provide confidence in the modeling capabilities. The existing FPR at the NSTTF was retrofitted to explore the performance of the RVR, the SNOUT, and the StAIR. The results of these test campaigns are discussed in more detail below, but both testing campaigns have demonstrated that the identified features have improved the overall receiver thermal efficiency. In addition, on-sun testing of the StAIR concept has demonstrated that the multistage design has increased the curtain opacity and the particle distribution while decreasing back wall temperatures in the cavity. As such, a single stage from the StAIR design was integrated in the final G3P3 FPR design.

The remainder of this section provides additional details about the initial design considerations and the design studies to evaluate each feature described in Figure 4.

3.1.1.1.1. Initial Receiver Design Considerations

At the onset of this project, initial design considerations included the use of a north-facing, cavity-type receiver and an increased target input power over existing FPR designs. Cavity-type FPRs are a proven design that have been experimentally shown to reach particle outlet temperatures in excess of 800°C, and the majority of FPR designs to date have been cavity-type receivers that help to minimize radiative losses to the environment and the effect of wind on the falling particles. As such, a cavity-type receiver is the basis for the G3P3 design given the experience and success at the NSTTF. A north-facing design was selected to be compatible with the NSTTF heliostat field. Preliminary ray-tracing simulations were performed on the NSTTF heliostat field and demonstrated that between 2 – 3 MW of input power was available consistently throughout the year. Previous numerical studies have shown that the receiver efficiency is increased at higher powers due to a decrease in the relative fraction of energy lost advectively [16].

3.1.1.1.2. Hood/Tunnel

Conclusions drawn from the 2018 NSTTF FPR test campaign suggested that the inclusion of a 'hood' over the aperture could offer improved thermal performance by decreasing advective losses, susceptibility to wind, and increasing the concentration of radiative flux into the receiver. Numerical

models of the NSTTF 1 MW_{th} FPR were developed with and without a candidate hood over the aperture to investigate this effect subject to different wind conditions. The results of the study suggested that advective losses from the receiver with this feature saw as much as a 10-50% decrease for relevant wind conditions. Additional details about this study can be found in the Phase 1 continuation report. From the positive results of this study, a similar converging 'tunnel' concept was then explored in the cavity optimization study described below.

3.1.1.1.3. Quartz Half Shells

Quartz half shell aperture covers were studied extensively both experimentally and numerically as a means to obstruct advective losses through the aperture. Quartz is mostly transparent to radiation in the solar spectrum and opaque in the thermal spectrum. Using a quartz half shell geometry allowed for minimizing reflections to the environment from radiation aimed at the aperture at an off-normal angle. Furthermore, early numerical simulations of the existing NSTTF FPR suggested that theoretical efficiencies of 90% could be achieved by eliminating advective losses.

Experimentally, the response of a single quartz half shell to concentrated solar radiation was investigated using an existing radiometer test stand at the NSTTF. Both the survivability and the solar transmissivity of pristine and soiled quartz half shells oriented with the convex and concave side towards the heliostat field were studied. Average total transmissivities were found to be between 0.94-0.97 depending on the half shell orientation. Qualitatively, a soiled quartz half shell (*i.e.* fingerprints and visible dust) handled several minutes of exposure to high flux (~1.2 MW/m^2) without any visible signs of change or damage.

Numerically, a simplified receiver subdomain CFD model was used to study the change in the thermal efficiency with the inclusion a partially covered and fully covered aperture using quartz half shells. Simulation results showed that quartz aperture covers can increase radiative losses, and in a partially covered case, half shells can also increase advective losses from the aperture. However, with sufficiently high transmissivity in the solar spectrum, decreases in the advective losses can outweigh increased radiative losses at higher receiver operating temperatures. Although the improvement in thermal efficiency was not expected to approach the targeted millstone metric of 5%-points (M.2.2). Quartz transmissivity was shown experimentally to be relatively high, but the expected high sustained operating temperatures, the inconclusive results from the numerical study, and question about scalability led the team to suspend further investigation of quartz aperture covers for the G3P3 FPR. As a result, on-sun tests with quartz half shells were not pursued as defined in Milestone 2.3. Additional information about these studies and the conclusions can be found in [17].

3.1.1.1.4. Active Air Flow

Active airflow control in a cavity-type FPR offers a path to mitigate both advective and particle losses. Two active airflow configurations were considered: (1) once-through suction and (2) forced air injection in front of the aperture (i.e. an "aerowindow"). In the case of once-through suction, energy lost from the hot air being removed from the cavity needs to be minimized so that cold ambient air does not get pulled into the cavity and convect heat away from the particles. Recirculation of the hot air back into the cavity at a different location can offset this effect, but the high temperature equipment and flow rate control required to accommodate different wind conditions and the modest benefit observed numerically precluded further investigation of this strategy.

For forced air injection, a properly configured aerowindow across the aperture can reduce advective losses substantially for calm conditions. Although some improvement was observed in numerical

models for windy conditions, an aerowindow in the presence of wind did not definitively show an ability to mitigate advective losses at high wind speeds. Therefore, the inconsistent improvements to the thermal efficiency were deemed not to justify the added complexity and cost of implementing an active airflow system. Furthermore, while active airflow methods are tractable for a 1 MW_{th} cavity receiver with an ~1 m^2 aperture, the scalability of these active airflow methods is questionable when considering commercial scale receivers with 100 to 500 m^2 apertures. Additional information about these studies can be found in [18].

3.1.1.1.5. Cavity Optimization

Although advective losses from cavity receivers has been studied extensively in the literature, FPRs introduce new challenges since the falling particles induce more complex flow inside the cavity. As a result, an optimization study was undertaken to minimize advective losses starting from the existing NSTTF FPR geometry integrated with a converging tunnel concept (based on the positive hood/tunnel results described above). In total, twelve geometric parameters were optimized to minimize advective losses using CFD simulations of the different FPR realizations. Details on the methodology and results of the optimization study were published in [19]. The final optimized geometry was refined further to accommodate practical considerations. For clarity, the converging tunnel integrated with this optimized cavity geometry is referred to as the SNOUT.

A CFD simulation of the final FPR optimized geometry was performed and the resulting thermal efficiency was found to be 86.9% in quiescent conditions for a nominal input power of 2.5 MW. The flow field inside the cavity colored by the air temperature (K) and the different loss mechanisms for the FPR are depicted in Figure 5. A preliminary wind study on the geometry demonstrated minimum thermal efficiencies of 80% subject to more northern winds up to 15 m/s. Further optimizations to the geometry are described below including a more expansive study of the effect of wind on the thermal efficiency.

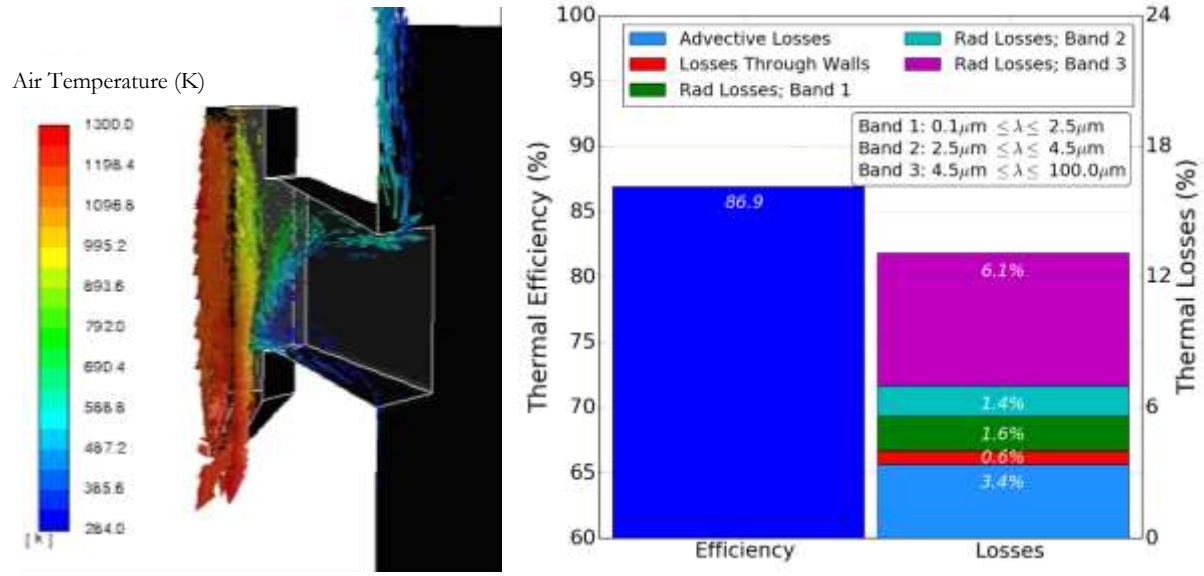

Figure 5. CFD simulation of the velocity field inside the optimized cavity geometry colored by the air temperature (K) (left) and the thermal efficiency and fraction of energy lost from different loss mechanisms (right)

3.1.1.1.6. Multistage Release

To slow the speed of falling particles through the cavity and increase the curtain opacity, a multistage receiver concept was investigated. A "catch-and-release" style multistage system was pursued where particles passively fall into angle-iron troughs where they overfill and continue falling through the cavity (i.e. staggered angle iron receiver or StAIR). By spilling the particles over the front lip of the trough facing the irradiation, no bare surfaces are directly exposed. A cold flow testing rig was designed and constructed to confirm improved curtain opacities and test for optimal spacing, number of troughs, and trough shapes. Four basic trough geometries (depicted in Figure 6) were evaluated using this rig. Full details on the methodology and results of this study were published in [20]. Ultimately, the "hybrid" trough geometry was found to be the most resilient to fluctuations in the curtain impact location and minimized the curtain transmissivity upon re-release. The hybrid trough design was used in subsequent on-sun testing.

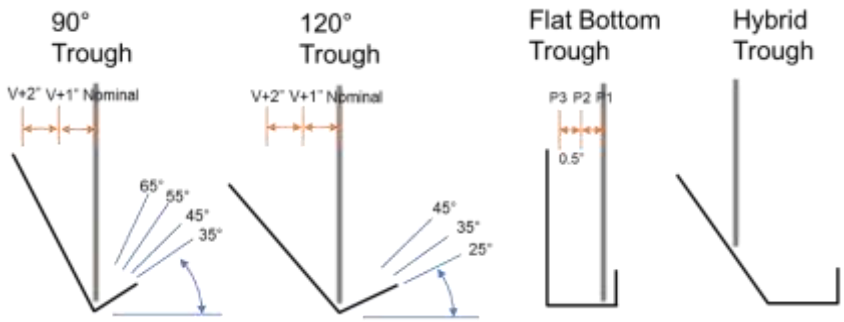

Figure 6. Cross section (black lines) of four trough geometries with orientations (blue lines) for angle iron troughs and horizontal positions (orange lines) relative to the particle curtain (gray vertical line) for the angle iron and flat bottom troughs.

Numerical CFD models of the StAIR concept integrated with the NSTTF FPR were developed using simplified physical models for the particle-trough interactions. Models demonstrated that troughs significantly changed the velocity field inside the cavity depending on the number of troughs and the location. Translating the particle curtain closer to the aperture with each stage minimized the cold air being entrained in the cavity. This had the effect of improving the thermal efficiency in quiescent conditions though optimal trough placement could not be realized in on-sun testing due to competing test objectives (investigating a cavity truncation) and limitations in how troughs could be retrofitted inside the cavity. Furthermore, back wall temperatures behind the curtain were significantly lower with a multistage design from the increased curtain opacity. The full results of the study are published in [21].

Milestone 2.4 called for a parity plot comparing the thermal efficiency with and without a multistage design. The number of possible configurations for the trough shape, trough location, and the number of troughs indicated that a parity plot would not be the ideal tool to show higher thermal efficiencies for a multistage release. Reference [21] summarized various trough configurations and numerically identified an improved design for the NSTTF FPR increasing the thermal efficiency by 4.9%-points. However, some configurations were also found to reduce the thermal efficiency. Furthermore, including wind in the simulations for a multistage FPR did not yield different conclusions compared to a FPR without multistage features. Given that a multistage design for the NSTTF FPR was found that improved the thermal efficiency (and provided other benefits to the

thermal performance such as decreasing the back wall temperature), it was declared that the objectives of Milestone 2.4 were achieved.

3.1.1.1.7. Receiver Chimney and Wind Relief Features

A 'chimney' was proposed as a potential feature that could be integrated with the SNOUT, and additional obstructions, or wind-relief features, were considered on the exterior of the G3P3 tower spillage boards to disrupt winds coming from specific directions. Additional details about the implementation of a chimney into the SNOUT are published in [22]. While a chimney showed positive benefits to the receiver performance, the increased complexity of adding a chimney to the SNOUT and the decision to filter particle fines exiting the particle lift instead (see next section) prompted the removal of a chimney from the G3P3 FPR design. Opportunities to recuperate advective losses on utility scale receivers suggests that a chimney may be advantageous on larger particle-based CSP systems. Wind-relief features on the G3P3 spillage board were found to reduce advective losses from the most detrimental wind directions. However, like the chimney, the added complexity was deemed not to justify the inclusion of these features for the final G3P3 design. It still shows merit for future FPRs.

3.1.1.1.8. Particle Dust Removal

Published G3P3 studies including both on-sun particle sampling and modeling indicated that particle emissions from the open aperture of the falling particle receiver will be well below EPA and NIOSH standards for particulate pollution and inhalation hazards [23, 24]. However, to minimize particle emissions and potentially adverse impacts on the aperture irradiance, a cyclonic particle filtration system was designed for integration into the piping exiting the particle lift. We held meetings with Aerodyne, a manufacturer of cyclonic separators, and designed a small (~26-inch) SV50 cyclonic in-line particle separation system with a 0.25 HP DeKalb high-temperature blower to reduce particles fines above 2 microns by 75%.

3.1.1.1.9. Optimization and Final G3P3 FPR Design

A number of further geometric optimizations were performed on the RVR with SNOUT to arrive at the final receiver geometry to be implemented as the G3P3 FPR. Most of these optimizations were driven from ray-tracing simulations of the NSTTF heliostat field to minimize peak temperatures in the walls and other practical considerations. They include chamfered aperture openings, increased SNOUT angles to accommodate closer heliostats, and an increased aperture size (1.5→1.75 m^2). A slotted lip along the SNOUT's bottom surface recaptures larger particles ejected from the cavity minimizing overall particle inventory loss. Some of these design decisions are discussed in more detail in the quarterly reports and in [22].

An aperture size of 1.75 m^2, provides two primary benefits. First, it reduces the number of heliostats required to achieve 2 MW of power delivered to the aperture by decreasing the amount of irradiance that might otherwise be spillage. For a clear day in Albuquerque providing a DNI of 1000 W/m^2 at solar noon on the equinox, only 110 heliostats are required to deliver the design point 2 MW of power to the aperture. At this power, flux from spillage around the periphery of the SNOUT is calculated to be a maximum of 500 kW/m^2 (previously ~700 kW/m^2). Using a study summarized in the above citation, fluxes of 500 kW/m^2 will result in maximum temperatures on the SNOUT surfaces < 1250°C, well within acceptable ranges.

Based on the success of the StAIR receiver in on-sun testing (particularly with regards to the reduction in back wall temperature), a single hybrid trough was implemented in the RVR with

SNOUT. A single trough was used to minimize forward translation of the curtain, and the rear wall of the cavity was angled to accommodate the trough. Along with the geometric optimizations described above, these changes did adversely affect the FPR thermal efficiency from the original optimized cavity, but as will be shown later, the cumulative effect of these changes was small. The final recommended dimensions for the G3P3 FPR are depicted in Figure 7a, and a solid model realization of the geometry is in Figure 7b.

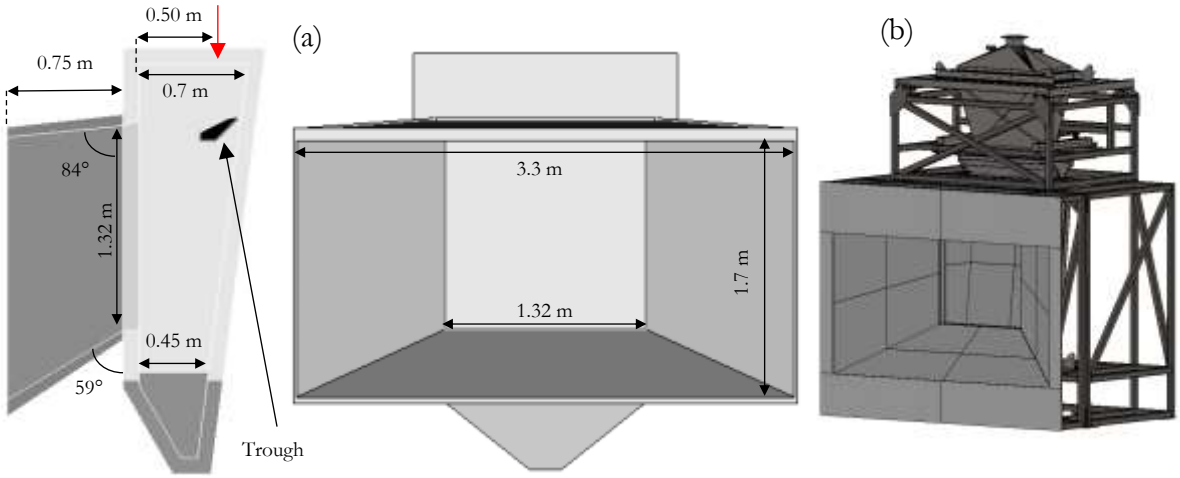

Figure 7. (a) Dimensioned drawing of the recommended G3P3 FPR, (b) a solid model realization of G3P3 FPR

3.1.1.2. G3P3 Falling Particle Receiver Modeling and Wind Characterization

Numerical models of FPRs were an integral component in the development of the final G3P3 FPR described above. In this section, the models of the G3P3 FPR are described and used to evaluate the performance of the design subject to the anticipated operating conditions. The nominal performance of the FPR is simulated subject to quiescent conditions followed by the anticipated performance to various wind speeds and directions. The effect of transient winds is also explored in addition to the computation of the annualized thermal efficiency of the final G3P3 FPR subject to anticipated winds and DNI throughout a typical year.

3.1.1.2.1. FPR Modeling Strategy

The CFD modeling strategy used to simulate an FPR receiver is briefly described here for reference. For a more complete description, a number of articles are available in the literature that describe the methodology [16, 25, 26]. The CFD models used a Lagrangian/Eulerian framework to simulate discrete particle parcels falling though an air continuum using either ANSYS Fluent® or Sandia's in-house SIERRA code suite. The particles were coupled to the air continuum inside and outside of the receiver via drag forces, heat transfer, and turbulent interactions. The realizable k-ε turbulence models were implemented in the domain.

A non-grey, discrete ordinates (DO) radiation model is coupled with the CFD model to include radiative transport into the receiver from the heliostat field. The non-grey model is divided into three bands: 0.1–2.5 μm, 2.5–4.5 μm, and 4.5–100 μm. All incident solar irradiance enters the domain in the smallest wavelength band. Ray-tracing simulations (NREL's SolTrace or SolarPILOT) of the associated heliostat field are used to define radiative boundary conditions (including both the

direction and intensity) on the north surface of the computational domain. The FPR thermal efficiency is computed by calculating the fraction of incident radiative energy on the aperture that is absorbed by the particles.

3.1.1.2.2. G3P3 FPR Quiescent Thermal Performance

CFD models of the final G3P3 FPR were exercised to quantify the thermal efficiency of the receiver and the losses from different loss mechanisms. Ray-tracing models of the NSTTF heliostat field have found that >2 MW of radiative power is available throughout the year for an aperture area >1.6 m^2 between -3 and +3 hours of solar noon with a DNI of at least 950 W/m^2 (additional details about this study are found in the Phase 1 continuation report). An average particle input temperature of 615°C was assumed with a desired average particle outlet temperature of 775°C. For an incident radiative power of 2 and 1.5 MW with a particle mass flow rate of 8.75 kg/s, the thermal efficiency of the receiver was simulated to be 85.1% and 81.8%, respectively. A visualization of the 2 MW simulation is presented in Figure 8 colored by the air and particle temperatures.

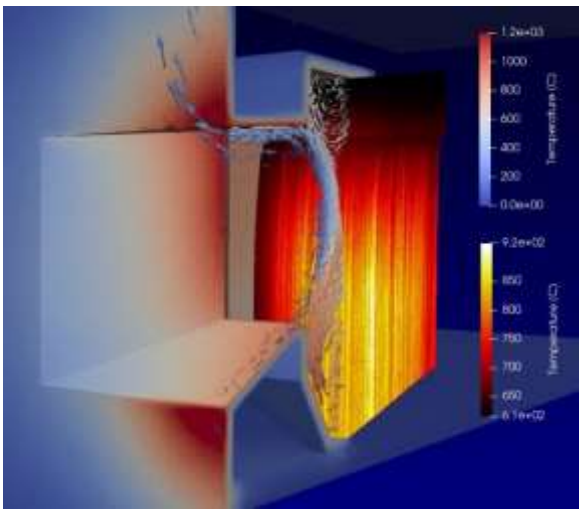

Figure 8. CFD simulation of the final G3P3 FPR design colored by fluid/wall temperature and the particle temperature (°C)

Energy is lost from the FPR radiatively or advectively through the aperture or via conduction through the receiver walls. For 2 MW of incident power, radiative losses accounted for 8.6% of the thermal energy lost (with the largest contribution, 4.4%, in the smallest wavelength band associated with reflections). Advective losses accounted for only 5.9% of the thermal energy lost owing to the receiver features implemented in the final G3P3 from the R&D effort described herein. For 1.5 MW of incident power, radiative and advective losses increased to 10.8% and 7%, respectively.

3.1.1.2.3. Model Uncertainty Estimation

The uncertainty in the numerical receiver thermal efficiency was estimated using early models of the existing NSTTF receiver. Given the similar scales between the G3P3 receiver and the NSTTF receiver, it was assumed that the model uncertainty would also be representative for the G3P3 FPR. A representative case from the 2018 test campaign was selected from among the set of experiments to help approximate the numerical uncertainty. This case specified an incident thermal power of 1 MW on the receiver aperture. An ensemble of simulations was then performed on this representative case varying a number model inputs based on very conservative estimates for the

uncertainty in these parameters. Engineering judgement was used to select these bounds from discussions with experimentalists and the chosen values are listed in Table 3.

Table 3. Model Input Uncertainties from Experiments

Input Parameter	Uncertainty
Avg. Incident Radiative Power	±8%
Wind Speed	±10%
Wind Direction	±10°
Particle Mass Flow Rate	±2%

Input Parameter	Uncertainty
Particle Inlet Temperature	±5°C
Avg. Particle Diameter	-25 μm
Ambient Temperature	±3°C

The incremental Latin-hypercube sampling (LHS) method was used to sample this space assuming a uniform distribution in the uncertainty of each model input. The receiver efficiency was computed for each of these cases to help quantify the variability in these responses from uncertainty in these model inputs. Note that this approach did not account for model form uncertainty inherent in CFD models with turbulence (more challenging to accurately estimate); however, the conservatism in the values were assumed to help capture some of this missing variability. From this LHS study, uncertainty in the average particle ΔT and the receiver efficiency was estimated to be ±11.1°C and ±9.9%-points, respectively.

3.1.1.2.4. Steady-state Wind Study

An earlier iteration of the G3P3 FPR was studied extensively subject to various steady-state winds at different speeds and directions. Previous numerical studies had shown that wind primarily affects the thermal efficiency through increased advective losses [16]. Therefore, a simplified CFD model that excluded radiative transport was used to quantify the changes in advective losses from winds while minimizing the computational expense. A total of 124 simulations were performed varying the wind speed (2.5 – 15 m/s), the horizontal wind direction (0 – 180° from the aperture normal), and the angle of attack (0 – 10° from the horizonal plane).

The results of the study are shown in Figure 9. The advective losses were normalized to an incident thermal power of 2 MW to more intuitively convey the detriment to the thermal efficiency from different wind conditions. Several conclusions were drawn from this study summarized as follows:

1. in the cases that completed, the angle of attack minimally affected the final thermal efficiency increasing it by approximately 1-2%-points,
2. the thermal efficiency from more southern winds had no discernable effect on the thermal efficiency compared to quiescent simulations,
3. the maximum advective losses from the receiver were computed to be 14% of the incident radiative power from winds 45 – 90° from the aperture normal at speeds of 15 m/s,
4. and wind speeds of 5 m/s or lower showed only very small increases in the advective losses.

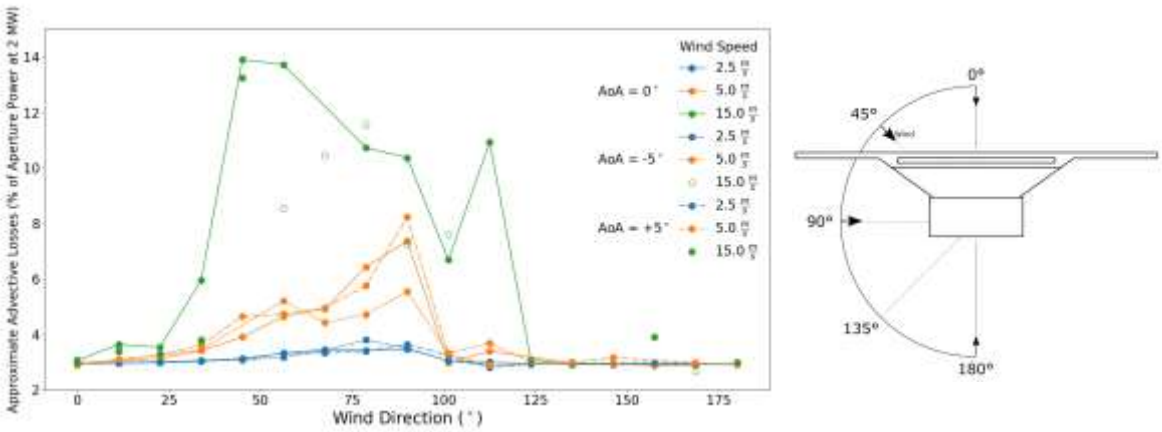

Figure 9. Advective losses for the G3P3 FPR at various wind speeds, wind directions, and angles of attack

3.1.1.2.5. Wind Transients

The previous wind study on the thermal performance investigated steady-state CFD simulations on a candidate G3P3 FPR subject to different wind speeds and directions. While these simulations are analogous to the effect that sustained winds would have upon the receiver, winds are inherently variable and further simulations were needed to understand the effect of wind transients. It is intractable to simulate every conceivable wind condition that could occur throughout a year; therefore, an anticipated worst-case gust condition was simulated using CFD models to bound the effect that a transient wind gust has on the FPR thermal efficiency. A realistic transient wind gust profile extracted from measured data at the TTU 200 m meteorological tower in Lubbock, TX was also simulated to further bolster the credibility of the following conclusions.

The two transient simulations are presented here, and additional details from these simulations can be found in the quarterly Phase 2 reports. For the worst-case wind transient, the G3P3 FPR was simulated with a time-varying wind impinging at 45° to the aperture plane (for a north-facing FPR this corresponds to a northwest wind). A long duration 15 m/s gust was simulated to understand the receiver timescale and to determine if the receiver would approach a steady-state condition. A steady-state simulation was used as the initial condition in quiescent conditions.

Radiative losses and losses from conduction through the walls were found to be negligibly affected by the wind transient and remained approximately constant. The particle curtain trajectory was also minimally affected by the gust. Changes in the advective losses during the gust from the initial condition accounted for the decrease in the thermal efficiency depicted in Figure 10 (left). Note that the thermal efficiency quickly reached a steady value during the gust. The timescale of the changes to the thermal efficiency was between 6-8 seconds. Furthermore, the new steady thermal efficiency was consistent with steady-state simulations of an equivalent wind speed and direction. Finally, after the wind transient had subsided, the thermal efficiency quickly returned to the initial thermal efficiency.

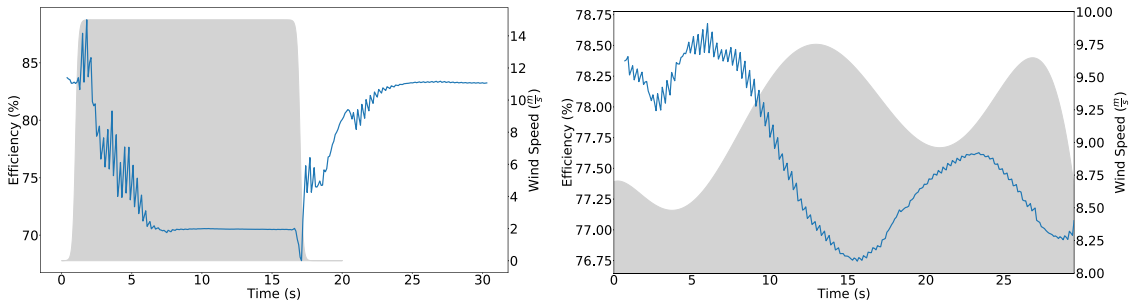

Figure 10. The G3P3 FPR thermal efficiency experiencing a 15 m/s wind gust (left) and more realistic wind gust profile (right)

The same conclusions were reached using a more realistic wind gust profile. For this profile, measured wind data at the TTU tower was analyzed to find a strong and representative gust profile that the FPR may experience at an elevation of ~47 m. The thermal efficiency of the FPR and the transient wind profile are depicted in Figure 10 (right). For this simulation, a steady-state simulation at the initial wind velocity was used for the initial condition. Note that the same timescales were observed in the thermal efficiency profile as before using a more severe wind gust profile.

Although Milestone 2.11 defines three wind profiles to be simulated, the low thermal timescale of the receiver suggested that the two simulated profiles were sufficient to draw conclusions from this study. These conclusions drive many of the assumptions used in estimating the G3P3 annualized thermal efficiency below and are summarized as follows:

1. wind transients primarily affect the receiver thermal performance through advective losses,
2. the timescale of the response to a gust was ~6-8 s for the G3P3 FPR,
3. during a gust, the thermal efficiency approached values simulated using steady-state simulations of equivalent speed and direction,
4. and the trajectory of the particle curtain was minimally affected by a wind transient.

3.1.1.2.6. Annual G3P3 Thermal Efficiency

Using lessons learned from the preceding studies, the annual thermal efficiency of the G3P3 FPR was estimated for anticipated conditions throughout the year at the NSTTF. For this study, the effect of wind was divided into two categories: sustained winds and wind transients. Sustained winds included average wind speeds recorded over intervals of several minutes to hours. Wind transients included wind characteristics on the order of seconds to minutes that significantly deviate from the sustained wind speed and/or direction. Using the historical Automated Surface Observing System (ASOS) dataset managed by the National Weather Service, the Federal Aviation Administration, and the Department of Defense, wind transients may be further categorized into wind gusts, variable winds (significant changes in wind direction), and squalls. The modeling approach presented here has reasonably captured the cumulative effects of wind transients including wind gusts and squalls. While 'variable winds' as defined are not included in this annual analysis, the *net* effect of this specific type of wind transient is presently assumed to be small.

The overall approach for accounting for the effects of wind on the FPR is as follows. At each hour throughout a typical year defined by the TMY2 dataset, the DNI, wind speed, and wind direction are used to compute a thermal efficiency for the receiver defined by the complementary ensemble of steady-state simulations of the FPR subject to wind. Linear interpolation between cases in the simulation ensemble is utilized to account for wind conditions not precisely simulated. The atmospheric boundary layer (ABL) "log-law" is leveraged to extrapolate wind speeds measured near

ground level (as in the TMY2 dataset) to a representative wind speed at the G3P3 FPR at ~47 m. More details about this extrapolation method are described in the Phase 2 first quarter report.

Hourly averaged wind conditions described in the TMY2 dataset are representative of sustained winds on the FPR throughout the year. To account for the effect of wind transients, the ASOS dataset is leveraged in five-minute intervals to provide estimates for the anticipated wind gust/squall frequency and intensity throughout a typical year. First, the dataset is used to generate typical wind gust speeds and frequencies at each hour throughout a typical year. The wind speeds are likewise extrapolated using the previous approach to account for the real receiver aperture elevation. Then, the wind gust speed, frequency, and direction are all used to compute an hourly 'derate factor' that further penalizes the receiver efficiency solely from the effect of wind transients. The derate factor is concatenated with the TMY2 dataset to incorporate an additional penalty into the subsequent annualized thermal efficiency calculation at each hour throughout the year. Additional details about steps involved in the derate factor calculations are described in the Phase 2 quarterly reports.

The methodology described above to account for winds annually on the FPR is applied here to meet the milestone criteria defined in Milestone 2.10 and calculate an annualized G3P3 receiver thermal efficiency for Albuquerque, NM. Using the DNI provided in the TMY2 dataset, the receiver is only assumed to operate when DNI values are > 800 W/m^2 within the window of time at least 1.5 MW of radiative power can be delivered from the NSTTF field. For DNI less than 800 W/m^2, the power delivered to the aperture is assumed to not meet the designed incident power from excessive cloud cover or haze. When extrapolated sustained wind speeds exceed 15 m/s, the receiver is also conservatively assumed to not operate since these speeds would likely approach maximum operating ground wind speeds of the NSTTF heliostats (but this assumption has only a modest impact on the available number of testing hours).

For the G3P3 FPR, the derate factor for each hour in which testing could occur was found to be ≥0.974 owing to the infrequency of gusts and the limitation that no testing takes place on excessively windy days with sustained winds exceeding 15 m/s. The final, annualized thermal efficiency of the G3P3 FPR is 83.6% with 1216 hours of testing at nominal conditions (out of a possible 1249 hours if no hours were excluded with excessive winds). It should be emphasized that the annualized thermal efficiency for the G3P3 FPR including the effects of wind was only ~1.5%-points lower than the simulated quiescent thermal efficiency of 85.1%.

3.1.1.3. Ground-Based Receiver Testing

A ground-based receiver test campaign was conducted on the existing NSTTF FPR to support the receiver R&D effort. The purpose of ground-based testing is two-fold: to build confidence in receiver models and to demonstrate the ability of the RVR and SNOUT features to improve receiver thermal performance. The tests are denoted as ground-based since the testing took place on the ground floor inside the existing NSTTF tower. These tests obviously did not utilize the heliostat field which removed the variability of the solar input. In addition, the variability of the ambient temperature, wind, and unsteady operation is also reduced since the tests are conducted inside the tower and allowed to reach steady-state.

In the ground-based tests, hot particles were circulated through the existing NSTTF receiver or a modified receiver featuring either a cavity truncation (approximating the RVR), a SNOUT, or both features. The receiver was integrated into a particle flow loop module as shown in Figure 11. In normal operation, particles fall through the receiver cavity and out the bottom hopper where they are redirected to an Olds (screw) elevator (behind the receiver module). They are then lifted back

into the top feed hopper of the receiver to be dropped through the receiver again. In this test series, the particles are redirected through a 150 kW_e, moving packed bed type heat exchanger that uses a staggered horizontal tube array of electrical cartridge heaters and PID control to heat particles to a desired temperature. Particles then flow through a particle-to-sCO_2 heat exchanger that is not utilized in this test campaign. The particle mass flow rate through the particle heater is controlled by a linear actuated slide gate at the particle-to-sCO_2 heat exchanger exit. A bucket elevator then lifts the heated particles exiting the heat exchanger to the Olds elevator, where they are then lifted to the feed hopper and recirculated through the receiver.

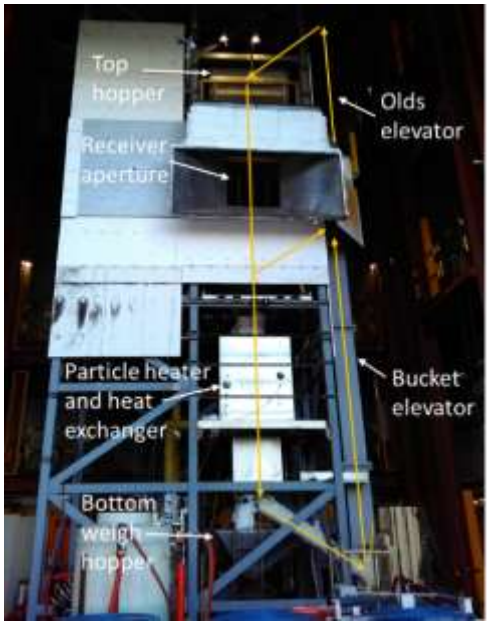

Figure 11. Falling particle receiver and particle flow loop module (left). Particle pathways are shown with yellow arrows.

A total of eight cases were considered: four receiver configurations and two test conditions. The four considered receiver configurations are: (1) no modifications ("baseline"), (2) SNOUT, (3) RVR insert, and (4) both SNOUT with RVR insert. Similar views of the front of the receiver with and without the SNOUT are shown in Figure 12. Depictions of the receiver cavity with and without the reduced volume receiver insert are shown in Figure 13. The RVR configuration shown in Figure 13b was an attempt to retrofit the existing NSTTF receiver with a more optimized cavity design similar to that used for the G3P3. The two test conditions were a higher (~6 kg/s) and a lower particle mass flow rate (~3 kg/s).

Figure 12. Receiver aperture and front face: (a) baseline and (b) with SNOUT

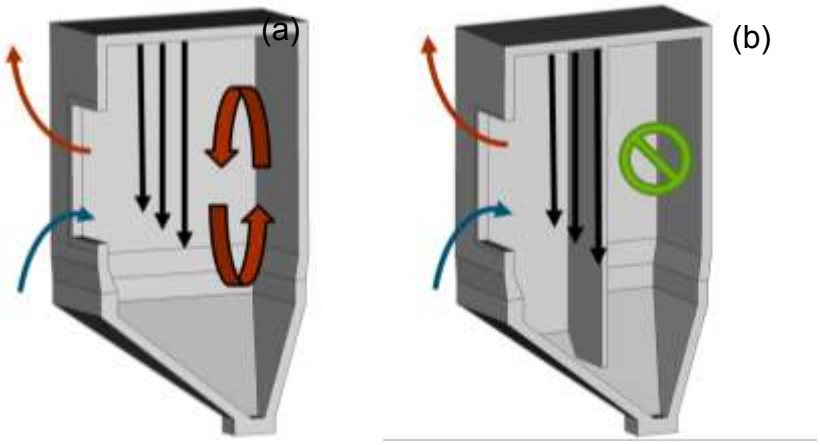

Figure 13. Baseline cavity (a) and with reduced volume receiver (RVR) insert (b)

Particles were circulated through the loop until the system reached steady-state. Once the system was at steady-state, advective losses out of the open aperture were computed with air temperature and air velocity measurements at 11 locations on the aperture plane using a thermocouple tree and a hand-held anemometer. Advective flow in and out of the aperture was visualized using smoke emitters, ignited below the receiver aperture. Fourteen different experimental steady-state cases were collected, and complementary CFD models of the tests were created to compare with the experimental results. Additional details about these experiments were summarized in the Phase 1 continuation report.

The results of the test campaign are summarized in Figure 14. In the left plot of Figure 14, the advective losses through the receiver aperture from each steady-state experiment were computed. The advective losses from equivalent CFD simulations of each experiment were then compared with the experimental results. For all but the baseline configuration, the model predicted the advective losses within experimental uncertainty, and if numerical uncertainty in the models was included, then all configurations would be captured within uncertainty. Overall, the model-driven features to improve the thermal performance that were integrated with the existing FPR resulted in decreased advective losses in all tests. Models confirmed this same behavior providing additional confidence in the CFD model's ability to predict the flow field in FPRs. In testing, advective losses were decreased by approximately 37.5% with the inclusion of a reduced volume in the receiver (~40 kW → ~25 kW).

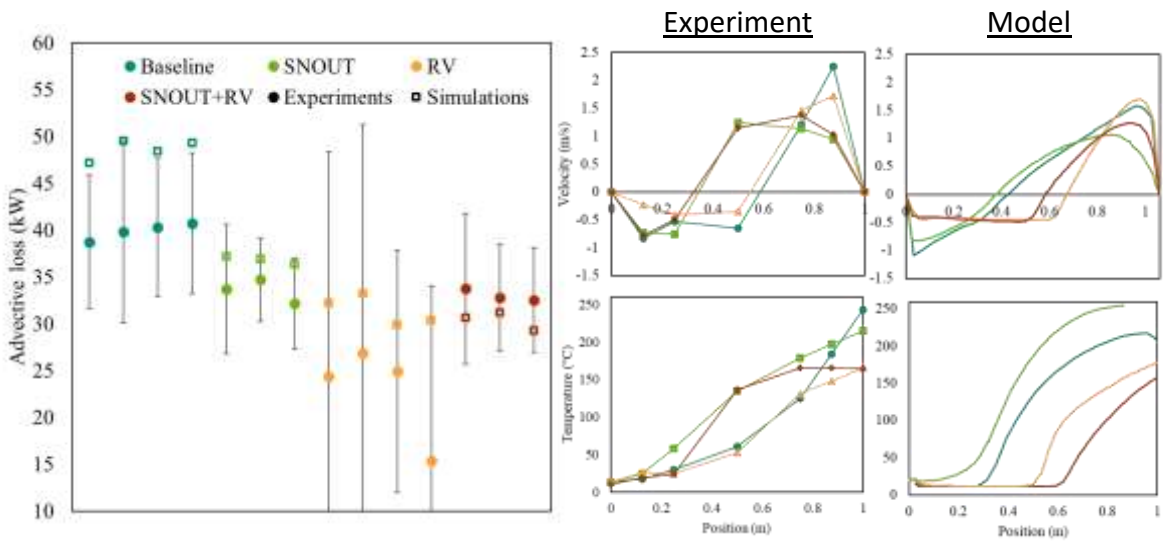

Figure 14. Net advective losses measured in ground-based tests for different configurations compared with models (left) and velocity and temperature profiles along the vertical midline of the aperture for different configurations (right)

In the plots on the right side of Figure 14, velocity and temperature profiles along the vertical midline of the aperture were compared between the tests and the models. While differences in the temperature and velocity profiles were observed for some configurations, there was close agreement in the RVR profiles between the tests and the model.

3.1.1.4. On-Sun Receiver Testing

To continue building support for FPR technology, an on-sun test campaign was conducted in Phase 2. There were a number of objectives in the on-sun testing including: evaluation of features and designs that showed promise in reducing receiver heat losses for the G3P3 system, collecting model validation data to build confidence in the modeling strategy, and demonstration of the approach to control particle outlet temperatures using a proportional-integral-derivative (PID) controller implemented in the data acquisition and control system. On-sun tests utilized the existing FPR and flow loop module on top of the NSTTF solar tower with appropriate modifications to explore each of the objectives described above.

The primary receiver features evaluated in the on-sun testing included the RVR cavity and a StAIR or multistage receiver. Both of these features were retrofitted into the existing receiver cavity and could be tested simultaneously. The RVR modification utilized the same cavity truncation as in the ground-testing depicted in Figure 13b. For the multistage receiver, up to two hybrid troughs (Figure 6) were implemented into the cavity that could be removed as desired for testing. The final retrofitted multistage receiver with two troughs is depicted in Figure 15 with particles flowing. The improved curtain uniformity and opacity after the first stage can be observed visually in the figure. Note that a SNOUT feature was not evaluated in on-sun testing from concerns over its use with the smaller aperture of the existing FPR. To test relevant fluxes on the receiver with a SNOUT could have resulted in damage to the receiver aperture hindering testing of other features.

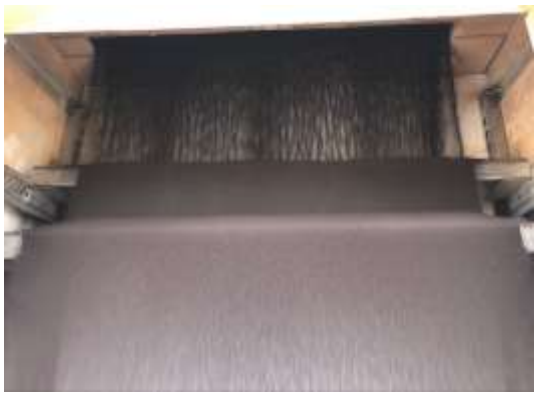

Figure 15. Particle flow over two troughs in receiver showing improvement in particle flow and opacity relative to free-fall particle flow and opacity above the troughs.

A PID controlled linear actuator was used to adjust a slide gate to automatically vary the particle mass flow rates entering the cavity from the feed hopper based on the particle outlet temperatures. If the particle outlet temperature exceeded the desired setpoint, the PID would adjust the slide gate to increase the particle mass flow into the receiver to reduce the particle temperatures, and vice-versa. This control system is an improvement over previous iterations that only utilized a proportional controller in the slide gate control.

Other changes to the experiment from previous test campaigns included the addition of 3-D ultrasonic wind anemometers installed around the receiver to measure wind velocity data. These anemometers provided a better understanding of the impact of wind on the FPR thermal performance. More general information about the instrumentation, data acquisition, and protocols used during on-sun testing of the falling particle receiver have been documented in previous publications [11, 27-30].

Table 4 summarizes the high-level objectives of the 2020 test campaign.

Table 4. Summary of objectives for on-sun receiver tests in 2020.

Feature	Conditions	Objective
Reduced volume receiver (RVR)	Up to 700 °C particle temperature; 500 – 1000 kW/m^2; 5 – 10 kg/s particle flow	Measure impact of reduced receiver cavity volume on thermal efficiency. Validate models.
Multistage release (StAIR)	Up to 700 °C particle temperature; 500 – 1000 kW/m^2; 5 – 10 kg/s particle flow	Ensure survivability. Measure impact of catch-and-release devices on backwall temperatures and thermal efficiency. Validate models.
Temperature control using PID control	Perturb irradiance by ~20% by adjusting the number of heliostats and recording change in incident power level	Use closed-loop feedback to maintain particle temperatures (±2σ ≤ 10°C) at a setpoint temperature using slide gate-controlled particle mass flow.

As discussed above, the thermal efficiency of the receiver, η_{th}, is defined as the fraction of incident radiative energy from the heliostats, Q_{in}, that is absorbed in the particles, Q_{abs}. The energy absorbed by the particles is computed experimentally by the change in particle temperature as follows:

$$\eta_{th} = \frac{Q_{abs}}{Q_{in}} = \frac{\dot{m}\left(h_{out} - h_{in}\right)}{Q_{in}} = \frac{\dot{m}\int_{T_{in}}^{T_{out}} c_P\left(T\right)dT}{Q_{in}} \quad (1)$$

where $\dot{m}$ is the mass flow rate, and h is the enthalpy of the particles. For the CARBO particles used by Sandia and others, the particle specific heat as a function of temperature has been measured by different sources over the years, though there is variation in the reported values at high temperatures. Three reported correlations are summarized in Table 5. Unless noted otherwise, the correlation developed by the Georgia Institute of Technology (correlation 3) is used in the following calculations for the receiver efficiency.

Table 5. Summary of specific heat correlations for CARBO particles.

#	Source	Specific Heat (J/kg·K)	Notes
1	Sandia (2013)	$365 \cdot T^{0.18}$ for 50°C $\leq T \leq$ 1100°C	Accucast ID50K; NETZSCH STA 409 C/CD Ar gas
2	Sandia (2017)	$148.2 \cdot T^{0.3093}$ for 323 K $\leq T \leq$ 1243 K	HSP 40/70; NETZSCH STA 409 C/CD Ar gas
3	Georgia Institute of Technology (2020)	$388.4 \cdot T^{0.1523}$ for 473 K $\leq T \leq$ 1053 K	HSP 40/70; NETZSCH STA 449 F3 Jupiter

3.1.1.4.1. Reduced Volume Receiver (RVR) Performance

Preliminary simulations of the NSTTF FPR including a backwall truncation as depicted in Figure 13b suggested that significant improvement to the thermal efficiency (exceeding 80%) could be realized for incident powers approaching 1 MW. These preliminary simulations are summarized in the Phase 1 continuation report. Recall that this backwall truncation approximated the optimized cavity design of the G3P3 FPR or the RVR concept. The improved thermal performance of the RVR was confirmed in the ground-based testing as shown from the reduced advective losses in Figure 14. As a result, this model-driven feature was tested in the on-sun test campaign to demonstrate the improvements to the experimental thermal efficiency over the existing receiver design ("baseline" design).

Since the backwall truncation was a permanent fixture in the receiver and could only be removed once at the top of the tower, the experimental receiver thermal efficiencies without the truncation were not measured in the present test campaign. Instead, thermal efficiencies measured during the 2018 test campaign were used for comparison as the "baseline" receiver without the truncation (*i.e.* Figure 16a). A total of 12 experiments were performed with the receiver featuring the cavity truncation with similar conditions to those of the 2018 tests. While the exact wind conditions during testing could not be precisely matched between test campaigns, the net improvement in the cavity with the truncation could be readily observed. A parity plot of the thermal efficiency from each test campaign is shown in Figure 16. For this comparison, the same correlations for the particle specific heat were used between test campaigns (*i.e.* correlation 2 from Table 5).

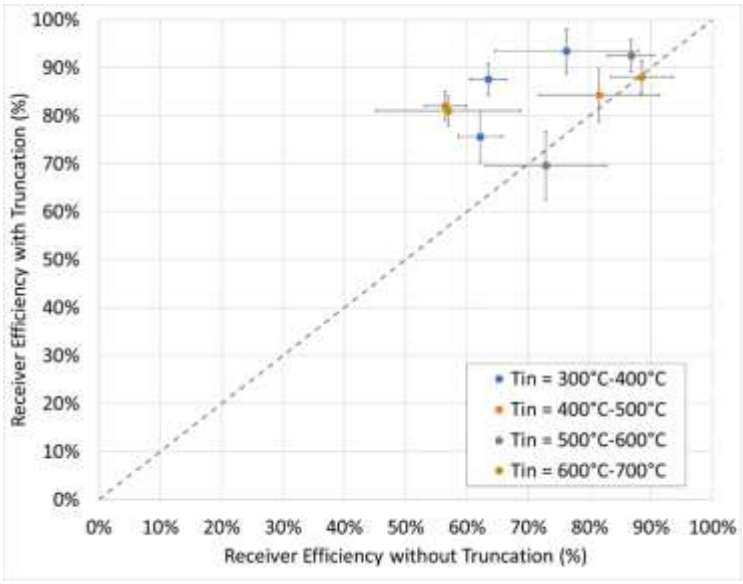

Figure 16. Parity plot NSTTF FPR featuring the cavity truncation (RVR) compared with comparable experiments of the NSTTF FPR without any modifications

As observed in Figure 16, the thermal efficiency of the receiver including the truncation (RVR) was on average higher in testing compared to comparable conditions of the receiver without this modification. Tests with similar inlet temperature and incident powers were compared as these variables have the largest effect on receiver efficiency. At higher inlet temperatures thermal losses increase and thus the effect of the RVR is seen to be more significant for an inlet temperature of 600–700°C. This conclusion supports the use of model-driven enhancements to the FPR and the RVR concept integrated with the G3P3 concept.

3.1.1.4.2. Multistage Receiver (StAIR) Performance

As observed in the cold-flow testing, higher opacities were measured in the particle curtains featuring multiple stages compared to freely falling particles. Since, the hybrid trough showed the best overall performance, up to two hybrid troughs were integrated in the existing receiver to study the effects of a multistage concept on-sun. Testing demonstrated significantly improved curtain uniformity over the freely falling curtain as shown in Figure 15. In addition, the troughs were tested on-sun for several hundred hours at peak fluxes that exceeded 1 MW/m^2 at times without any relevant degradation or deformation.

Simulations of the multistage concept showed highly variable changes to the thermal efficiency depending on the location and number of the troughs within the cavity. Recall that the trough location could not be optimized inside the existing NSTTF cavity due to space limitations and were not expected to show consistent improvements to the thermal efficiency. As a result, the thermal efficiency criteria laid out in Milestone 2.5 could not be met. However, visual inspections of the troughs after >100 hours of testing observed only superficial damage fulfilling part of the criteria in Milestone 2.5. The backwall temperatures behind the curtain were also expected to be consistently lower than temperatures with a freely falling curtain. The back-wall temperatures were measured for a freefalling receiver flowing at 9.7 kg/s and a single-stair receiver flowing at 5.1 kg/s for a similar incident power, 780 kW, and particle inlet temperature. The back-wall temperature profile for the single-stair receiver approached a *lower* steady-state back wall temperature than that of the freefalling

receiver despite utilizing approximately half the mass flow rate. This supports the hypothesis that a multistage receiver can significantly increase curtain opacity.

3.1.1.4.3. PID Slide Gate Control

Experiments during the 2018 test campaign had demonstrated that a control system integrated with the slide gate could successfully target an average particle outlet temperature. However, in these tests the previous control system used a simple proportional control that would experience oscillations around the target outlet temperature. This motivated the testing of a more sophisticated PID control for Phase 2. The objective of this testing was to control the average particle outlet temperature, $\pm 2\sigma \leq 10°C$, following a 20% perturbation in the incident solar energy from the heliostats. Initial testing was performed to manually tune the proportional, integral, and derivative values used for the controller to achieve an optimal response. A MATLAB extension was leveraged to generate a transfer function for the system based on its response characteristics, and the PID parameters were obtained to create a suitable system response. Additional tuning of the PID parameters was needed, but the approach used enables fast and automated tuning.

This type of testing was complicated by the "pseudo steady-state" behavior inherent in the experimental setup (since relevant radiative energy from the heliostats could not be fully rejected by the system). PID tests were performed as follows. First, the particles in the system were brought to relevant temperatures in the system. Then, the particle outlet temperature was set to a fixed value for a measured irradiance from the heliostats. During this time, the particle inlet temperature increased slowly, and the slide gate opened slowly to increase the particle mass flow rate and maintain the specified outlet temperature. This behavior is plotted in Figure 17a for a long duration where the PID controller maintains the outlet temperature at the setpoint before the temperature difference eventually gets so small that the mass flow rate cannot be increased further. The slide gate position in the figure is normalized with 1 being fully open and 0 being fully closed. Alternatively, a group of heliostats could be removed creating a perturbation in the irradiance on the receiver. The slide gate will respond by decreasing the mass flow rate to maintain the desired particle outlet temperature. Eventually, as the particle inlet temperature continues to increase, the slide gate will again begin to increase the particle mass flow rate.

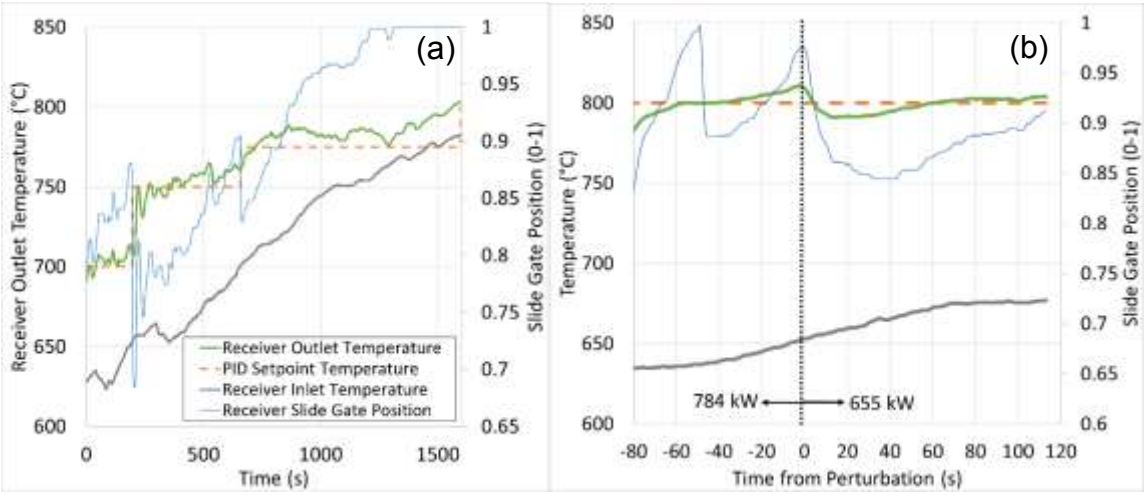

Figure 17. The PID controlled particle outlet temperature for an extended timescale (a) and responding to a 16% perturbation in the irradiance (b)

A plot of the particle outlet temperature during the perturbation described above is also shown in Figure 17b. Once the final set point temperature was defined at 83 s before the perturbation, the slide gate adjusted to maintain the desired outlet temperature and accommodate the increasing inlet temperature. Large fluctuations in receiver slide gate position were attributed to the controller's reaction to varying ambient conditions such as wind. Following the 16% perturbation in the incident radiative power, the slide gate initially lowered the particle mass flow rate to increase the particle outlet temperature. As the inlet temperature continued to increase, the slide gate then began to increase the mass flow rate to maintain the desired outlet temperature. For 120 s following the perturbation, 2σ in the average particle temperature was 0.92°C and the maximum average temperature deviation was less than 25°C, well within the success criteria defined in Milestone 2.12 and 2.7, respectively. Note that the oscillations described in the 2018 tests were not observed here. Continued refinement of the appropriate PID parameters for the PID controller will further improve the response time to perturbations.

The PID controller was also tested on a day with dense high clouds shown in Figure 18. The peak DNI recorded between clouds was 840 W/m^2 with dips down to 65 W/m^2 as the clouds passed over the heliostat field. The PID controller maintained the average receiver outlet temperature close to the setpoint, but insufficient irradiance while the field was shaded cause the outlet temperature to decrease. Between clouds, during periods of high irradiance, the receiver outlet temperature overshoots the setpoint. The slide gate opens to allow for the maximum flow rate of particles, but the maximum mass flow is not sufficient to maintain the setpoint temperature. The inverse is true for periods of low irradiance. A heliostat defocusing strategy used a PID controller to maintain the particle outlet temperature during heat exchanger testing conducted during this campaign. The defocusing PID controller adjusted heliostats radially outward from the aperture, decreasing the incident power thus decreasing the particle outlet temperature. A combination defocusing and receiver slide gate outlet temperature controller is being considered to allow for system operation for larger weather extremes.

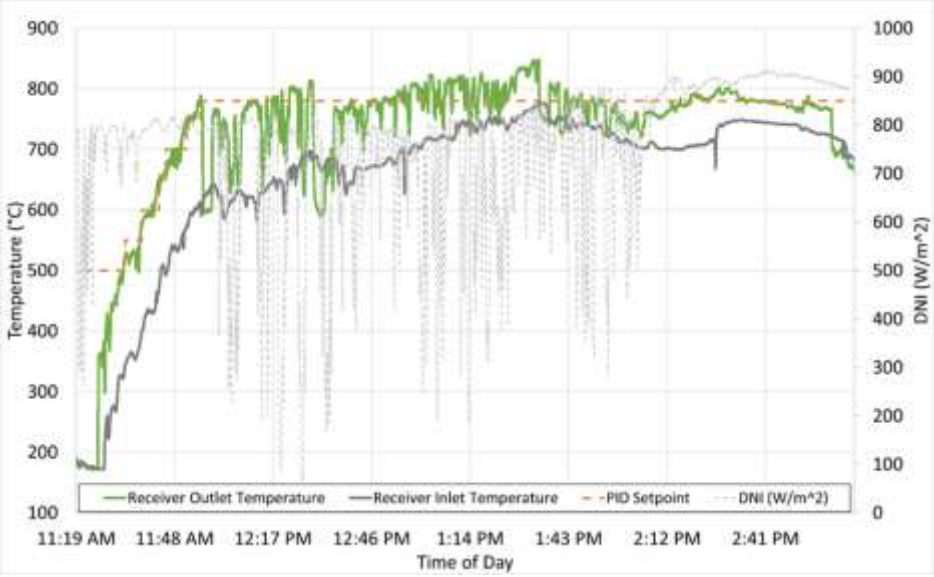

Figure 18. The particle outlet temperature responding to extreme transients in DNI caused by passing clouds.

The slide gate was found to largely meet reliability milestone criteria defined in Milestone 2.8 although a visual inspection of the system after the test campaign has not been completed. Full slide

gate operation was observed for the final 100 hours of testing. No servo failures and tripping of the over torque limit were recorded.

3.1.1.4.4. Feed Hopper Inventory Control

Milestone 2.6 was defined to ensure an adequate control system could be integrated into the feed hopper system to guarantee a sufficient emergency particle inventory in the feed hopper. However, inclusion of the SuNLaMP heat exchanger in the particle flow loop necessitated moving the mass flow rate measurement system to the top hopper. As a result, control systems designed to meet this milestone conflicted with accurately measuring mass flow rates during experiments. Therefore, this milestone was not explicitly addressed in the test. The success of the PID control algorithm for the receiver slide gate suggested that the same control strategy may be applied to the feed hopper inventory in the G3P3 system to guarantee a minimum inventory at the maximum mass flow rate (accounting for the delay created by the particle lift). Additional features including the receiver bypass line in G3P3 ensures that overflow protection is also provided.

3.1.1.4.5. On-sun Testing Experimental Summary

Over 100 hours of on-sun tests were performed at the NSTTF to evaluate the receiver features and processes described in the previous sections. Figure 19 shows photos of the control room and the falling particle receiver during on-sun tests. Three separate control systems are used during the tests to control the heliostat field, falling particle receiver, and sCO2 loop. Metrology (DNI, wind, temperature) and cameras are also implemented to record relevant data during the tests.

The complete ensemble of steady-state experiments is summarized here for all configurations explored in the test campaign. In total, 79 experiments were selected from the data and the experimentally measured receiver efficiency is plotted in Figure 20 at the various incident radiative powers of each experiment. The theoretical maximum efficiency (only considering radiative losses) at varying incident powers is also plotted.

Of the 93 experiments, 33 (35%) of which were above 80% efficiency, and 59 (63%) were above 70% efficiency. Note that several experiments were expected to have a low efficiency due to low incident powers used. Non-physical efficiencies were measured in some cases, and these values were explained by the average particle outlet temperature not being measured accurately. Throughout the test campaign, modifications were made to the slide gate to provide a more consistent and even curtain distribution from the top hopper, but this was not realized in all experiments. Retrofitting troughs into the receiver cavity also translated the curtain forward significantly closer to the aperture and this made it more susceptible to wind. Small fluctuations in how the curtain fell into particle temperature troughs also likely contributed to some additional uncertainty in the calculated average particle outlet temperature as this could not be observed in-situ.

Figure 19. NSTTF control room (left) and on-sun testing (right).

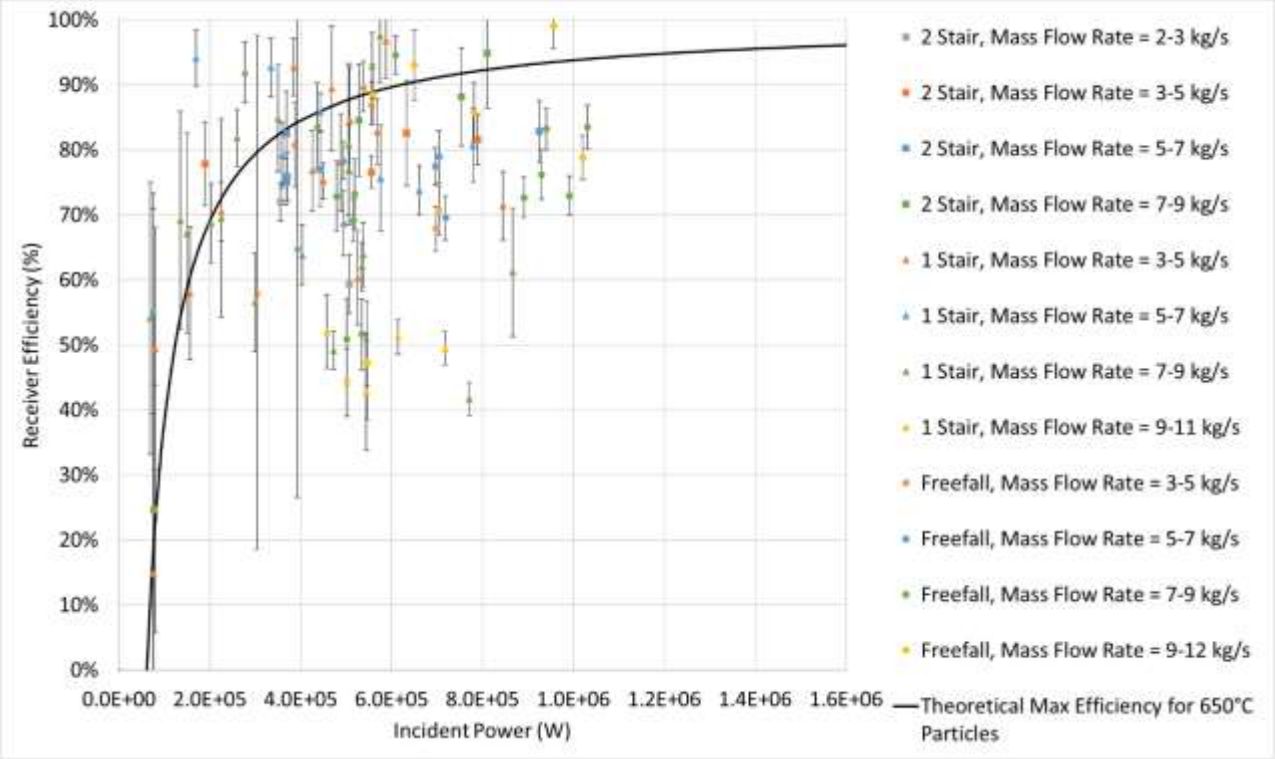

Figure 20. Experimental receiver efficiency from 2020 tests for applicable freefalling, 1-stair, and 2-stair configurations as a function of incident power

Figure 21a and Figure 21b plot the efficiency for only the freefalling and single trough configurations, respectively, at various flow rates. In Figure 21a, very few experiments were observed to have efficiencies lower than 70% and only at the lowest incident powers tested. Furthermore, as incident power increased up to 1 MW, the receiver efficiency was measured to exceed 80% as preliminary models of the truncated receiver cavity indicated (summarized in the Phase 1 continuation report). In single troughs tests plotted in Figure 21b, more scatter was observed in the data but most of the experiments followed the anticipated theoretical maximum

efficiency curve within experimental uncertainty. This implies generally low advective losses from the receiver. Outliers include the highest particle mass flow rates for the one trough configuration that will require additional investigation (all of this data was collected on the same day).

Overall, many multistage cases showed lower thermal efficiencies than comparable freefall cases indicating that many of the benefits provided by the truncation were being negated by the multistage implementation. As alluded to previously, limitations in how the troughs could be mounted within the existing receiver prevented installing them in the most optimal locations. As described in [21], the flow field inside the cavity is very sensitive to the location of the troughs and with the present trough locations, cold air was allowed to get behind the curtain (as with the baseline receiver configuration) and reduce the receiver efficiency. However, the primary benefits of troughs are found through improved curtain behavior, increased curtain opacity, and lower back wall temperatures. These benefits were observed in testing. For the G3P3, a more optimal location (including a sloped back wall) was specified for the trough to prevent degraded thermal performance from cold air getting behind the curtain.

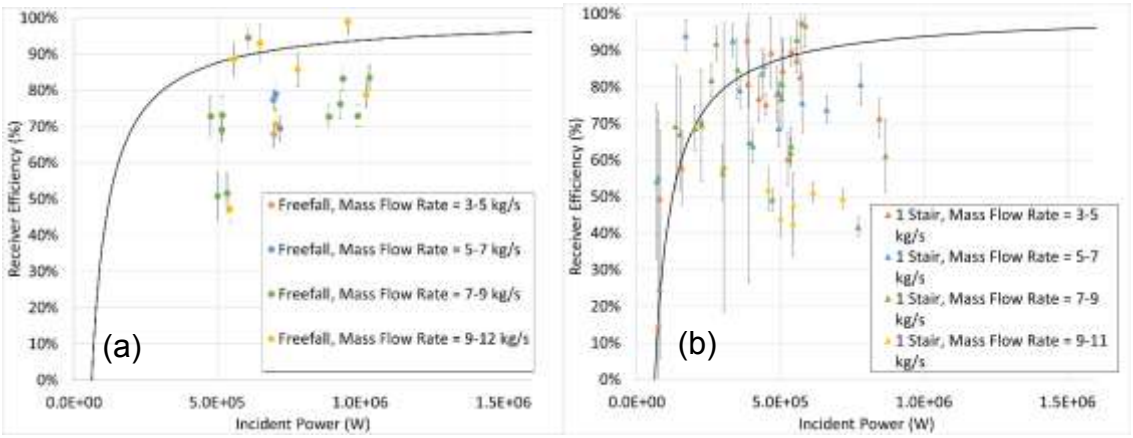

Figure 21: Receiver efficiencies for freefalling (a) and single trough (b) receiver configurations. The black line indicates theoretical maximum efficiency for 650°C particles

3.1.1.5. On-Sun Receiver Model Validation

In addition to the model validation performed on the ground-based tests, experiments from the recent 2020 on-sun test campaign were also used to validate the FPR modeling strategy. The purpose of these validation studies is to build confidence in the models used to design next-generation FPRs.

3.1.1.5.1. Model Validation of 2020 On-sun Receiver Tests

In addition to evaluating different receiver features to improve the thermal performance of the existing FPR, additional focus was given to measure wind velocity and direction around the tower using 3D ultrasonic anemometers placed at strategic locations. These new wind velocity measurements were important in specifying the boundary conditions in the CFD models of each steady-state experiment. As discussed in the on-sun testing, three different receiver configurations were investigated in the new test series: a truncated back wall (approximating the RVR), a truncated back wall with a single hybrid trough, and a truncated back wall with two hybrid troughs.

In total, 18 experiments were selected for comparison with receiver models of the test. Several cases were excluded from the validation study for a number of reasons, but the primary reasons included

insufficient data (e.g. wind wasn't measured on a particular day due to technical difficulties), concerns over the particle temperature distribution measurements, models did not converge, or the incident power was low (< 250 kW, resulting in large uncertainty in the experimentally measured efficiency). Other cases were collected too late in the campaign to be included in this study. As before, the average particle temperature ΔT and the receiver efficiency are compared each experimental case in the parity plot shown in Figure 22.

A linear fit of the data is provided in the two figures with a corresponding coefficient of determination R^2. A target slope of between 0.8 and 1.2 with an $R^2 > 0.8$ was identified for a successful validation in project milestone M.2.1. Note that, only three cases were available at this time in the study with incident powers > 700 kW. This likely explains the decreased slope in the ΔT over previous validation efforts where large ΔT cases were in short supply while still having an improved R^2. Additional wind measurements for the validation offered an improvement in the predicted efficiency over the previous validation study, but it still falls short of the desired milestone metric (slope=0.37, R^2=0.52). If we exclude low power cases (< 450 kW), then the R^2 improves significantly to 0.76. This indicates that most disagreement with the experiments is at lower powers. Furthermore, it should also be emphasized that the models are conservative since most of the predicted higher efficiencies are lower than corresponding measured values.

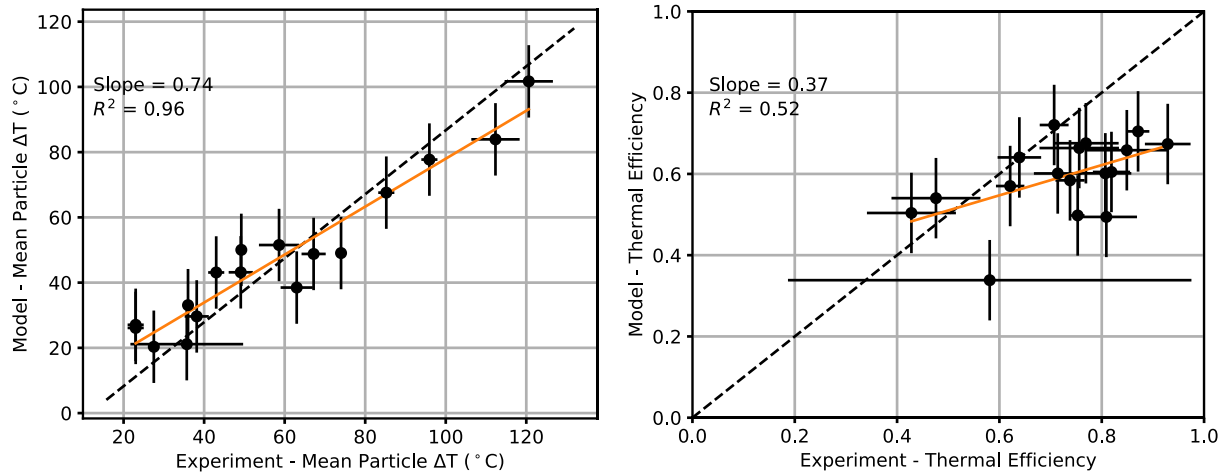

Figure 22. Parity plot of the average particle temperature change (left) and the receiver efficiency (right) in models of the 2020 on-sun receiver tests

3.1.1.6. G3P3 Receiver Materials and Costs

A number of different components are required to support the FPR in the G3P3 aside from the receiver cavity and feed hopper. These include the feed hopper slide gate, spillage board, the weigh hopper, calibration panel, cooling flow loops, and temperature, velocity, and flow rate measurement instrumentation. The total costs for each of these receiver components is summarized below in Figure 23. Note that previous cost estimates for the receiver provided in Phase 2 quarterly reports included preliminary estimates of labor for fabrication and installation. Those are excluded here (but included in Section 3.2.1.6) to focus the discussion on the purchases and materials only. Total cost for the receiver and associated components is $836,958.

Unlike other major components in the G3P3 system, many of the items listed in Figure 23 will be fabricated onsite leveraging the expertise of Sandia's technicians in manufacturing particle receiver

components. Receiver components fabricated onsite by Sandia technicians include: the falling particle receiver module, the calibration panel, the slide gate, and the weigh hopper. Receiver instrumentation (primarily thermocouples, anemometers, and associated data acquisition systems) will also be installed by Sandia technicians. For each of these components built onsite, the major COTS parts necessary for the fabrication were identified and included in the estimates above.

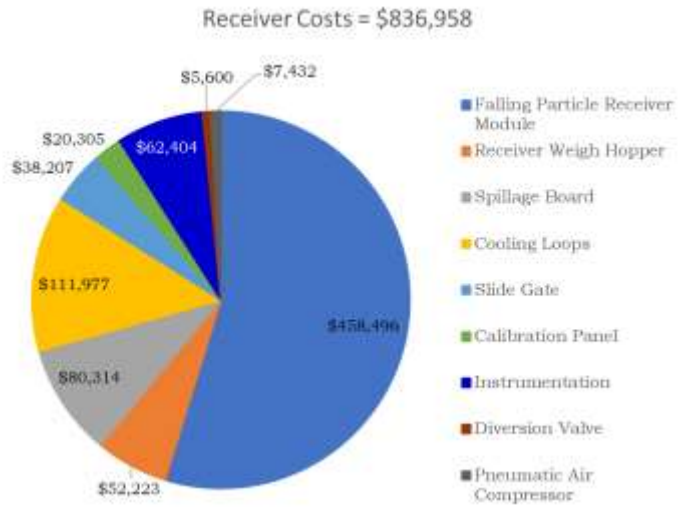

Figure 23. Receiver Costs Pie Chart Broken Down by Components

The falling particle receiver module is the most expensive element and is further subdivided into the receiver cavity, the SNOUT, the receiver feed hopper, the troughs, and the supporting module structure. Of these components, the receiver cavity and the SNOUT comprise most of this cost largely due to the use of 0.5" thick RSLE refractory board lining the high flux surfaces. Additional insulation behind the RSLE boards is comprised of the more affordable Duraboard® HD boards. Although the RSLE board is more expensive, it has been used successfully in the existing on-sun receiver testing and survived large incident fluxes. Approximately 180 ft^2 are required to cover the inner receiver cavity and SNOUT surfaces resulting in approximately ~$197,000 in RSLE boards alone. Additional saving could potentially be realized by only using RSLE on the back and side walls of the receiver.

Two cooling loops are identified for use in receiver components with the G3P3. The first loop is a fluid cooler to reject ~400-500 kW of heat from the calibration panel at 95°F. A Bell & Gossett e1510 5 HP motor circulates the water/glycol mixture at 100 gpm and 50 psi through the calibration panel and heat is subsequently removed from the loop using a 6-fan, 1.5 HP fluid cooler supplied by General Air Products. A large 500 gallon water/glycol tank increases the loop inventory. The second loop utilizes a packaged chiller for the Kendal radiometer and flux gauges. The 3-ton (~10 kW at 95 °F ambient) packaged chiller is a Model ACWC-36-Q supplied by Cold Shot Chillers®. Piping, valves, and manifolds to support the cooling loops has been specified. Installation of the piping for these components will be handled by Sandia technicians.

A National Instruments cRIO-9047 has been specified to record measurements for the receiver components and the cooling loops. A total of 90 type-K thermocouples are specified to be integrated into receiver module and feed/weigh hoppers measuring temperature in the walls and in the particles. Temperature and velocity of the wind around the receiver cavity are measured with five 3-D ultrasonic wind anemometers.

3.1.1.7. 100 MW_e Receiver Design

To support the scalability of particle technology, a 100 MW_e particle receiver was designed with sufficient thermal performance for a utility-scale particle CSP plant. Several designs were considered for the receiver, but ultimately a three-receiver falling particle system was conceived leveraging many of the design features developed for the G3P3 FPR (*i.e.* RVR cavity shape and a SNOUT). This multi-receiver concept shares similarities with the existing Khi Solar One CSP facility in South Africa.

3.1.1.7.1. Three-Receiver Design

A three-receiver design enabled more efficient use of the land surrounding the power tower than a comparable north-facing single-receiver design. Another advantage of a three-receiver design is the decreased aperture area, making it less susceptible to advective losses and wind. A receiver aperture size of 13 m x 13 m was targeted for each receiver cavity. Using NREL's SolarPILOT 1.3.8, an aperture area of that size corresponded to peak fluxes around the periphery of the aperture of ~600 kW/m^2. Fluxes of ~600 kW/m^2 were deemed to be acceptable based on previous experience at the NSTTF. The azimuthal angle of each receiver location was set to 90° (*i.e.* one receiver was north-facing, one receiver was east-facing, and the last receiver was west-facing) based on results from an optimization study on that variable.

Other assumptions to the SolarPILOT model included a solar multiple of 2.5, a thermal-to-electric efficiency of 50%, a receiver thermal efficiency of 85%, and an optical height of 250 m. For a 100 MW_e, this corresponds to a design point power of 588 MW_{th} delivered to the receiver apertures from the field. A simple aimpoint in the center of the aperture is used. The final heliostat field layout under these constraints is depicted in Figure 24a. The optical efficiency of the field at the vernal equinox was 58.5%, and the annual optical efficiency of the field was 52.3%. As shown in Figure 24b, the peak flux on the center receiver aperture was 4.68 MW/m^2 with an average irradiance of 1.34 MW/m^2. This was acceptable for particle technology since there are no practical flux limitations on particles unlike other competing technologies.

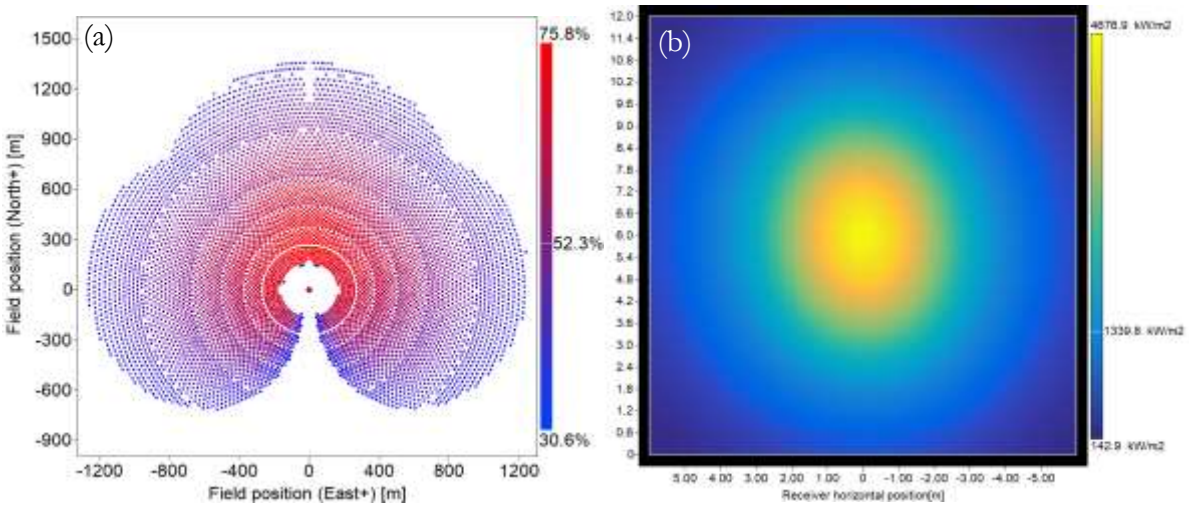

Figure 24. (a) Heliostat layout of the three-receiver concept depicting annual optical efficiency, and (b) the irradiance on the central aperture at the vernal equinox.

3.1.1.7.2. Parametric Receiver Study

An earlier iteration of the final proposed 100 MW_e FPR was studied numerically for different steady-state wind speeds, wind directions, incident powers, and particle mass flow rates. In total, 51 steady-state simulations were performed for wind speeds from 5 to 15 m/s, wind directions from 0° to 180° of the aperture normal, incident powers of 100 to 300 MW_{th}, and particle mass flow rates from 400 to 1040 kg/s. Note that not all combinations in the simulation ensemble were realized from a lack of numerical convergence. An average particle inlet temperature of 615°C was used for all simulations resulting in different particle outlet temperatures depending on the receiver efficiency and incident power. A CFD model of the receiver was utilized implementing the same physical models as described above for the G3P3 FPR. The final results were used to characterize the variability in the thermal efficiency for a 100 MW_e receiver and the develop correlations quantifying the advective losses from the receiver subject to different operating and environmental conditions. These correlations are subsequently used in technoeconomic models described later in this report to calculate levelized cost of electricity for utility scale, particle-based CSP plants. Correlations of this type are also useful for the broader CSP community to estimate advective loss contributions for FPR receivers. A visualization of the simulation for the candidate 100 MW_e FPR used in this study is depicted in Figure 25a. A parity plot showing the agreement of correlations for the thermal efficiency with CFD simulations thermal efficiency results is depicted in Figure 25b. Thermal efficiency varied in the parametric study between ~70% and 86% (where all cases below ~76% efficiency were limited to incident powers of only 100 MW_{th}).

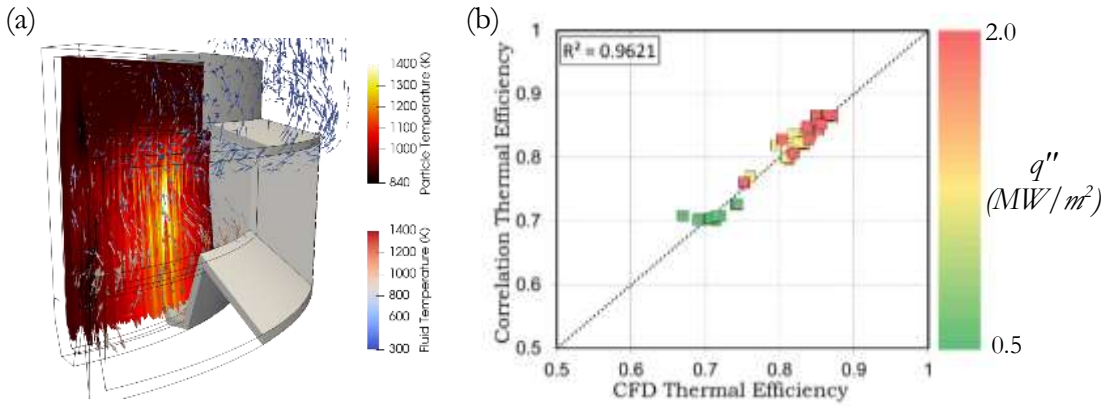

Figure 25. (a) CFD simulation of a candidate 100 MW_e FPR depicting particle and air temperature, and (b) resulting parity plot of the thermal efficiency.

3.1.1.7.3. Proposed 100 MW_e Receiver

A concave receiver cavity is specified for the final proposed 100 MW_e FPR leveraging a similar cavity profile as used in the G3P3 FPR. A concave cavity and particle curtain profile helped to minimize radiative losses to the environment, and the comparable profile with the G3P3 FPR helped to minimize advective losses from the cavity. Each of the three receivers is anticipated to receive approximately 200 MW_{th} from the heliostat field at solar noon with particle inlet temperatures of 615°C and particle mass flow rates of 885.5 kg/s. For a curtain length of 18.27 m, this resulted in a linear particle mass flow rate of 48.5 kg/s/m. To evaluate the thermal efficiency of the FPR, CFD models of the receiver performance under quiescent conditions were developed and exercised. The FPR geometry is depicted in Figure 26a, and a visualization of the cavity subject to the above conditions is depicted in Figure 26b. The quiescent thermal efficiency of the FPR was

83.1%. Radiative losses from the FPR were 6.9% of the total incident radiative power, and advective losses were 10.1% of the total incident radiative power.

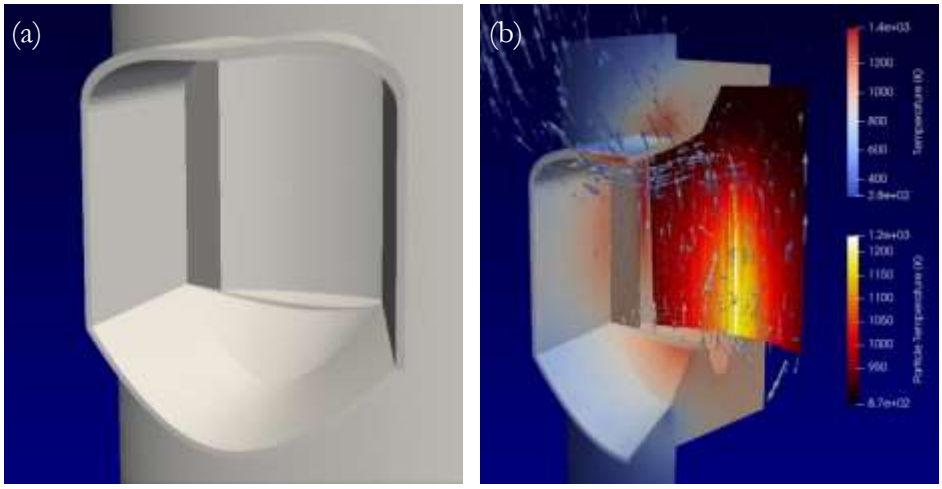

Figure 26. (a) Depiction of the 100 MWe scale FPR in the tower, and (b) visualization of the particle curtain temperature at quiescent conditions

3.1.1.7.4. 100 MW_e Wind Transient Derate Factor

Using the same methodology described previously for the G3P3 FPR, a wind transient derate factor can be computed leveraging the parametric wind study for 100 MW_e receivers to further penalize the FPR thermal efficiency from anticipated wind transients throughout a typical year. The derate factors and the cumulative derate penalty are plotted for both the G3P3 FPR and the 100 MW_e FPR in Figure 27. Daggett, CA was the CSP plant location for the 100 MW_e FPR. In this computation, it was assumed that the G3P3 FPR would not operate for conditions when DNI < 800 W/m^2 and the 100 MWe receiver would not operate when DNI < 100 kW/m^2 (under the assumption a commercial plant would need to operate at larger extremes than a pilot plant). Note that the higher optical tower height of the 100 MWe FPR (250 m vs. 47 m; resulting in stronger winds) results in a significantly larger cumulative derate penalty throughout a typical year. This derate factor for a 100 MWe FPR has been implemented in particle-based technoeconomic models to account for wind transients.

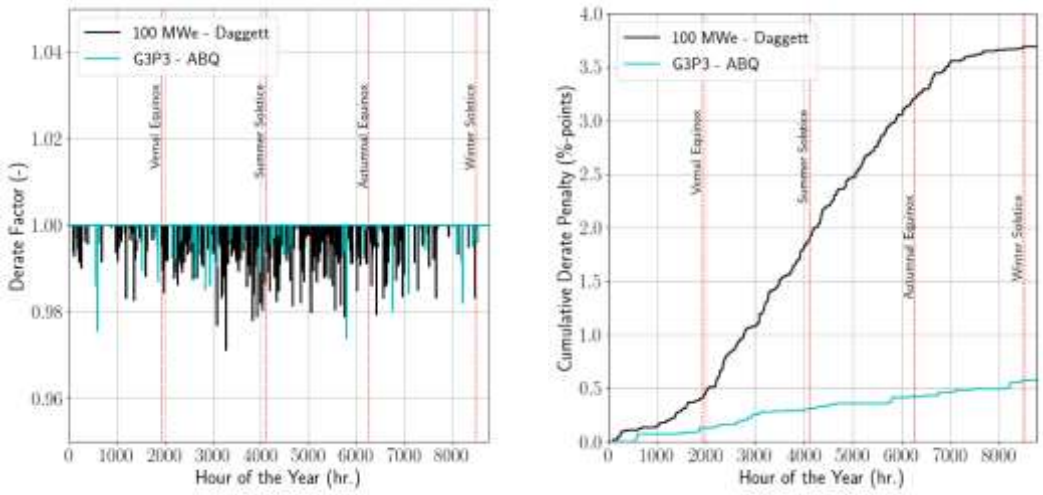

Figure 27. Derate factors for the G3P3 FPR (ABQ) and a 100 MWe FPR (DAG) (left) and the cumulative derate penalty for each receiver (right) throughout a typical year

3.1.1.8. Supporting Receiver Studies

Complementary receiver studies were performed by G3P3 partner institutions to (1) provide additional characterization and de-risking of the baseline FPR design and (2) evaluate alternative particle-receiver designs as a contingency to the FPR. The following sections summarize these activities and findings from Phases 1 and 2.

King Saud University (KSU)

Table 1 summarizes the key features and differences in the falling particle receiver designs used in G3P3-USA and G3P3-KSA. The larger G3P3-KSA receiver will employ a ceramic obstructed-flow receiver with multiple slide gates to demonstrate the ability to match particle flow to non-uniform irradiance profiles. The use of CARBO particles is being considered as the baseline, but evaluation of ultra-cheap silica sands for larger-scale systems is still being pursued. Laboratory and on-sun test results of the receiver design have been published [4, 31] and are detailed in the G3P3-KSA report [32].

Australian Solar Thermal Research Institute (ASTRI)

Our G3P3 partners at ASTRI consist of Commonwealth Scientific and Industrial Research Organization (CSIRO), U. Adelaide, and Australian National University (ANU). Each has contributed to the advancement of our particle receiver technology.

The Australian Commonwealth Scientific and Industrial Research Organization (CSIRO)

CSIRO has designed, constructed, and tested a multi-stage, truncated-cone (MsTC) receiver that complements the G3P3-USA StAIR design (Figure 28). Particle-flow testing revealed a stable, opaque particle flow over the catch-and-release troughs with dense converging flow where the irradiance will be greatest. Optimal trough spacing was determined using Monte Carlo radiation modeling [33], and numerical modeling revealed a reduction in reflective losses by 50% [34]. Experimental and numerical evaluation of adverse solar absorptance by particle dust emitted through the open receiver aperture showed that less than 0.5% of the irradiance would be absorbed by particle dust when considering different particle plume thicknesses and a measured particle size

of 2.5 microns. On-sun testing of the MsTC receiver system (with storage and heat exchange) is expected in early 2021. See the CSIRO final report for more details [35].

Figure 28. CSIRO multi-stage truncated-cone receiver design and testing.

U. Adelaide

Adelaide performed state-of-the-art laser-diagnostic experiments and CFD simulations to better understand factors that can either contribute to or mitigate particle egress from the receiver aperture. Key findings are detailed in the final Adelaide G3P3 report [36] and are summarized as follows:

- Horizontal baffles between the main receiver cavity and the particle collection chamber were shown to reduce particle egress by up to 70% for cases where the baffle opening was approximately 7 times the thickness of the curtain
- Placing the hopper exit midway between the aperture plane and the back wall generally resulted in the lowest amount of particle egress. However, this was not universal for all flow conditions and receiver geometries.
- Tapered sections designed to reduce the volume of the cavity where the tapered section was long (in the streamwise direction) reduced particle egress by approximately 40%.
- Decreasing particle sphericity increased the flow rate of entrained air, which in turn increased particle egress
- Head-on wind was found to increase particle egress by up to 350%. Particle egress was found to be insensitive to rear winds.
- Particle curtains with a larger particle size distribution resulted in greater particle egress
- The application of suction near the bottom of the collection chamber, in conjunction with downward co-flow next to the curtain was found to reduce particle egress by approximately 90% relative to the base case

The Australian National University

ANU has contributed to the radiation and heat transfer analyses of particle-light interactions in a falling particle receiver [34, 37] (in addition to systems analyses for G3P3 technology as summarized in Section 3.3). Detailed CFD models found a strong particle-size dependence on heat transfer characteristics and that it was possible to control the radiation absorption profile and location of peak absorption by tuning the particle size distribution and volume fraction of particles within the falling particle curtain. Spectral properties were also obtained for CARBO HSP and similar materials. These studies provide insight into radiative and heat-transfer mechanisms that can be

further considered to improve receiver thermal efficiency. Additional systems modeling can be found in the final ANU report [38].

DLR

As part of G3P3, DLR continued to design, test, and evaluate their CentRec® centrifugal particle receiver system [39, 40]. Ceramic particle temperatures >900 °C were achieved, and receiver efficiencies of 90% were projected based on increasing irradiance values up to 2 MW/m^2 (from tested values of 200 kW/m^2). A technoeconomic analysis was performed (see Section 3.3), and modular multi-tower, multi-receiver CentRec® systems were evaluated. One-, two-, and three-receiver configurations on a single tower were evaluated and compared to minimize LCOE. The CentRec® receiver is being shipped to Sandia as part of a Technology Commercialization Fund award to test the CentRec® at higher design fluxes of ~2 MW/m^2. Although this system is not part of the G3P3 baseline design, lessons learned from CentRec® will add to the body of knowledge for testing and improving particle receiver systems.

CNRS-PROMES

In Phases 1 and 2, CNRS-PROMES performed tests and analyses of their fluidized particle-in-tube receiver system [41, 42]. One of the objectives was to determine the maximum potential particle mass flow rate to scale the receiver to larger sizes. Tests using olivine sand (~30 micron dia) showed that up to ~0.54 kg/s could be obtained and controlled in a 3-m-long, 5-cm-ID tube (~300 kg/m^2/s). Different regimes of fluidized flow were delineated along the length of the tube. For a 50 MW$_t$ receiver, 5 panels with 360 tubes (7 m high) in an arc was designed. For a particle outlet temperature of 750 °C, the wall temperature was 950 °C. The receiver geometry and aperture dimensions were studied numerically and optimized, yielding receiver efficiencies of ~85%. On-sun testing of the fluidized particle-in-tube receiver is being planned at the Themis solar power tower in Phase 3.

3.1.2. G3P3 Particle Storage Risk-Reduction R&D

3.1.2.1. Storage Bin Design Evolution

The G3P3 storage bin design evolution merges existing knowledge of refractory insulation from the metallurgy and furnace industry with large-scale storage bin designs from the agriculture and mining industries. Figure 29 illustrates the primary design considerations as follows:

1. Aspect Ratio: Elongated silos are often chosen to store bulk solids because the form increases the area of particles in contact with the walls. Friction forces along the walls transfers through the particle bed and reduces floor stresses. However, increased surface area results in increased heat losses. Analysis revealed that stresses were minor and optimizing for heat loss was the best option.
2. Floor Design: Angled hoppers are used to fully evacuate the particle inventory which can reduce costs. However, flat-bottomed bins are stronger and less costly to construct. The weight requirements of commercial-scale particle storage make flat-bottomed designs more practical.
3. Flow Profile: Mass flow hoppers cause all particles to move with equal downward velocity resulting in predictable outlet temperatures close to the average temperature throughout the bin. Funnel flow designs may be thermally advantageous with smaller surface areas due to

the absence of the elongated hopper and insulating contributions from the non-flowing material along the flat-bottomed bin.

4. Refractory Insulation Layers: Low-density refractories have lower conductivities but may be vulnerable to erosion by hot particles. A multi-layer approach was selected with a high-density layer that was shown to be impervious to particle erosion on the inside followed by subsequent layers of low-density refractory and a microporous insulation.

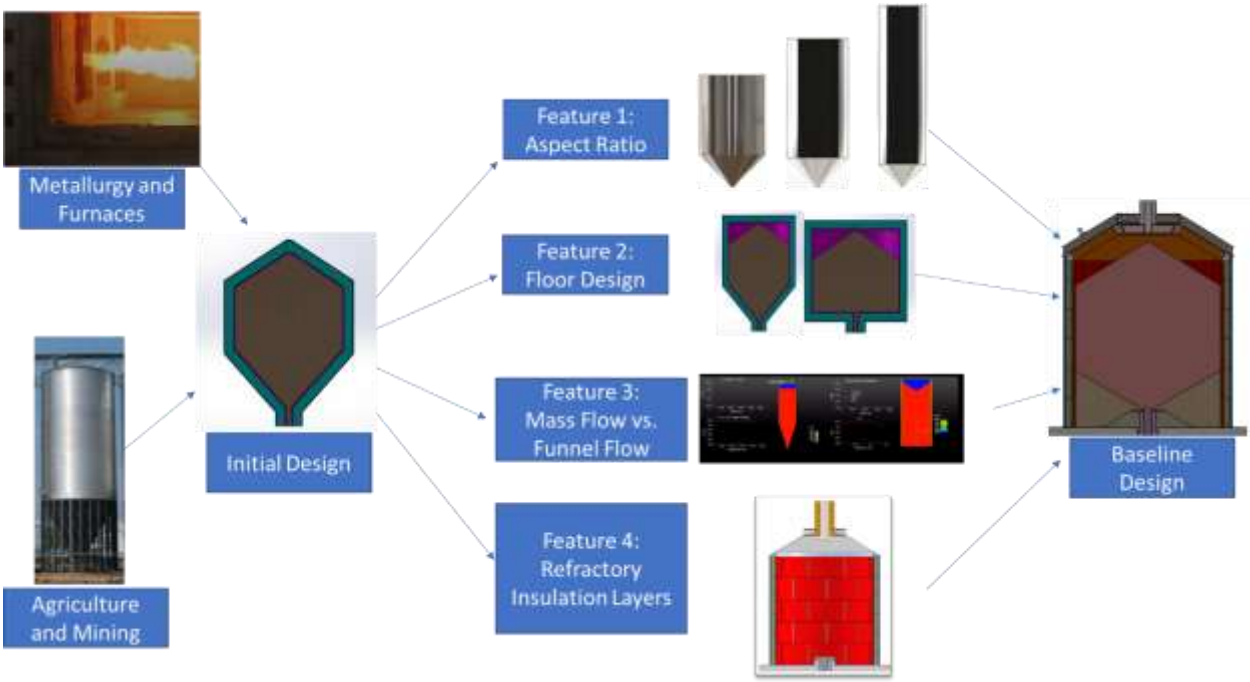

Figure 29. Design evolution flow chart for hot particle storage bin

3.1.2.2. Bin Design

The G3P3 thermal energy storage (TES) system is designed to deliver 6 MWh of thermal energy after 10 hours of deferred storage. The identical hot and cold bins are designed to be a passive system without trace heating or mechanical transport of particles other than by force of gravity.

Physical properties of the stored material (CARBO HSP 40/70) required for the design of the storage bin have been determined from flowability testing by Jenike and Johanson. Additional flowability expertise has been provided by Dr. Greg Mehos. The storage bin does not have a hopper system. Rather, the material will flow on itself moving away from the walls on the top surface to a central flow channel with the top surface exiting the bin first. When emptied of material, non-recoverable (stagnant) material will remain inside the bin in an inverted conical anulus around the outlet.

The characteristic outlet temperature profile for funnel flow bins was compared to that of mass flow to inform the decision to use a funnel flow bin. Figure 30 shows results from two bins with equivalent particle mass (~65 kg) and initial temperatures (800° C). The mass flow cone is shown in the upper left figure and the flat-bottomed funnel flow bin (modeled after a small test bin) is in the lower left corner. The outlet temperature results from the level-set model (described in section 3.1.2.3) are shown in the graph to the right. The yellow curve representing the mass flow design shows increased heat loss likely due to the increased surface area of the flow cone. The same result

was found using a heat kernel model (described below) simulating a bin with a different initial mass and flow rate.

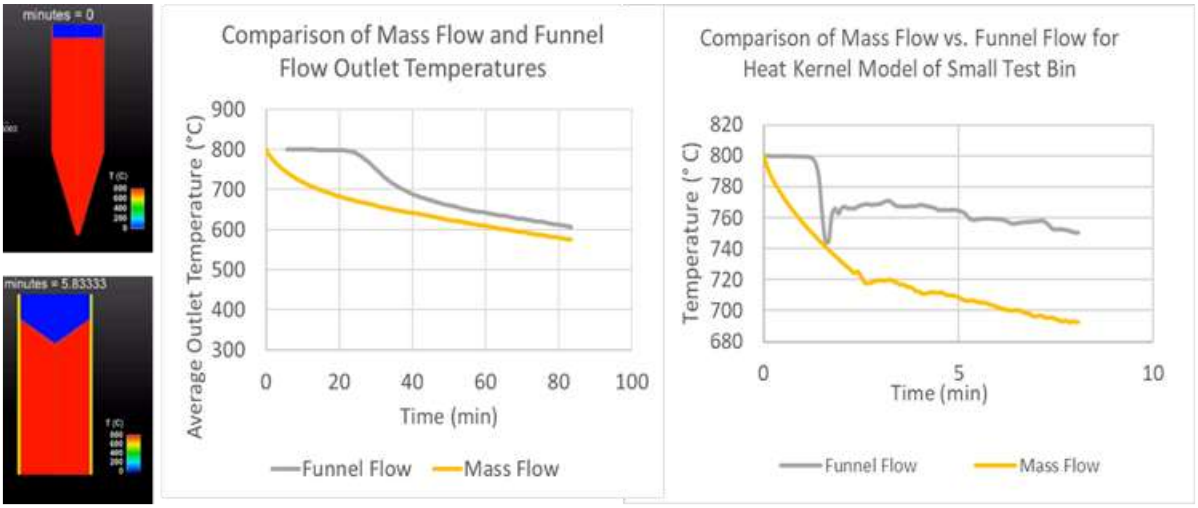

Figure 30. Two different models comparing outlet temperatures from mass flow and funnel flow bins independently show higher outlet temperatures for funnel flow than mass flow.

The storage bin design is shown in Figure 31 along with section view, exploded view and an abridged bill of materials. The bins each have a capacity to store 161,100 kg of CARBO HSP 40/70 particles which includes 108,600 kg of flowing particles for the required heat transfer media, 10,800 kg of extra particles for margin (~36 minutes) and system particle handling, and 40,600 kg of non-flowing particles covering the floor and forming a drawdown anulus around the outlet. The internal volume of the bin is ~85.0 m^3.

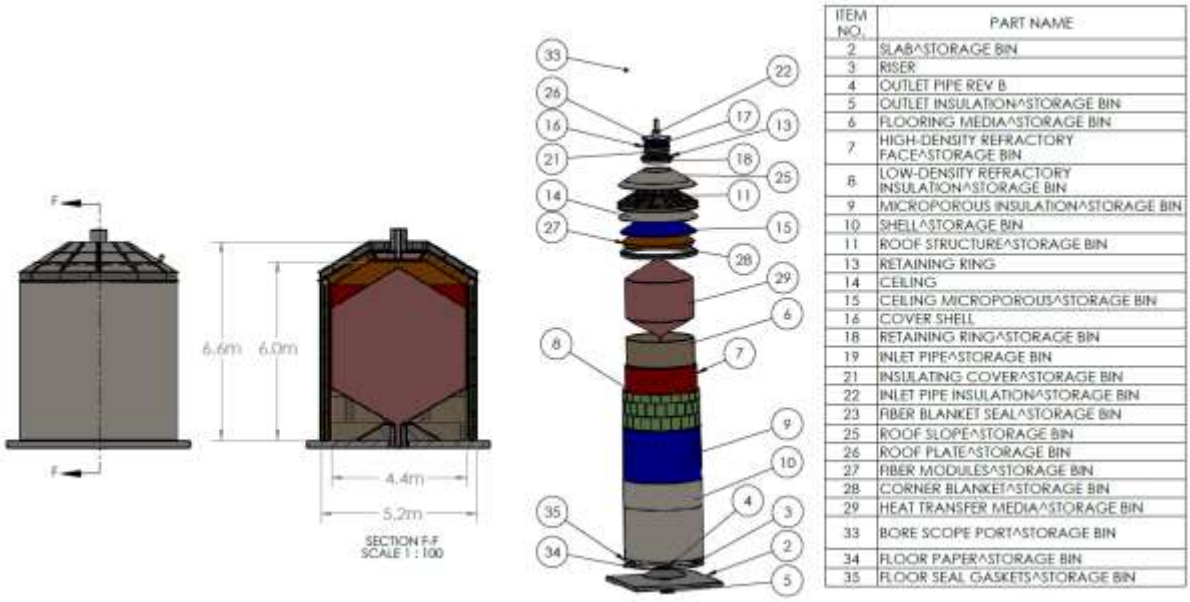

ITEM NO.	PART NAME
2	SLAB^STORAGE BIN
3	RISER
4	OUTLET PIPE REV B
5	OUTLET INSULATION^STORAGE BIN
6	FLOORING MEDIA^STORAGE BIN
7	HIGH-DENSITY REFRACTORY FACE^STORAGE BIN
8	LOW-DENSITY REFRACTORY INSULATION^STORAGE BIN
9	MICROPOROUS INSULATION^STORAGE BIN
10	SHELL^STORAGE BIN
11	ROOF STRUCTURE^STORAGE BIN
13	RETAINING RING
14	CEILING
15	CEILING MICROPOROUS^STORAGE BIN
16	COVER SHELL
18	RETAINING RING^STORAGE BIN
19	INLET PIPE^STORAGE BIN
21	INSULATING COVER^STORAGE BIN
22	INLET PIPE INSULATION^STORAGE BIN
23	FIBER BLANKET SEAL^STORAGE BIN
25	ROOF SLOPE^STORAGE BIN
26	ROOF PLATE^STORAGE BIN
27	FIBER MODULES^STORAGE BIN
28	CORNER BLANKET^STORAGE BIN
29	HEAT TRANSFER MEDIA^STORAGE BIN
33	BORE SCOPE PORT^STORAGE BIN
34	FLOOR PAPER^STORAGE BIN
35	FLOOR SEAL GASKETS^STORAGE BIN

Figure 31. 6MWh Thermal Energy Storage Bin (Left), section view (Middle-Left), Exploded View (Middle-Right), Bill of Materials (Right)

The interior geometry of the bins is designed to keep the flowing heat transfer media in a formation with minimal surface area when the bin is full to minimize heat loss. The bins will have an interior diameter of 4.4 meters and a maximum interior ceiling height of 6.0 meters which accommodates an ullage volume of 5% of the required heat transfer material. The exterior diameter is 5.2 m and the total height, not including ducting is 6.6 m.

The particles will be insulated with 3 layers of insulation. From the innermost to outermost layer this includes a 100 mm thick high-density refractory liner produced by project partner Allied Mineral Products called TUFFCRETE® 47 [43] comprised of Aluminum oxide (47.1%)/Silicon dioxide (46.5%), a 200 mm thick insulative layer comprised of two 100 mm thick back to back panels of Skamol Super-1100 E Calcium Silicate board made by Skamol, and a layer of 100 mm thick filament reinforced microporous silica boards called Elmtherm 1000MP made by Elmelin, and an 8 mm (5/16 inch) AISI 316 stainless steel shell.

The density of the refractory layers was selected to balance the durability and erosion resistance requirements with thermal resistance. In general, the properties of a ceramic lining material follow the property relationships in the equation below. A material that is resilient to heat and mechanical abuse will generally have a higher density to meet those goals and therefore have a lower porosity and a higher thermal conductivity. As such, installed refractory linings are typically multilayer, with dense materials at the hot face and insulating materials behind to the cold face. This can then provide a lining that is both resilient to the high temperature process and efficiently retains the heat of that process. Details of the insulation design can be found in the final report by Allied Mineral Products [44].

$$\boldsymbol{density \propto heat\ resistance \propto strength \propto abrasion\ resistance \propto conductivity}$$

The bin is supported on a slab of reinforced heat-resistant Calcium-Aluminate-based concrete called Fondag made by Imerys [44]. The bin will be sealed at all joints and interfaces with refractory fiber caulk called Max Moldable by Nutec to mitigate external air infiltration but will remain non-hermetic. To eliminate openings at the floor due to flatness and surface tolerances of the slab and bin, the bin walls, in addition to the refractory fiber caulk, are set on a 6 mm cushion of Alumina-silica ceramic fiber called SuperPly by Nutec with a perimeter ring of Fiberfrax silica rope by Unifrax.

The storage system utilizes a flat-bottomed design as opposed to a sloped hopper which has five key advantages:

1. A flat-bottom is cheaper than a hopper to make as inventory can be placed directly on a concrete slab.
2. The surface area of the flowing particle mass is smaller and thus less prone to heat loss as particles do not reside in an elongated cone or wedge-shaped section as in a mass flow hopper.
3. The risk of erosion along the refractory bin liner may be reduced as the design causes *funnel flow* where particles flow away from the walls and into a central flow channel with zero vertical velocity along the walls.
4. The stagnant particle region has been shown to be an effective insulator
5. The stagnant particle region protects the floor of the bin from abrasion caused by hot high velocity falling particles impinging on the floor.

During system testing, temperature data will be measured at discrete intervals along the inner walls of the bin. Prior to the shotcrete application of the inner wall layer, thermocouples (TC) will be routed through nutted fixtures in the shell and insulation as shown in Figure 32. The TCs will be capped for protection during the shotcrete application. After the application of the inner wall, the caps will be cut open and TCs can be expeditiously inserted into position. TCs will be spaced at 0.9 meter intervals over the height of the walls and along the roof and 120° radially. Temperature information will be used for thermal analysis and to determine the level of the particle bed. TCs will also be placed in a radial array over the outlet (Figure 32) to measure outlet temperatures at multiple points.

Figure 32. Nutted TC fixtures in radial array in early test demonstration

The bin is designed to be evacuated, repaired, and inspected. A bore scope port through the roof allows for non-invasive inspection of the interior. The cover shell is a removeable hatch to allow for unexpected repair and to allow human entry in postmortem to assess the survivability of the interior bin liner after multiple charge/discharge cycles. The plug is formed with a steel ring precast with refractory insulation and a compressible seal made of a ceramic fiber blanket. To enter the bin, ductwork, the top plate, and inlet plug can be removed with bolts and lifted by a jib crane mounted to the tower framing. Once the roof has been opened, the outlet plug at the bottom of the bin can be lifted out by hoist anchors welded to the top plate and moved to the side to fully evacuate the bin of the stagnant particles and investigate the interior surfaces.

Structurally, the outlet uses a base plate with attached metal pipe. A steel hemispherical steel grate will cover the opening to protect from complete blockages of the outlet hole. A sloped riser is designed to alleviate thermal ratcheting when the bin contracts in cooling.

The exterior shell of the bin will be made of welded stainless steel 8 mm thick plates. The proposed storage bins will be designed for the internal vertical and lateral pressures, and vertical friction forces, imparted on the bin shell by the stored material.

The preliminary design of the steel storage bins by Tim Harvey (PE) of Matrix PDM follows the general design guidelines of the American Institute of Steel Construction and per the guidelines of "Design of Steel Bins for Storage of Bulk Solids" by Gaylord and Gaylord (Prentice Hall, 1984).

The bin roof structure (Figure 33) is designed for the weight of the roof structure checkered steel plate, the suspended insulating materials, and a uniform live load. An additional uniform live load of 4788 N/m^2 is recommended to accommodate personnel and unforeseen future loadings. In addition, the roof is designed to support the weight of the bin bottom plug when lifting for maintenance or replacement.

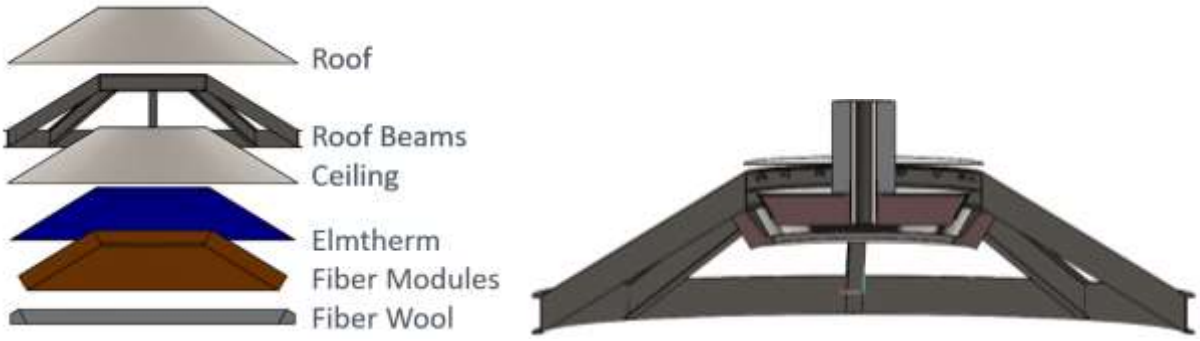

Figure 33. Roof layers exploded view (right). Removable inlet plug partial exploded view (left)

The estimated shell thickness of 8 mm (5/16 in) is adequate for the loadings on the shell wall noted above. The preliminary steel bin size and loading is not unusually large for a welded steel plate bin. Should it become necessary or advantageous to adjust the diameter or height of the steel bin, the modifications to the design would not be significant. The small size (5.2 m diameter by 6.6 m height) allows the bin to be erected at grade and lifted into place, or constructed in place on the floor slab. The roof structure is a stiff conical shell that can be lifted from three or more locations.

All vertical and circumferential welds in the shell are to be full penetration. Should it not be possible to fabricate the entire bin at grade and lift it into place, the shell could be welded at grade into manageable sizes, lifted into place, with the final welding performed in the tower. All full penetration welds shall be performed by AWS qualified welders and shall be inspected for weld integrity using ultrasonic or other non-destructive means.

3.1.2.3. Storage-Bin Modeling

3.1.2.3.1. G3P3 Heat Loss (Milestone 3.1)

The hot storage bin is required to pass particles from the receiver to the heat exchanger within an acceptable temperature range. Heat exchanger and receiver materials limit the upper temperature to 800° C. Minimum temperatures need to be between 765-775° C to meet both the thermal duty and efficiency requirements for particle to sCO_2 heat exchange process. Particles will enter cold storage at a temperature near 615° C and must exit between 570 and 615° C during continuous operation in order to achieve the required temperature rise at a particle curtain thickness that does not risk damage to the receiver. As a result of its higher temperature, the temperature drop in the hot storage bin will be greater than that of the cold storage bin. For this reason, only the hot storage bin is included in this analysis.

The minimum outlet temperature of the particles will be the average temperature from the receiver (T_{rec}) which is nominally expected to be 775° C ± 12° C with a max achievable temperature of 800° C minus the average temperature drop over the charging, storage, and discharge operations:

$$\boldsymbol{T_{HX} = T_{rec} - \Delta T_{charge} - \Delta T_{storage\_10hrs} - \Delta T_{discharge\_6hrs}}$$

The capacitance of the refractory materials over time, intrinsic thermal resistance of the bulk particle bed, and thermal kinetics of particles in funnel flow as they move from the cool walls and into the hot central flow channel were considered when determining the temperature deltas in all operational modes.

A semi-analytic model based on the theory of Green's functions was developed (K. Plewe, UT Austin) to determine the heat losses during the charging operation (ΔT_{charge}). A concept of "heat

kernels" was employed whereby a partial domain was derived using standard analytical methods and coupled to the remaining particle domains with a set of transfer functions. These transfer functions can be either analytically or numerically derived. For the funnel flow regime, the particle domains are separated according to Figure 34-left into: 1) a top flow surface, 2) a center flow channel and 3) a stagnant region. The heat transfer modes are shown in Figure 34-right. Details are published in SolarPACES 2020 [45].

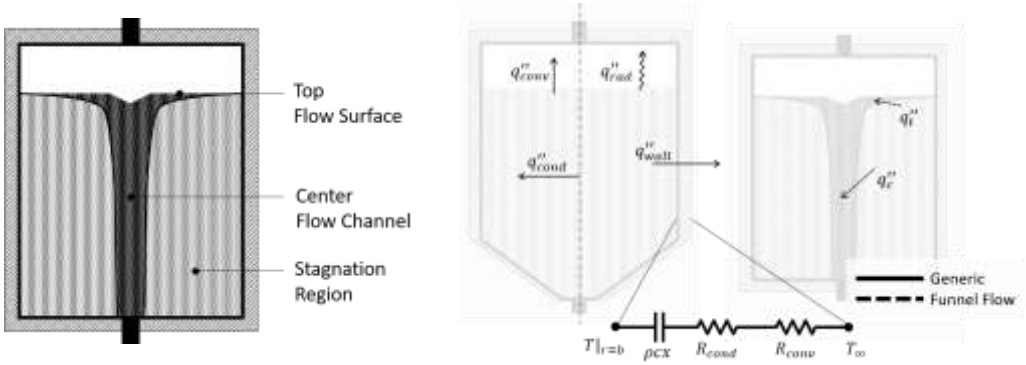

Figure 34. Left: Funnel-flow regimes. Right: heat-transfer modes considered.

The volumetric average temperature of the particles in the bin over the 6.6-8.0 hour charging period are shown in Figure 35. At 5 kg/s the bin will be fully charged in 6.6 hours. A thin layer of particles enters the bin at 800° C at each time step and conducts heat to the walls and pre-existing particle layers and loses heat to the interior air through convection and radiation. ΔT_{charge} is 15.5-21.1° C depending on whether the charging time is 6.6 or 8.0 hours.

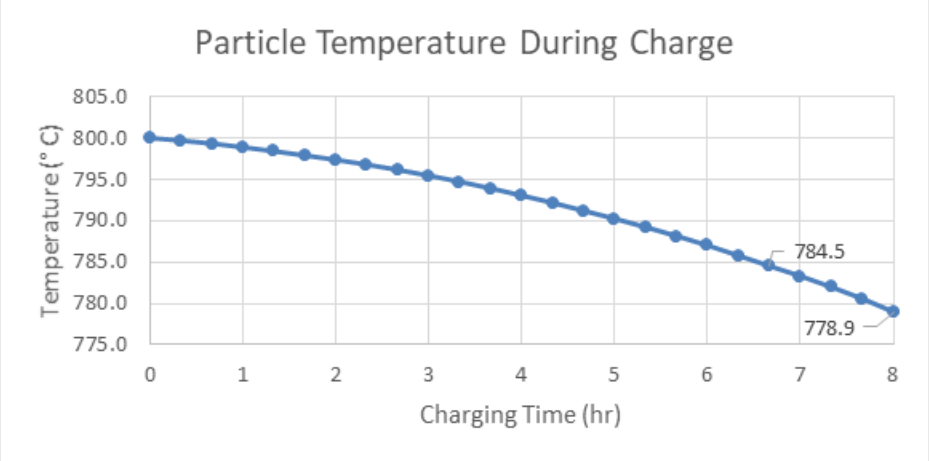

Figure 35. Average particle temperature of all particles in bin during 6-8 hour charging operation.

Modeling was performed to understand cyclic steady-state temperatures of the refractory materials and particle temperatures over the 10-hour duration of deferred storage through diurnal operational cycles ($\Delta T_{storage\_10hr}$). A 2D axisymmetric finite-element model was designed where 800° C particles enter a cold bin with refractory layers initially at 25° C at the beginning of each day and are held for 10 hours where they impart their thermal energy to the refractory layers, floor, and roof. After 10 hours the particles are instantly discharged, and for the remaining 14 hours of the day, the refractory layers release thermal energy to the external environment (heat transfer coefficient = 20

W/m^{2}K) until the following daily cycle where particles again arrive at 800° C and the walls begin the subsequent day with the heat from the prior cycle [46].

Figure 37 shows that the refractory layers rise to steady-state temperatures and level off. The volumetric average temperature of the flowing particles reaches cyclic steady-state equilibrium after approximately 15 consecutive days where the minimum temperature converges to approximately 789-791° C ($\Delta T_{storage\_10hr}$ = 8.9-16.3 ° C).

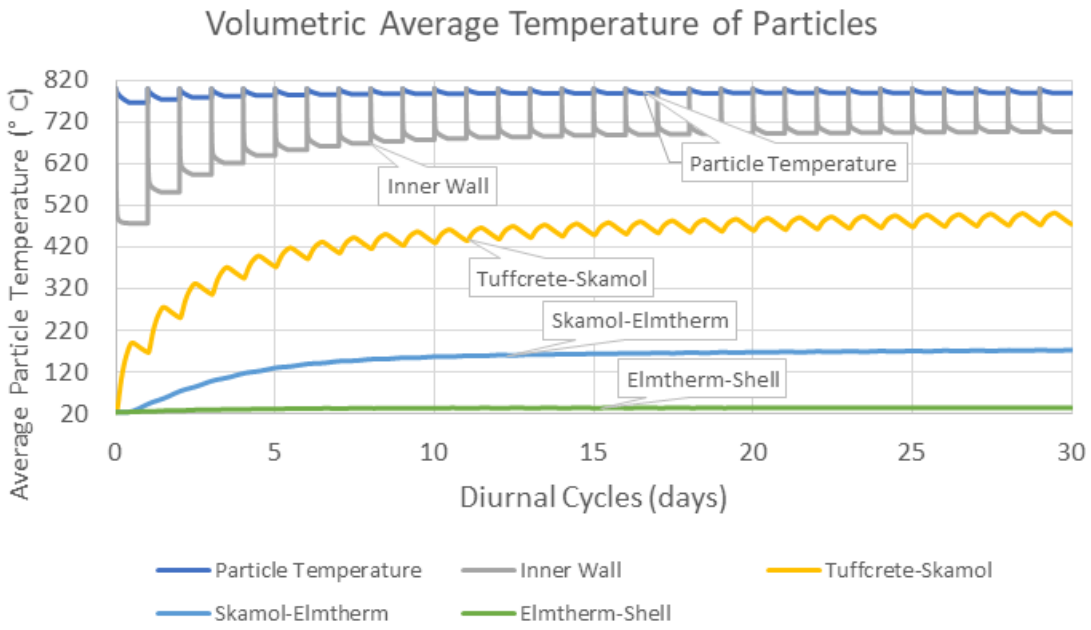

Figure 36. 1 MW$_t$ Cyclic steady-state thermal analysis.

Figure 37 shows the temperature gradients across the centerline of axisymmetric domain after 30 days of cycles. The results show stable particle temperatures from the central bin axis until about 15 cm from the inner wall. Temperatures are relatively steady through the high-density concrete (Tuffcrete) as expected due to the relationship between density and conductivity. The low-density refractory (Skamol) reduces temperatures by about 300° C followed by the microporous layer (Elmtherm) that reduces the temperature to 40° C at the shell making it safe for human contact.

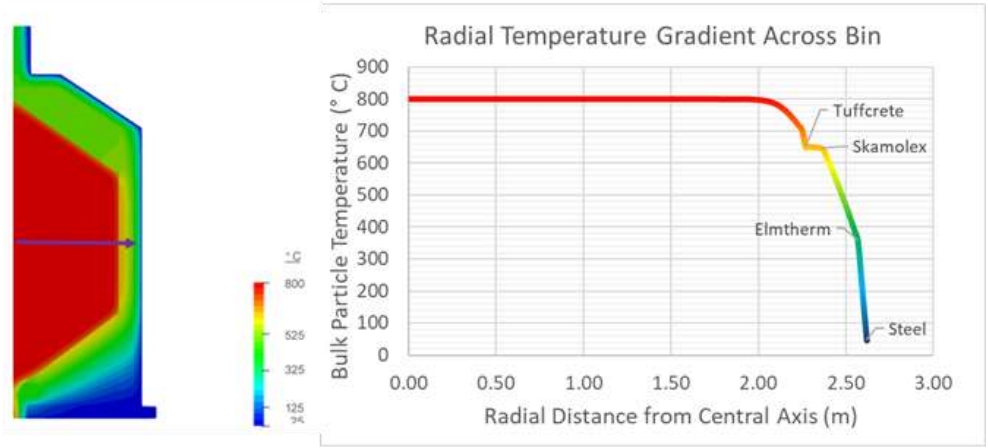

Figure 37. Radial temperature gradient from central axis to shell along center line (purple arrow) after 30 days of cycling with bin full of particle (Albrecht).

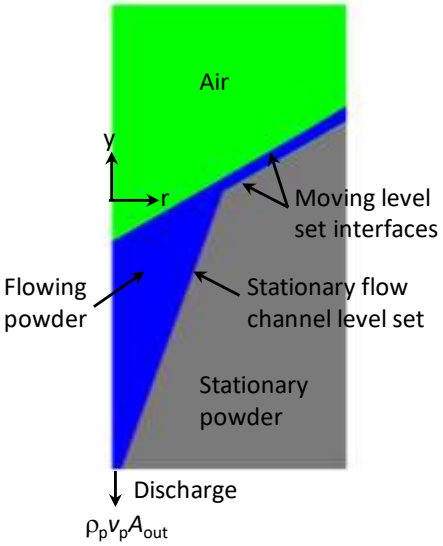

Figure 38: Axisymmetric particle bin model geometry

A second CFD model was developed by M. Martinez to capture the unique kinetics of particles in funnel flow needed to determine the dynamic discharge temperatures at the outlet ($\Delta T_{discharge\_6hr}$). Figure 38 depicts an axisymmetric model for flow and energy transport in a particle-filled bin. The flowing particles are treated as a pseudo fluid, and the flow and energy transport is modeled using conservation equations for flow and convective-diffusive energy transport through a pseudo porous medium in which the particle region is decomposed as a flowing region in a funnel flow configuration, a non-flowing, stationary particle region, and the air-filled region above the particles. The three regions are separated by level set interfaces with velocities to match the specified outflow of particles from the funnel flow region. The level sets separate the different fluid regions, allowing different physics and/or transport properties to be specified in each region [46].

In a discharge simulation, the two moving levels translate downward at a rate matching the discharge rate of hot particles from the bin. The pseudo-fluid flows through the drawdown channel and into the funnel region, finally issuing out the discharge port. Energy transport in the flowing particles is via convection and conduction and by heat conduction only in the stationary particle region, and from heat loss to the interior wall. The bin loses heat by radiation and convection from its surface to a fixed ambient temperature. Heat loss from the upper surface of the particles is modeled similarly. The main mode of cooling of the discharge stream is by convection of cold particles adjacent to the bin walls as they flow through the funnel.

The results of the level-set model are shown in Table 6 and reflect the outlet temperature profile through the distinct phases of the funnel flow process. Average outlet temperatures over the area of the outlet are shown in green. Centerline temperatures located furthest from the hot non-flowing particle regions shown in red. The contour plot is a mirrored image of the axisymmetric model and includes wall temperatures and isotherms. At the completion of the 6-hour discharge, average outlet temperatures have leveled off at approximately 794° C ($\Delta T_{discharge\_6hr} = 6.1°C$).

The ΔT's above are directly related to initial particle temperatures with an assumed uniform 800°C initial condition. Combining results from the three models as proposed, the overall outlet temperature drop (milestone 3.1) can be stated as:

$$T_{HX} = T_{rec} - \Delta T_{charge} - \Delta T_{storage\_10hrs} - \Delta T_{discharge\_6hrs}$$

$$T_{HX} = 800.0℃ - 15.5℃ - 8.9℃ - 6.1℃ = 770.0℃$$

Table 6. Particle average outlet (green) and outlet centerline (red) temperatures with contour plot at key phases of funnel flow discharge (Martinez)

Process	Result	Level-Set Model Temperature Profile
Discharge of the hot central core	Steady outlet temperatures near maximum (800° C)	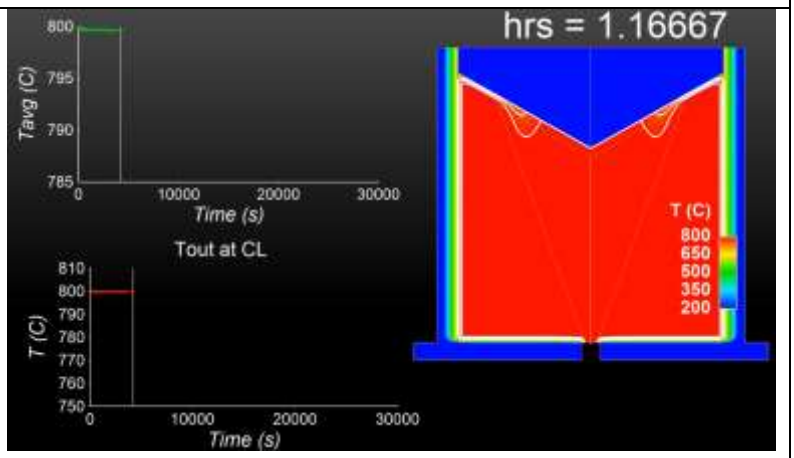
Coolest upper layers with longer time spent on exposed upper surface during storage time leave the bin	Precipitous drop in outlet temperatures	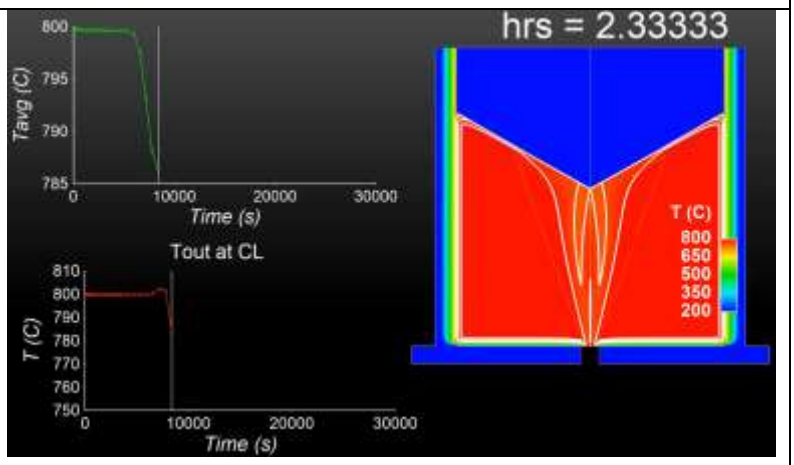
Subsequent layers with less exposure time spent on upper surface leave the bin	Temperatures rebound	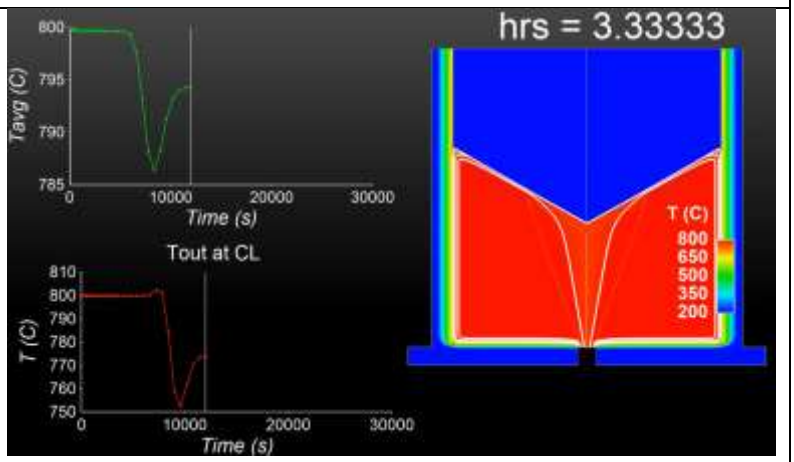

Process	Result	Level-Set Model Temperature Profile
Particles continue to cool along walls. Flow channel depth decreases and has diminishing effect on particle temperatures	Temperatures drop more gradually and resemble Newtonian cooling once flow channel is sufficiently short	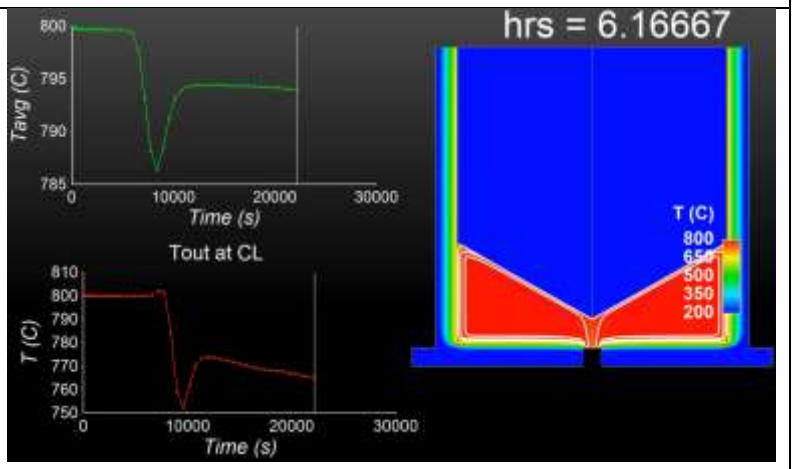

The transient discharge temperature profile with losses from charging and holding is shown in Figure 39 relative to the maximum and minimum particle inlet temperatures from the receiver 763-800° C. Internal air conditions were varied from still to blowing air at 0-10 W/(m^2·K) and internal air temperatures from 25°C to 800° C resulting in particle temperature variability of ±36.6° C. Variable external convection was also modeled from 10-100 W/(m^2·K) having a net effect of ±2° C on average particle temperatures. The effective conductivity of bin structure when refractory anchors are considered resulted in particle temperature variability of ±1.8° C.

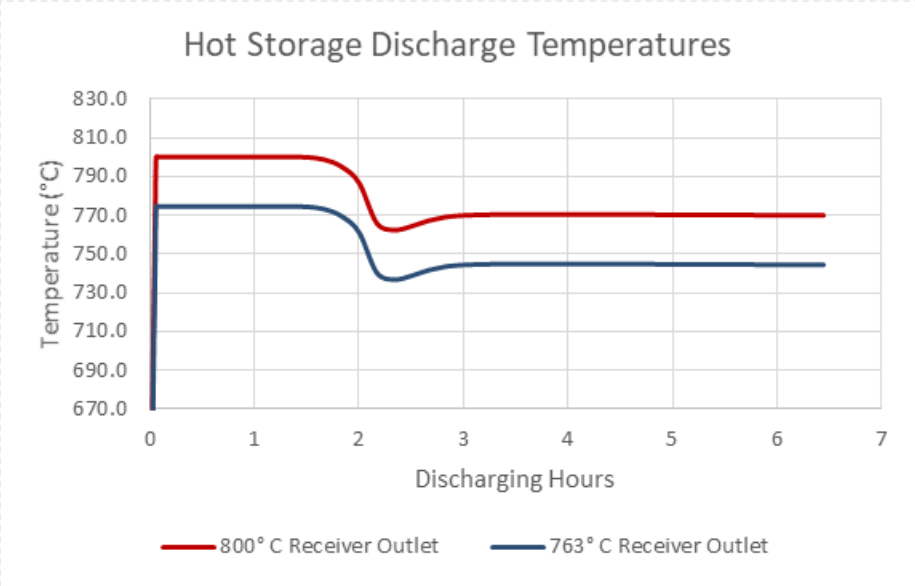

Figure 39. Expected transient outlet temperatures from hot storage bin

For storage operations, the ability to deliver particles to the heat exchanger at temperatures >765° C will likely require the receiver to heat particles to near 800° C when charging the storage bin. Contingency operations for periods of time when the storage system cannot deliver particles in the optimal range include:

1. operating the PHX particle/sCO_2 flow rate to heat sCO_2 to 715° C but at less than 1 MW thermal duty
2. operating the PHX to produce sCO_2 at <715° C but at the 1 MW thermal duty
3. adding heat to the storage bin using electric air heaters to evaluate impacts on particle outlet temperature

Further discussion of these contingencies is included in the heat exchanger section.

3.1.2.3.2. Storage Model Validation Testing

To build confidence in the 1 MW_t scale model, testing was performed on a small steel bin made of a 250 mm pipe that could be heated in a furnace and allowed to discharge while logging data from thermocouples. Figure 40 shows the test set-up. The hot bin is lifted out of the furnace from the lifting frame and placed on a rack with an insulated pathway to an identical lower bin (shown with white insulation below the uninsulated hot bin). A ceramic slide gate (center image) is used to open a small hole and allow particles to flow to the catch bin.

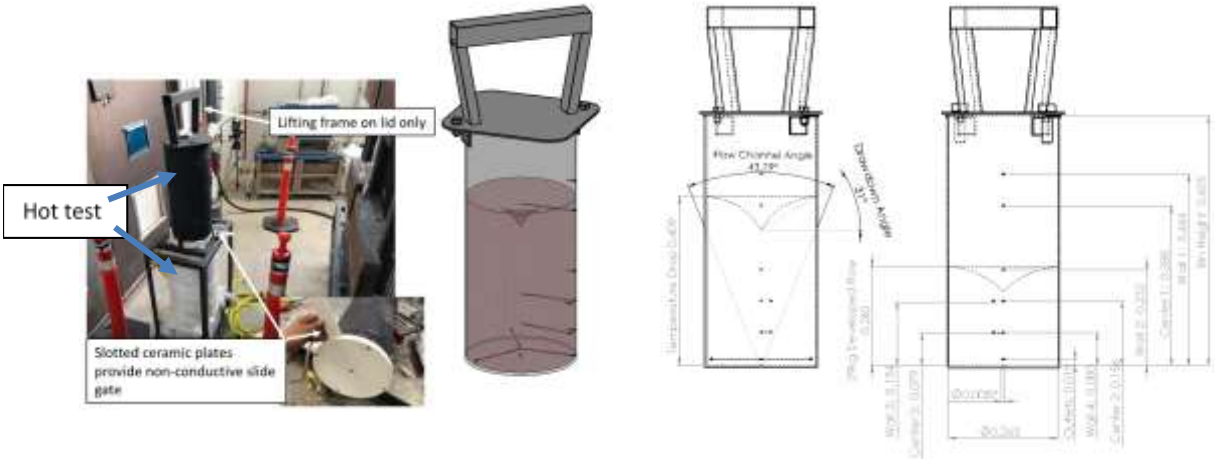

Figure 40. Left: Small particle test bin used for model validation. Right: TC locations.

TCs were located along the central bin axis, near the walls, and at three points over the outlet hole. The center image shows the calculated flow channel geometry determined from material properties tested by Jenike and Johanson [47]. The right image shows the basic bin dimensions.

Observations of the top surface during discharge were made with ambient temperature particles. A crater can be observed on the top surface initially. The diameter of the crater decreases and eventually converges to a point. The timing at which the crater converged on the top surface corresponded to the time of the characteristic dip in temperatures from hot flow testing shown in Figure 41 which supports the hypothesis that the initial fall in temperature (marked at 1084 seconds) corresponds to the draining of the flow channel.

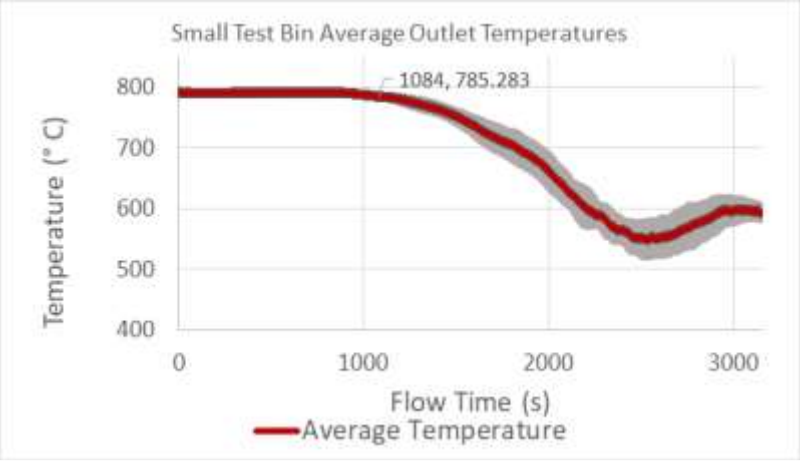

Figure 41. Average outlet temperatures in small test bin. Uncertainty bounds represent 2 standard deviations. Temperature profile matches simulated profile explained in Table 6.

Level-set and heat kernel models used the small bin tests to evaluate their accuracy. Both models were found to have captured many of the salient features of the funnel flow temperature profile as shown in Figure 42.

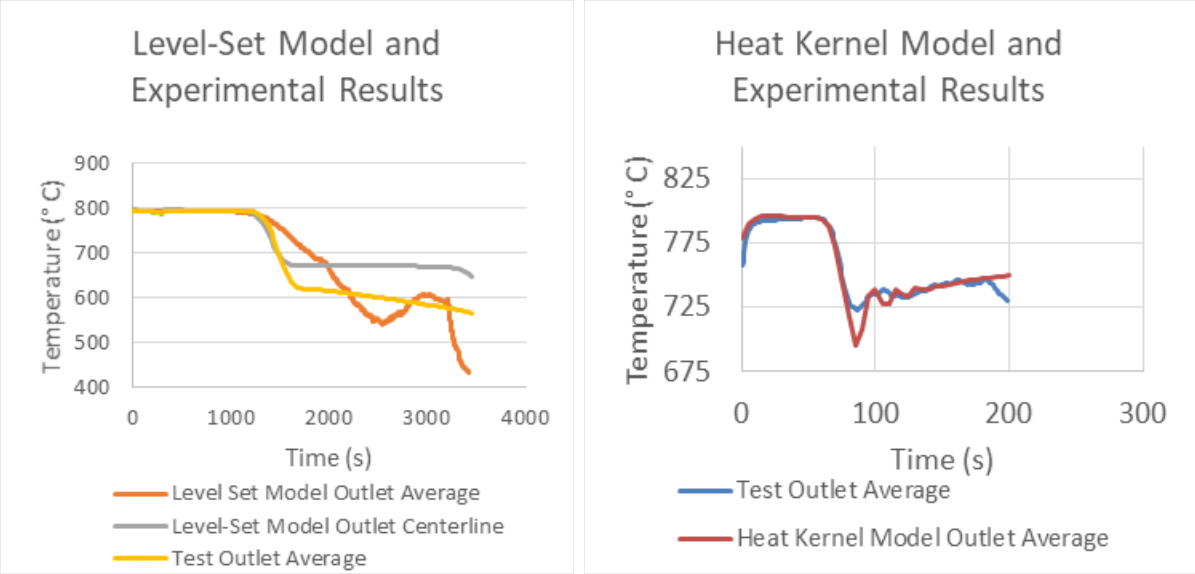

Figure 42: Left, level-set model overlaid with experimentally measured data from slow flow test. (right) heat-kernel model overlaid with experimentally measured data from fast flow-rate test.

The semi-analytic heat kernel model is designed to couple the charging, holding, and discharging phases to provide a refined estimate of the bin's transient cyclic performance relative to the arithmetic approach used herein. Future efforts will include experimental validation and hardware-in-the-loop testing to evaluate transient charging behavior of the bin walls, roof, and base before these results can be applied to the storage bin design.

3.1.2.3.3. Stress

Stresses caused by thermal expansion, hydrostatic pressure from the particles, and ratcheting from packed particles were considered in the bin design. The inner refractory layer will be applied pneumatically (shotcrete) and baked dry in-situ. Vertical and horizontal thermal expansion joints

will be maintained at 1 m intervals. The initial width of the joints was informed by thermal expansion testing performed by Allied Mineral Products on several refractory specimens under consideration. At 800° C, the Tuffcrete panels are expected to expand ~0.2%, or 2 mm during the initial bakeout process and then recede upon initial cooling to a permanent linear change (PLC) of -0.25% of the initial condition to -2.5 mm (Figure 43). On subsequent thermal cycles, the 0.2% expansion will occur relative to the PLC dimensions. A 5 mm expansion gap will be placed around each hot face panel during the shotcrete application to accommodate the initial expansion. Once the panels have reached PLC, a 10 mm gap will remain. The Skamol and Elmtherm will be predried and will not experience PLC in the bin assembly.

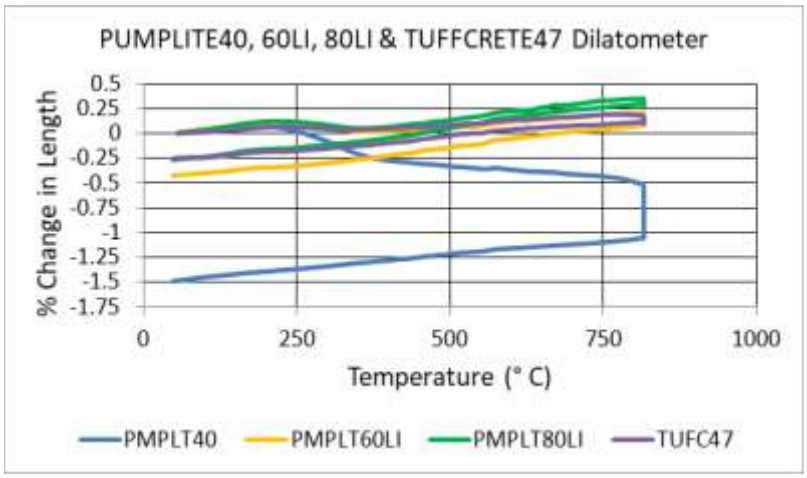

Figure 43. The percent change in length of high-density "hot face" materials

To prevent particles from entering the joints and escaping or damaging the refractory through thermal ratcheting, two parallel approaches were developed. In the first, a high-temperature fabric or steel plate would be mounted over the joints and held in place with drilled anchors (Figure 44). Testing was performed by Allied Mineral Products to verify that the steel anchors would not pull away from or crack the refractory in thermal expansion. Holes were predrilled per manufacturer instructions and a 1.5 mm thick 316 stainless steel plate was attached to the test sample with either 410 stainless steel self-tapping anchors or 316 stainless steel stud anchors, both ¼-20 threads. The entire assembly was rapidly cycled ten times between 250°C and 815°C. After the cycles, the self-tapping anchors could be pried out of the sample while the anchor studs were firmly intact. Based on this work, the use of stainless-steel stud anchors in the refractory hot face of the TES is feasible for mounting internal hardware.

Given the number of joints, the anchoring process could be cost prohibitive in very large commercial-scale bins. For this reason, a less labor-intensive method of stuffing the joints is being selected as the G3P3 baseline. The remaining 10 mm gap between the Tuffcrete panels will be stuffed to the full 100 mm depth with *Supermag* bulk fiber and sealed along the inner surface with *MaxMoldable* 2300 ceramic fiber caulk. Similar to the high-temperature fiber solution above, small openings around the caulk are still possible. The stuffing is designed to prevent a situation where particles can pack into the joints and cause damage due to thermal ratcheting. Instead, particles are expected to initially fill into and remain suspended in the fibrous voids.

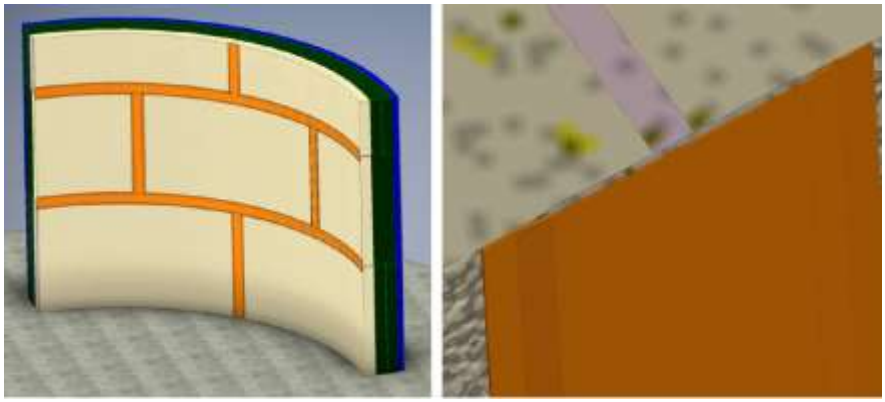

Figure 44. Proposed placement of gaskets in refractory joints (dimensions of panels does not reflect 1 x 1 m final design).

Given the difficulties in predicting particle interactions with the walls, G3P3 has been designed for inspection, maintenance, and repair. During bin commissioning, the internal temperature will be cycled to verify the integrity of the joints and joint-gaskets. The gradual filling process will provide an opportunity to detect any unexpected interactions before completely filling of the bin with particles. In the event of degradation, high-temperature cloth can be installed over the joints using the anchor studs. The borescope hole will be used to inspect the walls routinely. In addition to the hemispherical grate over the outlet hole designed to prevent large chunks of refractory from clogging the hole, a removeable fine filter will be placed below the bin to be routinely inspected for evidence of refractory degradation that could appear as small fragments of wall material. The application method of the Tuffcrete has also been changed to shotcrete from pre-cast in order to facilitate discrete repairs of a small section if needed. Shotcrete is supported by the wall anchors while pre-cast panels are stacked requiring unstacking of the entire portion of wall when repairs are needed. Prior to downselecting shotcrete, Allied Mineral performed testing to evaluate adherence of the Tuffcrete to Skamolex, damage to the Skamolex from high-velocity shotcrete, and effectiveness of a sodium silicate moisture barrier [48]. Results shown in Figure 45 verify that the Skamolex is unlikely to sustain damage from impact from shotcrete, moisture penetration, or thermal expansion mismatch.

The effects of radial expansion into the shell were also considered. The Skamol Calcium Silicate boards were not tested but the manufacturer published a coefficient of thermal expansion of 5.5E-6. The Skamolex is expected to expand 0.44 mm at maximum modeled wall temperatures.

Figure 45. Left: Tuffcrete shows good adherence to Skamolex during shotcrete testing. Right: When Tuffcrete is pried off of Skamolex to simulate thermal expansion mismatch, there is minor damage (pitting), and no observable water damage.

The resulting stresses from thermal expansion was estimated using models with bonded cylinder layers. However, this is conservative since gaps and voids exist between the Skamol panels and the panels can translate relative to each other. In these models it was assumed the particle bed was incompressible and that thermal expansion of the refractory layers would be taken up by the Elmtherm layer. There is no linear elasticity in microporous insulation, so all deformations are expected to be permanent. There is also no cold compression strength due to the fibrous nature of the material. Due to the increase in density and proportional conductivity of compressed material, a deformation of 10% of the original thickness (10 mm) is taken as the point of failure. Compression testing was performed on the Elmtherm to determine the effects of the Skamol expanding into this outer layer. After 30 minutes of being compressed at 138 kPa (20 psi) the board had a permanent deformation of 2.7 mm (6 times the expected compression) with a corresponding increase in density of 14 kg/m^3.

Temperature outputs from a cyclic steady-state model were applied to the wall faces as boundary conditions and allowed to come to equilibrium to approximate the thermal state of the walls. Horizontal pressure from the particles was applied to the inner wall. The inner surface (left side) of the steel shell was assumed to be static and all displacements move to the right. The maximum displacement is shown to be 1.5 mm. It is therefore assumed the Elmtherm will be permanently compressed to ~1.5 mm (<<10%) and the pressure exerted on the shell will be less than 130 kPa – several orders of magnitude less than the tensile strength of steel. At the time of the test, there was no appropriate equipment to measure the change of thermal conductivity, but the change of density will result in higher thermal conductivity.

Stresses of the particles on the bin walls and floor were evaluated. When full of 800° C particles, the vertical pressure on the outlet of the TES bin was estimated at 0.13-0.17 MPa (20-25 psi). At that temperature and pressure, there is some potential for creep deformation of refractory materials. Thermal expansion and creep testing (ASTM C832) were performed on two refractory ceramic materials proposed for the riser at the outlet of the TES [49]. Thermal expansion was measured from room temperature to 870°C and the sample was held at temperature for 24 hours to determine if there were changes over time. The creep was measured in a similar manner, with pressure applied at room temperature and the materials held at 870°C for 24 hours to determine the stability of the material. In both cases, the refractory material was stable after achieving temperature.

Particles will also exert a horizontal hydrostatic force and a vertical friction force on the wallsThis force was determined analytically by the Janssen equation which accounts for the portion of particle weight transferred to the walls as a result of the self-supporting properties of bulk solids [50]. The horizontal component is assumed to be 40% of the vertical force which is a common value for these types of materials. The maximum vertical pressure (weight) on the bin floor at the wall is 61 kPa. The outward horizontal pressure at the same point is 21 kPa. The friction drag force is 148 kPa. These stresses are added to the material weight to determine the bending moments applied to the steel shell by the steel anchors. As shown in Table 7, the materials can easily handle the hydrostatic pressure of the particles.

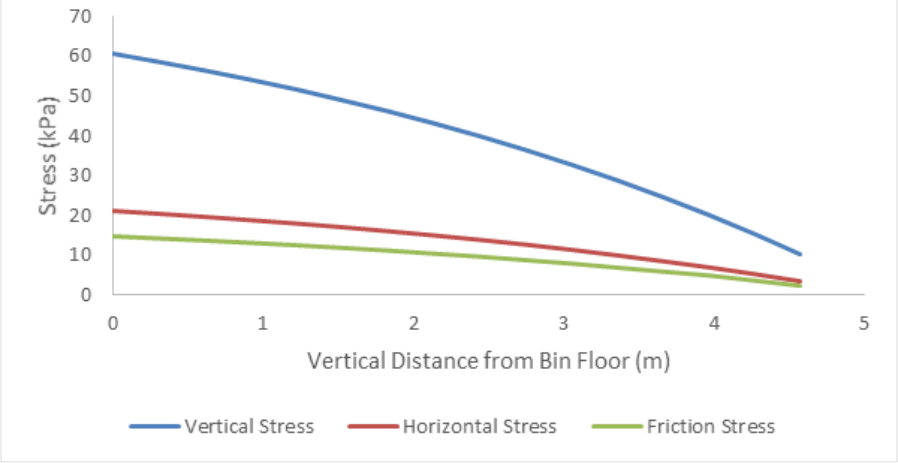

Figure 46. Particle stress imparted to wall as a function of height.

Table 7. Thermal expansion and permanent linear change of refractory materials (Skamolex was not tested but is similar to Pumplite)

Property	Pumplite 40 (kPa)	Pumplite 60LI (kPa)	Pumplite 80LI (kPa)	Skamolex 1100 E (kPa)	Tuffcrete 47 (kPa)
Modulus of Rupture at 650° C	420	1,931	2,840	1,800	16,478
Modulus of Rupture at 800° C	434	2,051	1,407	1,800	9,225
Cold Crush Strength at 800° C	1,000	4,100	6,200	2,700	70,900

The steel anchor design is shown in Figure 47. It features an 8 mm diameter 316 Stainless Steel RA-14 nutted V-anchor spaced at 225 mm intervals over the surface of the inner refractory layer. Each anchor will use a plastic tip to accommodate thermal expansion of the anchor inside the refractory. This plastic tip also acts to reduce thermal bridging to the anchors. A study was conducted to evaluate the effect of shotcrete anchors on the effective thermal conductivity of the walls [51]. The conductive modeling resulted in an additional 1.8° C temperature drop of the bulk particles. This effect has also been shown to be partially offset by the plastic coating of the anchors, the filler material, and incidental gaps in the expansion joints and between layers [52].

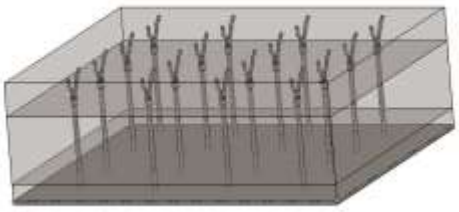

Figure 47. Steel anchors in transparent view of 1 m^2 of bin wall

3.1.2.4. G3P3 Storage Materials and Costs

Cost estimates for materials, assembly, and installation of the storage bin design are shown in Figure 5. Material costs for all refractory and insulation materials as well as labor costs for casting refractory sub-components have been provided by Allied Mineral Products. Material and assembly costs for the structural bin elements were provided by Matrix PDM. A cost estimate for lifting and inserting the bin into the tower was completed by Thornton-Tomasetti. A cost estimate for installing the insulation layers and shotcrete was completed by JT Thorpe. Detailed drawings for fabricating steel parts for the outlet plates and inlet features were sent to potential vendors for cost estimates. Particle cost quotes were provided by CARBO. In total, the cost of each bin is expected to be approximately $1.1 million including a corporate tax of 15%. Structural materials are ~$450 k. Particles are ~$213k. Labor is ~$458k.

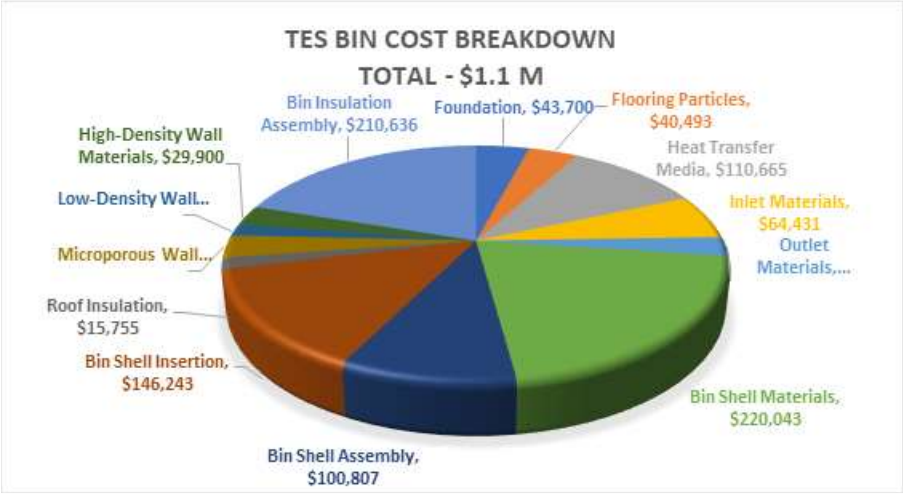

Figure 48. Cost breakdown for storage bin materials, assembly, and heat transfer media.

3.1.2.5. 100 MW$_e$ Storage Design (Milestone 3.2)

Commercial design concepts were evaluated for both tower-integrated and external storage systems [53]. The particle receiver tower is assumed to be cylindrical and made of reinforced concrete designed for slipform construction. The conceptual design of the tower has been performed using the requirements of the International Building Code (IBC) [54], the American Concrete Institute (ACI) 318-14 Building Code Requirements for Structural Concrete, and the ACI 313-16 Design Specifications for Concrete Silos and Stacking Tubes for Storing Granular Materials [55].

Figure 49 shows the general layout of a tower-integrated system. The towers evaluated assumed a component arrangement similar to the G3P3 pilot design. The CSP components were arranged with the cold storage at ground level with turbomachinery, heat exchanger and hot storage bin vertically integrated above and a three receiver configuration on the roof. The hot bin floor is supported by a concrete inverted cone . The insulation for the bins was similar to the G3P3 storage bin configuration with 100 mm thick layer of particle-contact high-density (1990 kg/m3) refractory (Tuffcrete 47) with a 500 mm thick layer of low-density (1110 kg/m3) refractory insulation (Pumplite 60) was between the particles and the tower walls. Fiber modules were used as bin ceiling insulation. Bin floors assumed a low cost filler material based on lava rock for 90% of the volume of the non-flowing drawdown regions. A 5-hole outlet was assumed to reduce the volume of non-flowing material. Size and weight of the CSP components were considered in determining the heights and thicknesses of the floors.

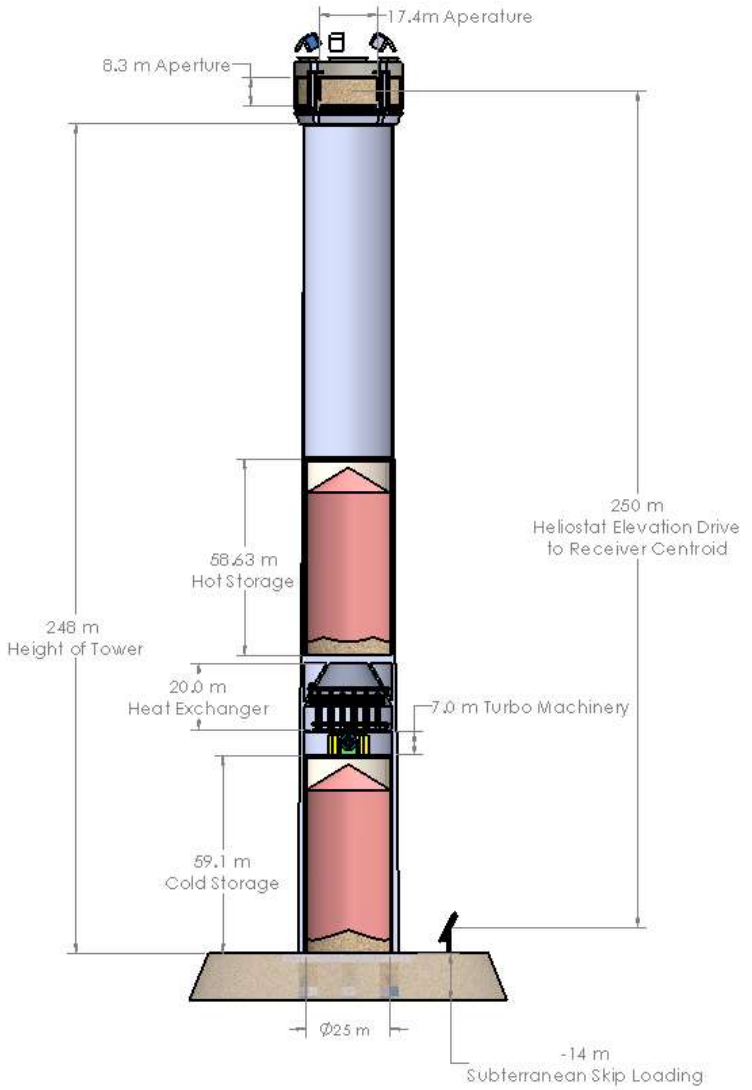

Figure 49. Tower-integrated CSP component dimensions for 25 m diameter 250 m height.

The mass distribution in tower-integrated structures makes them sensitive to seismic action requiring additional concrete and steel reinforcement. The lateral shear and overturning moment of the tower

structures is location dependent. Three locations were assumed that respectively represent low, medium, and high seismic zones:

- Tucson, AZ – where a receiver tower cost analysis used in the System Advisor Model (SAM) was performed [56]
- Tabernas, Spain – where a receiver tower cost analysis performed by Schlaich Bergermann & Partners (SBP) was performed [57]
- Daggett, CA – the baseline location for Gen 3 Topic 1 assessments [58].

Table 8 summarizes the commercial scale capacities considered to provide a range over peaker and baseload plants.

Table 8. Commercial scale capacities evaluated

Plant Capacity (MWt)	Storage Capacity (hr)	Heat Transfer Material Mass (kg)	Heat Transfer Material Volume (m3)
10	6	2,173,038	153.59
50	6	10,865,191	714.05
50	14	25,352,113	1536.01
100	14	50,704,225	2906.56
150	14	76,056,338	4378.75

The large seismic overturning moments estimated in areas of high seismic risk may preclude placing both storage bins in the tower. Concrete monolithic domes were evaluated as a cost effective way to construct storage bins. Experts from Dome Technologies advised the feasibility of the design and provided cost information. Figure 50 shows an arrangement for external storage. On the right, a concrete monolithic dome is constructed with extended stem walls. The walls are transparent to reveal the location of the hot particle storage (red). Particles must be delivered to the heat exchangers at temperatures >800° C in an insulated environment. Mechanical conveyance systems cannot sustain these temperatures without being cooled. By locating the heat exchanger assembly below the hot storage bin, the hottest transition can be gravity driven through ducts. Mechanical belt conveyors can then be used to transport particles at ≤650° C horizontally to a intermediate skip hoist that feeds the cold storage bin. The storage floor would be supported by 1 m diameter concrete pillars spaced at 5-6 m intervals. Dome Technologies was consulted on the possible arrangements and it was determined that a subterranean heat exchanger room would be more costly than an elevated floor. Research toward a detailed design is ongoing as part of the SETO FY21 Lab Call.

Figure 52 summarizes the range of unit costs for both tower-integrated and external storage configurations. Tower-integrated storage includes the material costs of modifying a nominal receiver tower with thicker walls capable of holding the particle storage and internal components. An effort was made to identify and isolate the additional material costs from the nominal receiver tower costs that would be assumed without storage in order to then add these additional costs to

one of two comprehensive tower cost models by SAM (C_{SAM}), as the upper bound, or SBP (C_{SBP}), as the lower bound. The process of isolating the material costs is as follows:

- Step 1. Concrete and steel reinforcement costs were calculated for a tower-integrated system with a given height and mass distribution in a given seismic location using formulas in the International Building Code and a numerical model by Tim Harvey to derive the fundamental period of the structure.
- Step 2. Material cost results were subtracted from the materials-only cost curves in the SBP salt receiver tower model to isolate the additional costs.
- Step 3. The cost of refractory insulation, heat resistant concrete (where necessary), flooring materials, ceiling insulation, and ductwork were calculated based on the resulting inner diameter of the tower. Tower diameters were partially dependent on storage mass. $(C_{insul} + C_{HRC} + C_{floor} + C_{ceiling} + C_{duct})$
- Step 4. The additional tower materials and storage bin costs were added to the comprehensive models from SAM and SBP.

$$C_{integrated,min} = C_{SBP} + (C_{Harvey} - C_{SBP,materials}) + (C_{insul} + C_{HRC} + C_{floor} + C_{ceiling} + C_{duct})$$
$$C_{integrated,max} = C_{SAM} + (C_{Harvey} - C_{SBP,materials}) + (C_{insul} + C_{HRC} + C_{floor} + C_{ceiling} + C_{duct})$$

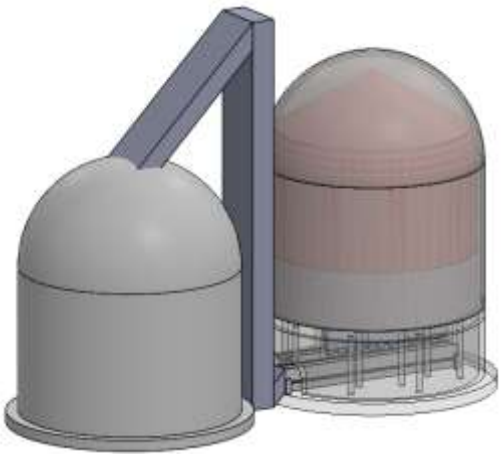

Figure 50. External hot particle storage configuration. Hot bin walls are shown as transparent to reveal heat exchanger and belt conveyor.

Dome costs were estimated by consultants from *Dome Technology*. The nominal configuration was sized with a height to diameter aspect ratio that would minimize the particle-contact surface area. The refractory and flooring materials were considered to be the same. Figure 50 shows the basic geometries used in the quote and Table 10 summarizes the costs of the storage bins. The 200 MW_t (100 MW_e) storage bin with 14 hours of thermal storage has a unit cost of ~\$40/kWh_t.

Table 9. Basic geometry considerations for concrete monolithic dome storage.

Plant Capacity (MW_t)	Storage Capacity (hr)	Heat Transfer Material Mass (kg)	Heat Transfer Material Volume (m^3)	Inner Diameter (m)	Ceiling Height (m)	Structural Wall Thickness (m)
20	6	2.2M	1000	12	14	0.25
100	6	11M	5000	20	24	0.4
100	14	25M	12000	27	32	0.5
200	14	51M	24000	34	41	0.6
300	14	76M	36,000	39	47	0.7

Table 10. Summary of storage bin costs.

Plant Capacity (MW_t)	Storage Capacity (hr)	Particles (million $US)	Storage Materials (million $US)	Nominal Domes as Built (million $US)	Total Cost (million $US)	Unit Cost including particles ($US/kWht)
20	6	$1.3	$4.24 M	$1.40	$1.7-3.5 M	44.2-81.5
100	6	$6.5	$8.38 M	$3.00	$4.6-9.7 M	27.7-48.2
100	14	$15.2	$13.2 M	$5.00	$8.5-17.3 M	22.2-36.2
200	14	$30.4	$19.6 M	$7.60	$14.5-28.3 M	20.5-34.7
300	14	$45.6	$24.1 M	$9.28	$19.6-37.2 M	20.0-35.3

Cyclic steady-state finite-element modeling was used to evaluate the heat loss expected in commercial scale domes. Figure 51 shows the results from a thermal model used to determine whether the dome storage could meet heat loss goals of <1% and if the concrete temperatures would be too hot to remain structurally reliable. The results show the daily heat loss to be <1% in the nominal design scenario which includes 600 mm of refractory insulation and cement. Dome and foundation temperatures however are far beyond the 100° C maximum temperature requirement so a heat resistant layer (4, Wall Layer 2-3) must be used in tandem with the standard concrete.

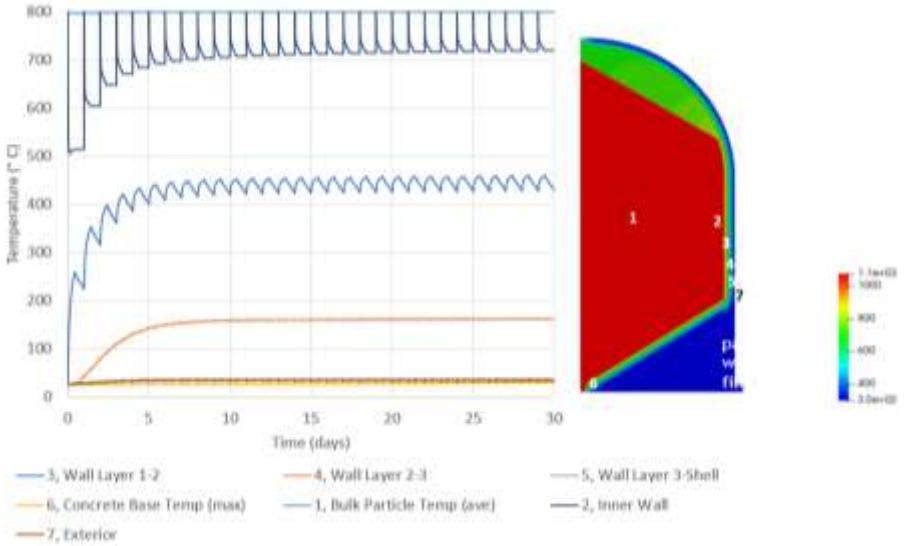

Figure 51. Diurnal temperatures of 100 MW_e hot-particle storage system.

Unlike towers, domes can be built out of heat-resistant concrete alleviating the requirement to maintain structural wall temperatures below 100° C. This allows for more freedom in the thickness of the refractory layers. As a lower bound, storage domes can hypothetically be built without any insulation as shown in grey in Figure 52. The upper bound (yellow) is considered to be the thickest

layer of refractory that can be conventionally applied through a shotcrete application without engineering special support structures. External storage costs also include estimates for horizontal and vertical conveyance.

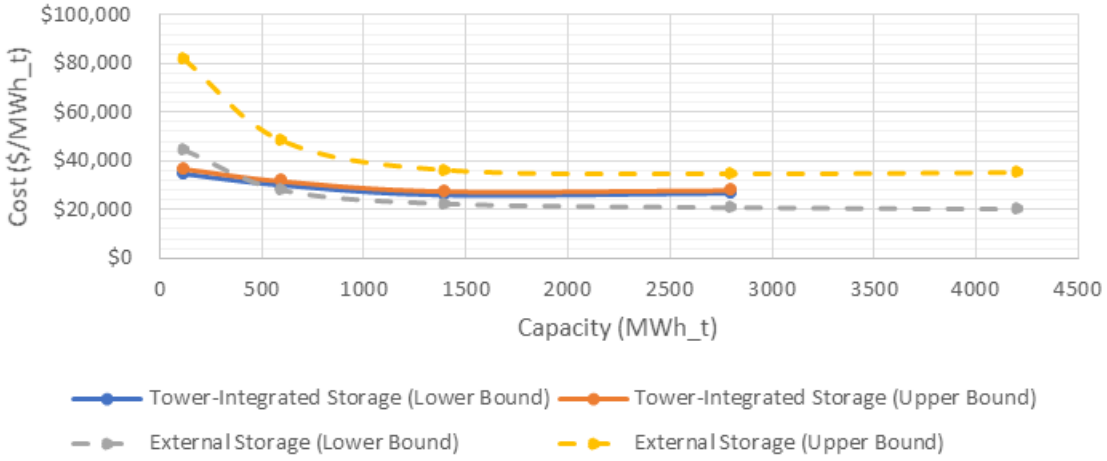

Figure 52. Unit costs per MW_t for thermal energy storage. Maximum and minimum ranges for both tower-integrated (solid) and external storage (dashed) are overlaid.

Heat losses between the upper and lower bound scenarios were modeled using the cyclic steady-state model [46]. The volumetric average temperature of particles in an uninsulated bin is 4.1° C cooler than a similarly shaped bin with 600 mm of insulation and a microporous insulation layer. This amounts to 2% of the total thermal duty. Thermal analyses were performed with the cyclic steady-state CFD model to determine the dependency of heat loss on aspect ratio of the bin and quantity of refractory insulation. Towers with narrow diameters may result in having very tall and narrow storage bins with the associated increases in surface area. Figure 53 summarizes the results. For a fully insulated bin, there is little increase in heat lost due to elongation of the bins. With this result in mind, tower diameters were minimized to reduce structural costs. Figure 53 also shows the resulting increase in heat loss for the uninsulated bin in Figure 49which was used as the configuration for the minimum cost scenario for systems with external storage.

Tim Harvey and Matrix PDM performed analysis to determine the largest system that could be tower-integrated [59]. Results showed that a 10 MWe tower-integrated particle storage system was feasible in all locations investigated. 100 MW_e systems with 14 hours of storage were also feasible in low seismic regions such as Tucson, AZ (milestone 3.2). However, at 100 MWe, ground-based storage systems were necessary if the region was seismically active such as Daggett, CA. The maximum tower that could be sustained in Daggett is 178 m high with about 420 MWh_t capacity (35 MW_e with 6 hr storage).

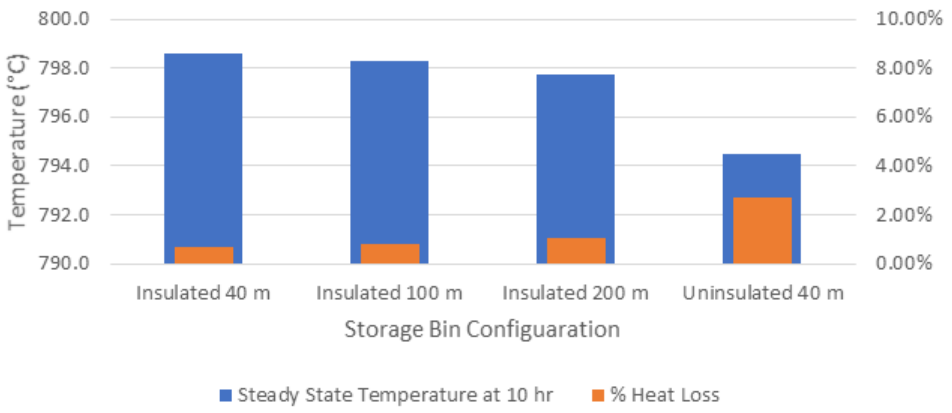

Figure 53. Volumetric average temperature of 51 million kg CARBO HSP after 10 hours of deferred storage in different storage conditions

To put this seismic relationship in context, a study was performed to determine whether a particle based system would be viable in the location of eight similar CSP tower systems around the world [60]. Figure 54 shows the locations of the towers around the world. Representative systems with molten salt storage are shown in blue dots and non-representative systems without storage are shown with yellow pins. The majority of the representative systems were located in China in areas with low seismicity similar to Tucson [61]. Noor III is in an area of Morocco with minimal seismicity [62]. Crescent Dunes had a medium to high seismicity that was higher than the Tucson reference but less than Daggett [63]. The mass of the components was calculated based on the plant storage capacity. In all situations, a viable tower geometry could be found. The comparable systems and material costs are shown in Table 11.

Figure 54. Locations of Solar Towers. Comparable molten salt towers with TES used in Table 6 have been indicated with blue circles [60].

Table 11. Particle-Based CSP Plant Viability at Location of Comparable Systems. Material Costs Include Receiver Tower Enhancements

Site Name	Location	Net Capacity (MW_e)	Storage Capacity (hr)	Tower Height (m)	Particle-based Tower Diameter (m)	Tower-Integrated Storage Material Costs ($/kWh$_t$)
Crescent Dunes	Tonopah (US)	110	10	195	30	$26.9
Hami	Hami (CN)	50	8	180	15	$31.3
Luneng Haixi	Haixi Zhou (CN)	50	12	188	20	$28.9
NOOR III	Ouarzazate (MA)	134	7.5	250	25	$29.4
Qinghai Gonghe	Gonghe (CN)	50	6	171	15	$17.0
Shouhang Dunhuang Phase I	Jiuquan Shi (CN)	10	15	138	10	$26.2
Shouhang Dunhuang Phase II	Jiuquan Shi (CN)	100	11	220	25	$28.7
SUPCON Delingha	Haixi Zhou (CN)	50	7	200	15	$32.2

3.1.3. G3P3 Heat Exchanger Risk-Reduction R&D

Within the first two phases of the G3P3 project, progress on the heat exchanger focused on developing and derisking a 1 MW_t prototype that is applicable to commercial scale systems and integrates the lessons learned from prior efforts in particle/sCO_2 heat exchanger development [64-66]. The 1 MW_t G3P3 prototype was developed targeting the performance requirements specified in the design basis document for the G3P3 system which are highlighted in the project milestones. The performance targets and operating considerations for the heat exchanger are outlined in Table 12. Since the approach temperature is a key design variable to be optimized for the system, the design requirements don't establish specific temperatures, but rather specifies the range of acceptable approach temperatures. In general, the design requirements have been established to be consistent with a 1 MW_t prototype operating at a temperature and pressure that would be required for a 50% efficient dry-cooled recompression sCO_2 power cycle.

Table 12. Design requirements for G3P3 pilot-scale particle-to-sCO_2 heat exchanger

Target Metrics		Basis
15 °C Approach	50 °C Approach	
Thermal duty ≥ 1 MW_t		Thermal duty meets Gen 3 FOA goals and matches capability at NSTTF
Cost ≤ \$150/kW_t		Technoeconomic analysis of commercial scale cost to meet DOE SunShot goals (prototype/pilot unit may exceed this cost)
U_{HX} ≥ 300 W/m^2-K		Recent technoeconomic analysis has suggested that overall heat transfer coefficients of 300 W/m^2-K are required for achieving cost targets
T_{design} = 800 °C		The heat exchanger design and material selection should be performed providing sufficient margin over the maximum particle inlet temperature
$T_{s,in}$ = 775 °C		The maximum particle temperature at the inlet of the heat exchanger
Min($T_{s,in}$) ≥ 765 °C		The minimum heat exchanger inlet temperature due to heat loss in the particle storage bin while still expecting 1 MW_t duty.
$T_{s,out}$ ≤ 580 °C	$T_{s,out}$ ≤ 615 °C	The heat exchanger particle outlet temperature must be below 580 °C

Target Metrics		Basis
15 °C Approach	50 °C Approach	
$T_{CO2,out} \geq 715$ °C		The CO_2 outlet temperature must be consistent with a turbine inlet temperature required for 50% efficiency in a dry-cooled RCBC cycle
$T_{CO2,in}$ ~565 °C		The sCO_2 inlet temperature must be consistent with the high-temperature recuperator outlet temperature of an RCBC cycle
$\dot{m}_s$ = 4.15 kg/s	$\dot{m}_s$ = 5.03 kg/s	Mass flow based on required thermal duty at design point inlet temperature
$\dot{m}_{CO_2}$ = 5.26 kg/s		
$P_{CO2} \leq 25.0$ MPa		The maximum sCO_2 operating pressure meets Gen 3 FOA goals
$P_{CO_2,design}$ = 28.0 MPa		The sCO_2 design pressure should allow for a safe operating margin
$\Delta P_{CO_2} < 2\%$		The maximum sCO_2 pressure drop should be kept below 2% of the operating pressure to prevent large compressor parasitics, but pressure drops up to 4% can be tested

In addition to the targeted operating conditions of the heat exchanger, operational requirements were developed for the particle/sCO_2 heat exchanger. Table 13 provides a list of important operational characteristics for a heat exchanger to be used in a CSP plant integrated with an sCO_2 cycle. Many items on the list were established based on conversations with operators of existing CSP plants and sCO_2 cycle developers such that current requirements, limitations, and areas of improvement were identified. More in-depth discussion on the specific metrics is provided in the G3P3 design basis document.

Table 13. Operational considerations for G3P3 pilot-scale particle-to-sCO_2 heat exchanger

Design Criteria	Notes
Reliability/Maintainability	In-field repair and maintenance of the heat exchanger must be possible
Lifetime/Erosion/Corrosion	Material selection, particle erosion, and sCO_2 corrosion must allow for a 30-year lifetime
Ramp rate	Start and stop operation of the particle heat exchanger must occur at > 10 °C/min
Turndown ratio	Minimum particle and sCO_2 flow rates must allow for 90% turndown
Controls	Maintain sCO_2 outlet temperature with disturbance in inlet temperature
Overnight hold/Idle	Maintain device at low storage temperature while not in use
Heat loss/Parasitics	Less than 1% thermal duty for combined thermal and electrical parasitics
Tolerance to misuse/failure	Robust design that can tolerate reasonable user error

The design requirements and operational considerations tables outline the objectives of the heat exchanger phase one and two research agenda, which can be summarized as follows.

- Develop scalable and cost-effective design for commercial scale particle systems
- Provide confidence in the thermal performance, pressure drop, and sizing of a prototype heat exchanger
- Confirm heat exchanger design can be operated as anticipated in a CSP plant meeting startup, control, transient, turndown, and idle requirements

- Develop required manufacturing processes for a 1 MW_t prototype and evaluate costs at scale

The following sections detail the design of the prototype particle-to-sCO_2 heat exchanger and the efforts to derisk the device prior to the construction of a 1MW_t pilot unit in phase three.

3.1.3.1. Heat Exchanger Design Evolution

Prior to the G3P3 project, Sandia led a project on evaluating different particle heat exchanger technologies [67] and partnered with VPE and Solex thermal science to develop a prototype moving packed-bed, shell-and-plate, particle/sCO_2 heat exchanger to be tested on-sun with the falling particle receiver under the SuNLaMP program. Since the initial heat exchanger downselection and lessons learned from a prior effort motivate the research in the present project, the history and design evolution of the particle/sCO_2 heat exchanger is outlined in this section. Details surrounding the initial downselection and justification of pursing a moving packed-bed heat exchanger can be found in [68].

Figure 55 summarizes the evolution of the G3P3 design and mentions the challenges that were encountered and addressed with each iteration. The figure begins with the 100 kW_t geometry from the SuNLaMP project, which was a prototype designed and tested in a separate effort [67]. Through the construction and testing of the initial prototype, the key performance limitations were identified to be sCO_2 pressure drop, thermal performance, and manufacturability. Many of these issues and others can be tied to the complex external piping network of the heat exchanger that was implemented to connect the individual plates that are contained in the particle case. Therefore, a more monolithic heat exchanger design was pursued which leveraged features from microchannel recuperators and air coolers but implemented in a geometry to accommodate particle flow. The novel feature of the second iteration of the design is the limited use of external piping through the elimination of individual plates. This is accomplished through a microchannel heat exchanger geometry known as integral porting where flow distribution is accomplished inside of the plate itself and some of the plate surface area is used as the header rather than external piping. Although the second iteration was shown to be a large improvement over the initial effort in terms of pressure drop and modeled heat transfer coefficient, the pressure drop was still over twice the required value for a primary sCO_2 power cycle heat exchanger. Much of the sCO_2 pressure drop can be attributed to the heat exchanger geometry which implemented multiple cross flow banks arranged in a counter-flow configuration. This geometry allows for the heat exchanger to be constructed from multiple materials with dissimilar metal welds between the banks. Although the multi bank concept allows for cost reductions in the lower temperature areas of the heat exchanger through the use of stainless steel or lower cost Ni alloys (800H), the sCO_2 path length and multiple flow distribution regions result in a high sCO_2 pressure drop. Thus, the multi-bank concept was abandoned in favor of a single counter-flow heat exchanger bank that minimizes sCO_2 pressure drop through reducing the path length and number of entrance and exit regions. The heat exchanger design shown in the final image of Figure 55 is the geometry that is being proposed for the 1 MW_t pilot plant. The most notable design improvements in the final iteration are a low pressure drop from limited external piping and minimizing sCO_2 flow distribution regions, improved heat transfer coefficient from a manufacturing technique to create narrow particle channels and pure counter flow arrangement, and conceptually scalable to a multi-megawatt plant. The commercial scale version of this heat exchanger will be discussed in a future section.

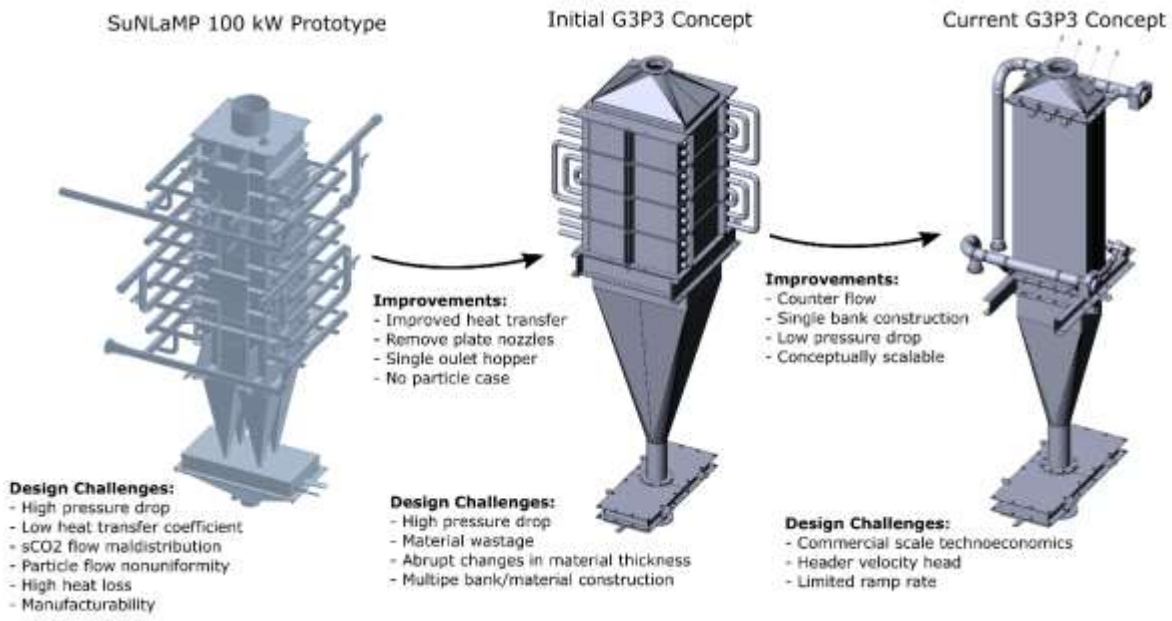

Figure 55. Evolution of the G3P3 heat exchanger design

3.1.3.2. Heat Exchanger Modeling

Modeling of the 1MW$_t$ prototype and 20 kW$_t$ subscale geometry was conducted using computational fluid dynamics and finite element modeling tools developed in Sandia's SIERRA high performance computing code to investigate the following items.

- Pressure drop and flow uniformity of the sCO_2 microchannel layout
- Sensitivity of the overall heat transfer coefficient to model inputs
- Thermal stress during steady-state and transient operation

The findings from the modeling efforts are reported in the following section to satisfy the research milestones.

sCO_2 Channel Modeling: The flow uniformity and pressure drop within the sCO_2 microchannel network was evaluated using computational fluid dynamics over the entire anticipated operating range of the heat exchanger. It is not only necessary to determine if the flow through the heat exchanger is uniform at the design point, but rather the entire space where the heat exchanger may operate such that the required turndown and off-design operation can be achieved. The layout of the channels was initially performed by VPE based on experience developing fluid-fluid microchannel heat exchangers which implement similar integrally ported geometries and internal features to promote uniform flow of sCO_2 through the core. Following the initial geometry development, Sandia performed CFD analysis and iterated on the design with VPE and Solex to ensure uniform flow was obtained on the sCO_2 side without creating blockages or flow non-uniformities on the particle side.

The exact channel layout cannot be presented here since it contains information proprietary to VPE. CFD simulations were conducted using the exact microchannel network with all of the features that promote uniformity and reduce pressure drop. CFD simulations were conducted using the exact

microchannel network with all of the features that promote uniformity and reduce pressure drop. However, no contour plots of the sCO_2 flow are provided in this section to protect the proprietary microchannel layout. However, the important metrics (flow distribution and pressure drop) post processed from the modeled results are reported below.

The CFD simulations for the sCO_2 microchannel layout were conducted at 100 °C intervals considering flow rates from 25% to 125% of the specified design flow rate (5.26 kg/s). Pressure drop was post processed from the simulation by taking the difference between the inlet and outlet for each simulation and plotted as a function of flow rate and temperature in Figure 56. In addition to total pressure drop of the heat exchanger, the contributions to pressure drop were identified by postprocessing intermediate values to identify the most significant contributions.

The target for pressure drop was set at 2% (500 kPa) of the operating pressure which was established based on the pump pressure rise for the prototype system (Gen3 sCO_2 Flow Loop). Commercial systems with turbomachinery will have similar pressure drop requirements to prevent large parasitics on the compressor. The results in Figure 56 show that for an isothermal 700 °C operating condition the pressure drop is anticipated to be 580 kPa for the design flow rate. Similarly, the simulations indicate a pressure drop of 450 kPa for the design flow rate at 500 °C. Since the heat exchanger will have an average operating temperature between these two values at the design point, the pressure drop will be less than the targeted 2% metric. The breakdown of pressure drop contributions can be observed in the second plot in Figure 56. The primary contribution to pressure drop is shown to be the inlet flow distribution region with the outlet and straight channel region only having small contributions. This is primarily due to the inlet being fed by only two ports at either side to prevent particle obstructions where the outlet contains multiple ports.

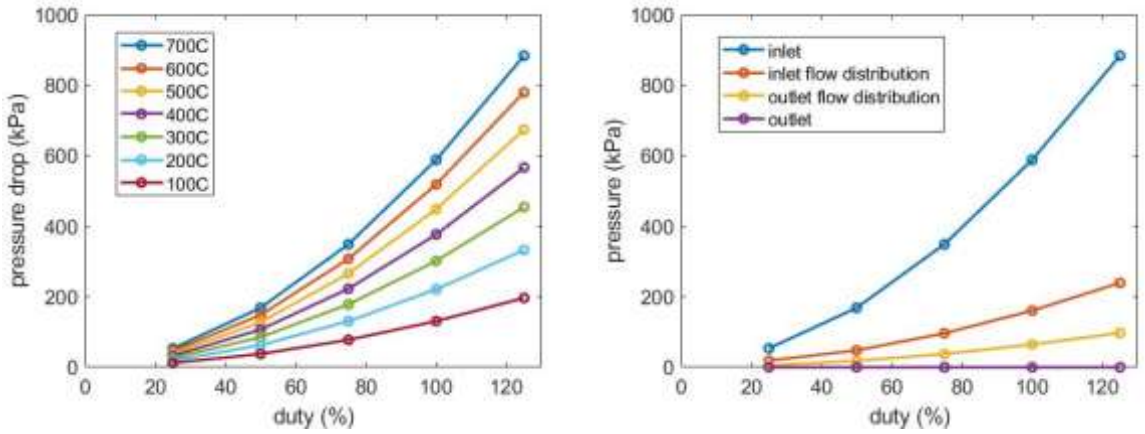

Figure 56. Pressure drop as a function of flow rate and temperature from CFD analysis on the microchannel network (left) and breakdown pressure drop contributions by heat exchanger location at 700 °C (right)

The second important metric that can be post processed from the CFD simulations is the flow uniformity. Non-uniform sCO_2 flow can have a negative impact on the heat exchanger thermal performance, but more importantly cause temperature gradients leading to high mechanical stress. Prior analysis set the target for flow non-uniformity to less than 10%. The results for the design point case are shown in Figure 57. The individual channel flow rates are plotted for half of the plate (102 channels) due to the symmetry present at the plate centerline. Using the variance as the measure of the flow non-uniformity, the design point is calculated to have a flow non-uniformity of 5.98% and the range of flow rates is observed to always fall within ±10% of the average.

The flow non-uniformity was similarly postprocessed form the CFD simulations over the entire operating range and plotted in Figure 58. Heat exchangers are typically observed to have poor flow uniformity at significant turndown which results in a minimum flow rate to prevent large flow non-uniformities from leading to heat exchanger failure. For the microchannel layout in the 1 MW heat exchanger geometry, the flow rates between 25% and 125% of the design condition are observed to not result in any significant additional flow non-uniformity. Over the entire temperature and flow rate range, the flow uniformity is observed to remain below 7%, which falls within the establish 10% metric.

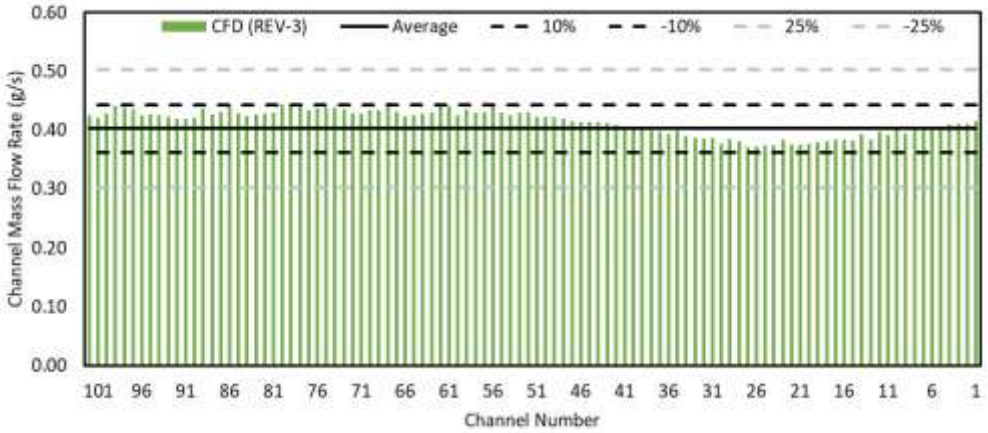

Figure 57. Individual microchannel flow rates at the heat exchanger design point operating conditions

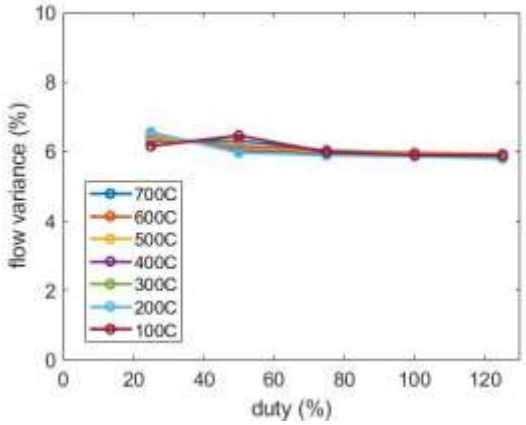

Figure 58. Flow nonuniformity as a function of temperature and pressure from CFD analysis on the microchannel network

Thermal Performance Modeling: The initial sizing of the heat exchanger was performed using Solex' reduced order model. The reduced order model can be used to rapidly iterate on a heat exchanger design and specify the required heat transfer surface area based on the particle side geometry for a simple counter-flow arrangement. However, a higher fidelity model capable of resolving 3-D temperature distributions is desired to verify the sizing and inform mechanical stress calculations. The modeling framework used in this project was initially developed in the SuNLaMP project and is in the process of being verified/validated against the 20 kW_t prototype heat exchanger experimental data to provide confidence in the modeling results for the 1 MW_t heat exchanger design. The model resolves all of the individual sCO_2 microchannels through coupling an isothermal CFD simulation to

the thermal models of the particle and plate domain. This simplification allows for a reduction in simulation time due to the small timestep requirements of the CFD simulation being decoupled from the thermal model.

The predicted temperature distribution in the heat exchanger plate, particle, and sCO2 domains are not shown due to proprietary details. The inlet and outlet temperatures can be used to post process the overall heat transfer coefficient at the design condition which is calculated to be 412 W/m^2-K. It is important to note that this modeling result is in line with the reduced order modeling technique typically used for sizing moving packed bed heat exchangers.

In addition to the baseline modeling result, a sensitivity analysis was performed on the key model inputs and assumptions to evaluate the uncertainty in the heat exchanger thermal performance. The key model uncertainties considered are particle flow non-uniformity (±25%), near-wall thermal conductance (±50%), and packed-bed effective conductivity (±10%) with uniform distributions. The ensemble of simulations yields an uncertainty in the modeled overall heat transfer coefficient of 412 ±### W/m^2-K

Mechanical Stress Modeling (Milestone 4.5): The heat exchanger microchannel layout and dimensions were established by VPE based on ASME BPVC allowable stress for IN617 at the 800 °C and 28 MPa design conditions, which establishes the heat exchanger mechanical integrity for the primary stress of pressure containment for a 100,000 hour lifetime. In addition to the pressure containment, secondary stresses due to temperature gradients also need to be considered to understand if the heat exchanger geometric configuration is a significant contribution to the stress field. The simulated temperature distribution within the heat exchanger plate that were generated from the thermal model were coupled to a mechanical modeling tool in SIERRA to resolve plate stress and strain fields considering the sCO_2 operating pressure (25 MPa). It is important to note that it is not strictly necessary for the combination of secondary and primary stresses to not exceed the ASME allowable stress for the material, but the allowable stress can be used to understand the significance of the stress magnitude observed in the thermomecanical analysis. Rather, the stress field observed in the thermo mechanical analysis should be used in a creep/fatigue analysis to evaluate the effect on the heat exchanger lifetime.

The next step is to compare the maximum stress change from the steady-state operating condition to the idle condition to establish the stress amplitude for fatigue analysis. The 100,000 cycle fatigue stress reported for IN617 at 760 °C is approximately 300 MPa, which falls well below both the peak value of stress and stress amplitude of 160 MPa observed in cycling between idle and design point operation. Finally, the design point operating conditions need to be evaluated considering the rupture lifetime from material creep. The 10,000-hour rupture life for IN617 at 760 °C is reported to be ~100 MPa, which does fall below the peak stress value observed in the simulation. However, the location of peak stress (sCO_2 outlet port) will operate well below the particle inlet temperature and follow the sCO_2 outlet temperature (715 °C). In addition, the secondary thermal stress present will relax with time making the value extremely conservative compared to a comprehensive creep model. Though interpolating values of creep data for IN617 the heat exchanger lifetime is conservatively estimated to be 8000 hours. However, the G3P3 1 MW_t prototype is only anticipated to operate for up to 2,000 hours over its lifetime so it will satisfy the operational requirements of the pilot plant, but further analysis needs to be conducted on the lifetime of commercial units to better estimate lifetime where a 30-year lifetime is required. In addition, significant improvements could be made by optimizing the microchannel layout around the integral sCO_2 ports to reduce temperature gradients.

Transient Modeling (Milestone 4.7): Although the prior steady-state thermomechanical analysis indicated acceptable levels of stress within the heat exchanger at design point conditions with daily cycling for the pilot plant. Additional analysis is required to understand if the stresses observed during heat exchanger startup could reduce the fatigue life of the heat exchanger. In order to understand the startup limitations of the G3P3 heat exchanger design, transient thermomechanical simulations were conducted. When not in operation, the heat exchanger will be held at the cold storage bin condition through recirculating particles from the cold storage bin through the heat exchanger. In other words, the heat exchanger is held at an isothermal condition of 615 °C prior to startup. The approach to starting the heat exchanger was simulated using two different methods to identify the best approach. The first approach (Figure 59 top) was to ramp the particle inlet temperature from the cold storage temperature (615 °C) to the hot storage temperature (775 °C) with the sCO_2 and particle flow rates held at their design condition. Four different ramp rates (10, 20, 40, and 80 °C/min) were investigated to determine the limitations on startup time. All of the ramp rates above 10 °C/min indicated stress values during the transient period that exceeded the stress at steady-state operating conditions. The second approach (Figure 59) to startup was to ramp the particle side flow rate with a step change in inlet temperature.

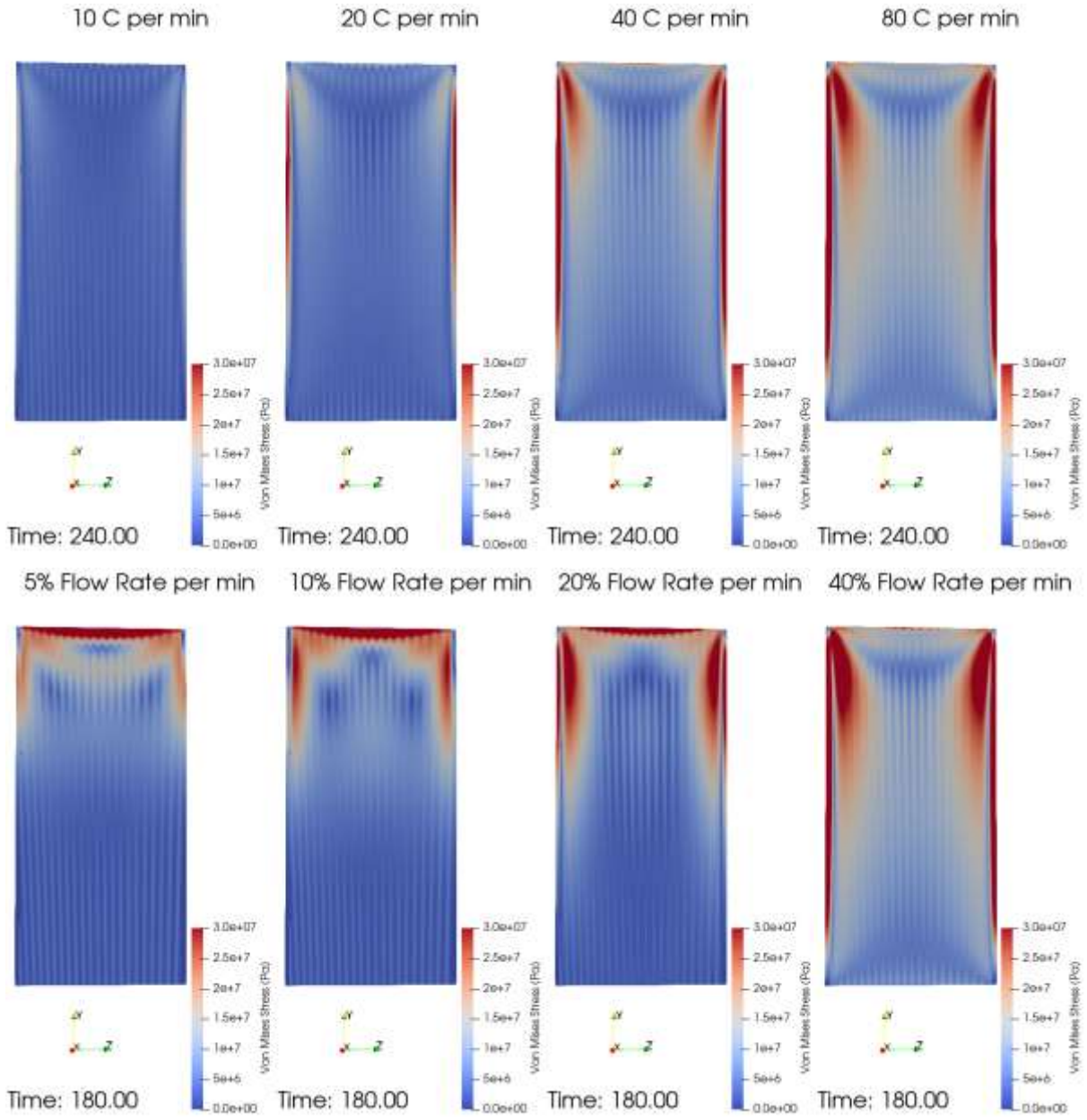

Figure 59. Von-mises stress distributions from transient thermomechanical simulations with variations in ramp rate of particle inlet temperature (top) and particle flow rate (bottom).

This approach is desirable because mixing particles to ramp inlet temperature would not be required, which has been a challenge in molten salt plants. Four different ramp rates of particle flow (5, 10, 20, and 40 %/min) were investigated. All simulations indicated stress values at the plate leading edge significantly higher than steady-state values and issues were experienced at the plate vertical edges as well. Ultimately, the limiting issue with the design is the thermal lag of the plate vertical edges and the enhanced heat transfer on the particle side at the plate leading edge that significantly exceed steady state values of stress. Future studies will investigate removal of some of the edge material and including the sCO_2 flow distribution around the integral ports, which were shown to be the most problematic areas in the heat exchanger.

Heat Loss: A heat loss analysis was performed for the G3P3 heat exchanger geometry to specify the insulation design and understand how significant heat loss would be for the performance measurements. Finite element simulations for steady-state conduction were performed with various insulation thickness. The results are plotted in Figure 60 for an insulation design that consists of either SuperWool or a combination of SuperWool and microporous. In order to keep the heat loss below 0.5% of the heat exchanger thermal duty, a design consisting of one inch of microporous and four inches of SuperWool was selected.

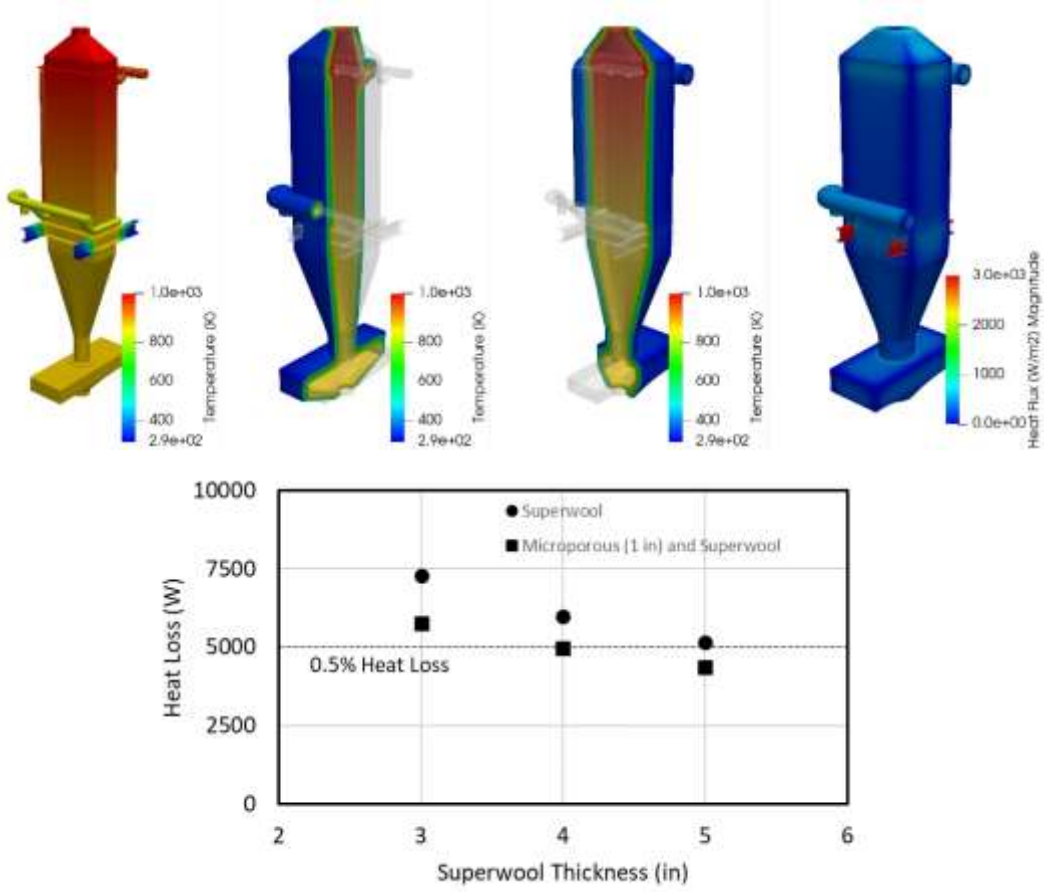

Figure 60. Heat loss analysis for 1 MW_t G3P3 heat exchanger insulation design (top: FEA simulation result for the specified design of 1 inch Microporous and 4-inch SuperWool, bottom: parametric study of heat loss as a function of insulation thickness)

3.1.3.3. Heat-Exchanger Testing

Two experimental test campaigns were undertaken to verify that the particle flow within the heat exchanger behaves as expected and that the performance agrees with model results. The first experiment involved a particle flow visualization study to investigate the uniformity of particle flow in the adjacent parallel channels to verify mass flow. The second experiment involved performance evaluation of the previously discussed 20 kW prototype.

Particle Flow Uniformity: High-temperature particle flow testing was conducted to identify the practical limits of the flow in narrow vertical channels (Milestones 4.4.1 and 4.4.2) [69]. Since moving packed-bed heat exchanger performance is improved with reduced particle channels widths (heat diffusion length), it is desirable to use the smallest particle channel possible without causing

unreliable or nonuniform particle flow. Evaluating the flow uniformity at high flow rates and at 650 °C provide an indication of the plate spacing limitations of moving packed-bed heat exchangers using HSP 40/70 particles.

Prior studies on high-temperature particle flow testing [69] indicated that a mass flow regime through a parallel plate heat exchanger can be achieved by using a 77° flow cone below the parallel plate test block, but didn't investigate channel widths other than ¼" (6.35 mm). The present work implemented the same mass flow cone at an elevated temperature of 650 °C based on the targeted heat exchanger outlet temperature, but investigated with channel widths between 6.35 mm to 1.5 mm. Channel widths were selected based on commonly available material thicknesses to act as plate spacers including ¼" (6.35 mm), 3/16" (4.76 mm), 12 GA (2.66 mm), and 16 GA (1.58 mm). Cold flow tests were also conducted for the various channel widths to identify if elevated temperature contributes to flow non-uniformity. The results from this study were documented in an ASME conference paper [69] and are only summarized below.

The flow distribution values are summarized in Table 14, Table 15 and Table 16 which were calculated with the following equation:

$$Flow\ variation\ (\%) = \frac{V_{max} - V_{min}}{V_{max}} \times 100$$

A sample flow visualization experiment at 650 °C with ~3 mm particle channel width is shown in Figure 61. Velocity is extracted from the snapshots through measuring the heights of the particle levels in the individual channels. The particle flow maldistribution is as a function of plate spacing at temperature is reported in Table 15. Flow non-uniformity is shown to increase with decreasing particle channel width. Cold flow testing at ambient temperature conditions has also been conducted and shows similar values of flow nonuniformity as the tests conducted at operating temperature. The smallest particle channel (~ 1.5 mm) indicated some a higher overall resistance between the particles and the channel walls that resulted in minor discontinuities in the flow of the particles. The flow seems to have small air pockets between the parallel plates as observed through the quartz window. It is unknown if these air pockets only exist at the window or throughout the bulk flow.

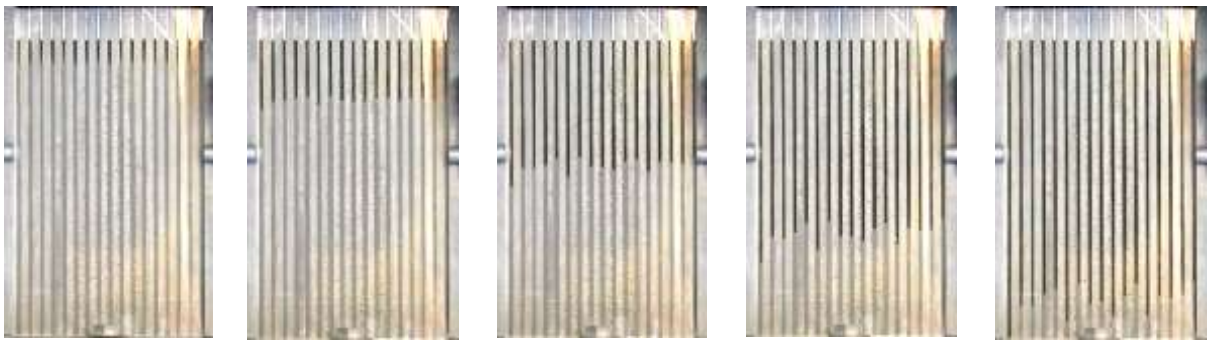

Time: 0 sec
Distance: 0"

Time: 5 sec

Time: 10 sec

Time: 15 sec

Time: 20 sec

Figure 61: Hot flow testing of 0.105" (2.66 mm) particle channel width [69].

Table 14: flow distribution results summary for 25 °C testing

Channel Spacing	Mass Flow Variability [%]	Mass Flow [kg/s]	Flow velocity [mm/s]
¼"	5.69	0.146	6.14
3/16"	8.95	0.147	6.77
12 GA	16.4	0.148	10.8
16 GA	18.53	0.150	18.57

Table 15: flow distribution results summary for 650 °C testing

Channel Spacing	Mass Flow Variability %	Mass Flow [kg/s]	Flow velocity [mm/s]
¼"	7.75	0.146	5.3
3/16"	11.94	0.147	6.2
12 GA	15.32	0.146	9
16 GA	20.08	0.149	13.3

Bridging of particles between parallel plates can potentially be introduced if there is any form of obstruction or contamination that is close to the size of the channel width (within a couple of particle diameters below the channel spacing). The ~1.5 mm spacing, which is the smallest gap spacing tested in this series of experiments, showed some bridging of particles between the parallel plates only at the end of the parallel plates where there is contact with the quartz window. In this scenario, the particles are in contact with three walls and form a bridge only on the surface of the quartz window as illustrated in Figure 62.

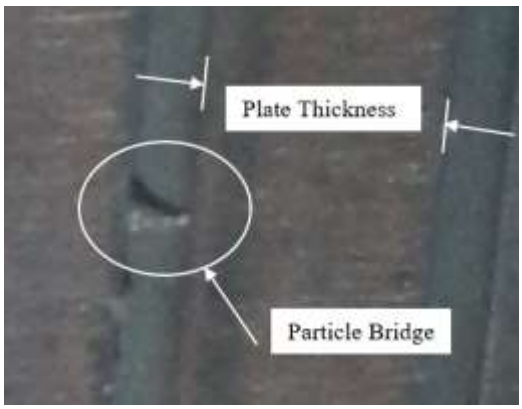

Figure 62. Particle bridging for 1/16" gap spacing

Flow nonuniformity was measured at increased flow rate (Table 16) to evaluate the effect of higher particle velocities that could result from different heat exchanger aspect ratios. The measured flow variation decreased slightly with increasing velocity. In addition, the flow variation measurements are reported at ambient and operating temperature. The operating temperature did not have a significant impact on the flow non-uniformity.

Table 16: Flow distribution results for 2.66 mm channel width with variations in flow velocity and operating temperature

Flow temperature	Mass Flow Variability [%]	Mass Flow [kg/s]	Flow velocity [mm/s]
Hot	15.32	0.146	9
Ambient	16.4	0.148	10.8
Hot	12.88	0.64	38.22
Ambient	14.39	0.67	41.83

20kW Heat Exchanger Prototype and Testing:

Performance testing of the 20-kW_t prototype heat exchanger was conducted using integrated particle and sCO_2 flow loops that were constructed under a parallel Gen3 Lab Call support project and documented in an ASME conference paper [70]. The piping and instrumentation diagram of the test system shown in Figure 63 closely matches the sCO_2 flow loop configuration under development for the Gen3 pilot system and heat exchanger integration into the 1 MW_t G3P3 pilot plant. The sCO2 side is an isobaric flow loop and uses a dense phase pump rather than turbomachinery to circulate the working fluid. The particle flow loop is electrically heated and able to operate continuously due to particle recirculation. This results in true steady-state heat exchanger data and significant test time rather evaluating performance from short batch mode tests.

An illustration of the particle/sCO_2 heat exchanger test facility is provided in Figure 64. The particle flow loop uses a vertically integrated design with gravity driven flow, which allows for the particle flow rate through the entire system to be governed using one control valve at the outlet of the heat exchanger. The particle lift is a custom high-temperature screw auger constructed from stainless steel using standard pipe sections. The electrical heater is designed using commonly available cartridge heaters and custom formed hoppers to create a staggered tube array for heating the particle flow. Mass flow measurements are made gravimetrically using an inline weigh hopper that is continuously charged and discharged during operation. The system layout was designed based on many lessons-learned from system integration and instrumentation in the prior 100 kW SuNLaMP testing. Many of the same design features (inline weigh hopper, thermal equilibration length, redundant instrumentation) have also been included in the 1 MW_t G3P3 heat exchanger subsystem.

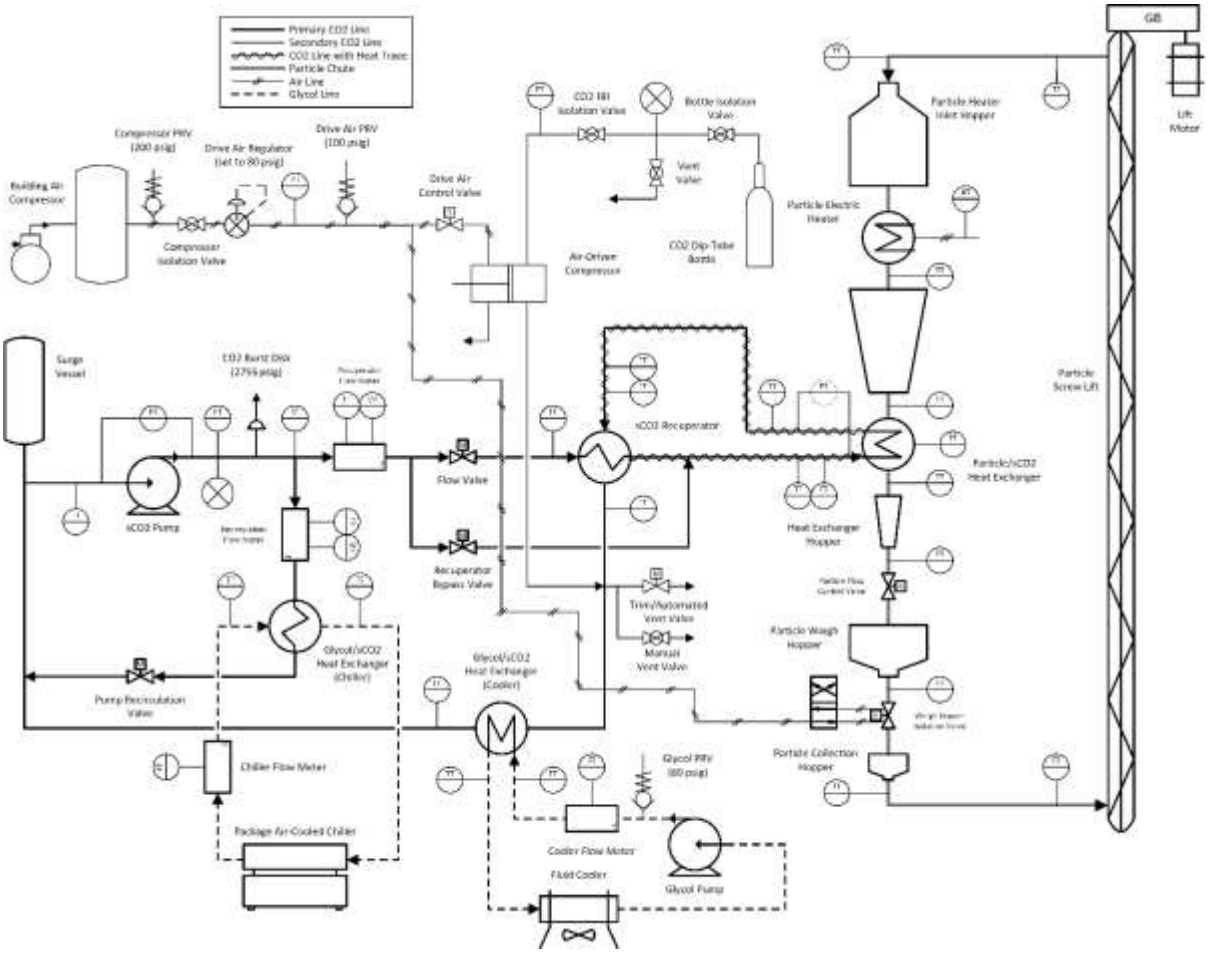

Figure 63. Piping and instrumentation diagram of the 20-kW_t particle-to-sCO_2 heat exchanger test stand

Testing of the 20-kW_t subscale prototype heat exchanger occurred through starting flow on the particle and sCO_2 at ambient temperature. The particle heat exchanger inlet temperature was slowly ramped to the desired operating temperature by controlling the electrical heat addition in the heater. Once the electric heater reached the target inlet temperature, PID control of the electric heater was enabled and the flow valves on the sCO_2 side were adjusted to manipulate the sCO_2 inlet temperature and flow rate. The temperature measurements were allowed to stabilize and remain at steady state for approximately one hour prior to moving to a new operating condition. Steady-state operating conditions for performance evaluation were identified as periods of greater than 15 min with less than ±1 °C of variation at all four heat exchanger boundaries.

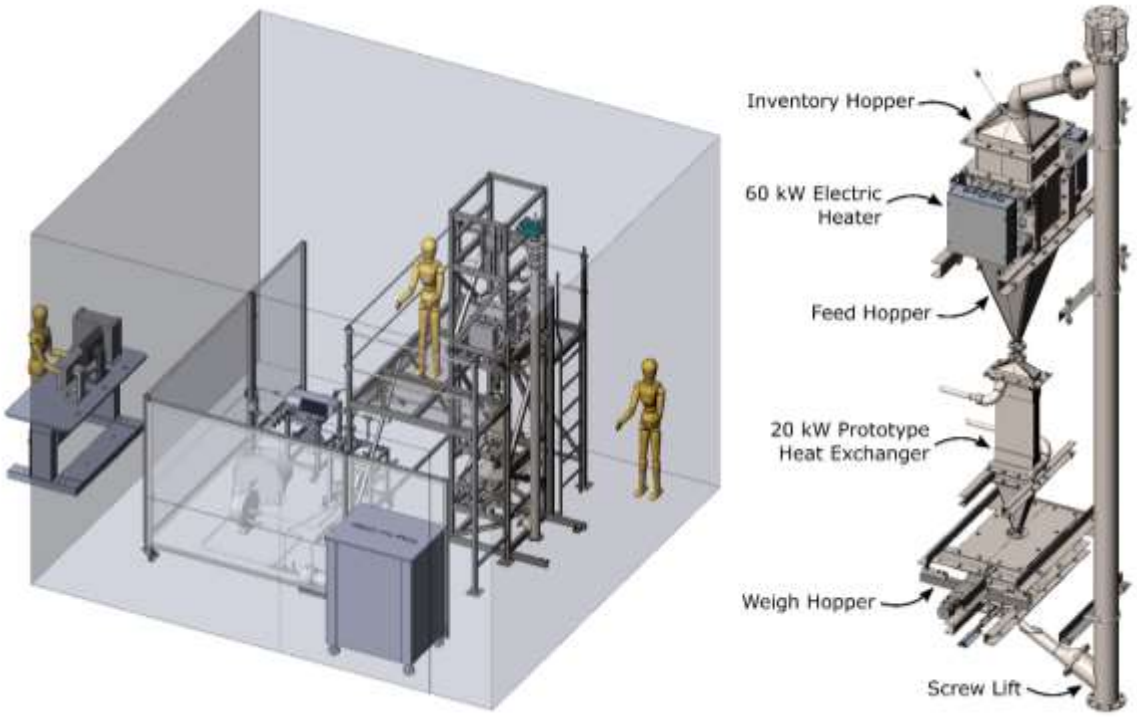

Figure 64. Illustration of the integrated particle and sCO_2 flow loops and detailed layout of the particle flow loop with integrated 20 kW_t subscale heat exchanger

The steady-state measurements of thermal performance for the 20-kW_t subscale prototype are displayed in Figure 65. The overall heat transfer coefficient is observed to be approximately 300 W/m^2-K at the intermediate temperature operating conditions (400-600 °C) and displays a slight dependence on particle inlet temperature in the ranger of 200-400 °C. The measured values of performance were verified through evaluating closure of the heat exchanger energy balance and agreement between upstream and downstream temperature measurements. The measured performance for the G3P3 20 kW_t subscale prototype is a large improvement over the performance of the first 100 kW_t prototype developed in a prior project that had overall heat transfer coefficient values of 50-70 W/m^2-K [67] and difficulty in measuring the performance due to system integration issues. The observed overall heat transfer coefficient for the 20 kW_t prototype is between a factor of 4-6 times better than any other known particle to sCO_2 heat exchanger in existence. Pressure drop (Figure 66) was measured from inlet to outlet of the heat exchanger and observed to be less than 7 kPa (0.04%) at the design point conditions which is in line with CFD modeling results and builds confidence in the pressure drop estimations for the 1 MW_t prototype. The measured pressure drop of the 20 kW_t prototype was expected to be substantially lower than the 2% target of the 1 MW_t design due to a combination of the intermediate temperature sCO_2 properties (lower viscosity and higher density), larger channel dimensions because the allowable stress of stainless steel (105 MPa) at 550 °C is more than triple the value of IN617 (30 MPa) at 800 °C, and the small plate dimensions resulting in shorter flow path lengths. Overall, the measured performance and operation of the 20-kW_t subscale prototype provides confidence in the modeled results of the 1 MW_t pilot plant design.

Table 17. Steady state datapoints for 20 kW_t subscale prototype heat exchanger performance measurements

Particle Inlet (°C)	Particle Outlet (°C)	CO2 Inlet (°C)	CO2 Outlet (°C)	Particle Flow (kg/s)	CO2 Flow (kg/s)	HTC (W/m^2-K)	Thermal Duty (kW)	Pressure Drop (kPa)
205.6	54.24	15.98	65.74	0.09122	0.9791	269.1±9.5	12.30±0.13	1.688
254.8	81.98	40.89	92.2	0.08943	0.09979	280.1±8.9	14.43±0.13	2.264
313.3	155.3	103.7	190.3	0.08865	0.09947	290.7±8.5	13.91±0.09	4.262
357.4	200.3	136.6	243.0	0.08859	0.09858	286.6±7.5	14.48±0.08	4.691
398.7	219.6	147.4	272.0	0.09204	0.1032	302.9±7.1	17.11±0.08	5.920
445.8	259.6	178.7	319.1	0.08765	0.1024	305.3±6.7	18.17±0.08	6.347
506.8	305.3	214.9	372.6	0.08669	0.1012	303.7±6.1	19.63±0.07	6.940

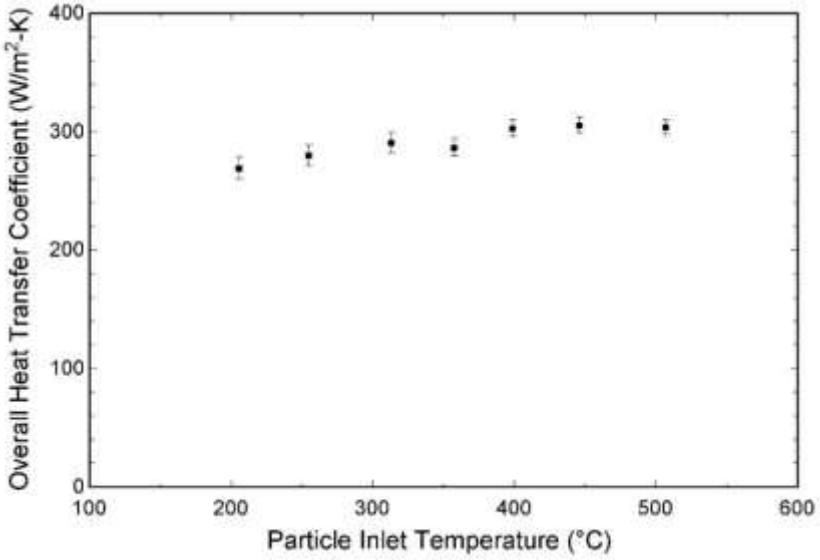

Figure 65. Steady-state measurements of overall heat transfer coefficient of the 20-kW_t subscale prototype particle/sCO_2 heat exchanger at various particle inlet temperature

3.1.3.4. G3P3 Heat Exchanger Materials and Costs

The total cost for the 1 MW_t G3P3 heat exchanger subsystem is estimated to be $1.9M based on quotes for manufacturing the novel components and vendor pricing for the common off-the-shelf components. The breakdown of costs is provided in Figure 67 which is dominated by the raw material and manufacturing costs of the heat exchanger core. The remaining components including the hoppers/valves, control system and instrumentation, insulation, and assembly/commissioning make up approximately 25% of the budget.

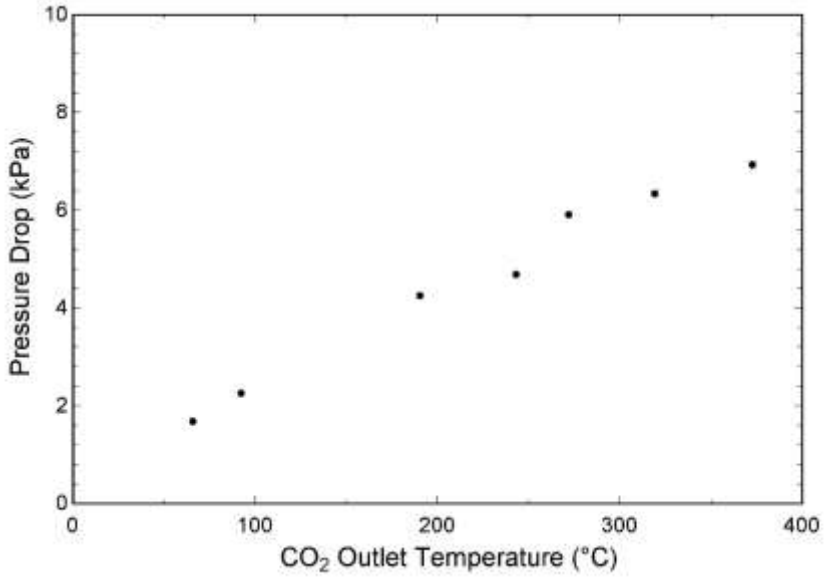

Figure 66. Steady-state measurements of pressure drop over the entire 20-kW_t subscale prototype particle/sCO_2 heat exchanger at sCO_2 design flow rate (~0.1 kg/s)

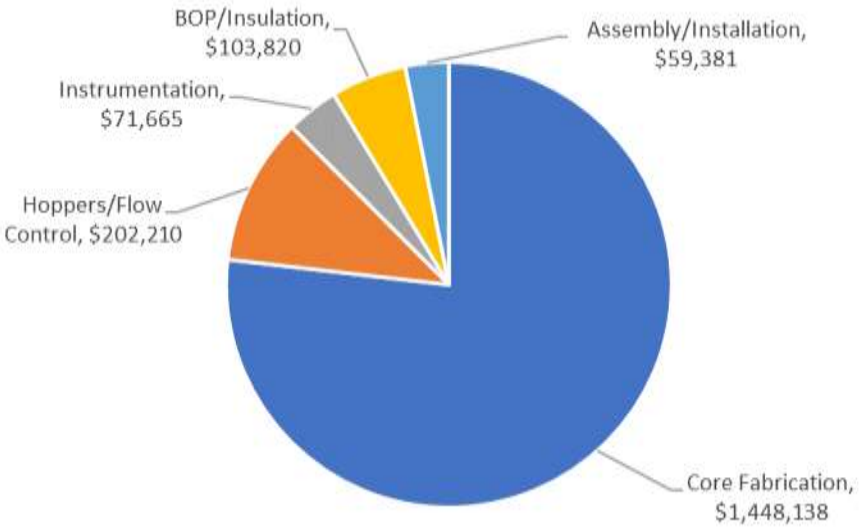

Figure 67. Heat exchanger costs for the 1 MW_t G3P3 pilot unit. Total cost ~$1.9M.

3.1.3.5. 100 MW_e Heat Exchanger Design

Scaling of the 1 MW_t G3P3 heat exchanger prototype is anticipated to occur through a combination of increasing the size of a single unit as well as numbering up the heat exchangers with parallel units. The largest single moving packed-bed heat exchanger unit is envisioned to be a 33 MW_t design, which is constructed from eight individually bonded and brazed cores that are welded together. The 33 MW_t units are numbered up with six parallel units to achieve a baseload application thermal duty of 200 MW_t (Figure 68). The dimensions of the microchannel plates were scaled to 2 m tall by 0.76 m wide to increase the total surface area of a single plate. This plate size is currently constrained by the capacity of diffusion bonding furnaces and plate etching equipment. The header configuration

for the heat exchanger at the inlet is consistent with the G3P3 design, but the header configuration at the outlet has be modified to allow for a larger cross-sectional flow area to minimize velocity head that can lead to flow non-uniformity. The sCO_2 side pressure drop is estimated to be 2.5% based on the plate dimensions and header configuration. The overall heat transfer coefficient should be consistent with the 1 MW_t G3P3 prototype (>400 W/m^2-K) based on low-dimensional modeling results.

The manufacturing of the single 33 MW_t heat exchanger unit does slightly differ from the 1 MW_t G3P3 prototype since the total heat exchanger height will be limited by the bonding/brazing furnace capacity. However, the large-scale plates can be bonded together into sub-cores of the diffusion bonding furnace capacity and then welded together to form a single large-scale core (bank).

Figure 68. Two configurations for 200 MW_t moving packed-bed particle-to-sCO_2 heat exchanger concept (6 x 33 MW_t exchangers). Left: Drag-conveyor for ground-based system. Right: Gravity-driven feeder concept for tower-integrated or single-lift design. (Solex, VPE, and Sandia)

Due to the aspect ratio of the heat exchanger core, two inlets and two outlet hoppers are implemented to minimize the overall height of the heat exchanger. The parallel feeders will be individually controlled which shouldn't suffer from the same issues as the SuNLaMP multiple discharge devices that was gang controlled. The parallel heat exchangers will be fed using side-by-side drag conveyors (Figure 68, left) that take particles from the high-temperature storage bin to the heat exchanger inlets. The drag conveyor will operate at a slightly higher flow rate than the heat exchanger to ensure the heat exchangers remain filled. The excess flow will be recycled back to the inlet. Drag conveyors are also implemented at the outlet to convey particles into a single inlet for the cold storage bin. For installations which could be installed inside of a solar tower; where the heat exchangers are located between the hot and cold silos; the exchangers can be simply gravity fed by particles through chutes as particles flow from the hot bin, into the exchanger, and out to the cold silo.

Initially, some bulk solids conveyance suppliers did indicate that the high-temperature drag concept could be feasible. However, further evaluation as part of a parallel investigation indicated that the alloys and wear that a drag would experience at high temperatures would make the concept impractical. Instead, the concept was revised so that cool particles would be transported by high-

temperature steel belt conveyors while hot particles could be feasibly choke-fed to each exchanger by a local distribution bin and discharge chute (Figure 68, right). There would be a single high-temperature bulk particle transport conveyor or hoist to supply particles to the bin. The bin would have a small control volume and distribute solids to each exchanger. While this concept is currently envisioned as reducing heat losses by refractory lining the distribution bin and chutes, the exact refractory specification, and how thick any additional insulation would be (e.g. 2" or 8" on chute OD, with 4-5" of refractory on chute ID) remain subject to future project definition.

Commercial Scale Cost Analysis: The scaling concept for a 200 MW_t moving packed-bed particle-to-sCO_2 heat exchanger was used to estimate cost for a commercial scale plant. The baseline 200 MW_t design, which has similar thermal performance and pressure drop to the 1MW_t G3P3 heat exchanger, was estimated at a cost of \$88.1M (\$440/kW_t). The estimated cost was based on industry provided estimates for heat exchanger core material and manufacturing (assuming large scale purchasing and high demand for nickel alloy sheet stock), external piping for flow distribution, a high temperature particle distribution and collection system, and structural supports. It is important to note that this cost is not based on a learning curve for an N^{th} of a kind component, but rather industry estimates on what will be available in the near term. The estimated cost of the 200 MW_t design is significantly above the DOE metric of \$30M (\$150/kW_t), but ultimately the system LCOE is the important metric for the development of particle technology. To understand the implications of a heat exchanger cost that is significantly above the DOE target on the system LCOE, the new cost estimate was used to build a new heat exchanger cost model that can be integrated in the baseload technoeconomic tool. The results are discussed in the system technoeconomic analysis section. The new heat exchanger cost curves were shown to increase LCOE from 5.8 ¢/kW-hr to 6.5 ¢/kW-hr. The majority of the increase in LCOE is attributed to the heat exchanger capital cost and a small portion is attributed to the pressure drop being above the target. Although the heat exchanger cost is higher than anticipated by almost a factor of three, the LCOE increase is only about 10% due to the capital cost of the heat exchanger not been a dominate piece of the system.

Prior Industry Experience: Solex has experience with high-temperature bulk solids coolers and units which must be operated in parallel. These units are typically controlled by level as measured in the exchanger inlet hopper, with the level controller modulating the product flow through the discharge device on the exchanger. Solex has many large fertilizer coolers operating in parallel (+100 ton/h for each unit) on level control in the inlet hopper. However, these are not high temperature units. One example of a similar system is the Bunge Rio Grande plant in southern Brazil with 6 parallel exchangers heating soybean & fed with a drag conveyor.

Although the heat exchanger technology and manufacturing described in this report is new, the operating methodology described in this report is consistent with what Solex would consider 'normal' for comparable equipment operating in comparable high-temperature cooling applications. These comparable applications utilize Solex's typical high temperature plate technology which differs from a microchannel sCO_2 cooler in that water is typically used as the working fluid and the decades long run-life of the plate-and-case design has demonstrated that the equipment can handle thermal shocking/high ramp rates. Obtaining comparable operating demonstration time will be valuable for particle/sCO_2 heat exchanger in potential future demonstration-scale facilities.

3.1.4. G3P3 Particle Lift Risk Reduction R&D

Sandia and its G3P3 partners have investigated several particle lift technologies, which are summarized in Table 18. For G3P3 and commercial-scale systems, we have downselected to the use

of a bucket lift (for cost and proven reliability) and a skip hoist (for lift efficiency and reduced heat loss), respectively.

Table 18. Particle lift technologies investigated [71, 72].

Lift Type	Method	Advantages	Challenges
Screw*	Rotating screw or casing lifts particles by friction up the flights of the screw	• Entire assembly can be made of stainless steel, allowing T>800°C • Continuous feed and control of mass flow	• Lowest lift efficiency (~5%) • More expensive than bucket elevator • High heat loss
Bucket*	Series of buckets on a chain lift particles	• Lowest cost • Proven reliability	• Low lift efficiency (~15-20%) • High heat loss
Skip Hoist	Large individual skips pulled by cable	• Lowest heat loss • Pair of skips can be counterbalanced • 4000-8000 tonnes/hr can be achieved (FLSmidth)	• High-temperature operation (~600 °C) needs to be demonstrated • Particle and heat loss during charging/discharging • Discrete feed
Pneumatic	Air flow is used to carry particles through ducts	• Potential for high reliability with no moving parts • Continuous feed and control of mass flow	• Erosion of duct walls from fluidized particles • Parasitic power consumption of fluidizing air • Heat loss from hot air flow

*Tested at the NSTTF during Phases 1 and 2.

3.1.4.1. G3P3 Bucket Lift

Analyses were performed to evaluate both bucket elevators and skip hoists to lift the particles from the cold storage bin to the top of the receiver [15, 71]. Skip hoists are the preferred choice for commercial-scale systems due to its higher overall lift efficiency and reduce area for heat loss. However, a skip hoist is cost prohibitive at the relative small scale of G3P3. Therefore, a bucket elevator will be used in G3P3 with concurrent analyses and testing of the skip hoist by KSU.

The proposed bucket elevator (BE) consists of 54.1m x 1.3m x 0.5m casing made from 10 guage (3.4 mm) carbon steel casing. There are approximately 340 carbon steel buckets with a holding capacity of 0.12 ft3 (3.4 L3) per bucket. The particles are HSP 40/70 entering at a temperature between 550 and 615 °C and a mass flow rate of 12 kg/s. The casing is insulated with 6 lb. Superwool Blanket material.

CFD simulations were developed of an existing 26-ft-tall bucket elevator from MHE that is being used at the NSTTF to lift particles up to ~600 °C at a rate of up to ~6 kg/s. The bulk particles were treated as a fluid with properties of CARBO HSP 40/70 and "flowed" along a path in a closed column defined by the movement and capacity of the individual buckets in the elevator [73]. Convective and radiative heat transfer to the walls were simulated. Results of simulated temperature profiles on the walls of the bucket elevator were compared to IR images of the physical bucket elevator during operation to gain confidence in the models (Figure 69). A parameter study was then performed on the G3P3 pilot-scale bucket elevator for a variety of superwool insulation thicknesses. These results showed that a few inches of insulation sharply reduced heat loss, and four inches of insulation were sufficient to reduce the particle temperature drop to less than 3 °C. Beyond ~4 inches of insulation, the heat losses and particle outlet temperatures began to reach an asymptote.

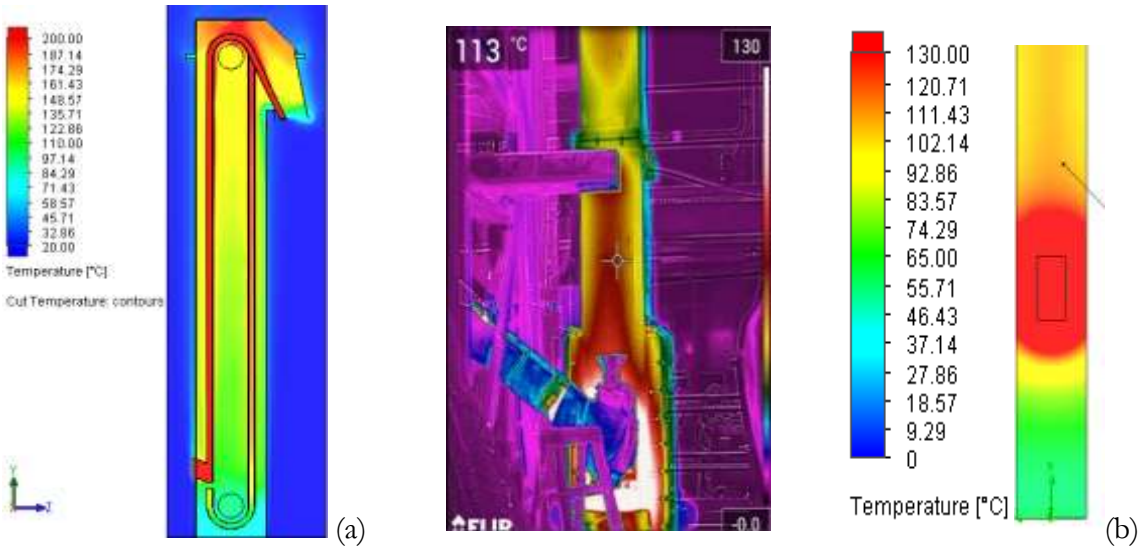

Figure 69. (a) Simulated temperature profile of particles flowing through a bucket elevator. (b) Comparison of measured (left) and simulated (right) casing temperatures.

3.1.4.2. 100 MW_e Particle Lift Design

Based on heat-loss and lift-efficiency analyses [15, 73, 74], the skip hoist is the most suitable solution for a commercial scale CSP system of 100 MW_e (Figure 70). Many different CSP configurations were analyzed ranging from a system with 1 receiver and a 2-skip hoist system to a 3-receiver tower with three pairs of skip-hoist units devoted to each receiver.

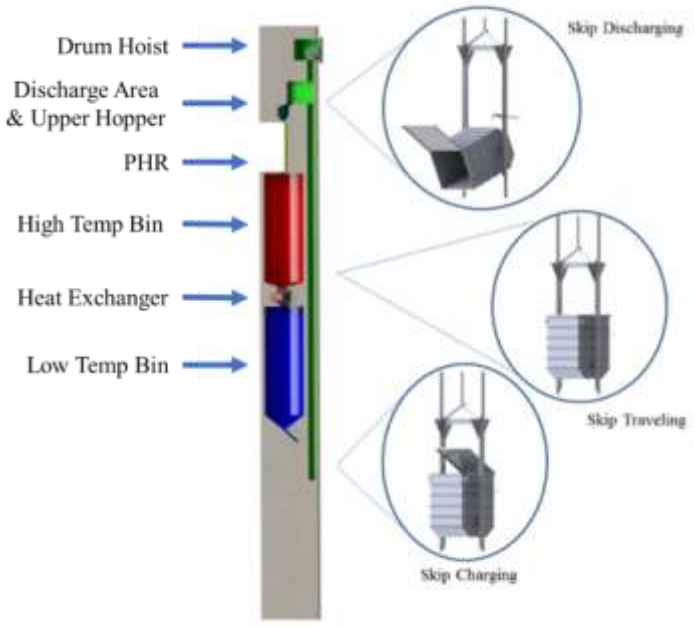

Figure 70. Schematic CSP Power Tower and Particle Lift Skip System [75]

A particular skip hoist design is a double Blair drum Kimberly skip hoist configuration. The configuration only has a single hatch or lid, which acts as both the charging and discharging port; and this design simplifies internal and external insulation and promotes minimal heat loss. All configurations share the same overall characteristics as shown in Table 19.

Table 19. Commerical Scale CSP Design Charateristics

Design Characteristics	Values
Electrical Power Generation	100 MW-e
Power-cycle Efficiency	0.5
Particle ΔT	160 K
Cp of HSP 40/70	1.209 kJ/kg-K
Low Temp	615°C
Solar Multiplier	2.75

3.1.4.2.1. Commercial Scale Thermal and Cost Analysis

The cost and thermal analysis of a skip-hoist system is summarized in Table 20. With a specified solar multiple of 2.75, the corresponding thermal input is 550 MW-th; however, the thermal capacity must be divided amongst each of the three lift systems. Consequently, the skip hoist designs are analyzed for three 33 MW-e units in the table. These configurations are represented as Config #1 to #3.

Table 20. Thermal and Cost analysis for different Commercial Scale CSP designs.

Config #	# of PHR	Power Elec Per PHR (MW-e)	Lift Height (m)	Thermal Capacity Per PHR (MW-th)	Mass Flow Rate (kg/s)	Bare Cost ($/kW-th)	# of ropes Per skip	# of skips per PHR	Rope Diameter (inches)
S1	3	33*	40	183	1000	9	2	2	1.37
S2	3	33*	45	183	1000	10	2	2	1.39

Config #	# of PHR	Power Elec Per PHR (MW-e)	Lift Height (m)	Thermal Capacity Per PHR (MW-th)	Mass Flow Rate (kg/s)	Bare Cost ($/kW-th)	# of ropes Per skip	# of skips per PHR	Rope Diameter (inches)
S3	3	33*	50	183	1000	10	2	2	1.41
1	3	33*	250	183	947	21	2	2	1.90
2	3	33*	275	183	947	22	2	2	1.86
3	3	33*	300	183	947	23	2	2	1.92
4	1	1.3	63	10	28	28	1	2	0.34
5	1	5.0	92	26	65	18	1	2	0.54
6	1	27	150	228	379	7	1	2	1.44
7	1	100	250	550	2841	18	2	2	3.28
8	1	100	275	550	2841	19	2	2	2.35

* 3 PHR configuration is current more evolved design. Config with S* means a supporting Skip

From the analysis of Table 20, with the current lift height ranging between 250 – 300 m, some of the skip hoist configurations, which are 1-PHR only, go outside or approach the operating range of the skip hoist wire rope of less than 3 inches in diameter, making these configurations unfeasible. These configurations are Config #7 & #8 in the table. However, by increasing either the number of skips or the number of wire ropes per skip, the diameter of the skip wire rope can be reduced to within the acceptable range. By using a 3-PHR configuration the mass flow rate for each PHR is reduced, thereby reducing the skip size requirements and mass payload of each skip, and thus reducing the wire rope diameter requirements. As noted in the table, even with these variations the bare cost per kW-th remains within the range of $18 per kW-th to $25 per kW-th per skip hoist. These bare costs were calculated without the cost of the shaft construction included which is assumed to be accounted for in the construction of the tower. Similar calculations exist for the G3-KSA project and can be found in that final report. The G3-KSA configurations are labeled Config #4 to #6 in the table.

Costs in Table 20, from most expensive to least expensive, included the variable frequency drive, skip, electric motor, hoist, reducer, rope, bearing, intermediate lift, and rope, in addition to labor and taxes.

3.1.4.2.2. Thermal Model Comparison for Skip Hoist.

Independent thermal models, based on different approaches, were developed by GT and Sandia for the bucket elevator and the skip hoist. Sandia produced CFD based models and GT used the transient lumped capacity approach. Even with some differences in the design specs, both approaches returned comparable estimates of the temperature drops, and both showed that the exiting particle temperatures stabilize within the first 60 minutes of a cold start. A side-by-side graphical analysis between both models is shown in Figure 71.

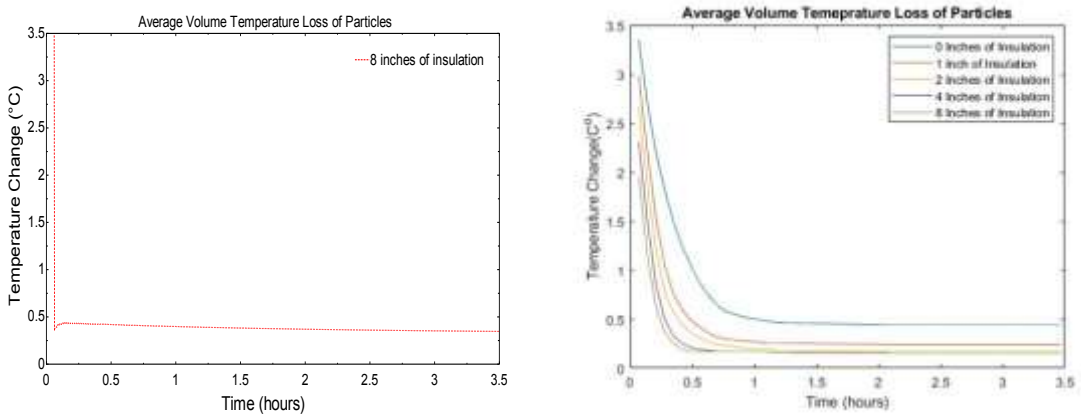

Figure 71. Comparison of the lumped capacitance and CFD model results for the transient skip-hoist heat-loss analysis.

The models show that the particles in the upper hopper reach a steady temperature within 1 to 2 hours of starting from a cold start. Moreover, all scenarios indicate that particle temperature falls less than 0.2% after leaving the low temperature bin. As for the percentage heat loss rate, all three scenarios indicate less than 0.3% loss.Finally a physics-based transient model was developed by GT to simulate the response and the ability of the skip hoist to recover from a break in a lifting rope, suddenly unloading the drive. Even in the case of this dramatic failure, the control system was simulated to quickly respond and maintain safe operation of the surviving skip.

3.1.5. Particles R&D

Studies of different particle types have confirmed our selection of CARBO HSP 40/70 (~350 micron diameter) as the best baseline particle for G3P3-USA. CARBO HSP, a commercially available ceramic particle used in the oil-and-gas industry as a high-strength proppant for hydraulic fracking, has excellent high-temperature strength, durability, flowability, and optical properties, with no observed sintering over 1000 °C and no potential for respirable crystalline silica hazards [1, 27, 76]. Although the cost of CARBO HSP (~$1/kg) is higher than silica sand, LCOE calculations have shown that we can still achieve $0.06/kWh$_e$ with CARBO HSP in a 100 MW$_e$ CSP plant (see Section 3.3.1). As described in Section 3.1.1.8, we are also considering alternative particles (sand) with partners G3P3-KSA and CNRS-PROMES (fluidized particle-in-tube receiver). The ultra-low cost of sand will provide additional opportunities for LCOE reductions.

3.1.5.1. Summary of Particle Studies

The following particle-based studies have been performed in Phases 1 and 2:

- Collaborations have been established with UC San Diego (R. Chen) and Georgia Institute of Technology (P. Loutzenhiser, Z. Zhang, and S. Yee), who measured relevant thermophysical and optical properties as part of their Topic 2 Gen 3 projects that have been used in G3P3 studies
- We have worked with U. Tulsa (T. Otanicar, now at Boise State) to evaluate erosion and particle attrition during impact and sliding of particles along refractory and metal materials being used in our G3P3 storage bins and heat exchangers. Results have led to the selection of refractory materials for the G3P3 storage tanks.

- The U. Adelaide has developed laser diagnostic methods to evaluate particle flow and fines generation in small-scale receivers for model validation and to better understand fundamental processes associated with a falling particle receiver (see Section 3.1.1.8)
- Sandia and UNM have developed optical imaging techniques for in-situ characterization of particle and convective heat losses from the open aperture of a falling particle receiver
- KSU has characterized a number of low-cost alternative particles for particle-based CSP technologies [77]
- Carbo Ceramics has provided discounted particles to Sandia and G3P3 partner institutions as part of its cost share. CARBO has also provided Sandia with new formulations consisting of darker, smoother, and rounder particles for testing.

3.1.5.2. Particle Fines Generation

Sandia and CSIRO have characterized particle fines generation from an open cavity receiver. In addition, an in-line dust removal system has been designed with Aerodyne. See Section 3.1.1.1 for additional details.

3.2. Phase 3 Management, Design, and Construction Basis

As part of downselection criterion 2, DOE provided a list of required documents to be submitted with the Gen 3 down-select application. Table 21 provides a summary of these documents, which were submitted as part of the G3P3 Phase 3 down-select continuation application.

Table 21. Summary of required Gen 3 documents.

Item #	Required Document*
1	List of documents to be shared with DOE for review / comment
2	Plot Plan showing site layout
3	Overall Engineering schedule (Phase 1/2) and Construction / Erection schedule (Phase 3 (Later)), with logic ties showing interdependencies
4	Heat balances (full sun, charging/discharging for now. Other operating modes can come later).
5	Mechanical Equipment List, showing power consumption and nominal equipment ratings, and subcontract package (preferably grouped by system)
6	System List
7	Terminal Point List (wherever a scope break exists between Lead Company (and sub-suppliers/partners) and Others
8	Aux Load List, including expected power consumption, nominal power ratings, list of items on Battery Backup and list of items on Emergency DC power

Item #	Required Document*
9	Material Assignment schedule, showing each package to be awarded, potential suppliers, country /place of origin, including key dates for (working backwards): I. required date of initial operation II. required date for energization III. date for on-site delivery IV. ex-works shipment date V. permission to proceed for fabrication date VI. PO placement date VII. Date for RFP/specification release
10	Quality assurance plan, detailing the level and type of sub-supplier oversight required / planned (hold points, inspection points, in-process observation points)
11	Key specifications for major equipment and EPC Contract
12	Site conditions (seismic, climate data, wind data, rainfall, wind, solar data)
13	Automation Plan (DCS, PLCs, Field / Remote I/O, central control, etc)
14	Staffing Plan (Each engineering office and field construction labor)
15	Project execution Plan (plan for management of labor, craft, safety (LOTO), construction procedures, laydown requirements, traffic and logistics, etc)
16	Project financial reporting Plan (metrics, work breakdown structure, Earned Value against budget)
17	Permit compliance Matrix
18	Piping and instrument diagrams
19	Logic Diagrams
20	Single Line Diagrams
21	Startup / Commissioning procedures
22	List of applicable Codes and Standards
23	Building List (with required utility consumption requirements)
24	Utility List (and usage)
25	DOR between Consortium Partners
26	Piping isometrics and orthographics
27	Risk Mitigation Plan (FMEA)
28	Foundation Load Summary
29	Project Completion Plan
30	Progress reporting against SOPO
31	List of Work NOT Included (by others)
32	3D Model (if available) review / turnover plan
33	Key Calculations
34	Key vendor documents (general arrangements, data sheets, test procedures, O&M Manuals, P&IDs, logic, equipment specifications, coatings, weld procedures, etc)
35	Line lists
36	Valve Lists
37	A “Design Philosophy” document produced to ensure consistency among items such as redundancy requirements, vendor selection (e.g. all Rosemount pressure transmitters, site conditions, seismic criterion, Pipe Velocity Guidelines, Codes and standards, pipe weld

Item #	Required Document*
	end prep, field PWHT, weld repair procedures, coating guidelines, ES&H procedures, construction procedures, adherement to the other documents and procedures listed herein, etc, etc, etc)
38	Cost estimates (capital and operating)- Pilot Plant / 100 MW Facility
39	Document Control Procedures – document numbering, revision control, review/approval procedure
40	Hazardous area Review
41	On-site Chemical List
42	Pile Map
43	Soil Study
44	Construction Sequence Description
45	Instrument List
46	Flowability Studies (if applicable)

*Per DOE Gen 3 CSP Topic 1 – Phase 3 Test Facility Down-Selection Criteria, issued 4/25/19, Revised 9/23/20.

3.2.1. Project Execution Plan

A G3P3 Project Execution Plan (PEP) has been published to document the process for executing, monitoring, controlling and closing-out Phase 3 of the Gen 3 Particle Pilot Plant [78]. The plan is intended to be used by the development partners, principal investigator, and the federal project director. Project objectives are derived from the mission needs statement, and an integrated project team assisted in the development of the PEP. The PEP is a living document and will be updated throughout the project to describe current and future processes and procedures as follows:

- Cost, schedule, and scope
- Organizational and management structure
- Project reporting, communication
- Staffing plan
- Quality assurance plan (follows Sandia quality plan for procurement and work planning and controls)
- Environment, safety, security, and health (follows Sandia's requirements for ES&H, see Section 3.2.4.3 for permitting requirements)

3.2.1.1. Roles and Responsibilities

Phase 3 will involve integration of several organizations with general lines of communication and project authority flow-down. Roles and responsibilities are defined in organizational charts in the PEP. Central to the project is the core research and development team and technicians employed on-site at the NSTTF under the supervision of the principal investigator. The construction of the G3P3 tower will be managed by Sandia Facilities, who are tasked as experts in contracting and construction.

3.2.1.2. Scope Management Plan

Upon funds posting, the engineer-stamped drawings will be released for bid. While the contracting process is underway, component leads will begin to procure components and materials and the NSTTF technical staff will begin to fabricate the receiver, hoppers, and sCO_2 loop. Fabrication and procurement are expected to continue after tower construction begins. The general contractor will completely manage the construction sequence with oversight from Sandia Facilities.

By the time the tower has been constructed, all procurements will have been completed and delivered. NSTTF staff will have fabricated steel framing and insulation for each component and the calibration panel, so it is ready for lifting and setting. Sandia Facilities will manage all final inspections and certify that the tower is ready for occupancy.

NSTTF staff will connect data acquisition and control software and commission the system. Once hot particles have been routed through all pathways and control and data acquisition system has been demonstrated component and systems leads will certify that the system is ready for testing.

Data will be logged continuously for G3P3 allowing all system and component test objectives to be tested simultaneously. System operations include start-up/shutdown, continuous operations, load follow, storage, off-design and emergency shutdown. Component leads will be responsible for accessing, analyzing, and reporting the data concurrently with testing.

The G3P3 timeline is summarized as follows:

- **Phase 3 (Year 1)**
    a. Initiate contracts with Sandia Facilities and EPC (integrator)
    b. Initiate procurement of G3P3 system components
    c. Complete NSTTF facilities preparation (NEPA, permitting, utilities, ES&H)
    d. Begin construction of G3P3 tower
    e. Fabrication of components
    f. Initiate commissioning and off-sun testing of available components
    g. Work with R&D teams to refine and improve component technologies
    h. Procurements Received
    - **Expected outcome**: Completion of G3P3 facilities preparation and procurement contracts; tower construction begins; publication and dissemination of R&D
    - **Go/No-No Go**: Successful completion of facilities preparation and procurements
- **Phase 3 (Year 2)**
    a. Final delivery of G3P3 system components
    b. Construction and assembly of structural support/framing
    c. Installation of CSP components into tower
    d. Commissioning of G3P3 components and system
    e. Work with R&D teams to refine and improve component technologies
    - **Expected outcome**: Successful construction and assembly of G3P3 system; commissioning has begun
    - **Go/No-No Go**: Completion of construction and installation
- **Phase 3 (Year 3)**
    a. On-sun testing begins
    b. Parametric performance evaluation

c. Long-term on-sun operational testing and demonstration with start-up/shut-down procedures (includes 6-hour storage demonstration)
d. Development of scale-up and commercial deployment plan
e. Work with R&D teams to refine and improve component technologies

- **Expected Outcome:** > 1000 hours of testing between the G3P3-USA and G3P3-KSA systems that validate the performance of subsystem components under steady and transient conditions, including start-up, shut-down, and deferred storage

3.2.1.3. Work Breakdown Structure

The complete Work Breakdown Structure (WBS) is managed in the current MS Project file for G3P3 Phase 3. Information in the MS Project file supersedes information in the figures below. The Phase 3 WBS is divided into the following categories:

1. Programmatic
2. Procurements and Fabrication
3. Construction and Assembly
4. Commissioning of G3P3 System
5. Component Testing
6. System Testing
7. Scale-Up and Commercial Deployment Plan
8. Work from External Partners

3.2.1.4. Project Reporting Against SOPO

The scope of phase 3 includes all tasks required to build G3P3, conduct on-sun system testing (G3P3-USA), evaluate the system and subsystem performance in representative environmental conditions and publish analysis and results. The specific deliverables are identified in the work breakdown structure which describes all the work to be performed and the responsible party performing the work. Once the baseline scope is approved any changes to scope including adding or subtracting tasks will require approval by the PI and SETO. Milestones will be added as a means of tracking progress toward project completion. Milestones should follow "SMART" guidelines being specific, measurable, achievable, realistic and timely. Changes to milestones will be approved by the PI and SETO will be notified.

3.2.1.5. Schedule Management Plan

G3P3 is a five-year project in three phases that began Oct. 1, 2018. Phase 1 was 18 months, Phase 2 was ~6 months, and Phase 3 is scheduled to last three years including construction, procurement, commissioning, and testing. Phase 3 will begin when the award announcement is made by SETO and funds are received.

Figure 72 shows the major phases of the project including tower construction, component installation, commissioning and testing. A notional date of June 4 is posited as the start date. All scheduled dates will move to whatever date the funds actually post. The three timelines represent an optimistic, expected, and pessimistic scenario with optimistic and pessimistic scenarios based on

±20% of the expected task duration for the critical path. The On-Sun Testing task is shaded yellow and reflects approximately 11, 6 and 1 months of on-sun testing for the optimistic, expected, and pessimistic cases, respectively.

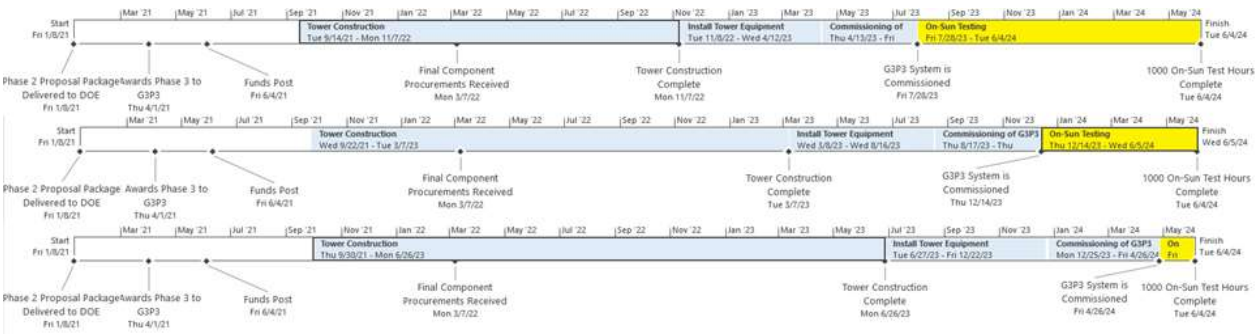

Figure 72. Projected timeline for G3P3 Phase 3 for optimistic (top), expected (middle), and pessimistic (bottom) scenarios.

Key milestones will be carefully managed to ensure the maximum amount of available on-sun test time. Tower construction is the largest task and hiring of the contractor as quickly as possible is the most important step. Contractors with the shortest quoted durations may be given preference. Efforts must be made to get the final inspections and approvals as soon as the tower is complete. Efforts must be made to sequence the lifting, setting, installation, and insulation of the CSP equipment with minimal lag. The schedule may be compressed by installing components into the tower as each respective floor is completed. These details will be negotiated with the general contractor during the bidding process.

3.2.1.5.1. Critical Path

The schedule has been planned by estimating all task durations in the Work Breakdown Structure and assigning dependencies and resources to identify the critical path. Tower construction was professionally estimated to last 18 months followed by 6 months of component installation and commissioning of the system, leaving ~6 months of system and component test time in the expected scenario. It is assumed that 66% of work days will exhibit weather conditions adequate for at least 6 hours of on-sun testing each day. This amounts to ~1000 hours available for on-sun testing. In addition, several project objectives can be met during off-sun testing (e.g., thermal storage, auxiliary heating).

3.2.1.5.2. Schedule Monitoring and Reporting

The schedule will be monitored continuously through routine meetings and communications at the individual and sub-team level. Progress toward a task will be asserted by each task owner at regular intervals to be assigned based on project priorities along with detailed presentations of progress quarterly to all stakeholders. Gantt chart and schedule management software tools including *MS Project* and *Visio* will be used to illustrate progress and communicate schedule requirements to staff and stakeholders. A copy of the full project schedule will be located and maintained in a Sandia collaborative folder accessible to SNL personnel.

3.2.1.5.3. Preventing Schedule Deviation

To prevent schedule deviations severe enough to impact budget or scope, the following procedures will be followed. If a schedule variance is substantial enough to impact the critical path, the project manager, PI, and owner of the affected task will meet to assess the situation and release an update to all stakeholders with a short list of options and solutions to resolve the variance.

During the tower construction the following activities must be performed concurrently in order to ensure minimal time lag:

- Minimize crane lift frequency and assembly complexity by prepping all components for robust handling and ease of installation.
- Minimize the time required to instrument components by pre-installing sensors or connection ports for quick connections in the tower.
- Minimize data connectivity issues by testing component connections via cRIO to the system controls prior to installing at the tower. Simulated instrumentation can be used to minimize commissioning of the control/DAQ system.

3.2.1.6. Budget Management Plan

Figure 73 shows the planned cash flow diagram for G3P3 Phase 3. The "optimistic," "expected," and "pessimistic" cumulative total spending over the three-year project is $21.2M, $22.3M, and $25M, respectively. For the pessimistic scenario, total costs were capped at the maximum allowable $25M budget by reducing the number of allowable test days (and associated labor) relative to the "expected" and "optimistic" scenarios. The bars represent the amount of spending per quarter beginning in April 2021. Figure 73 assumes an announcement date in March/April 2021 followed by spending on procurements and in-house fabrication of some components. Spending increases during tower construction and purchasing and is assumed to be pro-rated over an 18-month build. Labor rates are estimated based on actual charges made during Phases 1 and 2 of G3P3 and the building, commissioning, and testing of the SuNLamP HX and FPR module. During the tower construction period, R&D and Technologist labor is expected to decrease to about 50% of the phase 1-2 levels. Once the tower is constructed component installation and commissioning will increase labor charges to 100% of Phase 1 and 2 and are expected to level off in April of 2023 once routine system testing is underway.

Cost information was determined for tower construction by a professional estimator based on the 90% complete tower design. Costs include materials, labor, and work conditions specific to the NSTTF. All contractor costs that involve on-site construction include 15% corporate tax plus a 2% bond fee, a 2.76% escalation rate to Q4 in FY21, and a Sandia Facilities management fee that pays for acquiring, performing, and managing construction services on site. The estimate uses a 3-part project evaluation review technique (PERT) method to calculate the expected costs where uncertainty is captured as "expected," "optimistic," and "pessimistic." Optimistic costs are -5% and pessimistic are +15% for the 90% complete design. The same approach was applied to the component set and lift procedures and the storage bin refractory installation and assembly with -15% and +30% adjustments for the optimistic and pessimistic costs respectively. Additional uncertainties were captures as follows: budgetary estimates obtained from contractors or sales consultants ± 15%, items built in-house -5% +20%, commercially available items found by online

search ±5%, parametric estimates (ducts, valves) ±20%, quotes from vendors -0% +5%, labor ±5% FTE.

The parametric approach was used to estimate the hoppers, duct lines, and valves. A representative section was professionally estimated, and the cost was multiplied by the number and length of the remaining duct lines. Similarly, quotes from machinists to fabricate and assemble the valves were obtained for a representative valve and the cost was assumed for all other valves of similar size and complexity.

Figure 74 shows the high-level cost categories in G3P3 with the tower construction by a general contractor costing the most followed by R&D staff salaries and procurements. The installation of tower equipment will be performed by specialty contractors. Technologists will fabricate the receiver and sub-system components and will be responsible for connecting the CSP equipment once it has been set into place in the tower. Technologist labor charges are decrease as the tower is being build and expected to peak as the components are being installed and connected to the data acquisition system.

Contractor bids for the tower construction and invoices for purchased items will give an early indication of which scenario (optimistic/expected/pessimistic) will be realized. In the event that costs are following the pessimistic curve, a contingency plan has been made to protect the critical spending path and ensure successful building, commissioning and testing of the G3P3 tower. The critical path includes tower construction ($8.9M), Sandia Facilities management ($1.7M), procurements ($5.0M), installation of components ($1.6M), R&D labor/testing (~$5M), technologist labor/testing ($1.6M), and partner R&D (~$2M to enable required cost share). In the pessimistic case, the R&D labor is less than that of the optimistic and expected cases because a minimal staff allocation will be implemented to meet the $25M budget cap and perform a limited set of the most critical testing and demonstrations.

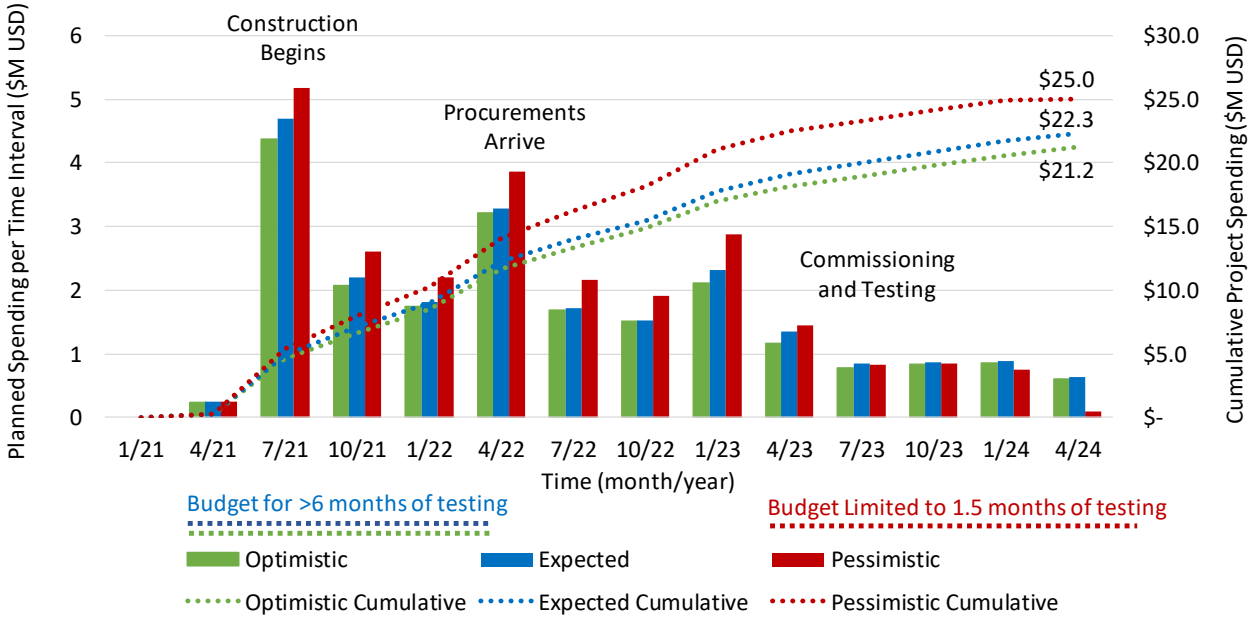

Figure 73. Planned spending over three-year Phase 3 project.

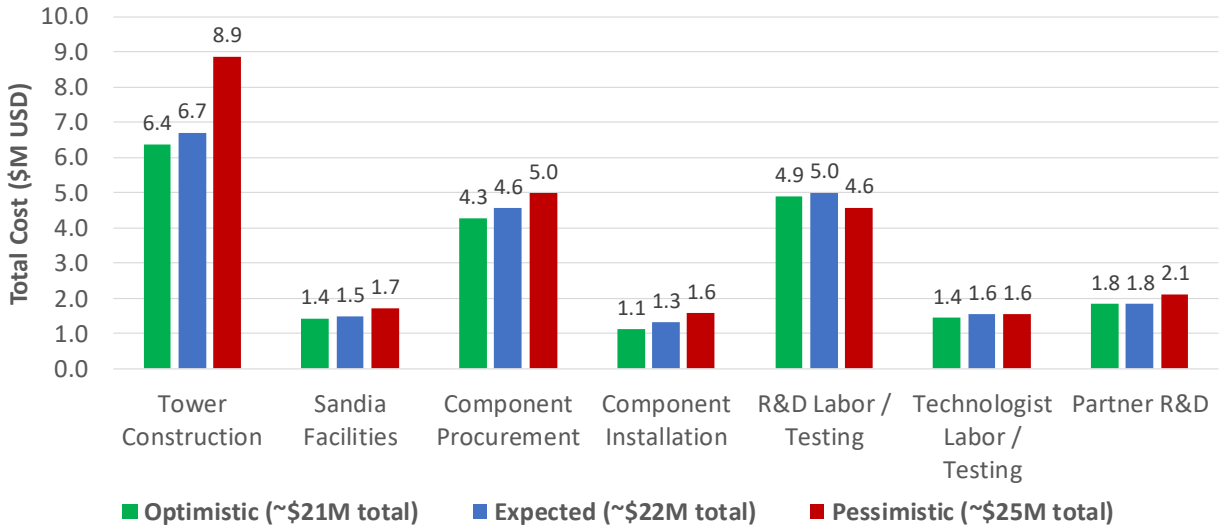

Figure 74. G3P3 Phase 3 costs by category.

3.2.2. Engineering Drawings – Process Flow Diagrams, Design Drawings, and P&ID

Design drawings, process flow diagrams, and piping and instrumentation diagrams have been completed for G3P3-USA. These drawings were used by Bridgers & Paxton and Bohannan Huston to develop 30%, 60%, 90%, and 100% G3P3 design packages in Phases 1 and 2 for the assembled tower. At the end of Phase 2, signed and sealed drawings and analyses were delivered to Sandia, which are ready for construction bid.

Analogous drawings for G3P3-KSA can be found in the final G3P3-KSA report.

3.2.2.1. Process Flow Diagram

The process flow diagram for the G3P3 system is shown in Figure 75. The primary flow loop is shown using solid lines, which includes the falling particle receiver, hot storage bin, particle heat exchanger, cold storage bin, and bucket elevator. The configuration of the diagram is consistent with the vertical layout of the components where particle lifting only occurs at a single location in the system and transport between the components occurs through gravity-driven flow. Additional component connections and equipment aside from the primary energy capture, storage, and dispatch equipment is present in the system to enable operational modes of the system including startup, shutdown, load-following, idle, turndown, extended duration testing, and emergency cooling. The different operating modes of the system and additional thermal equipment are described below.

The daily operation of the plant will require receiver and heat exchanger startup and shutdown. During the process of startup for the particle receiver, particle temperatures exiting the receiver will span the range between the hot and cold storage bins before stabilizing at the receiver outlet setpoint. Charging the hot storage bin with the wide variation of particle temperatures leaving the receiver during startup is undesirable because it can lead to a reduction in the temperature of the hot storage bin, temperature non-uniformities in the bin, or thermal shock of the internal refractory insulation. To overcome this challenge, a hot storage bypass line is included in the system to divert the particle flow at undesirable temperatures around the hot storage bin. Furthermore, this particle flow cannot be directly returned to the cold storage bin for the same reasons, so an intermediate

storage bin is placed between the two bins to temporarily store the particle flow during receiver startup. After the receiver has reached a steady operating temperature, the intermediate temperature storage bin will be discharged at a low flow rate (~1 kg/s) and mixed with the particles entering the bucket elevator through the cold storage bypass.

Receiver shutdown will essentially occur in reverse of the startup. After the concentrated light is be removed from the falling particle receiver aperture, the particle outlet temperature will begin to reduce. The hot storage bypass will be utilized to prevent the low temperature particles from entering the hot storage bin during shutdown, but they will not be held in the intermediate storage bin. The particles leaving the receiver during shutdown will be recirculated through the bucket elevator and receiver until the temperature is in an acceptable range where they can be returned to the cold storage bin.

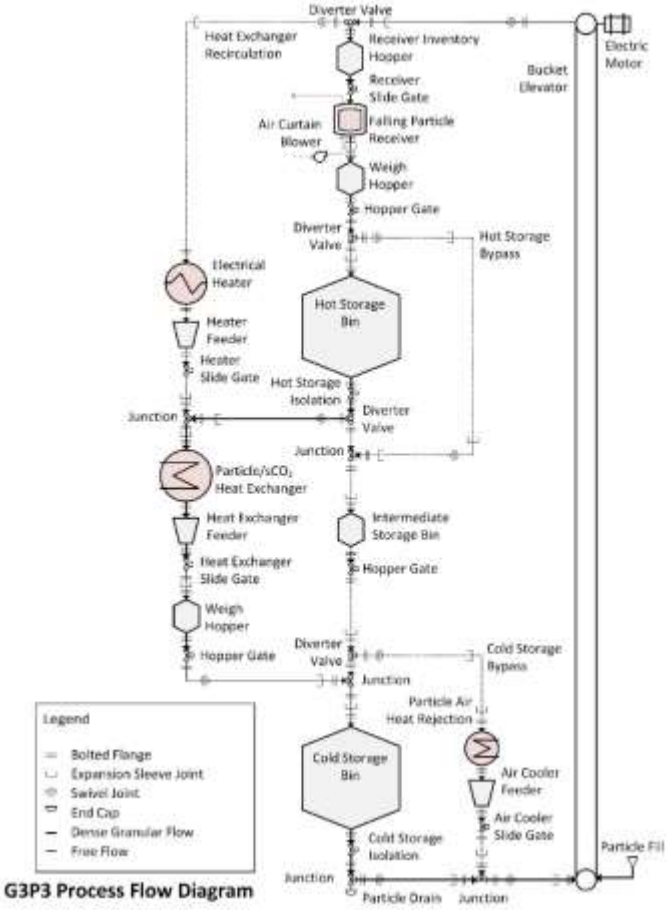

Figure 75. G3P3 process flow diagram including the major thermal equipment, connections and valves on the particle flow loop.

The same set of processes used during daily receiver startup and shutdown can be used to operate the system with intermittent cloud cover. The particle flow through the receiver can be controlled with the inlet slide gate, but if the irradiance on the aperture falls below the range where the receiver turndown allows for continuous operation, the hot and cold storage bypass ducts can be used to recirculate particles through the receiver until the irradiance returns to a value within the turndown range of the receiver.

Heat exchanger startup shutdown and idle are three additional operating modes that will occur on a daily basis and possibly at the same time as receiver operation. In addition to the particle/sCO_2 heat exchanger, an electric particle heater is included in the system upstream of the heat exchanger. This heater allows for maintenance heating of the entire system, but specifically allows for the heat exchanger to be maintained at the temperature of the cold storage bin when not heating sCO_2. Particles will be recirculated through the heat exchanger using the heat exchanger recirculation duct that bypasses the receiver and delivers particle from the cold storage bin to the electric heater. Maintaining the heat exchanger at the cold storage bin temperature when not in use minimizes the heat exchanger startup time and energy parasitics. During startup it is anticipated that the particle temperature at the inlet of the heat exchanger will be ramped to the operating temperature through mixing particles from the cold storage bin with particles from the hot storage bin. This allows the heat exchanger to safely be guided through the transient without placing undue stress on the equipment.

Depending on the duration of the hot storage bin deferral, it might be necessary to purge the particles in the hot storage bin outlet pipe due to heat loss. Allowing a cold slug of particle to enter the heat exchanger during startup could result in a thermal shock that consumes the fatigue life of the heat exchanger. Therefore, a purge duct is included to remove the cooled particles at the outlet of the hot storage bin and transport them into the intermediate storage bin such that a continuous stream of particles at the hot storage bin temperature is available for startup. The purge duct also serves the purpose of performing hot storage bin discharge should the heat exchanger be inoperable.

Heat exchanger shutdown will occur in the opposite direction through decreasing the particle and sCO_2 flow rates before returning the heat exchanger to an isothermal condition at the cold storage bin temperature.

The final piece of thermal equipment on the particle side is the particle air cooler located on the cold storage bypass. The primary use of the particle cooler is to allow for extended duration receiver operation through rejecting heat directly to air. Since the receiver (2 MW_t) is currently double the thermal duty of the heat exchanger (1 MW_t), operational windows will be limited to 3 hours given the 6 MW_t-hr capacity of the storage bins. If the particle/sCO_2 heat exchanger is operated simultaneously, the receiver operating window can be extended up to 6 hours. However, adding an additional 1 MW_t heat rejection to the particle stream will allow for the option to operate the receiver uninterrupted for the entire duration of the day. The secondary use of the particle air cooler is to provide a method of cooling the system should the heat exchanger or sCO_2 flow loop be inoperable.

3.2.2.2. Design Drawings

From the process flow diagram, the individual system component 3D models were laid out in SolidWorks (Figure 76) to provide the specifications for the tower floor heights and weights. In total, the system includes nine floors, with four obstructed by the hot and cold bins. The five remaining floors accommodate the particle receiver, receiver weigh hopper, particle heat exchanger, heat exchanger weigh hopper, intermediate storage bin, sCO_2 flow loop, and particle lift. A complete set of dimensioned drawings for the particle system and current design of the individual components was submitted to DOE.

In addition to the component layout, connections between the components were designed to transport particles throughout the vertical height of the tower in accordance with the process flow diagram. In a system implementing gravity-driven flow, it is necessary to have vertical height to

arrange the components as well as provide horizontal transport to accommodate the bypass ducts for particles around components. A modular system of high-temperature particle duct work and valves was design by Sandia from prior experience with particle flow loops. In general, the ductwork is either in a vertical orientation which uses standard schedule 10 pipe sections or inclined at a 35° angle from horizontal with square cross sections formed from 12 GA sheet. The 35° angle has been identified as the requirement for self-cleaning ducts with CARBO HSP particles at 800 °C. Two key challenges with particle ductwork at this temperature is accommodating the linear thermal expansion and angular misalignment due to preferential heating of one side of the duct. However, in particle systems the connections do not have to be hermetically sealed like gas or liquid systems. Linear thermal expansion in vertical ducts can be accommodated through the use of a tube-in-tube slip joint connection (Figure 77). Similar tube-in-tube connections can be used in ducts with an inclination angle, but they also require a flex joint to accommodate angular changes in the ducts due to preferential heating of the surface in contact with the particles during transients or thermal shock (Figure 77).

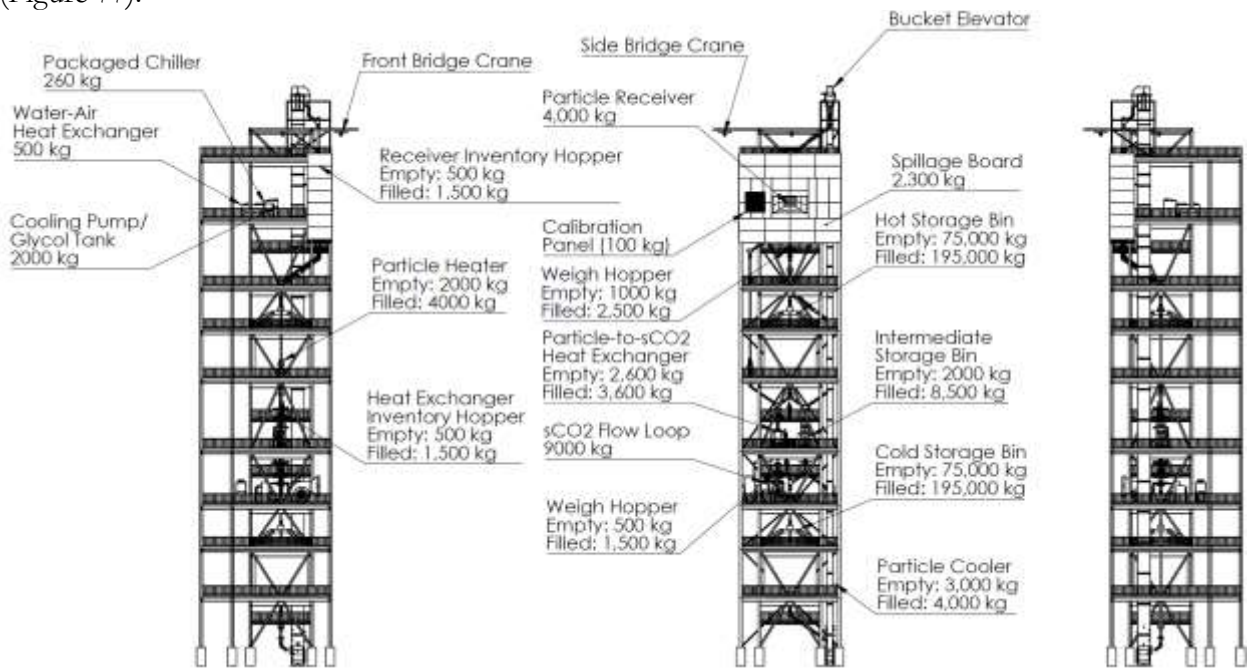

Figure 76. Front and side views of the tower highlighting component locations and weights

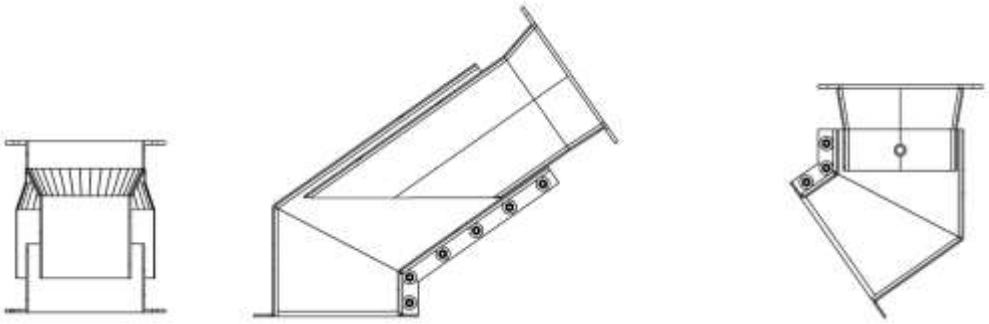

Figure 77. Cross-sectional views of a particle components used to accommodate thermal expansion (left: vertical tube-in-tube slip joint, center: inclined tube-in-tube slip joint, right: inclined elbow flex joint)

Particle flow control is accommodated through a custom set of valves designed to operate at high temperature. The current system design contains 13 particle valves which can be broadly categorized into four different types. The four different valve types in G3P3 are granular isolation, granular flow control, loose-flow diverter, and packed-flow diverter. The general concept for almost all of the valve designs implemented in G3P3 have been tested at smaller scales within Sandia's prior receiver and heat exchanger tests. Cross sectional views of the different valve types are provided in Figure 78. Valves are an area that currently limit the operation of a molten salt plants due to temperature transient limits to prevent thermal shock. Since tight tolerances are not required in particle valves to effectively throttle or stop flow, the allowable temperature transients are much greater without risk of deforming or damaging the valve. It is common for particle valves to have a free-floating slide gate with gaps between the valve body, inlet chute, and gate to prevent the moving parts from binding on particles which will also accommodate thermal expansion.

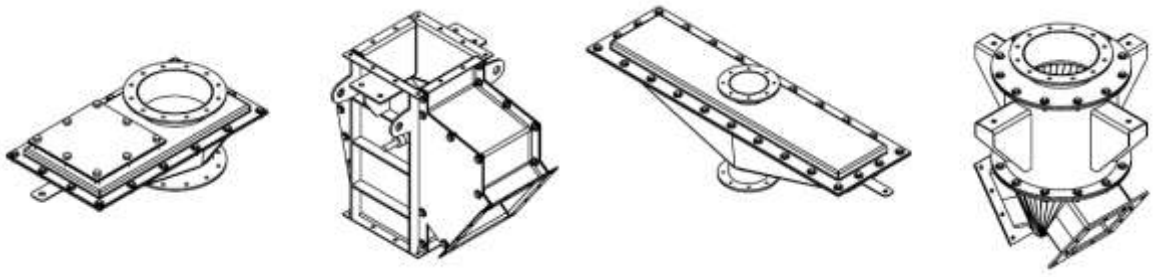

Figure 78. Four valve types used in G3P3 to provide the necessary particle flow control operations (granular isolation valve, loose-flow diverter valve, granular flow control valve, and packed-flow diverter)

3.2.2.3. Piping & Instrumentation Diagrams

Piping and instrumentation diagrams have been developed for the integrated G3P3 system, separated by level and subsystem. The diagrams currently include all of the equipment and locations of important instrumentation for control and performance measurements. From the P&ID, a list of the particle specific equipment was generated which is provided below. The G3P3 system is comprised of different modules such as the receiver and heat exchanger which can be broken down further into a specific list of components. The high-level equipment list was constructed to reflect the modular construction.

3.2.3. Equipment List

A comprehensive equipment list was assembled to improve cost estimation and expedite the procurement process. The equipment is broken down by subsystems including the particle lift, particle receiver, heat exchanger, sCO2 loop, hot storage bin, intermediate hopper, and cold storage bin. In addition to subsystems, the equipment list includes ductwork lines, valves, and data acquisition equipment. The equipment is further broken into parts which include descriptive specifications, materials, and drawing numbers. Quotes and cost/delivery time estimates are included with citations for the sources. Where applicable power requirements are noted. An insulation and cladding procurement was calculated based on equipment surface area.

The total costs for the major subsystems are shown in the master equipment list. The heat exchanger subsystem is the most expensive portion of the G3P3 budget and is expected to be ~$1.9

million. The heat exchanger also has the longest quoted lead time at 39 weeks. Cost estimates were obtained by requesting quotes, looking up items in online catalogues, and by parametric analysis where a detailed quote is obtained and scaled or multiplied to achieve the costs of similar items. Costs have been carefully tabulated. It is unlikely that significant cost savings could be achieved by cutting equipment inventory. However, sensors and data acquisition equipment reflect the optimal configuration and could potentially be reduced to a minimal configuration that still meets the test objectives. An analysis was performed to determine whether bulk purchases could be made to streamline the procurement process and potentially receive cost reductions. The following items can be procured as multi-use:

- Unistrut steel for building frames around each component
- RSLE insulative ceramic board
- Superwool insulation
- Aluminum cladding
- 316 Stainless Steel for receiver and hopper components
- Data Acquisition from National Instruments
- Thermocouples from Omega

Vendors in the equipment list include sole-source vendors who were identified as partners in Phases 1 and 2 and hold IP required for the project. These include Solex and VPE for the heat exchanger and Allied Mineral for the refractories in the storage bins. Other vendors cited in the equipment list provide parts with known specifications and costs that have been used reliably in the current test systems, including FPR and SuNLaMP or were found in the catalogues of trusted suppliers such as McMaster-Carr or Omega. While these parts can show that there is at least one vendor who can provide the needed equipment at an acceptable price and schedule, component leads will have the opportunity to find more cost competitive suppliers during the Phase 3 procurement process. The procurement plan is explained in more detail in the PEP.

In addition to the particle side equipment, several other items of importance are noted below, which primarily make up the fluid cooling system, sCO2 loop, and lifting equipment.

Non-Particle Equipment:

- Tower Side Bridge Crane
- Tower Face Bridge Crane
- sCO_2 Flow Loop
- Air Compressor

Particle Valve List:

- Receiver Bypass Diverter Valve (8 inch, loose-flow diverter)
- Receiver Flow Control Slide Gate (included in receiver design)
- Receiver Weigh Hopper Isolation Valve (8 inch, granular isolation)

- Hot Storage Bypass Diverter Valve (8 inch, loose-flow diverter)
- Electric Heater Flow Control Valve (6 inch, granular flow control valve)
- Hot Storage Bin Isolation Valve (8 inch, granular isolation)
- Hot Storage Bin Discharge Diverter Valve (8 inch, packed-flow diverter)
- Particle/sCO_2 Exchanger Flow Control Valve (6 inch, granular flow control valve)
- Intermediate Storage Bin Isolation Valve (8 inch, granular isolation)
- Cold Storage Bypass Diverter Valve (8 inch, loose-flow diverter)
- Air Cooler Flow Control Valve (6 inch, granular flow control valve)
- Cold Storage Bin Isolation Valve (8 inch, granular isolation)
- Cold Storage Bin Flow Control Valve (8 inch, granular flow control valve)

3.2.4. Tower Design and Facilities

3.2.4.1. Structural

Bridgers & Paxton and Bohannan Huston developed 30%, 60%, 90%, and 100% G3P3 design packages in Phases 1 and 2 including structural, civil, and electrical requirements for the assembled tower. At the end of Phase 2, signed and sealed drawings and analyses were delivered to Sandia, which are ready for construction bid.

Tower Overview

The structural steel tower will have a 30'-0" x 30'-0" square footprint with an additional 10'-0" by 30'-0" area to accommodate the required stairwell on the project South tower face. Inside the 30'-0" square, a concentric 20'-0" x 20'-0" square area has been designated as the main "core" of the tower, where the storage hoppers and other major components will be housed. The remaining 5'-0" wide outer perimeter is intended to provide maintenance access around test loop components. Plan gridlines will intersect all column locations.

The tower height is 160'-0" from finish grade elevation to the roof deck level. The bridge crane framing extends vertically 10'-0" from roof deck level, and the bucket elevator shaft requires framing that extends vertically 15'-0" from roof deck level, resulting in maximum structure height of 175'-0".

Constructability & Construction Sequencing

An independent constructability review was conducted by Thornton Thomasetti. The review resulted in a decision to temporarily omit specific lateral bracing members at hopper levels on the project East face of the tower, in order to move the two storage hoppers into place. While these members are displaced, hopper levels will be shored by temporary guyed cables that will transmit lateral forces to the ground.

This sequence allows the hopper shells to be fully constructed on grade and lifted/skated into place by the general contractor, while providing an unobstructed load-in path. Once load-in is complete, the omitted lateral force members can be installed, and the temporary guyed-cable shoring system can be removed. Design coordination and detailing efforts are being made for the implementation of this shoring system and the use of lifting skids required for hopper movement. In addition, two 6-

Ton rail cranes will be required above both hopper levels to pull the loaded hopper skates toward the core. It should be noted that insulation installation and final construction assembly efforts for the hoppers will take place inside the tower structure.

The component loading path requires concrete deck to be utilized across the entire footprint of each level; primarily to provide an un-stepped flat surface to allow component movement into the tower core from the walkway. A high-temperature concrete mix will be implemented to resist heat transfer to hopper level decks. Currently a proprietary mix product containing calcium aluminate (Fondag) is being considered for these slabs. The remainder of the concrete decks will be conventional reinforced concrete. Providing concrete deck across the entire footprint of each level also provides greater vertical structural strength and the diaphragm continuity needed to transfer forces to the lateral force resisting system. The maintenance walkway access areas will be sloped away from the tower to allow for positive drainage.

Foundation Design

The geotechnical investigation and associated report was completed on October 18th, 2019, by Wood Environment and Infrastructure solutions (Report No. 19-517 00063). The exploratory borings encountered soils that consisted of soft to very firm silty sands, and loose to medium dense sand mixed with gravel. No groundwater was encountered during the boring process. These soil conditions were slightly less stable than expected. Foundation changes have yet to be determined. Based on Wood's investigation and laboratory testing, a Soil Site Class C was determined for seismic design. Soil Site Class C has resulted in a Seismic Design Category C.

The construction sequencing of this tower will have to consider staged construction, where the main test loop components will be assembled on the level that they reside prior to the tower's progressive construction vertically. Details for shielding the structure from direct contact with the solar beam as well as direct contact with hot test loop components are still being developed.

Design & Analysis

Structural analysis and design efforts have been performed in accordance with the following codes and standards:

- ASCE 7-10 Minimum Design Loads for Building and Other Structures
- 2015 International Building Code
- American Institute of Steel Construction (AISC) Steel Construction Manual 15th Edition
- American Concrete Institute (ACI) Building Code Requirements for Structural Concrete 318-14
- DOE STD 1012-2012

Structural analysis and design calculations are being performed in RISA 3-D, Version 16.0.1, and via Microsoft Excel Spreadsheets.

Risk Category II Structure

Wind Velocity = 115 MPH

Seismic Design Parameters:

- Site peak ground acceleration = 0.186g

- Short-period spectral acceleration, S_{DS} = 0.359
- 1-second period spectral acceleration, S_{D1} = 0.151
- S_S = 0.449
- S_1 = 0.136
- S_{MS} = 0.539
- S_{M1} = 0.323

Equivalent Lateral Force Procedure of ASCE 7-10 Chapter 12 is being implemented in the seismic design. Special concentrically braced frames is the selected lateral force resisting system.

Detailed engineering analyses, drawings, and descriptions of the structural, civil, mechanical, and electrical design elements of the G3P3 tower were developed by Bridgers & Paxton and Bohannan Huston. Additional features of the G3P3 system and facilities are summarized below.

Lighting. All levels of the tower will include lighting fixtures to illuminate the entire floor. Supplemental lighting, as needed, will be task lighting (provided by the users) connected to the general-purpose receptacles. In addition, the entire stairway will be illuminated for safe night egress. Central switching/astronomical clock control will be at the bottom of the stairway to allow access for night work. Lighting will be backed-up via a lighting inverter for the entire tower structure. Lighting will be 277-volt LED-type fixtures.

In addition to the lighting system there will be a safety beacon installed at the top of the tower. While this is not required by FAA regulations, it was thought prudent to include it in the design to add an extra margin of safety. The beacon will be connected to the lighting inverter to assure operation in the event of a power outage. All lighting will be shown in the 60% submittal package.

Lightning Protection. A lightning protection system will be provided on the new tower, meeting NFPA 780 for lightning protection systems. It will feature air terminals at the top of the tower, and a counterpoise around the base perimeter. The counterpoise will connect to the existing solar tower grounding counterpoise and will serve as the grounding electrode for the new G3P3 tower electrical and mechanical equipment. This equipment will be grounded to the counterpoise. The system will be included in the 90% submittal package.

Data Acquisition and Instrumentation/Communication. A fiber optic link over existing fiber optic cable will connect the instrumentation and control CAT 5E cable to the site control room in Building 9981 via a media converter within an existing terminal/access enclosure located on the ground level within the solar tower. Full connection details to the control and instrumentation systems are under development. This system will be shown in the 90% submittal package once the data acquisition and control system and points are developed and can be connected.

G3P3 Major Electrical Equipment List

1. S&C Electric Co. PMH-19 Switchgear (SFM)
2. 1500 kVA, 4160/2400 V to 480/277 V Padmount Transformer
3. 1600 A, Exterior-Rated Service Entrance Switchboard
4. 2 - 75 kVA, 480 V to 208/120 V Dry-Type Transformers
5. 200 kW, 480 V UPS System for 30-Minute Ride-Through
6. 480/277 V, 225 A, 42-Circuit, Exterior-Rated Panelboard
7. 480/277 V, 150 A, 42-Circuit, Exterior-Rated Panelboard

8. 208/120 V, 225 A, 42-Circuit, Exterior-Rated Panelboard
9. 1-400 A, 600 V, Exterior-Rated, Non-Fusible Safety Switch
10. Misc. Safety Switches and Motor Controllers
11. 1-Lightning Protection System (To be designed/installed by a certified Lightning Protection Design/Install Contractor
12. 1-277 V Lighting Inverter

Tower Location Assessment. Currently the site West of 9980 is asphalt pavement which slopes to the southwest. There is a drainage swale that intercepts runoff from the north and west. This swale conveys runoff to the west. The proposed tower will block the drainage swale, which will require the swale to be relocated to the north. Asphalt pavement will be removed and replaced as necessary for the site improvements. A section of fence and gate are within the project limits. The fencing will be removed.

There is a 4" sanitary sewer line running through the proposed site. Prior to the 60% submittal, the design team and SNL analyzed the potential relocation of the new tower 35 feet SW from its current proposed location in order to avoid the 4" sanitary sewer line. An optical analysis was conducted with this new location to determine whether the solar beam would be adversely impacted. The results showed that there would be a reduction in output. Based on utilities located in the field it appears that the sewer line will not be impacted by construction activities if the tower is left in its current proposed location. Potholing will verify the location of this sewer line, and if required, the design team will make provisions to protect this sewer line during construction. Another option would be to provide a lift station adjacent to the adjacent solar tower and relocate the sewer line away from the proposed site. There is an existing heliostat foundation within the construction limits that will be removed. Associated electrical lines will also need to be removed.

The existing drainage swale will be relocated north of the tower. This will involve minor grading and asphalt paving. Minor excavation and grading will be necessary for the tower construction. Asphalt removed during construction will be replaced to the grades shown on the grading plan. Upon completion of the project, the site will continue to drain as it currently does.

The total disturbed area is estimated to be 2,800 square feet, but the project cost exceeds $5M. Based on the project cost, compliance with EISA Section 438 is required. The total retention volume required to comply with EISA Section 438 is approximately 180 cubic feet. The downstream location where a pond should be placed is within a potential pedestrian and vehicle circulation area and there are existing utilities in the area. With the site constraints it may not be technically feasible to comply with EISA Section 438. This will be further evaluated as design progresses.

There is no new water, sanitary sewer or storm drain utilities associated with this project. There is a potential during the remaining stages of design that the existing sanitary sewer line may be impinged by construction activity of the tower foundation, and ultimately requiring relocation and the addition of a lift station adjacent to the existing tower. Potholing this sanitary line is required to verify its actual location and whether it will potentially conflict with the new structure.

Optical analyses have been performed with the G3P3 tower to ensure sufficient annual irradiance can be provided from the existing heliostat field to heat the particles in the receiver to desired temperatures.

3.2.4.2. Design Basis Document

An interim design basis document was developed and used to define G3P3 component and system design requirements and ensure consistency among component interfaces, Topic 1 and Topic 2 researchers, and requests for quotes and information from vendors during Phases 1 and 2. The interim design basis document is referred to as the required "Design Philosophy" document in the DOE Phase 3 Down-Selection Criteria document. Drawings in the interim design basis document have been updated in the 100% design.

3.2.4.3. Permitting and Construction

All necessary ES&H (Environmental Safety & Health) and permitting requirements have been identified and completed in Phases 1 and 2, including NEPA, biological, stormwater, fire hazard, fugitive dust, and FAA requirements [78]. In addition, process flow diagrams summarizing Sandia Facilities' processes to acquire, perform, and manage construction activities were provided to DOE.

3.2.5. System Architecture, Controls, and Data Management

3.2.5.1. System Architecture

The Gen 3 Concentration Solar Power Particle Pilot Plant (G3P3) will require a complete plant control system to monitor and control a variety of individual subsystems. Several subsystems, including the receiver, primary heat exchanger (PHX), and sCO_2 loop have been developed and operated independently before, but have not before been integrated into a supervisory control and data acquisition (SCADA) system or debugged and maintained across multiple tower levels.

A network diagram of the envisioned G3P3 control architecture is shown as Figure 79. Data will be acquired from subsystems on each level of the G3P3 tower and sent to the National Solar Thermal Test Facility (NSTTF) control room for operation and monitoring. Finally, data may be sent to an additional data historian server for access outside of Sandia by Department of Energy (DOE) program managers and G3P3 partners.

A prototype of this architecture was tested during on-sun testing of the particle-sCO2 heat exchanger under the SuNLaMP project through July and December using separate independent subsystem controls. However, the SCADA system integration and remote data access capabilities have not yet been tested.

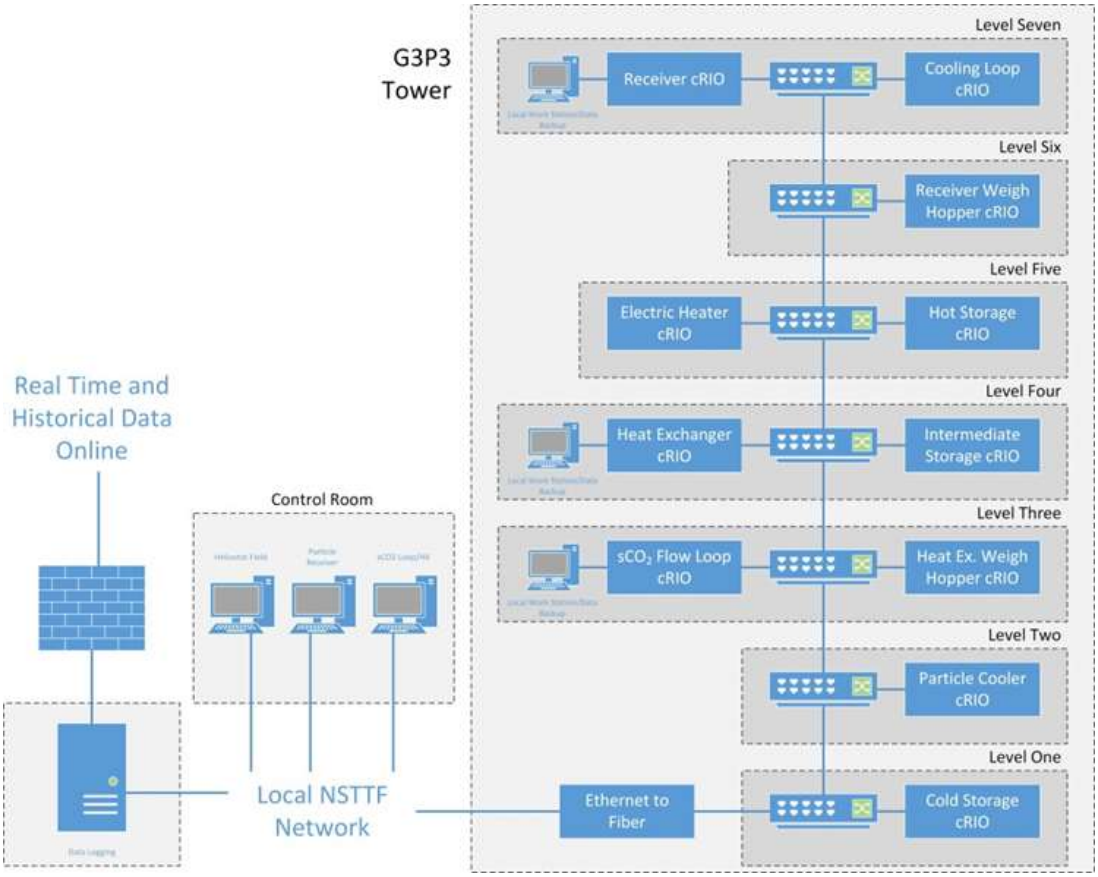

Figure 79. Network diagram of the overall G3P3 control system.

3.2.5.2. Data Acquisition (Input and Output Signals)

For each G3P3 subsystem, a high-level list of input and output signals has been compiled based on the planned instrumentation and need to generate command signals and read feedback signals for the equipment. From the I/O lists for the subsystems, an NI cRIO chassis and a series of cRIO cards that are compatible with the I/O types has been specified. Most components contain 0-20 mA AO, 0-20 mA AI, 24V relay, 5V DIO, and type K thermocouple measurement card. All subsystem chassis currently have at least one open slot for future expansion and interfacing with I/O types that are not preset in the current configuration. A deeper level of this table provides a list of channels on each card and specifies a unique identifier to the G3P3 system with the instrument or equipment in communication. These tables will form the basis for constructing the subsystem control panels, which will each be documented with a SolidWorks CAD file and wiring diagram.

3.2.5.3. Control Software

Two sets of control software programs will be implemented in LabView on National Instruments (NI) hardware, real-time control programs on each cRIO subsystem and a SCADA system in the control room.

Real-time control programs will operate on each cRIO subsystem to acquire signals, pass data to the SCADA system, and provide local automated control of the subsystem mode (operation or maintenance) and emergency response actions if critical signals cross through provided thresholds.

These real-time programs will also provide local Human Machine Interfaces (HMIs) for access and monitoring on local workstations within the G3P3 tower.

The SCADA system will integrate signals from individual subsystems for control, monitoring, and test operations from the NSTTF control room. This software will provide HMIs for the heliostats, receiver, sCO_2 loop, and other critical subsystems for operators. This software may also provide 'observer' displays for others in the control room or those viewing remotely, if possible, to observe conditions in the G3P3 tower without interfering with the operators.

3.2.5.4. Data Logging

Data logging will be implemented both within the G3P3 tower and the NSTTF control room to provide records for operation and maintenance of the G3P3 system.

Key cRIO units will continuously log data to local workstations for at least the last week of operation to validate data collected by the SCADA software program and as a backup dataset for potential network connectivity issues between the G3P3 tower and the NSTTF control system. This approach has been used successfully in previous LabView systems using a first-in first-out (FIFO) file buffer for other high-consequence testing at the sCO_2 Brayton lab. In this approach, a series of separate data files are created with the first file being overwritten once the last file has been completely written allowing for large quantities of data to be stored without disk access or memory limitations.

Data logging from the SCADA software will operate in a similar way to each individual cRIO software installation but will integrate data from each subsystem into the same database. Continuous data logging will occur in parallel to specific data collection over user-controlled periods of time to reduce the need to develop complex filtering schemes or manually identify data ranges for post-processing.

In addition to logging data, a time-stamped log file will be used to record SCADA software messages and user-provided comments to provide a real-time record of operator intentions and context for the data that isn't directly recorded by a signal. These log files have been successfully used at the sCO_2 Brayton lab for other high consequence testing and have been instrumental in debugging complex software and communication issues encountered previously.

3.2.5.5. Remote Data Access

G3P3 data will be posted outside the sandia.gov domain. The data would be collected in the data logging station and bridged via the VLAN to the SRN domain to publish through our corporate web publishing site. Attached to the station would be a Network Interface Card that will help with the bridging of the data between NSTTF LAN and SRN VLAN.

The data will be interchanged intermittently, i.e. once a day or once a week. Sandia Cyber Security is developing the proper approval of bridging data from a Lab Machine to the VLAN SRN domain. Once the Sandia Cyber Security team approves the data bridge, the data will make it outside the sandia.gov web domain to be published in a G3P3 live data website.

The G3P3 live website will illustrate current data from ongoing experiments. It will also have historical data where the data from previous experiments can be retracked and displayed for visual inspection.

3.2.5.6. Data Search and Retrieval

The Citadel database is the data logging component of the National Instruments *Run-Time System*. This choice for data management is advantageous because it utilizes data logging features native to the LabVIEW-based SCADA including plug-and-play network protocols that save time detecting and connecting to the cRIOs and other devices (even non-NI) throughout the network, and provides increased resilience to errors and malfunctions. Citadel also provides compatibility with TDMS binary data formats, saving conversion time, bandwidth, and storage space while still being exportable to csv or text file formats. Additionally, the NI platform utilizes metadata encoded into the signal by the cRIO including the I/O information, timestamp, and programmable metadata such as statistical summaries to facilitate retrieval and visualization. Citadel data structures are broken into small chunks of data called *traces*. Traces allow the metadata to be sorted and searched by any criteria that can be stated alphanumerically.

The database has features that will make continuous logging operations more practical. Citadel uses a compression algorithm on the data itself. Citadel reduces file size by not logging redundant data points on channels that remain essentially constant through a process called "ghost points." All data during a trace is held in cache. If there is no change in value over a determined timespan, a single ghost point is logged, if a change or failure does occur, the complete data is stored. The database will be archived routinely (every 5GB) to maintain smooth and efficient computations on the main SCADA computer.

DIADEM software will be used search and sort through the metadata in the trace files and to search and interface with waveform data. Figure 80 shows an example of DIADEM being used to sort files by maximum temperature. As it is not possible to "control" for weather events, this sorting feature will instead allow a researcher to 'Google search our data' quickly and retrieve all files meeting a given criteria such as a certain wind speed and direction by sorting and filtering on a desired channel.

Data will be "cleaned" and reviewed by R&D staff after each test and periodically between tests to identify any anomalies including instrumentation failures, data drift, or illogical readings. This will ensure the individuals with the most comprehensive system knowledge identify spurious results before they are propagated to external collaborators and the DOE.

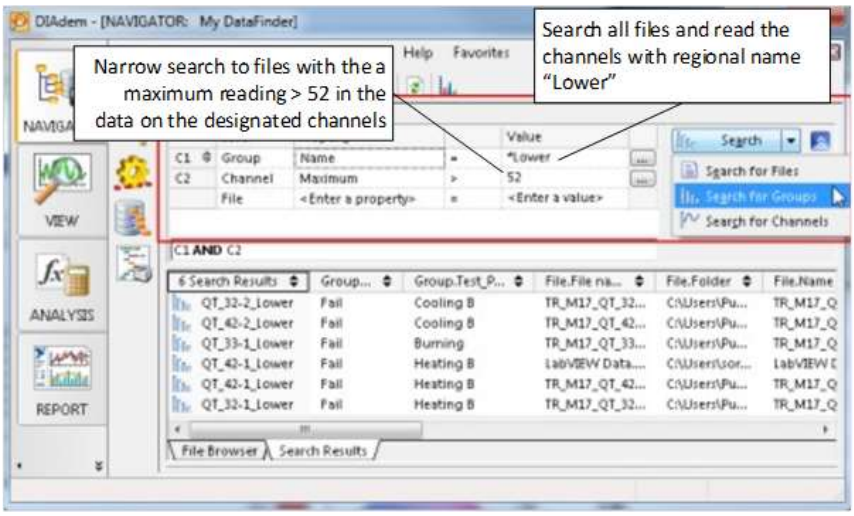

Figure 80. Example of sorting data by channel maximum

3.3. Technoeconomic Analyses and Market Adoption Study

3.3.1. Technoeconomic LCOE Analyses

A technoeconomic model for a commercial scale particle plant was developed in Engineering Equation Solver (EES) to investigate the sensitivity of the levelized cost of electricity (LCOE) to the operating conditions, particle properties, and performance metrics [79, 80]. The objective was to identify the path to achieve an LCOE = 0.06 $/kWh and inform the operating conditions of a pilot plant. The last version of the model presents several upgrades to previous particle systems models in order to increase its fidelity, accuracy, and representativeness of an actual system. Details of the particle-based EES model can be found in Gonzalez-Portillo (2021) [81]. A complementary technoeconomic analyses was performed by the Australian National University (ANU) and is summarized in Appendix D. The ANU modeling approach used a Modelica-based model (SolarTherm) and included different configurations and scenarios (e.g., receivers in series vs. parallel, optimal dispatch and peaker configurations). The purpose of the ANU analysis was to develop a model that included capabilities not available in EES (e.g., transient simulations) and to provide a benchmark for comparison.

The objective of the CSP system is to supply a net power of 100 MW_e. The CSP plant is designed to generate a greater gross power, considering that parasitic loads represent ~10% of the gross power. The plant performance is calculated hourly. The software from Dyreby [82] and Gavic [83] is used to calculate the power cycle performance and SolarPILOT [84] is used to calculate the solar field performance. The rest of the components, unique to particle CSP systems, are simulated in EES.

Special attention has been paid to the development of the receiver model. The performance calculation of the free-falling particle receiver has been upgraded by improving the calculation of thermal losses. Thermal losses have been benchmarked against CFD simulations under different conditions, which increase the model feasibility. Two of the main novelties in the current model are the advection heat loss dependence on the curtain height and the wind effect on the receiver efficiency.

The wind effect reduces the receiver efficiency depending on wind direction and wind speed, which increases the LCOE. The effect of geometrical concentration ratios (C = 2000 and C = 3000) was also investigated. The case with lower concentration ratio experiences a higher increase of LCOE due to the greater exposure to advection losses. This means that the optimum configuration with the current receiver model will tend to require higher concentration ratios than the previous models.

The calculation of the curtain optical properties has been also improved by developing a new analytical model, which is validated against ray-tracing [85]. While previous models [79] showed that the particle absorptivity did not have a big effect in the LCOE, the current model shows that low-absorptivity particles involve a higher LCOE even if they were free (see Figure 81). Thus, the use of CARBO particles is recommended.

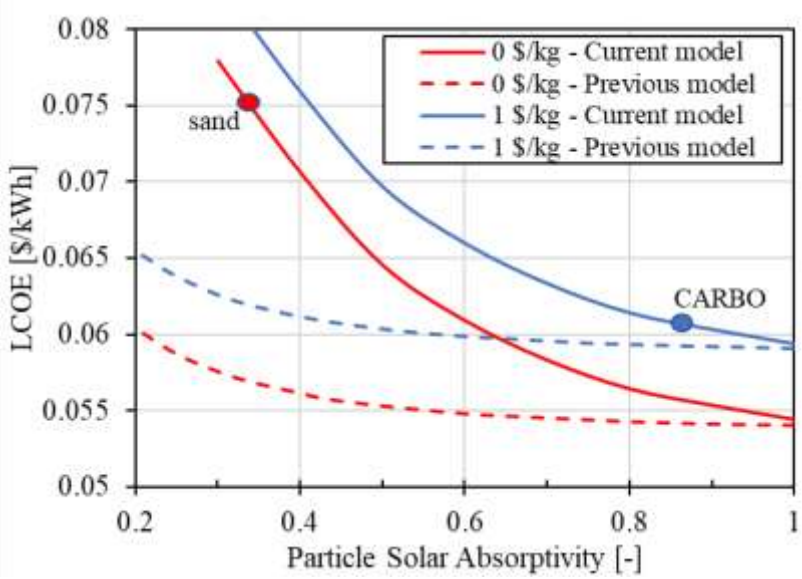

Figure 81. LCOE as a function of particle absorptivity for different particle cost (0 $/kg and 1 $/kg) with previous and current model.

Particle loss is one of the main challenges in particle CSP systems. Figure 82 shows the LCOE as a function of fraction of particle flow loss in three different scenarios: one in which the particle cost is 1 $/kg (estimated cost of CARBO particles), and other two with hypothetical costs of 0.1 $/kg and 0 $/kg. For the case of particle cost c = 1 $/kg shown in Figure 82, the fraction of particle flow loss should be limited to 0.0001%-0.001% to avoid high LCOE increments. If the particle cost were reduced by 10, c = 0.1 $/kg, then the limits would be 10 times bigger, 0.001%-0.01%. For the next results, the fraction of particle flow loss is maintained under 0.0001%.

The cost models used to estimate the LCOE have a nominal case and upper and lower bounds to analyze the range of potential LCOE values. The plant configuration used for this analysis has been obtained by minimizing the LCOE in the nominal case. Figure 83 and Figure 84 show the LCOE as a function of solar multiple, storage hours, geometrical concentration ratio and tower height for a system with ground-based storage and one receiver. The minimum LCOE is achieved for a plant with geometrical concentration ratio C = 3000, tower height H_{tower} = 270 m, solar multiple SM = 3 and 14 hours of storage. Since the LCOE obtained with tower height H_{tower} = 250 is very similar, this latter height is considered more appropriate due to the lower construction problems that a shorter tower could involve.

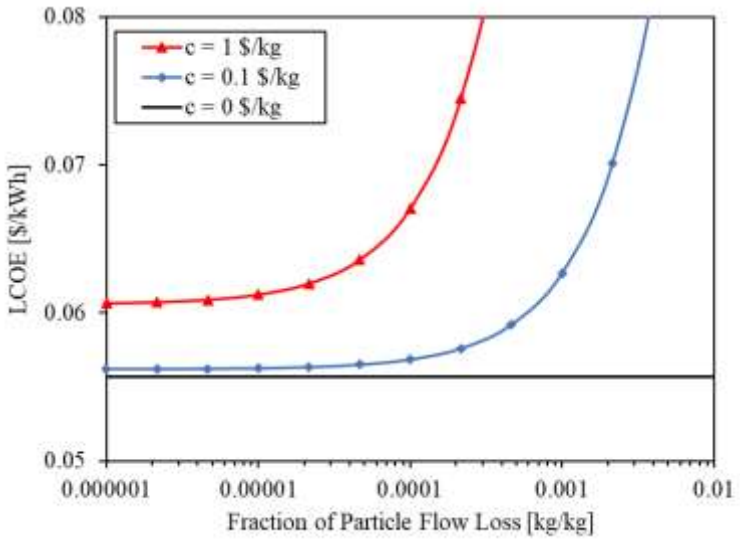

Figure 82. LCOE as a function of fraction of particle flow loss for different particle costs (0 $/kg, 0.1 $/kg and 1$/kg)

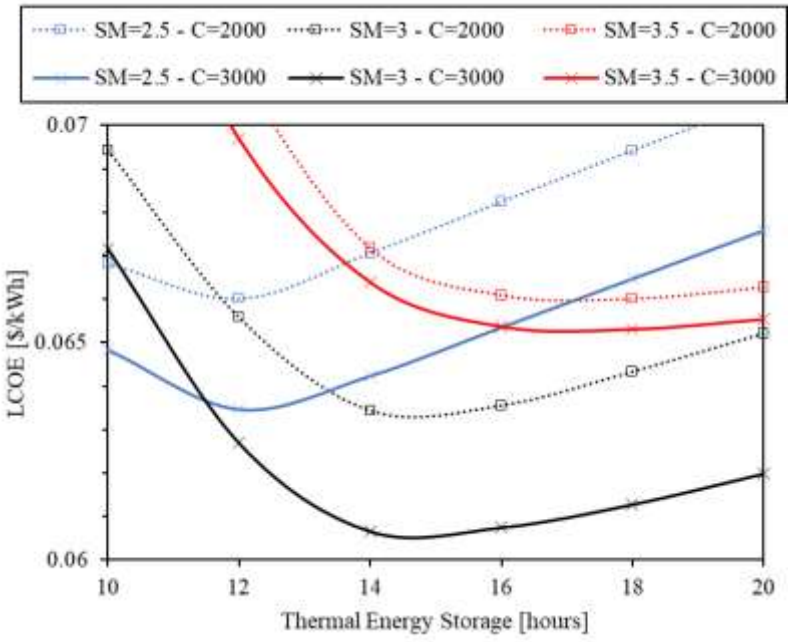

Figure 83. LCOE as a function of storage hours for differnt solar multiples, SM, and geometrical concentration ratios, C

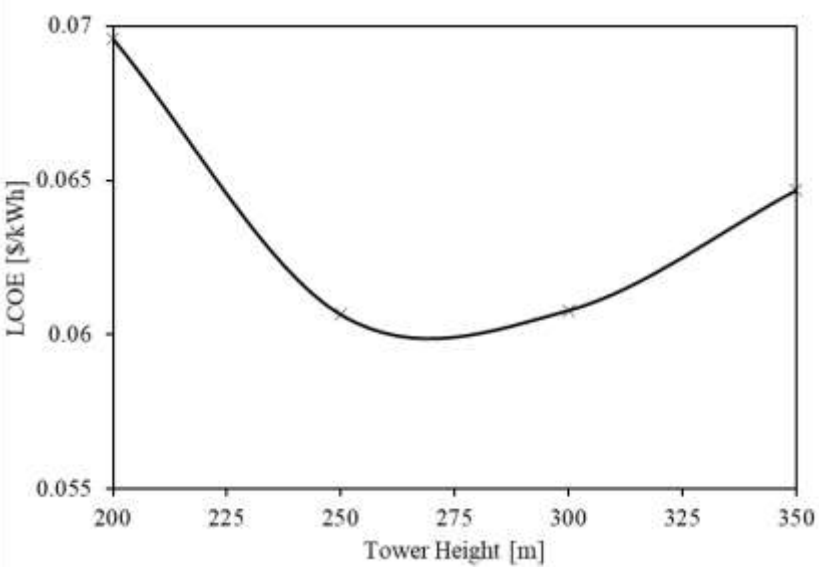

Figure 84. LCOE as a function of tower height

A probabilistic analysis was performed to analyze the potential range of LCOE values and to identify key parameters that impact the LCOE for four independent particle-based CSP configurations:

1. One-cavity receiver and ground storage
2. One-cavity receiver and tower-integrated storage
3. Three-cavity receiver and ground storage
4. Three-cavity receiver and tower-integrated storage

Uncertainty distributions were assigned to component costs and performance parameters that have a high-degree of uncertainty, and ~200 realizations using Latin Hypercube Sampling (LHS) were simulated. Uncertainty distributions for component costs were taken from vendor quotes, when available, and literature values.

The cumulative distribution functions (CDF) of the LCOE for the four independent particle-based CSP configurations (ground-based vs. tower-integrated storage and one-receiver vs. three-receiver tower systems) are shown in Figure 85. The probability of achieving less than $0.06/kWh is also tabulated for each of the four configurations. The single-receiver configuration generally yields lower LCOE than the three-receiver configurations, and the tower-integrated storage yields lower LCOE than the ground-based storage system for the same receiver configuration.

Figure 86 shows the median (50th percentile) LCOE for each of the four configurations with uncertainty bars representing the range between the 5th and 95th percentiles. While the single-receiver configurations are generally lower in LCOE than the three-receiver designs, the LCOE distributions are relatively similar, and the three-receiver design may provide additional availability if one of the particle lift systems goes down. The three-receiver design includes the potential to have up to three separate particle lifts (one for each receiver), enabling some redundancy. In addition, the optimized tower height for the single-receiver model was simply applied to the three-receiver model. It is likely the three-receiver configuration could be optimized with a shorter tower height that could reduce the LCOE.

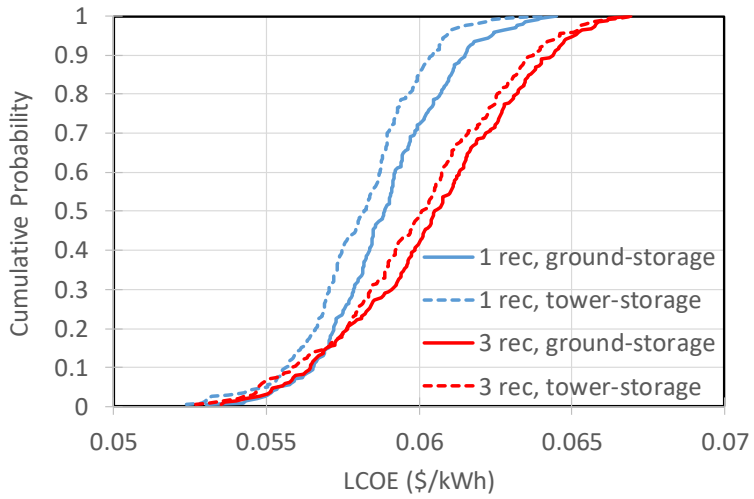

Configuration	Probability of LCOE ≤ $0.06 kWh
1 receiver, ground storage	72%
1 receiver, tower storage	85%
3 receivers, ground storage	42%
3 receivers, tower storage	49%

Figure 85. Left: Cumulative probability of LCOE for four particle tower configurations (ground storage vs. tower storage, one receiver vs. three receivers). Right: Probability of achieving LCOE ≤ $0.06/kWh.

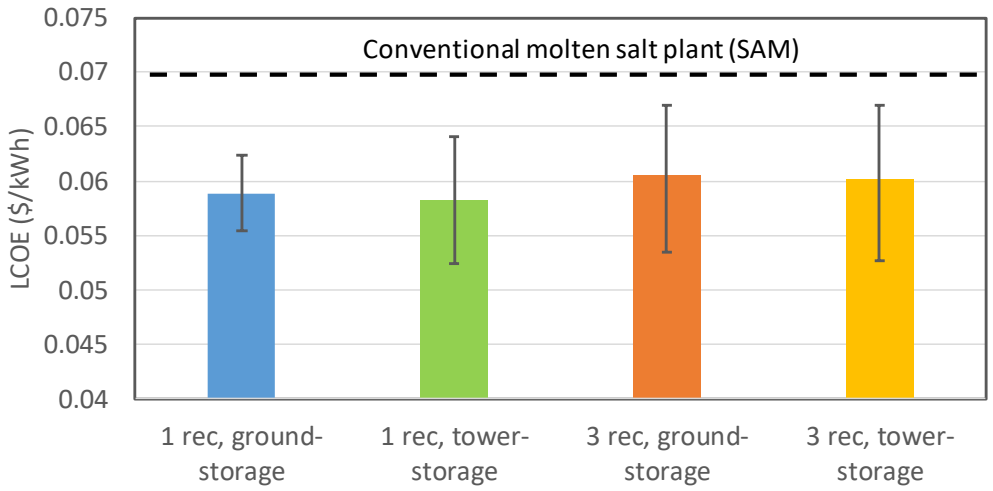

Figure 86. Summary of the LCOE probabilistic analysis for the four different scenarios. Colored bars represent the median LCOE (50th percentile) and uncertainty bars represent the range between 5th and 95th percentiles.

Figure 86 also shows the LCOE for a conventional molten-salt plant as calculated in System Advisor Model (SAM) using the same assumed costs and performance for common components (e.g., heliostat field, power block). The simulated LCOE values for all particle-based configurations are less than the LCOE for the molten-salt plant.

A stepwise rank-regression analysis was performed on the probabilistic results of each of the four system configurations to identify which stochastic input parameters had the most impact on LCOE. Figure 87 shows the rank-regressions coefficients for the statistically important input parameters that impact the magnitude of the LCOE, and Figure 88 shows the incremental coefficients of determination (ΔR^2) that indicate which parameters contribute most to the spread in LCOE.

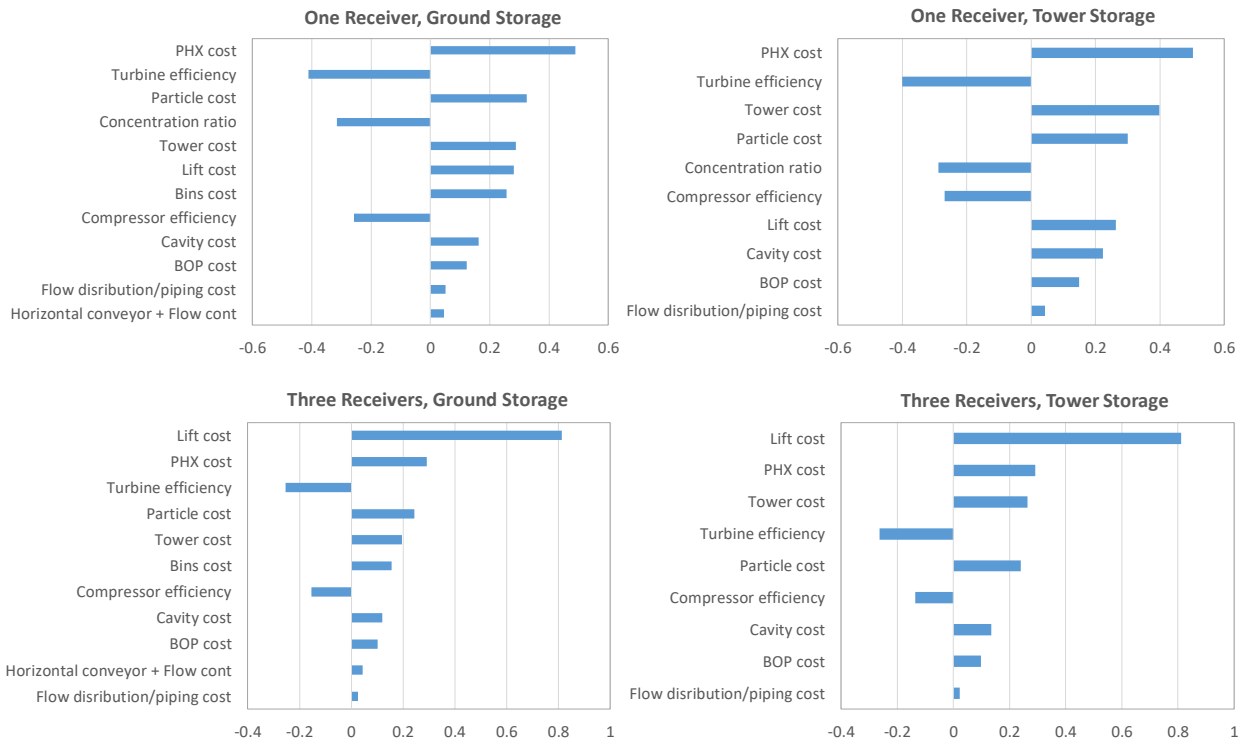

Figure 87. Rank regression coefficients indicating most important parameters to LCOE for four particle-based CSP configurations.

Figure 87 shows that for the single receiver configuration, the particle heat-exchanger cost is the most important, followed by turbine efficiency (higher turbine efficiency lowers LCOE; hence, the negative coefficient). Other important parameters include the particle cost, concentration ratio (receiver efficiency), tower cost, lift cost, compressor efficiency, cavity cost, BOP cost, flow distribution/piping cost. Storage bin cost and horizontal particle conveyance/distribution were also important for the ground-based storage with a single receiver.

For a three-receiver configuration, the lift cost was most important, followed by the particle heat exchanger cost, turbine efficiency, turbine efficiency, tower cost, particle cost, compressor efficiency, cavity cost, BOP cost and flow distribution/piping cost. The storage bin cost and horizontal particle conveyance/distribution were also important for the ground-based storage with a three-receiver tower. The lift cost was important for the three-receiver configuration because the uncertainty in lift cost accounted for up to three separate skip-hoist configurations.

The same input parameters that had the most impact on the magnitude of LCOE according to the rank-regression coefficients also had a commensurate impact on the variability in LCOE for each of the four configurations according to the incremental coefficients of determination shown in Figure 88.

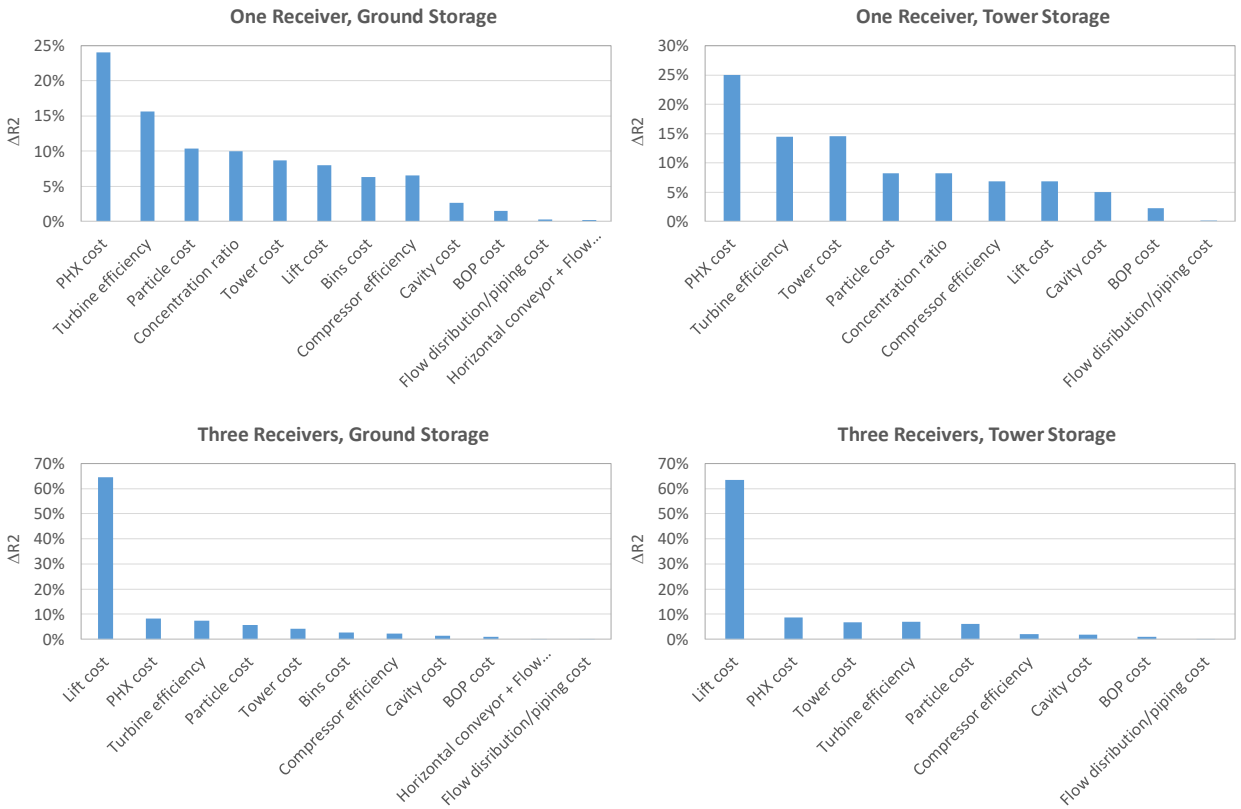

Figure 88. Percentage of real LCOE variability explained by input parameters for four particle-based CSP configurations.

3.3.2. Market Adoption Studies

Two market adoption studies were performed for G3P3 technology: (1) a market adoption study by KSU and Saudi Electricity Company (SEC) specific to Saudi Arabia and the Middle East, and (2) a more general market adoption study conducted by EPRI using production-cost modeling.

Middle East Market Adoption Study. SEC and KSU envision launching a joint venture called SOLENCORP that will interface with project developers and/or EPC contractors. SOLENCORP will design and build critical components for particle-based CSP systems and provide consulting services. Once G3P3-KSA is operational, it is expected that interest from the Saudi Ministry of Energy and renewable energy regulators in other countries will grow in particle-based CSP. KSU and SEC conservatively estimates that one particle-based project will be awarded every year thereafter. Initial commercial size of the particle CSP plants is expected to be 27 MW to correspond to GE's Frame 5C capacity. Each subsequent project for ~10 years will be about the same size to improve bankability of the technology, and then SOLENCORP expects to contribute to 265 MW of PPA projects over 10 years. In addition, installed capacity of off-grid power generation within SEC's network is ~540 MW, and particle-based CSP is expected to provide a cost-effective alternative to expensive diesel-based electricity generation in off-grid locations.

EPRI Market Adoption Study. EPRI, together with SolarDynamics and the TAC, commenced a market adoption pathway study to evaluate the unique value proposition for particle-based CSP technology and identify potential markets for early deployment. The team explored several key

differentiating characteristics of the G3P3 technology to assess the value relative to other CSP technologies and the value to a representative grid system. In Phase 2, production cost modeling was performed to quantify the grid benefits of the particle-based technology and evaluate different scenarios and market conditions that could promote greater deployment of the technology. Preferred plant design, configuration, and dispatch strategies were identified to guide further development efforts. Additionally, insights on domestic and international markets for particle-based technology, along with potential alternative applications of the technology outside of power generation, may be helpful in accelerating technology deployment. Objectives of the market adoption study include:

- Assess the relative value of particle-based CSP plant designs, plant configurations, dispatch strategies, and other characteristics from grid operator and plant owner perspectives
- Determine scenarios or market conditions in which particle-based CSP technology is competitive or provides greater system benefits
- Quantify the unique value proposition for a 100-MW Particle CSP Plant relative to an "Alternative Gen3 CSP Plant"
- Identify key market opportunities where particle-based CSP may have advantages based on technology-specific attributes

This effort was conducted early in the knowledge development stage of the Gen3 CSP technologies, before detailed designs, cost models, and performance models were available. As a result, much of the analysis is performed with preliminary data and relatively simplistic models, and thus the findings allow relative comparisons for an example grid network, and the absolute values presented are not broadly true or applicable to all systems. Full results are contained in a public EPRI report.

EPRI KEY FINDINGS

- *Particle CSP Plants reduce system operation costs.* Production cost simulation results show that adding a Particle CSP Plant can reduce the system operation cost. The annual reduction is approximately 6.5% higher than for Alternative Gen3 CSP Plant due to anticipated higher higher generation and great plant availability.
- *Peaker plants may provide greater system benefits and significantly higher plant revenue than baseload plant designs.* The system operation cost for the 250-MW peaker plant design is $4.4M (0.8%) lower than the 100-MW baseload plant design. Plant revenue for the peaker is $3.9M (23%) higher than the baseload.
- *Multiple modular units can reduce locational marginal price (LMP) and transmission congestion.* Ten modular 10-MW Particle CSP Plants distributed throughout the grid system provide greater power system flexibility than a single-tower 100-MW plant design in one location. The primary system benefits are a 15% reduction in LMP and 1.2% fewer binding events (congestion) on transmission lines.
- *Particle CSP Plant value increases in regions with high renewable penetration.* Particle CSP Plants provide needed flexibility in systems with high renewable penetration. Annual system operating cost falls by 33% with the addition of a Particle CSP Plant when the renewables penetration increases from 23% to 50%.
- *Particle CSP Plants have unique attributes that may be advantageous in certain markets.* The potential modularity of particle-based systems make it well-suited for markets that require smaller

systems (e.g., mining loads in Australia), have land limitations (e.g., Hawaii), or prefer to site generation closer to load centers in areas prone to fire (e.g., California). The potentially high reliability of particle-based systems may be advantageous in regions like South Africa where there is frequently insufficient baseload capacity during peak demand. Markets with incentives for economic development, such as South Africa, may provide incentives for Particle CSP Plant development, since the technology uses components that can potentially be manufactured locally. Additionally, key markets include countries known to be early adopters of new CSP technologies, such as Morocco and United Arab Emirates, and countries with ambitious CSP deployment targets (e.g., Spain) or decarbonization goals (e.g., U.S. states and utilities with 100% renewable/clean energy goals). There may also be opportunities to deploy particle-based systems in repowering or retrofit applications at conventional power plants, or in desalination, long-duration storage, solar fuels, or process heat applications.

- *The lowest levelized cost of electricity (LCOE) is $54.5/MWh for the peaker plant with TOD-adjusted capacity factor.* LCOE results for the baseload plants range from $63.8/MWh to $84.6/MWh for different design configurations and across a range of overnight capital costs. The lowest-LCOE baseload configuration has a solar multiple of 3 and 14 hours of thermal energy storage. The LCOE ranges for the 250-MW peaker without and with TOD adjustment are $89.6/MWh to $120/MWh and $54.5/MWh to $72.6/MWh, respectively.

3.4. Phase 3 Test Matrix and Risk Reduction

3.4.1. Phase 3 Risk Reduction

Phase 3 funding will create a unique high-temperature (>700 °C) test facility for the advancement of particle-based CSP technologies. The integrated tower facility will serve as an enduring resource, even beyond the scope of G3P3, that will bring conceptual prototypes to a technical readiness that is attractive to commercial investors and industry. Phase 3 deliverables will demonstrate component technologies at larger scales than previously tested and will provide additional data to improve our understanding of commercial-scale cost, risk, and performance.

The G3P3 Phase 3 proposal has been rigorously planned and engineered to ensure successful implementation and will provide results for the baseline design within the first 6-12 months of operation. The system can then be adapted to respond to emerging breakthroughs in alternative approaches in receivers, heat exchangers (e.g., fluidized-bed), and storage.

Figure 89 provides a high-level summary of the key components and technical milestones to be addressed in phase 3 and in alternative designs to be evaluated by international partners (e.g., G3P3-KSA).

System: Phase 3 makes two impactful technical leaps with the demonstration of TES which promises to provide a key market advantage for particle-based CSP systems and a demonstration of grid reliability by Saudi Electricity Company. Phase 3 testing will refine understanding of market compatibility by evaluating all operational modes: start-up/shutdown, steady-state at 1 MW design point, storage, and load-follow where the system will be controlled to follow fluctuating demand on a simulated grid. System testing will help to de-risk uncertainties system availability, component reliability, and particle heat losses throughout the balance of plant including ducts, valves, and hoppers, and to demonstrate safe practices in the use of hot particles.

Receiver: The test plan for Phase 3 is designed to demonstrate the robustness of receiver mechanical design and efficiency over the entire variety of weather variables over approximately a year including multiple wind events, transient DNI, clouds, dust, and ambient temperature. Efficiencies will be measured using thermopiles in the feed hopper (above cavity) and weigh hopper (below cavity). An array of thermocouples in the back wall will monitor for overheating and high temperature anomalies throughout the variation of test conditions over the test campaign. The cavity interiors will be assessed for heat and erosion degradation. The test campaign will also evaluate the risk of particle escape from the receiver and will improve upon existing control logic.

CFD analysis of the falling particle receiver (FPR) shows theoretical efficiencies near 85% with minimal performance degradation from wind with a cavity design that can be sustained throughout the range of flux and particle curtain thicknesses required to maintain particle temperature variation to <12° C. There is a risk that as the capacity and size of the FPR increases, the open cavity will make the system increasingly vulnerable to wind-induced variation and the associated risk that beam spillage will increase due to wind mitigating features such as the SNOUT. There are also risks associated with the ability of the receiver to sustain higher fluxes than have been previously demonstrated. As the particle curtain is thinned in order to increase the temperature rise, the real variability in curtain control and receiver production could result in overheating of the cavity. In addition to the open-cavity falling particle receiver, G3P3 partner DLR will be researching the *Centrec* rotating particle receiver and PROMES-CNRS will be researching the fluidized particle-in-tube receiver.

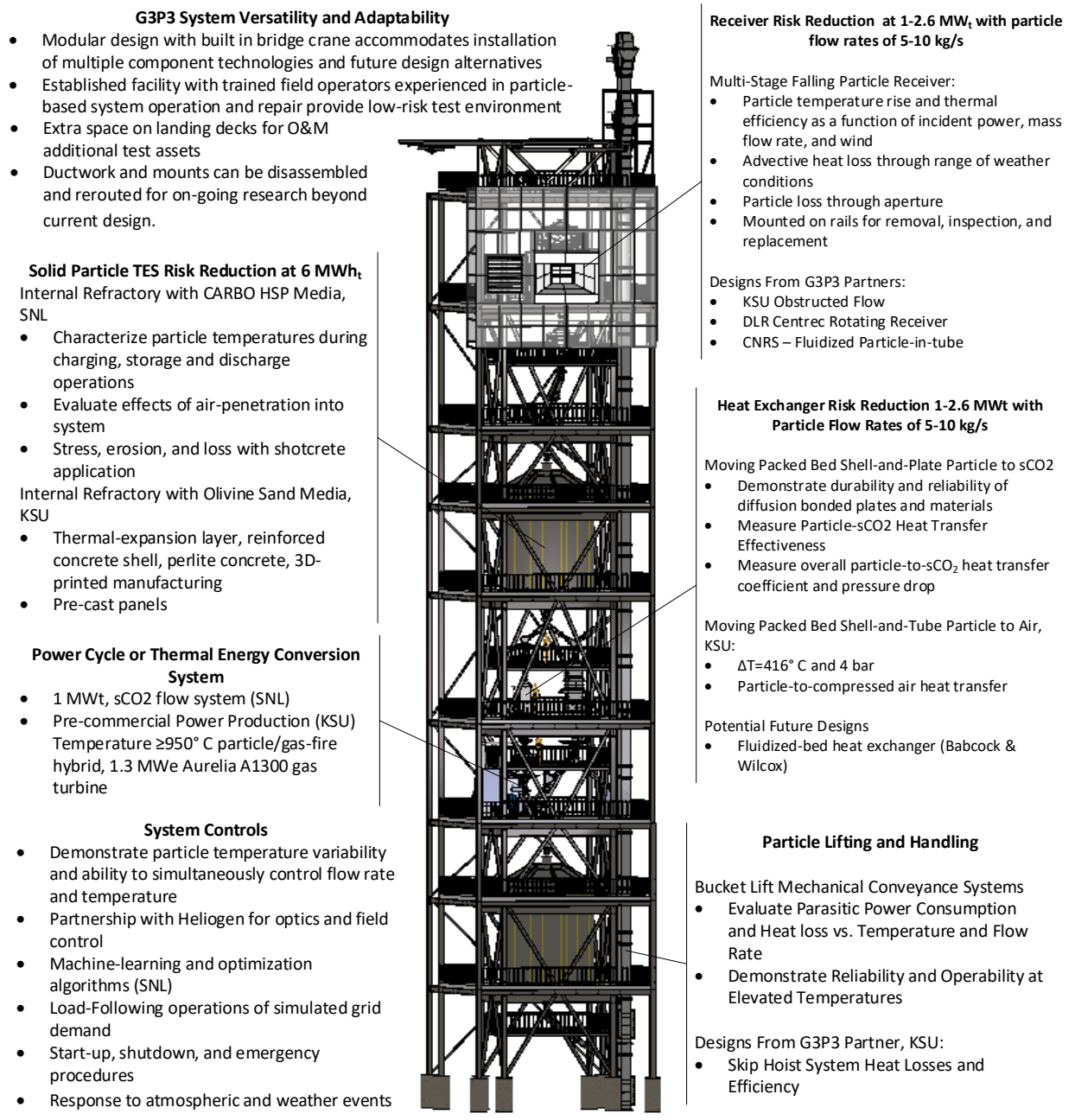

Figure 89. G3P3 Phase 3 testing and risk-reduction opportunities by component.

Storage: Bulk particles have been shown in Phase 1 and 2 to have distinct advantages over liquid storage because at low temperatures, particles do not freeze, and at high temperatures, do not degrade, are self-insulating, and provide a beneficial temperature distribution across the bin where they maintain a nearly constant temperature of 800° C throughout the volume of their bin with the exception of a shallow layer of cooling near the walls.

However, the knowledge base for storage and handling of bulk solids lacks precedence with temperatures as high as 800° C. Mass flow bins capable of holding the mass of the particles are difficult to construct and flat bottom bins are often implemented with the use of mechanical feeders.

Particle storage bins promise to reduce material costs because they do not have to be water-tight. The refractory insulation techniques used to construct the bin have been shown to be robust in furnace applications and larger hot solids such as clinker but the introduction of hot flowing particles of this size is possibly unprecedented at this scale and temperature. The interactions of particles with the cracks and crevices in a bin constructed with shotcrete refractories will be necessary to show viability of insulation materials applied at the commercial scale. Funnel flow particle bins also offer challenges in transient thermal modeling due to the evolving kinetics of funnel flow. Modeling performed in Phase 1 and 2 was compared to results from a small bin test, but is difficult to validate models at small scale because one cannot experimentally maintain similarity spatially (flow channel has non-representative proximity to wall-related cooling effects) and temporally (particles drain quickly without time to lose heat to walls and air on top surface) in a small bin. The phase 3 testing will provide the first measurements of heat losses during charging, storage, and discharging with adequate size and discharge times to be a valuable source for refining expected TES performance at the commercial scale. Post-mortem inspection will be performed to assess any impacts related to the interaction between fine hot particles and refractory joints.

Particle-to-sCO_2 Heat Exchanger: Particle to sCO_2 heat exchangers underwent significant evolutions in design as methods to reduce pressure drop, improve heat transfer coefficient, and correct sCO_2 flow maldistribution and particle flow non-uniformities. Phase 3 testing will demonstrate the manufacturability and effectiveness of the new heat exchanger design and the next increment in scalability of the heat exchanger from the 100 kW_t SuNLaMP prototype to 1 MW_t. In addition Phase 3 testing will validate models of heat transfer coefficient, mechanical stress models, and modeled estimates of achievable ramp rates. Heat exchanger testing in transient operations and start-up mode will inform risks related to limitations on achievable ramp rates.

***Particle Lift and* Conveyance:** High-temperature particle handling systems are well-established and CSP designs can be adopted from the mining, cement, and iron industry. There are three main risks in adopting these systems for CSP applications: increasing capacities, heat loss, and mechanical wear. Phase 3 testing at G3P3-KSA will empirically measure the electrical efficiency and thermal losses in skip hoists and reveal any issues related to mechanical interactions with hot particles. Prototype valve systems that charge and discharge the skips will be evaluated at a scale that is a significantly more representative of commercial plants. G3P3-USA will use a bucket lift. The bucket lift is representative of the types of conveyance systems that would be needed in plant configurations with ground-based storage bins such as pan-conveyors. Model validation of heat and parasitic losses during particle transit has been conducted at the 250 kW_t scale. Phase 3 will evaluate the same losses to provide inference into how these losses are likely to scale with increased capacity. Bucket lift evaluations will address risks related to particle loss, dust creation, erosion, and particle contamination of the mechanical system such as the chain or drive system.

3.4.2. Test Plan

G3P3 is designed to ensure successful testing of the baseline design within the 3-year project timeline while also being adaptable for ongoing research to de-risk multiple particle-based solar components. Wide decks and access ports allow for inspection, repair, replacement and even the evaluation of alternative technologies such as side-by-side comparisons of fluidized and moving particle heat exchangers. The ductwork can be detached and re-routed as necessary for versatility.

Instrumentation: At a high level, the instrumentation strategy prioritizes knowledge of particle mass and temperatures throughout the system environmental conditions including wind, air temperature, incident flux on the receiver, and DNI. The instrumentation is specified in the P&ID

diagrams and is described in detail in the test plan documentation. All components have been designed with pre-installed fixtures and ports to facilitate quick installation of the required instrumentation once the components have been lifted into the tower. Component leads and electromechanical technicians will install the instrumentation per the P&ID and connect the sensors to the appropriate I/O channels in the assigned cRIO mounted in a weatherproof cabinet adjacent to every component. A CAT 5 connection is available on all levels per the tower definition which connects all cRIOs to the SCADA system in the control room via existing underground transmission lines.

Temperature sensors, particle level indicators, and flow indicators are to be installed throughout the system. Particle inlet and outlet temperatures will be measured by thermocouple arrays installed in hoppers to ensure readings are averaged across many points and the TCs are adequately submerged in particles. Additional TCs will be located throughout the component bodies. Weather measurement instrumentation will include: an array of 3D ultrasonic anemometers located around the aperture, on top of the tower, and at a 10 m reference near the ground; a NIP on top of the tower, and multiple TCs to record ambient temperatures. The calibration panel will have a Kendall radiometer. Electric metering will be installed to evaluate parasitic losses in the bucket lift, electric particle heater, and particle cooling systems.

The test plan is divided into three primary sections: commissioning, system testing, and component testing.

Commissioning: Commissioning begins with verification of flow-control mechanism and DAQ functionality. Next, the system will be charged with particles at ambient temperatures using a platform and telehandler that can empty one full supersack (~1500 kg) of particles at a time into the bucket elevator inlet. Small amounts of particles will be circulated through the system to commission the bucket elevator, ensure system integrity, and check for leakage in the ducts, storage bins, and heat exchanger. After the system operation is verified, additional particles will be loaded and circulated through the system. The electric particle heater (and/or low solar flux on the particle receiver) will be used to gradually increase the particle temperatures. These heated particles will be circulated to gradually bring the storage bins, receiver body, and heat exchanger to ≤600° C.

Once particles have been successfully circulated at elevated temperatures, the receiver will be commissioned on-sun. The receiver must demonstrate that it can withstand peak flux at minimum particle flow without damage through a process of gradually increasing flux and then decreasing flow until it can be shown that it is safe to operate in the full range of expected conditions. Once the receiver is commissioned, particle temperatures can be gradually brought to 800 °C while circulating through the system, bringing all components to maximum operating temperature. During this period, the sCO2 loop will be tested and commissioned at operating temperatures, pressures, and flow rates. A final pressure test of the heat exchanger will be performed at 800° C.

The primary metrics for the commissioning phase are focused on detecting unexpected damage and verifying expected particle temperatures and flow rates throughout the system. Video information will be used to detect degradation of exposed surfaces including the receiver cavity. A bore-scope will be used to inspect the interior storage bin walls. Audio information may be able to detect abnormal noises such as cracks that could indicate stress or degradation of components. Particle temperatures, particle inventory in hoppers and bins, particle flow rate, bucket lift speed, and slide-gate positions will be monitored and compared to a system control simulation to ensure particle mass and temperatures throughout the system are within acceptable ranges of the expected values.

System Testing: Once commissioned, system and component testing will commence concurrently. As shown in Figure 90, system operations include start-up from cold, hot, and diurnal cycling; continuous operations where the system will be run for up to 10 hours per day for several consecutive days including steady state operations at the 1 MW_t system design point and off the design point and transient operations such as load-follow for a simulated grid demand and real and simulated DNI variations; storage operations including power generation from deferred storage and power production while simultaneously charging and discharging.

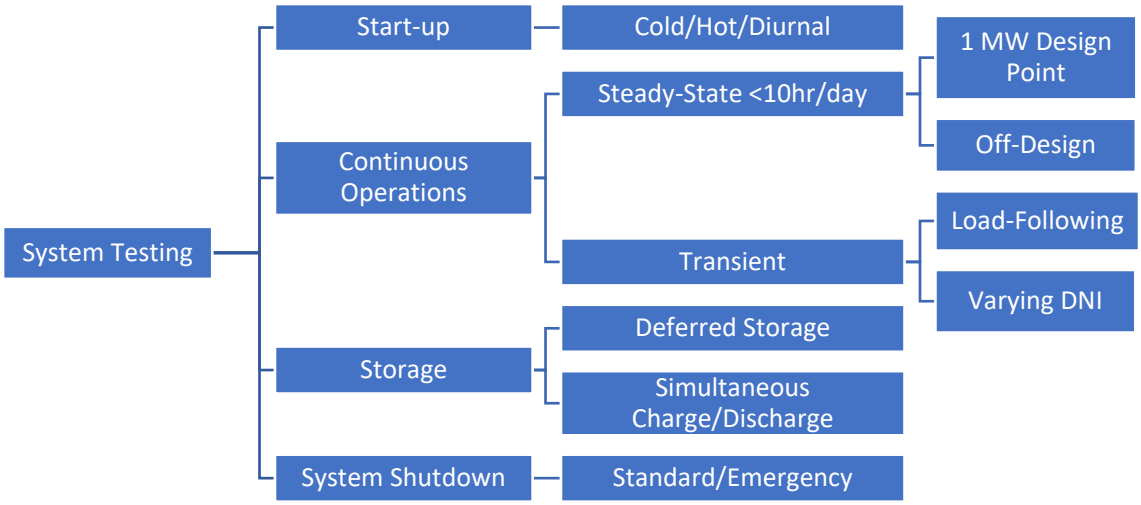

Figure 90. System Testing Flow Chart

Component Testing: During testing, data will be logged continuously from all channels enabling most system and component test objectives to be evaluated simultaneously. Continuous logging enables all metrics to be evaluated in the greatest number of operational modes and environmental conditions including wind and DNI.

Receiver. Testing will be performed to verify the ability of the FPR to achieve the required particle temperature rise to meet system performance requirements. Receiver efficiency will be evaluated as a function of mass flow rate, irradiance, and particle temperatures during naturally occurring weather and wind events. Maintaining particle outlet temperatures using automated PID controls will also be performed.

Storage. The 6 MWh storage bin provides adequate size to provide representative measurements of inlet, air, wall, and outlet temperatures that will be used to validate models which will inform developers of a more accurate temperature profile entering the heat exchanger. Heat loss will be characterized using TC arrays, and the effects of cool air entering the system will be measured and characterized.

Particle-to-sCO_2 Heat Exchanger. Three phases of tests will be conducted with the heat exchanger; hydraulic performance, mechanical integrity, and thermal performance testing. First, the sCO_2 coolant loop will be used to flow cool sCO_2 through the heat exchanger to measure the pressure drop on the sCO_2-side and estimate pressure drop at full operating conditions. Next, as described previously, the heat exchanger will be slowly brought up to operating temperature using particle heat and operating pressure using the sCO_2 coolant loop to demonstrate the ability of diffusion bonded nickel alloys to retain mechanical integrity at these conditions. Finally, particle-side measurements will be used in combination with measurements provided by the sCO_2 coolant loop to determine the

particle-side heat transfer coefficient and overall heat exchanger effectiveness under a variety of steady-state and transient operating conditions.

Particle Lift. The efficiency and parasitic power consumption of the particle lift will be measured using a dedicated power meter as a function of particle temperature and flow rate. Particle heat loss will be evaluated over a representative height similar to the intermediate conveyance systems that might be used in a commercial system to move particles from the heat exchanger to the cold storage bin. These losses are difficult to model due to the well-insulated but non-hermetic nature of the casing. Direct measurement on a system of representative length will help clarify these losses for commercial system designers.

Controls. Control systems will be employed in G3P3 Phase 3 testing as described in Sections 3.1.1.4 and 3.2.5. Sandia also intends to explore autonomous controls that can enhance system performance through optimization or machine learning algorithms. Controls experts at Sandia will have access to the G3P3 data for model development and implementation.

Key metrics include receiver efficiency, particle outlet temperature control, storage heat loss, heat exchanger performance (heat-transfer coefficient, pressure drop, thermal duty), sCO2 flow rate and temperature, particle lift efficiency and reliability, and controls operability. Additional metrics include heat loss in particle ductwork, control system error detection, and adaptation from induced failure modes such as sCO2 loop stoppage and heat exchanger bypass. All components will be assessed for particle erosion and/ thermal degradation.

3.4.3. G3P3 Phase 3 FMEA

A detailed Failure Modes and Effects Analysis (FMEA) was performed for the G3P3 Phase 3 activities. The work elements were separated into four categories: (1) Test Component/Work Package, (2) Construction/Facilities/O&M, (3) Environmental & Natural Hazards, and (4) Personnel. The Test Component/Work Package category considers failures in the major components of the G3P3 system (receiver, storage bins, heat exchanger, particle lift, ducting/piping, electrical systems, and heliostats (sCO2 loop has its own separate FMEA managed in a separate work package by M. Carlson). The Construction/Facilities/O&M category includes failures in the tower structure, foundation, electrical systems, welding and construction, and heavy machinery. Environmental & Natural Hazards include failures and hazards due to wind, earthquakes, lightning, and wildlife. Finally, the Personnel category considers fatigue, stress, and other human errors.

For each category, meetings were held with a variety of staff, subject matter experts, technologists, and manager. For each possible failure or hazard, a risk priority rating was determined, along with engineered and administrative controls. Personal protective equipment (PPE) was also identified. Prior to work commencing, the FMEA and all recommended controls will be reviewed and implemented, as appropriate. A spreadsheet summarizing the results of the G3P3 FMEA is presented in Appendix E.

3.5. Risks of Scaling Up to 100 MW_e

At the conclusion of the Phase 3 testing, a number of technological risks will have been addressed at a $\geq$ 1 MW_t scale through G3P3-USA and G3P3-KSA. These include multiple particle receiver technologies, $\geq$ 6 MWh of particle thermal storage, high-temperature particle-to-sCO_2 (and air) heat exchangers, and particle-based electricity production (via G3P3-KSA). As described in the Market Adoption Study (Section 3.3.2), Saudi Electricity Company is partnering with KSU to develop G3P3-KSA as a direct pathway toward commercialization and future deployment for grid-based

electricity production. In addition, as described in Section 3.3.2, particle-based CSP technologies can play a large role in other markets including energy storage, process heat for manufacturing, and thermochemical processes.

Nevertheless, additional barriers exist to scaling the G3P3 pilot system to commercial scales. In addition to technological risks, a number of market-barrier risks were identified by the G3P3 Technical Advisory Committee during periodic reviews in Phases 1 and 2. For example, without a prior demonstration of commercial-scale energy production, a first-time developer would face discounted projections from Engineering, Procurement, and Construction estimators due to high uncertainties arising from a lack of prior basis. Knowledge of grid connected performance with Saudi Electricity Company and KSU will help in this regard. Another risk is that there will be little basis on which to assess the long-term reliability of particle-based CSP components over the 30-year life of a plant despite several years of G3P3 operational experience. The reliability could be further impacted by a lack of knowledge of expected thermal transients. Vendors may not have adequate knowledge of thermal and stress requirements to ensure components are adequately robust. The supply chain for particle-based components has yet to receive demand causing a risk for delays and cost overruns as unforeseen issues arise with manufacturability. Labor issues could be a risk due to a lack of experience in maintaining and operating particle-based components.

With regard to technological risks of scaling up to a 100 MW_e commercial CSP plant, Figure 91 shows a combined image of two particle-based CSP plant configurations with associated risks and mitigation opportunities for each component. The baseline design utilizes tower-integrated components to move particles through the system by force of gravity. Commercial developers will risk delays and cost over-runs associated with construction requirements for additional concrete for the thicker walls foundations and floor supports. Components may need to be installed in the tower as it is constructed causing multiple construction entities to coordinate without schedule interruptions. Support concepts for the tower and hot storage bin floor supports have been proposed and discussed with tower construction professionals and vendors but will require significant additional engineering that could reveal additional impediments.

Tower-integrated storage risks are mitigated through an alternative system configuration with externally located components and an intermediate particle lift between the heat exchanger and the cold storage bin. External storage bins use well-established (>30 year) construction techniques for monolithic concrete domes. Mechanical conveyance systems such as pan conveyors and belt conveyors are limited in maximum achievable temperatures at the capacities required. Multiple conveyors will be used in parallel to achieve the necessary mass flow. Conveyors have been used in high-temperature situations but were allowed to dissipate heat to the environment instead of remaining in an insulated environment where heat was trapped inside the conveyance chamber. The heat exchanger would still need to be vertically integrated with the hot storage bin, but unlike the tower, floors could be suspended with standard pillars on the ground.

As the falling particle receiver is scaled in size, uncertainties related to the knowledge of curtain opacity, wind effects, convection and radiation losses, spillage losses, and the ability to control both mass flow rate and desired outlet temperature is uncertain. Many of these risks can be reduced through additional model validation at the pilot scale and detailed CFD modeling of commercial-scale systems (see Section 3.1.1.7). The design of a three-receiver tower minimizes the aperture area and lowers the required tower height, which also alleviates these risks.

Phase 3 testing will improve understanding of particle-to-sCO_2 heat exchangers both in predicting performance and in materials and nickel diffusion bonding manufacturing processes. Patents have

been filed on the shell-and-plate heat exchanger design which will advance a commercial heat exchanger supply chain. Modeling has shown structural viability of the commercial scale heat exchanger but commercial risks remain due to modeling uncertainties inherent in scaling temperature and pressure distributions. This can be mitigated by making commercial systems modular with banks of multiple 32 MW_t heat exchangers (see Section 3.1.3.5). Commercial developers will face risk in demonstrated heat exchanger reliability and durability in power production environments. While this risk will be mitigated with a modular design, the high costs of heat exchangers make repair and replacement risky to bottom line costs.

Particle heat-exchanger performance may be a risk to commercial developers needing to accurately predict power production. To mitigate this risk, alternative designs are being evaluated including shell-and-plate (Sandia), shell-and-tube (KSU), and fluidized-bed heat exchangers.

G3P3 commercial scale-up risks are summarized in Appendix F.

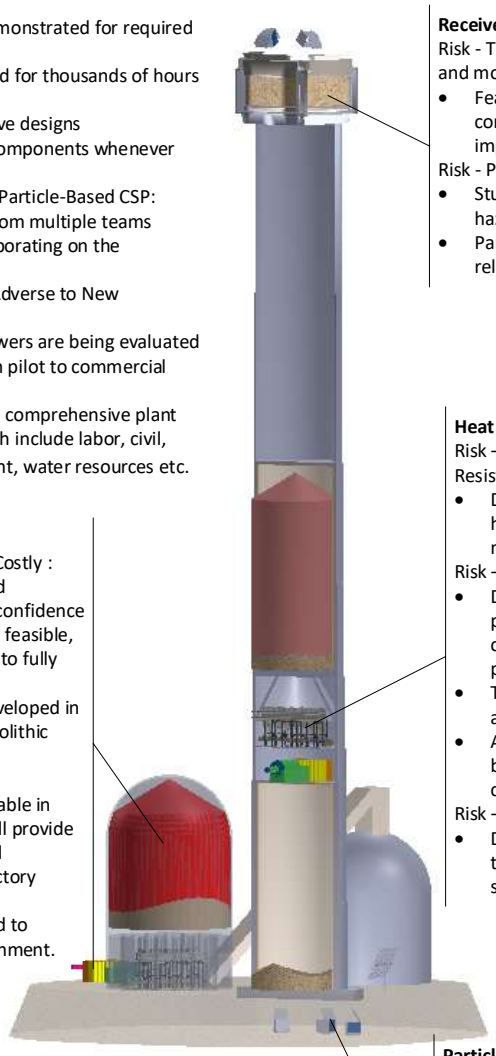

System
Risk – Reliability will not have been demonstrated for required service life:
- G3P3 USA and KSA will be operated for thousands of hours to identify reliability issues.
- Ongoing development of alternative designs
- Use of commercially established components whenever possible

Risk – Labor Force Lacks Experience in Particle-Based CSP:
- Established team of researchers from multiple teams around the world have been collaborating on the development of components.

Risk – Commercial Investors Are Risk-Adverse to New Technologies
- Modular systems with multiple towers are being evaluated to reduce the technology gap from pilot to commercial scale.
- Probabilistic cost models based on comprehensive plant cost studies by NREL and SBP which include labor, civil, electrical, piping, cables, equipment, water resources etc.

Receiver
Risk - Thermal efficiency is lower than expected and more vulnerable to wind impacts at 100 MWe
- Features such as nods or multi-stage release components may reduce wind effects and improve particle curtain opacity.

Risk - Particle loss through aperture:
- Studies performed do not show inhalation hazard from lost particles
- Particle loss is reduced with multi-stage release features

Heat Exchanger
Risk – Manufacturing and Scale-Up with Corrosion-Resistant Etched and Diffusion-Bonded Materials:
- Diffusion-bonded modular banks of 32 MWt units have been designed to accommodate multi-megawatt thermal duties

Risk – Low Particle-Side Heat-Transfer Coefficient:
- Detailed modeling studies and tests are being performed to improve particle-side heat-transfer coefficient and overall heat transfer performance.
- True-counterflow and cross-counterflow designs are being designed
- Alternative fluidized bed heat exchangers are being developed that show higher heat exchange coefficients

Risk – Low reliability and increased failure modes
- Detailed modeling studies are being performed to evaluate and mitigate thermomechanical stress

Storage
Risk – Tower-Integrated Storage is too Costly :
- Consultation with silo designers and construction managers resulted in confidence that the tower-integrated system is feasible, but detailed design work is needed to fully understand logistics and costs.
- Storage in external bins is being developed in parallel using well-established monolithic dome construction.

Risk – Excessive Heat Loss:
- Modeling shows heat loss is acceptable in large capacities. Phase 3 testing will provide improved understanding of thermal resistance and capacitance in refractory materials.
- Experimentation is being performed to understand the effects of air entrainment.

Particle Lift and Conveyance
Risk – Heat losses and Adequate Insulation :
- FLSmidth has experience at relevant capacities and believes they can accommodate thermal requirements.
- G3P3-KSA will test a small-scale skip hoist

Risk – Excessive Particle Temperatures on External Conveyors:
- Vendors of high-temperature particle conveyance equipment have been consulted and are participating in solutions to meet capacity and temperature requirements.
- Vertically integrated hot storage and heat exchanger system configurations are being designed for both tower-integrated and externally integrated systems.

System Controls
Risk – Ability to Control Both Flow Rate and Temperature of Particles Through Receiver
- Computer learning techniques can couple optics with flow rate controls to stabilize temperature variability.
- KSA will test a cogenerative system with a natural gas heating element
- Load-Follow operations will be tested in G3P3
- Supervisory control algorithms operational control response to stochastic weather events

Figure 91. Particle-based CSP system displaying tower-integrated and external storage configurations

Table 22 summarizes the key technological risks and mitigation measures for scaling the G3P3 technology to commercial systems.

Table 22. Commercial scale-up risks for G3P3 technology.

Component	Risk	Mitigation
Receiver	Low thermal efficiency and wind impacts at 100 MW_e scales	▪ Preliminary studies have shown that hoods or nods can be implemented to mitigate wind impacts at 100 MW_e scales ▪ Aperture covers using quartz-glass are likely limited to aperture sizes of a few meters ▪ Multi-cavity falling particle receiver designs (similar to Khi Solar One) are being considered to minimize aperture size and increase receiver efficiencies ▪ Scaleable multi-stage release designs being considered to reduce convective entrainment while maintaining high opacity of the particle curtain
Receiver	Particle loss through aperture	▪ Tests and studies are being performed; preliminary results show that particle loss does not pose an inhalation or environmental hazard ▪ Methods are being pursued to reduce particle losses using multi-stage release and active airflow.
Storage	Size of storage tanks for 100 MW_e system may be too big for tower integration	▪ Sandia, Matrix, and Allied are considering storage tank designs for 1, 10, and 100 MW_e systems. Conceptual designs for tower-integrated storage tanks have begun, and structural analysis plans are being developed to assess feasible sizes based on static and dynamic loads on the tower. Ground-based tanks and conveyance systems for 100 MW_e systems have also been considered and modeled in EES.
Storage	Heat loss may be excessive	▪ Cyclic modeling results have begun and preliminary results show that heat-loss and temperature requirements can be met
Storage	Cost may be excessive	▪ Novel designs that exploit funnel flow to reduce erosion on walls have been introduced and studied that will reduce the need for expensive refractory layers. ▪ Large volume to surface-area ratio for larger systems reduces heat loss relative to smaller-scale systems; expensive insulation layers (e.g., Elmtherm) may not be needed.
Heat Exchanger	Manufacturing scale-up and high cost for 100 MW_e system	▪ Alternative diffusion-bonded shell-and-plate designs are being developed by Solex and Sandia to accommodate multi-megawatt thermal duties ▪ Alternative multi-bank and multi-heat-exchanger designs and configurations are being considered to meet cost and performance metrics
Heat Exchanger	Low particle-side heat-transfer coefficient	▪ Detailed modeling studies and tests are being performed to increase particle-side heat-transfer coefficient and overall heat transfer performance. ▪ Decrease plate spacing ▪ Introduce designs for true counterflow configurations (vs. cross-counterflow designs used in SuNLaMP)
Heat Exchanger	Low reliability and increased failure modes	▪ Detailed modeling studies are being performed to evaluate thermomechanical stresses and how to address those in larger or modular units

Component	Risk	Mitigation
	at commercial scale	
Lift	Heat losses and adequate insulation associated with bucket lift	▪ Skip hoists have been designed and evaluated for commercial-scale systems [15], and a leading manufacturer, FLSmidth, believes they can accommodate such a design. ▪ KSU and GT intend to test a small-scale skip hoist
Lift	Adequate particle lift rate that can handle ~2000 kg/s (~8000 tons/hour)	▪ FLSmidth stated that they have manufactured mine hoists that can achieve these particle lift rates; insulation for high-temperature application would be needed
System	Reliability over 30 years will not be identified in G3P3	▪ Two G3P3 systems (G3P3-USA and G3P3-KSA) will be operated in parallel. Together, we hope to yield thousands of hours of operation that will identify potential concerns and reliability issues

4. CONCLUSIONS

In Phases 1 and 2, G3P3 component and system designs were developed, tested, and optimized to reduce risks associated with the particle-based CSP technology. Simulations and testing were performed to inform the design of the receiver, storage, heat exchanger, and particle-lift components. In addition, engineering drawings were drafted that detailed the integrated component and tower system. Process flow diagrams detailing various operational and maintenance scenarios were developed, along with piping and instrumentation diagrams that provided a basis for equipment lists and costs bases. Technoeconomic analyses were performed using optical and thermodynamic models and published cost curves, and both sensitivity and probabilistic simulations were performed to evaluate important factors and uncertainties impacting the LCOE. Phase 3 test plans were detailed along with scope, schedule, and cost for Phase 3 activities in a MS Project file. Finally, risk registers were drafted for both the Phase 3 testing and scaling up from G3P3 to 100 MW_e commercial plants.

In conclusion, we feel that the proposed G3P3-USA and G3P3-KSA systems will create a marketable pathway for next-generation, particle-based, high-temperature CSP systems.

A list of publications from G3P3 Phases 1 and 2 is summarized in Table 23. A compilation of reports and presentations from this study is available at the following website:

https://energy.sandia.gov/programs/renewable-energy/csp/current-research-projects/gen-3-particle-pilot-plant-g3p3/

Table 23. Summary of G3P3 publications in Phases 1 and 2.

Component	Publication
Receiver	Schroeder, N., H. Laubscher, B. Mills, and C.K. Ho, Year, *Receiver Outlet Temperature Control for Falling Particle Receiver Applications*, in *ASME 2021 15th International Conference on Energy Sustainability collocated with the ASME 2021 Heat Transfer Summer Conference*, Virtual Conference.
Receiver	Ortega, J.D., C.K. Ho, G. Anaya, P. Vorobieff, and G. Mohan, Year, *A Non-Intrusive Particle Temperature Measurement Methodology Using Thermogram and Visible-Light Image Sets*, in *ASME 2021 15th International Conference on Energy Sustainability collocated with the ASME 2021 Heat Transfer Summer Conference*, Virtual Conference.
Receiver	Ortega, J.D., G. Anaya, P. Vorobieff, C.K. Ho, and G. Mohan, Year, *Particle Plume Velocities Extracted From High-Speed Thermograms Through Particle Image Velocimetry*, in *ASME 2021 15th International Conference on Energy Sustainability collocated with the ASME 2021 Heat Transfer Summer Conference*, Virtual Conference.
Receiver	González-Portillo, L.F., R. Abbas, K. Albrecht, and C. Ho, 2021, Analysis of optical properties in particle curtains, *Solar Energy*, **213**, p. 211 - 224.

Component	Publication
Receiver	Glen, A., D. Dexheimer, A.L. Sanchez, C.K. Ho, S. China, F. Mei, and N.N. Lata, Year, *Near-Field and Far-Field Sampling of Aerosol Plumes to Evaluate Particulate Emission Rates From a Falling Particle Receiver During On-Sun Testing*, in *ASME 2021 15th International Conference on Energy Sustainability collocated with the ASME 2021 Heat Transfer Summer Conference*,
Receiver	Yue, L., N. Schroeder, and C.K. Ho, 2020, *Particle Flow Testing of a Multistage Falling Particle Receiver Concept: Staggered Angle Iron Receiver (StAIR)*, in *ASME 2020 14th International Conference on Energy Sustainability*, Virtual Online, June 17 - 18, 2020.
Receiver	Shaeffer, R., B. Mills, L. Yue, and C.K. Ho, 2020, *Evaluation of Performance Factors for a Multistage Falling Particle Receiver*, in *ASME 2020 14th International Conference on Energy Sustainability*, Virtual Online Conference, June 17 - 18, 2020.
Receiver	Mills, B., R. Shaeffer, L. Yue, and C.K. Ho, 2020, *Improving Next-generation Falling Particle Receiver Designs Subject to Anticipated Operating Conditions*, in *ASME 2020 14th International Conference on Energy Sustainability*, Denver, CO, June 7 - 11, 2020.
Receiver	Kumar, A., W. Lipinski, and J.S. Kim, 2020, Numerical modelling of radiation absorption in a novel multi-stage free-falling particle receiver, *International Journal of Heat and Mass Transfer*, **146**.
Receiver	J.-S. Kim et al., 2020, *Design and test of multi-stage truncated-cone falling particle receiver (MsTC-FPR)*, in *SolarPACES 2020*, Virtual, Sep. 28 - Oct. 2, 2020.
Receiver	Ho, C.K., L.F. Gonzalez-Portillo, and K.J. Albrecht, 2020, *Evaluating the Effective Solar Absorptance of Dilute Particle Configurations*, in *Proceedings of the ASME 2020 14th International Conference on Energy Sustainability*, ES2020-1676, Denver, CO, June 8 - 10, 2020.
Receiver	Chen, J., A. Kumar, J. Coventry, and W. Lipinski, 2020, Radiative transfer analysis for solar particle receiver applications, The Australian National University, Australian Solar Thermal Research Institute,
Receiver	Yue, L., R. Shaeffer, B. Mills, and C.K. Ho, 2019, *Active Airflow for Reducing Advective and Particle Loss in Falling Particle Receivers*, in *SolarPACES 2019*, Daegu, South Korea, October 1 - 4 2019.
Receiver	Yue, L., B. Mills, and C.K. Ho, 2019, *Effect of Quartz Aperture Covers on the Fluid Dynamics and Thermal Efficiency of Falling Particle Receivers*, in *Proceedings of the ASME 2019 13th International Conference on Energy Sustainability*, ES2019-3910, Bellevue, WA, July 15 - 18, 2019.

Component	Publication
Receiver	Yellowhair, J. and C.K. Ho, 2019, *Optical Ray-Tracing Performance Modeling Of Quartz Half-Shell Tubes Aperture Cover For Falling Particle Receiver*, in *Proceedings of the ASME 2019 13th International Conference on Energy Sustainability*, ES2019-3927, Bellevue, WA, July 15 - 18, 2019.
Receiver	Mills, B., R. Shaeffer, C.K. Ho, and L. Yue, 2019, *Modeling the Thermal Performance of Falling Particle Receivers Subject to External Wind*, in *Proceedings of the ASME 2019 13th International Conference on Energy Sustainability*, ES2019-3913, Bellevue, WA, July 15 - 18, 2019.
Receiver	Mills, B., B. Schroeder, L. Yue, R. Shaeffer, and C.K. Ho, 2019, *Optimizing a Falling Particle Receiver Geometry Using CFD Simulations to Maximize the Thermal Efficiency*, in *SolarPACES 2019*, Daegu, South Korea, October 1 - 4, 2019.
Receiver	Kim, J.S., A. Kumar, W. Gardner, and W. Lipinski, 2019, Numerical and Experimental Investigation of a Novel Multi-Stage Falling Particle Receiver, *Solarpaces 2018: International Conference on Concentrating Solar Power and Chemical Energy Systems*, **2126**.
Receiver	Ho, C.K., G. Peacock, J.M. Christian, K. Albrecht, J.E. Yellowhair, and D. Ray, 2019, On-Sun Testing of a 1 MWt Particle Receiver with Automated Particle Mass-Flow and Temperature Control, *Solarpaces 2018: International Conference on Concentrating Solar Power and Chemical Energy Systems*, **2126**.
Receiver	Ho, C.K. and C.A. Pattyn, 2019, *Investigating Environmental Impacts of Particle Emissions from a High-Temperature Falling Particle Receiver*, in *SolarPACES 2019*, Daegu, South Korea,
Receiver	Ho, C.K., S. Kinahan, J.D. Ortega, P. Vorobieff, A. Mammoli, and V. Martins, 2019, *Characterization of Particle and Heat Losses from Falling Particle Receivers*, in *Proceedings of the ASME 2019 13th International Conference on Energy Sustainability*, ES2019-3826, Bellevue, WA, July 15 - 18, 2019.
Receiver	Ho, C.K., J.M. Christian, J.E. Yellowhair, K. Armijo, W.J. Kolb, S. Jeter, M. Golob, and C. Nguyen, 2019, On-Sun Performance Evaluation of Alternative High-Temperature Falling Particle Receiver Designs, *Journal of Solar Energy Engineering-Transactions of the Asme*, **141**(1).
Storage	Sment, J.N., M. Lambert, K.J. Albrecht, C.K. Ho, and M. Davidson, Year, *Application Methods for Refractory Insulation in Hot Particle Storage Bins*, in *ASME 2021 15th International Conference on Energy Sustainability collocated with the ASME 2021 Heat Transfer Summer Conference*, Virtual Conference.

Component	Publication
Storage	Sment, J.N., M.J. Martinez, K.J. Albrecht, and C.K. Ho, 2020, *Testing and Simulations of Spatial and Temporal Temperature Variations in a Particle-Based Thermal Energy Storage Bin*, in *ASME 2020 14th International Conference on Energy Sustainability*, Denver, CO, June 7 - 11, 2020.
Storage	Sment, J., K. Albrecht, M.J. Martinez, and C.K. Ho, 2019, *Design Considerations for a High-Temperature Particle Storage Bin*, in *SolarPACES 2019*, Daegu, South Korea, October 1 - 4, 2019.
Storage	Sment, J., K. Albrecht, J. Christian, and C.K.Ho, 2019, *Optimization of Storage Bin Geometry for High Temperature Particle-Based CSP Systems*, in *Proceedings of the ASME 2019 13th International Conference on Energy Sustainability*, ES2019-3903, Bellevue, WA, July 15 - 18, 2019.
Storage	El-Leathy, A., S. Jeter, H. Al-Ansary, S.N. Danish, R. Saeed, S. Abdel-Khalik, M. Golob, E. Djajadiwinata, and Z. Al-Suhaibani, 2019, Thermal performance evaluation of lining materials used in thermal energy storage for a falling particle receiver based CSP system, *Solar Energy*, **178**, p. 268-277.
Storage	El-Leathy, A., S. Jeter, H. Al-Ansary, S. Abdel-Khalik, J. Roop, M. Golob, S. Danish, A. Alrished, E. Djajadiwinata, and Z. Al-Suhaibani, 2019, Thermal Performance Evaluation of Two Thermal Energy Storage Tank Design Concepts for Use with a Solid Particle Receiver-Based Solar Power Tower (vol 7, pg 8201, 2014), *Energies*, **12**(13).
Heat Exchanger	Albrecht, K.J., H.F. Laubscher, M.D. Carlson, and C.K. Ho, Year, *Development and Testing of a 20 kW Moving Packed-Bed Particle-To-sCO2 Heat Exchanger and Test Facility*, in *ASME 2021 15th International Conference on Energy Sustainability collocated with the ASME 2021 Heat Transfer Summer Conference*,
Heat Exchanger	Laubscher, H.F., K.J. Albrecht, and C.K. Ho, 2020, *High-Temperature Particle Flow Testing in Parallel Plates For Particle-To-Supercritical Co2 Heat Exchanger Applications*, in *ASME 2020 14th International Conference on Energy Sustainability*, Denver, CO, June 7 - 11, 2020.
Heat Exchanger	Albrecht, K., M.D. Carlson, H.F. Laubscher, R. Crandell, N. DeLovato, and C.K. Ho, 2019, *Testing and Model Validation of a Prototype Moving Packed-Bed Particle-to-sCO2 Heat Exchanger*, in *SolarPACES 2019*, Daegu, South Korea, October 1 - 4, 2019.
Heat Exchanger	DeLovato, N.A., K.J. Albrecht, and C.K. Ho, 2020, Finite Element Analysis of a Moving Packed-Bed Particle-to-sCO2 Heat Exchanger Testing and Performance, in Proceedings of the ASME 2020 14th International Conference on Energy Sustainability, June 17 - 18, 2020.
Heat Exchanger	Carlson, M.D., K.J. Albrecht, C.K. Ho, H.F. Laubscher, and F. Alvarez, 2020, High-Temperature Particle Heat Exchanger for sCO2

Component	Publication
	Power Cycles, SAND2020-14357, Sandia National Laboratories, Albuquerque, NM.
Heat Exchanger	Ho, C.K., M. Carlson, K.J. Albrecht, Z. Ma, S. Jeter, and C.M. Nguyen, 2019, Evaluation of Alternative Designs for a High Temperature Particle-to-sCO2 Heat Exchanger, J. Solar Energy Engineering, 141(2), p. 021001-1 - 021001-8.
Heat Exchanger	Albrecht, K. and C.K. Ho, 2019, Design and operating considerations for a shell-and-plate, moving packed-bed, particle-to-sCO2 heat exchanger, Solar Energy, 178, p. 331-340.
Lift and Conveyance	Jeter, K.R.a.S., 2020, *Transient Thermal Modeling for the Optimization of an Elevated Temperature Particle Lift Hoist System in a Solid Particle Concentrated Solar Power Plant*, in *SolarPACES 2020*, Virtual Conference, Sep. 28 - Oct. 2, 2020.
Lift and Conveyance	Cleal, M. and C.K. Ho, 2020, *Modeling thermal transients of bulk particle lifting systems with CFD simulations*, in *SolarPACES 2020*, Virtual Conference, September 28 - October 2, 2020.
Lift and Conveyance	Christian, J., J. Sment, C.K.Ho, L. Haden, and K. Albrecht, 2019, *Particle Lift Challenges and Solutions For Solid Particle Receiver Systems*, in *Proceedings of the ASME 2019 13th International Conference on Energy Sustainability*, ES2019-3833, Bellevue, WA, July 15 - 18, 2019.
Particles	Schroeder, N. and K. Albrecht, Year, *Assessment of Particle Candidates for Falling Particle Receiver Applications Through Irradiance and Thermal Cycling*, in *ASME 2021 15th International Conference on Energy Sustainability collocated with the ASME 2021 Heat Transfer Summer Conference*, Virtual Conference.
Particles	Yue, L., K. Albrecht, and C.K. Ho, 2020, Particles for solar thermal energy applications: An overview of selected properties and their influence on system performance, *Renewable and Sustainability Energy Reviews*, (in preparation).
Particles	Saeed, R.S., A. Alswaiyd, H. Al-Ansary, A. El-Leathy, S. Jeter, S. Alaqel, N.S. Saleh, E. Djajadiwinata, Z. Al-Suhaibani, S. Danish, and Z. Almutairi, 2020, *Effect of the Cyclic Heating (Aging) on the Solar Absorptance and Specific Heat of Particulate Materials*, in *SolarPACES 2020*, Virtual Conference, September 28 - October 2, 2020.
System and Technoeconomics	González-Portillo, L.F., K. Albrecht, and C.K. Ho, 2021, Techno-Economic Optimization of CSP Plants with Free-Falling Particle Receivers, *Entropy*, **23**(76).
System and Technoeconomics	Lau, T., M. Arjomandi, X. Bi, P. Guo, S. Han, G. Nathan, W. Saw, N. Sedaghatizadeh, and E. Sureshkumar, 2020, University of Adelaide Gen 3 Particle Pilot Plant (G3P3) Final Report, CET-G3P3-RPT-2020-001, University of Adelaide, Australia.

Component	Publication
System and Technoeconomics	González-Portillo, L.F., K. Albrecht, and C.K. Ho, 2020, *Improvements in the Techno-Economic Analysis of Particle CSP Systems*, in *SolarPACES 2020*, Virtual Conference, Sep. 28 - Oct. 2, 2020.
System and Technoeconomics	Albrecht, K.J., L. Yue, B. Mills, J.N. Sment, H.F. Laubscher, J.M. Christian, M.D. Carlson, and C.K. Ho, 2020, *Design Features and System Integration of a Next-Generation Concentrating Solar Power Particle Pilot Plant*, in *Proceedings of the ASME 2020 14th International Conference on Energy Sustainability*, ES2020-8596, Denver, CO, June 8 - 10, 2020.
System and Technoeconomics	H. Al-Ansary, e.a., 2021, Generation 3 Particle Pilot Plant Project - G3P3-KSA Final Report, King Saud University, Riyadh, Saudi Arabia. https://energy.sandia.gov/programs/renewable-energy/csp/current-research-projects/gen-3-particle-pilot-plant-g3p3/.
System and Technoeconomics	Lau, T., M. Armomandi, X. Bi, P. Guo, S. Han, G. Nathan, W. Saw, N. Sedaghatizadeh, and E. Sureshkumar, 2020, University of Adelaide Gen 3 Particle Pilot Plant (G3P3) Final Report, University of Adelaide, CET-G3P3-RPT-2020-001, Adelaide, Australia. https://energy.sandia.gov/programs/renewable-energy/csp/current-research-projects/gen-3-particle-pilot-plant-g3p3/.
System and Technoeconomics	Kim, J.-S., W. Gardner, D. Potter, S. Kuruneru, Y.-C.S. Too, A. Dawson, M. Are, R. Stiff, and S. Morgan, 2020, Final Report for SNL PO 2003034 and CISRO Cost Share Contribution to SNL G3P3 Project, CSIRO, Newcastle, Australia.
System and Technoeconomics	Gan, P.G., Y. Wang, and J. Pye, 2020, System modelling and optimisation of a particle-based CSP system, Australian National University, Canberra, Australia. https://energy.sandia.gov/programs/renewable-energy/csp/current-research-projects/gen-3-particle-pilot-plant-g3p3/.
System and Technoeconomics	Bataille, F., G. Flamant, B. Grange, R. Gueguen, and A. Le Gal, 2020, Contribution of CNRS to the G3P3 Project, CNRS-PROMES, Perpignan, France. https://energy.sandia.gov/programs/renewable-energy/csp/current-research-projects/gen-3-particle-pilot-plant-g3p3/.
System and Technoeconomics	Ho, C.K., K.J. Albrecht, L. Yue, B. Mils, J. Sment, J. Christian, and M. Carlson, 2019, *Overview and Design Basis for the Gen 3 Particle Pilot Plant (G3P3)*, in *SolarPACES 2019*, Daegu, South Korea,
System and Technoeconomics	Albrecht, K.J., M.L. Bauer, and C.K. Ho, 2019, *Parametric Analysis of Particle CSP System Performance and Cost to Intrinsic Particle Properties and Operating Conditions*, in *Proceedings of the ASME 2019 13th International Conference on Energy Sustainability*, ES2019-3893, Bellevue, WA, July 15 - 18, 2019.

REFERENCES

1. C. K. Ho, *A Review of High-Temperature Particle Receivers for Concentrating Solar Power*, Appl Therm Eng **109** (Part B), 958-969 (2016).
2. C. K. Ho, J. M. Christian, J. Yellowhair, K. Armijo and S. Jeter, *Performance Evaluation of a High-Temperature Falling Particle Receiver*, in *ASME Power & Energy Conference*, Charlotte, NC, June 26-30, 2016.
3. C. K. Ho, J. M. Christian, J. Yellowhair, S. Jeter, M. Golob, C. Nguyen, K. Repole, S. I. Abdel-Khalik, N. Siegel, H. Al-Ansary, A. El-Leathy and B. Gobereit, *Highlights of the High-Temperature Falling Particle Receiver Project: 2012 - 2016*, in *SolarPaces 2016: International Conference on Concentrating Solar Power and Chemical Energy Systems*, Abu Dhabi, UAE, October 11 - 14, 2016.
4. H. Al-Ansary, A. El-Leathy, S. Jeter, E. Djajadiwinata, S. Alaqel, M. Golob, C. Nguyen, R. Saad, T. Shafiq, S. Danish, S. Abdel-Khalik, Z. Al-Suhaibani, N. Abu-Shikhah, M. I. Haq, A. Al-Balawi and F. Al-Harthi, *On-Sun Experiments on a Particle Heating Receiver with Red Sand as the Working Medium*, International Conference on Concentrating Solar Power and Chemical Energy Systems (Solarpaces 2017) **2033** (2018).
5. C. K. Ho, J. M. Christian, J. Yellowhair, N. Siegel, S. Jeter, M. Golob, S. I. Abdel-Khalik, C. Nguyen and H. Al-Ansary, *On Sun Testing of an Advanced Falling Particle Receiver System*, in *SolarPACES 2015*, Cape Town, South Africa, October 13 - 16, 2015.
6. W. Wu, L. Amsbeck, R. Buck, R. Uhlig and R. Ritz-Paal, *Proof of concept test of a centrifugal particle receiver*, Proceedings of the Solarpaces 2013 International Conference **49**, 560-568 (2014).
7. W. Wu, R. Uhlig, R. Buck and R. Pitz-Paal, *Numerical Simulation of a Centrifugal Particle Receiver for High-Temperature Concentrating Solar Applications*, Numer Heat Tr a-Appl **68** (2), 133-149 (2015).
8. G. Flamant, D. Gauthier, H. Benoit, J. L. Sans, B. Boissiere, R. Ansart and M. Hemati, *A new heat transfer fluid for concentrating solar systems: Particle flow in tubes*, Proceedings of the Solarpaces 2013 International Conference **49**, 617-626 (2014).
9. G. Flamant, D. Hernandez, C. Bonet and J. P. Traverse, *Experimental Aspects of the Thermochemical Conversion of Solar-Energy - Decarbonation of Caco3*, Sol Energy **24** (4), 385-395 (1980).
10. Z. W. Ma, G. Glatzmaier and M. Mehos, *Fluidized Bed Technology for Concentrating Solar Power With Thermal Energy Storage*, J Sol Energ-T Asme **136** (3) (2014).
11. C. Ho, J. Christian, D. Gill, A. Moya, S. Jeter, S. Abdel-Khalik, D. Sadowski, N. Siegel, H. Al-Ansary, L. Amsbeck, B. Gobereit and R. Buck, *Technology advancements for next generation falling particle receivers*, Proceedings of the Solarpaces 2013 International Conference **49** (Energy Procedia), 398-407 (2014).
12. M. Röger, L. Amsbeck, B. Gobereit and R. Buck, *Face-Down Solid Particle Receiver Using Recirculation*, Journal of Solar Energy Engineering (2011).
13. B. Mills and C. K. Ho, *Annualized Thermal Performance of Intermediate-Scale Falling Particle Receivers*, in *SolarPACES 2017*, Santiago, Chile, September 19 - 22, 2017.
14. M. D. Carlson and C. K. Ho, *A Particle/Sco2 Heat Exchanger Testbed and Reference Cycle Cost Analysis*, Proceedings of the Asme 10th International Conference on Energy Sustainability, 2016, Vol 1 (2016).
15. K. D. Repole and S. M. Jeter, *Design and Analysis of a High Temperature Particulate Hoist for Proposed Particle Heating Concentrator Solar Power Systems*, in *ASME 2016 10th International Conference on Energy Sustainability, ES2016-59619*, Charlotte, NC, June 26 - 30, 2016.

16. B. Mills and C. K. Ho, *Simulation and Performance Evaluation of On-sun Particle Receiver Tests*, in *SolarPACES 2018*, Cassablanca, Morocco,
17. L. Yue, B. Mills and C. K. Ho, *Effect of Quartz Aperture Covers on the Fluid Dynamics and Thermal Efficiency of Falling Particle Receivers*, in *Proceedings of the ASME 2019 13th International Conference on Energy Sustainability*, ES2019-3910, Bellevue, WA, July 15 - 18, 2019.
18. L. Yue, R. Schaeffer, B. Mills and C. K. Ho, *Active Airflow for Reducing Advective and Particle Loss in Falling Particle Receivers*, in *SolarPACES 2019*, Daegu, South Korea, October 1 - 4, 2019.
19. B. Mills, B. Schroeder, L. Yue, R. Shaeffer and C. K. Ho, *Optimizing a Falling Particle Receiver Geometry Using CFD Simulations to Maximize the Thermal Efficiency*, in *SolarPACES 2019*, Daegu, South Korea, October 1 - 4, 2019.
20. L. Yue, N. Schroeder and C. K. Ho, *Particle Flow Testing of a Multistage Falling Particle Receiver Concept: Staggered Angle Iron Receiver (StAIR)*, in *ASME 2020 14th International Conference on Energy Sustainability*, Virtual Online, June 17 - 18, 2020.
21. R. Shaeffer, B. Mills, L. Yue and C. K. Ho, *Evaluation of Performance Factors for a Multistage Falling Particle Receiver*, in *ASME 2020 14th International Conference on Energy Sustainability*, Virtual Online Conference, June 17 - 18, 2020.
22. B. Mills, R. Shaeffer, L. Yue and C. K. Ho, *Improving Next-generation Falling Particle Receiver Designs Subject to Anticipated Operating Conditions*, in *ASME 2020 14th International Conference on Energy Sustainability*, Denver, CO, June 7 - 11, 2020.
23. C. K. Ho, S. Kinahan, J. D. Ortega, P. Vorobieff, A. Mammoli and V. Martins, *Characterization of Particle and Heat Losses from Falling Particle Receivers*, in *Proceedings of the ASME 2019 13th International Conference on Energy Sustainability*, ES2019-3826, Bellevue, WA, July 15 - 18, 2019.
24. C. K. Ho and C. A. Pattyn, *Investigating Environmental Impacts of Particle Emissions from a High-Temperature Falling Particle Receiver*, in *SolarPACES 2019*, Daegu, South Korea,
25. B. Mills and C. K. Ho, *Numerical Evaluation of Novel Particle Release Patterns in High-temperature Falling Particle Receivers*, in *ASME Power & Energy Conference*, Charlotte, NC, June 26-30, 2017.
26. B. Mills, C. K. Ho, J. M. Christian and G. Peacock, *Novel Particle Release Patterns for Increased Receiver Thermal Efficiency*, in *SolarPACES 2016*, Abu Dhabi, UAE,
27. C. K. Ho, J. M. Christian, D. Romano, J. Yellowhair, N. Siegel, L. Savoldi and R. Zanino, *Characterization of Particle Flow in a Free-Falling Solar Particle Receiver*, J Sol Energ-T Asme **139** (2) (2017).
28. C. K. Ho, J. M. Christian, J. Yellowhair, N. Siegel, S. Jeter, M. Golob, S. I. Abdel-Khalik, C. Nguyen and H. Al-Ansary, *On-Sun Testing of an Advanced Falling Particle Receiver System*, Solarpaces 2015: International Conference on Concentrating Solar Power and Chemical Energy Systems **1734** (2016).
29. C. K. Ho, G. Peacock, J. M. Christian, K. Albrecht, J. E. Yellowhair and D. Ray, *On-Sun Testing of a 1 MWt Particle Receiver with Automated Particle Mass-Flow and Temperature Control*, in *SolarPACES 2018*, Casablanca, Morocco, October 2 - 5, 2018.
30. C. K. Ho, G. Peacock, B. Mills, J. M. Christian, K. Albrecht, J. E. Yellowhair and D. Ray, *Particle Mass Flow Control for High-Temperature Concentrating Solar Receivers*, 2018.
31. A. El-Leathy, H. Al-Ansary, S. Jeter, E. Djajadiwinata, S. Alaqel, M. Golob, C. Nguyen, R. Saad, T. Shafiq, S. Danish, S. Abdel-Khalik, Z. Al-Suhaibani, N. Abu-Shikhah, M. I. Haq, A. Al-Balawi and F. Al-Harthi, *Preliminary Tests of an Integrated Gas Turbine-Solar Particle Heating and Energy Storage System*, International Conference on Concentrating Solar Power and Chemical Energy Systems (Solarpaces 2017) **2033** (2018).
32. e. a. H. Al-Ansary, *Generation 3 Particle Pilot Plant Project - G3P3-KSA Final Report*, 2021.

33. J.-S. Kim et al., *Design and test of multi-stage truncated-cone falling particle receiver (MsTC-FPR)*, in *SolarPACES 2020*, Virtual, Sep. 28 - Oct. 2, 2020.
34. A. Kumar, W. Lipinski and J. S. Kim, *Numerical modelling of radiation absorption in a novel multi-stage free-falling particle receiver*, Int J Heat Mass Tran **146** (2020).
35. J.-S. Kim, W. Gardner, D. Potter, S. Kuruneru, Y.-C. S. Too, A. Dawson, M. Are, R. Stiff and S. Morgan, *Final Report for SNL PO 2003034 and CISRO Cost Share Contribution to SNL G3P3 Project*, 2020.
36. T. Lau, M. Armomandi, X. Bi, P. Guo, S. Han, G. Nathan, W. Saw, N. Sedaghatizadeh and E. Sureshkumar, *University of Adelaide Gen 3 Particle Pilot Plant (G3P3) Final Report*, Report No. CET-G3P3-RPT-2020-001, 2020.
37. J. Chen, A. Kumar, J. Coventry and W. Lipinski, *Radiative transfer analysis for solar particle receiver applications*, 2020.
38. P. G. Gan, Y. Wang and J. Pye, *System modelling and optimisation of a particle-based CSP system*, 2020.
39. M. Ebert, L. Amsbeck, J. Rheinlander, B. Schlogl-Knothe, S. Schmitz, M. Sibum, R. Uhlig and R. Buck, *Operational Experience of a Centrifugal Particle Receiver Prototype*, in *SolarPACES 2018*, Casablanca, Morocco, October 2 - 5, 2018.
40. F. Bataille, G. Flamant, B. Grange, R. Gueguen and A. Le Gal, *Assessment of the Fluidized Particle-in-Tube Technology*, 2020.
41. A. Le Gal, B. Grange, M. Tessonneaud, A. Perez, C. Escape, J. L. Sans and G. Flamant, *Thermal analysis of fluidized particle flows in a finned tube solar receiver*, Sol Energy **191**, 19-33 (2019).
42. F. Bataille, G. Flamant, B. Grange, R. Gueguen and A. Le Gal, *Contribution of CNRS to the G3P3 Project*, 2020.
43. I. Allied Mineral Products, edited by I. Allied Mineral Products (2018), Vol. TUFC47.
44. , edited by K. Inc. (Kernius Inc.).
45. K. Plewe, Jeremy N. Sment, Mario J. Martinez, Clifford K. Ho, Dongmei Chen, *Transient Thermal Performance of High-Temperature Particle Storage Bins* in *SolarPACES 2020*, Online,
46. K. J. A. Jeremy N. Sment, Mario J. Martinez, Clifford K. Ho, *Design Considerations for a High-Temperature Particle Storage Bin*, presented at the SolarPACES, Degu, South Korea, 2020 (unpublished).
47. D. A. Craig, *Flow Properties Test Results for CARBOBEAD-HSP 40/70*, 2019.
48. M. M. D. Lambert, *Review of Gen 3 Particle Pilot Plant (G3P3) Project* 2021.
49. M. Lambert, *Measuremetn of Thermal Expansion and Thermally Cycled Mechanical Properties of Refractory Ceramic Insulation*, 2019.
50. J. Sment, (2019).
51. J. K. J. A. M. L. C. K. H. Sment, *Application methods for refractory insulation in hot-particle Storage bins*, in *ASME ES2021*, Virtual, Online,
52. T. H. Greg Palmer, *Heat Transfer Design Considerations for Refractory Linings with Steel Anchors, Part 2*, Refractories Worldforum **2** (94), 97-101 (2010).
53. T. H. Jeremy N. Sment, Murphy Davidson, Kevin J. Albrecht, Clifford K. Ho, Matthew Lambert, Bradley Bateman, *Design Considerations for Commercial Scale Particle-Based Thermal Energy Storage Systems*, in *SolarPACES 2020*, Online,
54. I. C. Council, in *IBC2018* (2018).
55. ACI_Committee_313, in *ACI 313-16*, edited by A. C. Institute (2016).
56. G. A. H. Craig S. Turchi, *Molten Salt Power Tower Cost Model for the System Advisor Model*, 2013.
57. S. G. Gerhard Weinrebe, Reiner Buck, Ansgar Macke, Anne Burghartz, Daniel Nieffer, Fabian Gross, Amadeus Rong, Tim Schlichting, Kristina Blume, *Kostensenkung bei Solarturmkraftwerken durch optimeierte Heliostatkonturen plus angepasstes Turm-und Felddesign*, 2019.

58. S. Powers, *Gen 3 CSP Topic 1 - Phase 3 Test Facility Down-Selection Criteria*, 2019.
59. P. E. Timothy A. Harvey, *100 MW Storage Options Report*, Report, October 13, 2019.
60. NREL, edited by SolarPACES (2020).
61. G. m. Yu Y., Xu G. . *Seismic Zonation*. Encyclopedia of Earth Sciences 2011 [cited 2020 October 25, 2020]; Available from: https://link.springer.com/referenceworkentry/10.1007%2F978-90-481-8702-7_184.
62. A. E. H. Taj-Eddine Cherkaoui, *Seismicity and Seismic Hazard in Morocco 1901-2010*, Bulletin de l'Institut Scientifique **Sciences de la Terre** (34), 45-55 (2012).
63. U. S. G. Survey. *Unified Hazard Tool*. Earthquake Hazards Program; Available from: https://earthquake.usgs.gov/hazards/interactive/.
64. K. Albrecht, M. D. Carlson, H. F. Laubscher, R. Crandell, N. DeLovato and C. K. Ho, *Testing and Model Validation of a Prototype Moving Packed-Bed Particle-to-sCO2 Heat Exchanger*, in *SolarPACES 2019*, Daegu, South Korea, October 1 - 4, 2019.
65. K. Albrecht and C. K. Ho, *Design and operating considerations for a shell-and-plate, moving packed-bed, particle-to-sCO2 heat exchanger*, Sol Energy **178**, 331-340 (2019).
66. K. J. Albrecht and C. K. Ho, *Heat Transfer Models of Moving Packed-Bed Particle-to-sCO(2) Heat Exchangers*, J Sol Energ-T Asme **141** (3) (2019).
67. M. D. Carlson, K. J. Albrecht, C. K. Ho, H. F. Laubscher and F. Alvarez, *High-Temperature Particle Heat Exchanger for sCO2 Power Cycles*, 2020.
68. C. K. Ho, M. Carlson, K. J. Albrecht, Z. Ma, S. Jeter and C. M. Nguyen, *Evaluation of Alternative Designs for a High Temperature Particle-to-sCO2 Heat Exchanger*, J. Solar Energy Engineering **141** (2), 021001-021001 - 021001-021008 (2019).
69. H. F. Laubscher, K. J. Albrecht and C. K. Ho, *High-Temperature Particle Flow Testing in Parallel Plates For Particle-To-Supercritical Co2 Heat Exchanger Applications*, in *ASME 2020 14th International Conference on Energy Sustainability*, Denver, CO, June 7 - 11, 2020.
70. K. J. Albrecht, H. F. Laubscher and C. K. Ho, *Development and Testing of a 20 Kwth Moving Packed-Bed Particle-to-Sco2 Heat Exchanger and Test Facility*, in *Proceedings of the ASME 2021 15th International Conference on Energy Sustainability*, Virtual Conference, June 16 - 18, 2021.
71. J. Christian, J. Sment, C.K.Ho, L. Haden and K. Albrecht, *Particle Lift Challenges and Solutions For Solid Particle Receiver Systems*, in *Proceedings of the ASME 2019 13th International Conference on Energy Sustainability*, ES2019-3833, Bellevue, WA, July 15 - 18, 2019.
72. T. Lau, M. Arjomandi, X. Bi, P. Guo, S. Han, G. Nathan, W. Saw, N. Sedaghatizadeh and E. Sureshkumar, *University of Adelaide Gen 3 Particle Pilot Plant (G3P3) Final Report*, 2020.
73. M. Cleal and C. K. Ho, *Modeling thermal transients of bulk particle lifting systems with CFD simulations*, in *SolarPACES 2020*, Virtual Conference, September 28 - October 2, 2020.
74. K. R. a. S. Jeter, *Transient Thermal Modeling for the Optimization of an Elevated Temperature Particle Lift Hoist System in a Solid Particle Concentrated Solar Power Plant*, in *SolarPACES 2020*, Virtual Conference, Sep. 28 - Oct. 2, 2020.
75. K. K. Repole, *The Development and Application of Design and Optimization Methods for Energy Intensive Mechanical Systems for Challenging Environments as Applied to a Concentrated Solar Power Particle Lift System*, Ph.D., Georgia Institute of Technology, 2019.
76. N. P. Siegel, M. D. Gross and R. Coury, *The Development of Direct Absorption and Storage Media for Falling Particle Solar Central Receivers*, ASME J. Solar Energy Eng. **137** (4), 041003-041003-041007 (2015).
77. R. S. Saeed, A. Alswaiyd, H. Al-Ansary, A. El-Leathy, S. Jeter, S. Alaqel, N. S. Saleh, E. Djajadiwinata, Z. Al-Suhaibani, S. Danish and Z. Almutairi, *Effect of the Cyclic Heating (Aging) on the Solar Absorptance and Specific Heat of Particulate Materials*, in *SolarPACES 2020*, Virtual Conference, September 28 - October 2, 2020.

78. J. N. Sment and C. K. Ho, *G3P3 Phase 3 Project Execution Plan Issue 1*, Report No. SAND2021-0151, 2021.
79. K. Albrecht, M. L. Bauer and C.K.Ho, *Parametric Analysis of Particle CSP System Performance and Cost to Intrinsic Particle Properties and Operating Conditions*, in *Proceedings of the ASME 2019 13th International Conference on Energy Sustainability*, ES2019-3893, Bellevue, WA, July 15 - 18, 2019.
80. L. F. González-Portillo, K. Albrecht and C. K. Ho, *Improvements in the Techno-Economic Analysis of Particle CSP Systems*, in *SolarPACES 2020*, Virtual Conference, Sep. 28 - Oct. 2, 2020.
81. L. F. González-Portillo, K. Albrecht and C. K. Ho, *Techno-Economic Optimization of CSP Plants with Free-Falling Particle Receivers*, Entropy-Switz **23** (76) (2021).
82. J. Dyreby, S. Klein, G. Nellis and D. Reindl, *Design Considerations for Supercritical Carbon Dioxide Brayton Cycles With Recompression*, J Eng Gas Turb Power **136** (10) (2014).
83. D. J. Gavic, *Investigation of Water, Air, and Hybrid Cooling for Supercritical Carbon Dioxide Brayton Cycles*, University of Wisconsin - Madison, 2012.
84. M. J. Wagner and T. Wendelin, *SolarPILOT: A power tower solar field layout and characterization tool*, Sol Energy **171**, 185-196 (2018).
85. L. F. González-Portillo, R. Abbas, K. Albrecht and C. Ho, *Analysis of optical properties in particle curtains*, Sol Energy **213**, 211 - 224 (2021).
86. Hany Al-Ansary et al., *On-Sun Experiments on a Particle Heating Receiver with Red Sand as the Working Medium*, in *SolarPACES 2017*, Santiago, Chile, September 26 - 29, 2017.
87. N. P. Siegel, C. K. Ho, S. S. Khalsa and G. J. Kolb, *Development and Evaluation of a Prototype Solid Particle Receiver: On-Sun Testing and Model Validation*, J Sol Energ-T Asme **132** (2) (2010).
88. C. K. Ho, J. M. Christian, A. C. Moya, J. Taylor, D. Ray and J. Kelton, *Experimental and Numerical Studies of Air Curtains for Falling Particle Receivers*, in *Proceedings of ASME 2014 8th International Conference on Energy Sustainability*, ES-FuelCell2014-6632, Minneapolis, MN, June 29 - July 2, 2014.
89. T. D. Tan and Y. T. Chen, *Protection of an Aerowindow, One Scheme to Enhance the Cavity Efficiency of a Solid Particle Solar Receiver*, in *HT2009: Proceedings of the Asme Summer Heat Transfer Conference 2009, Vol 2*, San Francisco, CA,
90. W. Wu, D. Trebing, L. Amsbeck, R. Buck and R. Pitz-Paal, *Prototype Testing of a Centrifugal Particle Receiver for High-Temperature Concentrating Solar Applications*, J Sol Energ-T Asme **137** (4) (2015).
91. W. Wu, L. Amsbeck, R. Buck, N. Waibel, P. Langner and R. Pitz-Paal, *On the influence of rotation on thermal convection in a rotating cavity for solar receiver applications*, Appl Therm Eng **70** (1), 694-704 (2014).
92. M. Ebert, L. Amsbeck, A. Jensch, J. Hertel, J. Rheinlander, D. Trebing, R. Uhlig and R. Buck, *Upscaling, Manufacturing and Test of a Centrifugal Particle Receiver*, Proceedings of the Asme 10th International Conference on Energy Sustainability, 2016, Vol 1 (2016).
93. H. Benoit, I. P. Lopez, D. Gauthier, J. L. Sans and G. Flamant, *On-sun demonstration of a 750 degrees C heat transfer fluid for concentrating solar systems: Dense particle suspension in tube*, Sol Energy **118**, 622-633 (2015).
94. G. Flamant, D. Gauthier, H. Benoit, J. L. Sans, R. Garcia, B. Boissiere, R. Ansart and M. Hemati, *Dense suspension of solid particles as a new heat transfer fluid for concentrated solar thermal plants: On-sun proof of concept*, Chem Eng Sci **102**, 567-576 (2013).
95. A. El-Leathy, H. Al-Ansary, S. Jeter, E. Djajadiwinata, S. Alqel, M. Golob, C. Nguyen, R. Saad, T. Shafiq, S. Danish, S. Abdel-Khalik, Z. Al-Suhaibani, N. Abu-Shikhah, A. Al-Balawi, M. Haq and F. Al-harthi, *Preliminary Tests of an Integrated Gas Turbine-Solar Particle Heating and energy Storage System*, in *SolarPACES 2017*, Santiago, Chile,

96. T. L. Saaty, *The analytic hierarchy process : planning, priority setting, resource allocation*. (McGraw-Hill International Book Co., New York ; London, 1980).

APPENDICES

APPENDIX A. G3P3 DOWN-SELECT CONTINUATION APPLICATION TITLE PAGE

Project Title:	Gen 3 Particle Pilot Plant (G3P3): Integrated High-Temperature Particle System for CSP
Project Period:	10/01/18 – 9/30/20
Budget Period:	Phase 1: 10/01/18 – 03/31/20 Phase 2: 04/01/20 – 12/31/20
Reporting Period:	10/01/18 – 12/31/20
Submission Date:	01/08/21
Recipient:	Sandia National Laboratories
Address:	P.O. Box 5800, MS-1127 Albuquerque, NM 87185-1127
Website:	www.sandia.gov/csp
Award Number:	DE-FOA-0001697-1503, CPS 34211
Project Team:	Georgia Institute of Technology, King Saud University, CSIRO, Australian National University, U. Adelaide, PROMES-CNRS, DLR, EPRI, Bridgers & Paxton, Solar Dynamics, SolarReserve, Carbo Ceramics, Solex Thermal Science, Vacuum Process Engineering, Allied Mineral Products, Matrix PDM, Saudi Electricity Company
Principal Investigator:	Clifford K. Ho, Sr. Scientist Phone: (505) 844-2384 Email: ckho@sandia.gov
Business Contact:	Andrew Kassir Phone: (505) 844-7534 Email: akassir@sandia.gov
HQ Tech Manager:	Matthew Bauer
HQ Project Officer:	Christine Bing

APPENDIX B. SUMMARY OF MILESTONES

Milestone Number	Milestone Title	Description	Metric	Success Value	Assessment Tool	Results (Pass/Fail)	Location in Report
Program Management							
1.1	Facility inspections	Ensure facility-related O&M and inspections are up to date and performed at regular intervals	Number of identified environmental, safety, and health (ES&H) violations associated with the G3P3 project	0	The CSP department performs frequent self-assessments led by our ES&H coordinator. We also get audited periodically by Sandia and DOE inspectors.	Pass	Section 3.2.4.3
1.2	Permitting	Obtain required permits to construct and operate G3P3 at Kirtland Air Force Base	Identify and obtain necessary permitting approvals via KAFB and Sandia Facilities	Permits approved	Follow Sandia and KAFB approved processes for new facility construction	Pass (with initial design); modifications requested after Phase 3 award triggered amended NEPA	Section 3.2.4.3
1.3	Procurement	Place POs for 13 subcontracts (partners) to perform work in Phases 1 and 2	Number of POs executed	13	Sandia will follow Sandia's standard procurement process, which includes all terms and conditions for the partners (IP, deliverables, timeline)	Pass	Section 3.2.4.3
Receiver							
2.1	Wind simulations	Develop simulations of receiver performance with impacts of external wind, considering both wind speed and direction	R2 and slope of parity plot of simulated vs. experimental particle temperature rise and receiver efficiencies	R2_wind/R2_no-wind > 1; |1 - Slope (with wind)|<|1 - Slope (no wind)| 0.8 < slope < 1.2; R2 > 0.8	Comparison of parity plots of simulated vs. experimental particle temperature rise and thermal efficiencies with and without the impacts of wind.	Fail	3.1.1.5.1 (Figure 21)

Milestone Number	Milestone Title	Description	Metric	Success Value	Assessment Tool	Results (Pass/Fail)	Location in Report
2.2	Quartz half-shells simulations	Develop simulations of receiver performance with quartz half-shells on the receiver. Evaluate different wind and irradiance scenarios with particle mass flow rates of 5 - 10 kg/s.	Comparison of thermal efficiency with and without quartz half-shells Simulation matrix will include wind speed/direction, irradiance, mass flow rate	For point comparisons, thermal efficiency is greater with quartz half-shells by 5% For parity plot, slope > 1.05 (Thermal efficiency) Constraint: Use existing test conditions from on-sun SuNLaMP tests and/or a combination of design and off-design conditions	Comparison of simulated receiver efficiency with and without quartz half shells for design and off-design conditions. Parity plot of simulated receiver efficiency with quartz half-shells vs. simulated receiver efficiency without quartz half-shells will also be evaluated.	Fail	3.1.1.1.3
2.3a	Quartz half-shell testing for efficiency improtment	Perform on-sun tests to evaluate temperature rise and thermal efficiency and any damage to quartz half-shells due to soiling or abrasion. Irradiance values should range from 500 suns to 1000 suns with particle mass flow rates of 5 - 10 kg/s.	Thermal efficiency (or temperature rise) and visible damage	Average thermal efficiency (or temperature rise) with quartz half-shells > average thermal efficiency (or temperature rise) without quartz half-shells for tests with similar test conditions. Variability in measured (and simulated) thermal efficiency as a function of wind speed/direction is reduced by >10%. No visible damage to quartz.	Student's t-test with 95% confidence for similar test conditions.	N/A	3.1.1.1.3

Milestone Number	Milestone Title	Description	Metric	Success Value	Assessment Tool	Results (Pass/Fail)	Location in Report
2.3b	Quartz half-shell testing for wind mitigation	Perform on-sun tests to evaluate impact of wind speed and direction on thermal efficiency.	Variability in thermal efficiency as defined by 2 standard deviations about the mean	20% Constraint: Tests include similar irradiance, particle mass flow, and partile inlet temperature conditions for different wind conditions	Evaluation of thermal efficiency variability about the mean using two standard deviations	N/A	3.1.1.1.3
2.4	Multi-stage release simulation	Develop simulations of multi-stage particle release and evaluate receiver thermal efficiency and temperature of troughs	Comparison of thermal efficiency with and without multi-stage release Simulation matrix will include wind speed/direction, irradiance, mass flow rate	Slope > 1.05 Constraint: Use existing test conditions from on-sun SuNLaMP tests. Success value may change depending on technoeconomic results and requirements in Milestone 8.2	Parity plot of simulated receiver efficiency with multi-stage release vs. simulated receiver efficiency without multistage release.	Pass	3.1.1.1.6
2.5	Multi-stage release testing	Perform tests using passive mass-flow control troughs. Evaluate temperature and potential need for active cooling of catch-and-release troughs. Perform on-sun durability test.	Thermal efficiency (or temperature rise) and visible damage	Average thermal efficiency (or temperature rise) with multi-stage release > average thermal efficiency (or temperature rise) without multi-stage release for tests with similar test conditions. Variability in measured (and simulated) thermal efficiency as a function of wind speed/direction is reduced by >10%. Minimal visible damage troughs. Temperature remained below softening point.	Student's t-test with 95% confidence for similar test conditions.	Partial	3.1.1.4.2

Milestone Number	Milestone Title	Description	Metric	Success Value	Assessment Tool	Results (Pass/Fail)	Location in Report
2.6	Feed hopper design and operation	Design feed hopper and control system to maintinain desired inventory during operation to allow sufficient emergency inventory through control of the particle lift and measurement of inventory	Measurement of average particle feed hopper inventory (mass or level) over time relative to changing mass flow rates	Measured average inventory does not reduce below desired setpoint for a maximum particle flow rate Particle inventory in feed hopper / particle mass flow rate > 60 seconds Constraint: For testing using the existing particle test loop, a max particle flow of 5 kg/s and a minimum time of 1 minute of inventory will be used.	Measured particle mass or level in feed hopper as a function of time and varying particle mass flow into the receiver.	N/A	3.1.1.4.4
2.7	Automated particle temperature control	Demonstrate that automated particle temperature control using closed-loop feedback can maintain particle temperatures to desired setpoint using new heat exchanger (Note: particle flow through heat exchanger will be limited to < 1 kg/s.	|Measured average particle outlet temperature - desired particle outlet temperature| or Particle outlet temperature minus particle inlet temperature	< 25 degrees	Student's t-test with 95% confidence. Note: Because the heat exchanger will not be able to cool large mass flow rates of particles, the test protocol will be to increase the particle temperature up to desired temperatures (500, 600 C) and then apply only the number of heliostats necessary to offset heat loss. Perturbations will be applied by adding or subtracting 1 or more heliostats to simulate a flux perturbation.	Pass	3.1.1.4.3 (Figure 16b)

Milestone Number	Milestone Title	Description	Metric	Success Value	Assessment Tool	Results (Pass/Fail)	Location in Report
2.8	Slide gate reliability	Demonstrate slide-gate reliability at high temperatures to control the amount of particle mass flow entering the receiver.	Slide gate moves according to commands from control system Slide gate moves according to commands from control system	No on-sun failures (jamming, linear bearing failure, servo failure, ball screw failure, gate wear) during Gen3 testing campaign No failures during operation for > 100 hours	Monitor the movement and operations of the slide gate during on-sun testing. Number of servo failures to respond to a command or tripping the over torque limit AND Visual inspection of mechanical parts after completed test campaign.	Pass (Visual inspection not completed)	3.1.1.4.3
2.9a	Receiver downselection criteria	Document downselection criteria and method for receiver design	Report that includes downselection criteria and method for G3P3 receiver	Collective agreement on downselection criteria and method from receiver developers and Technical Review Committee	Meetings and discussions with developers and TRC to identify appropriate downselection criteria for Phase 3	Pass	3.1.1
2.9b	Downselect G3P3 receiver design	Based on information from tasks to evaluate alternative receiver configurations, their efficiencies, cost, reliability, scalability, etc., determine the best option for G3P3.	Efficiency, cost, complexity, reliability, scalability Receiver partners will provide same milestone metrics for each receiver design, along with degree of uncertainty.	Collective agreement on receiver design	Design review by Technical Review Committee (e.g., Analytical Hierarchy Process).	Pass	3.1.1
2.10	Annual wind velocity and direction	A plan is needed to fully describe the annual wind velocity and direction in appropriate time increments	Time increments of desired parameters	5 minute increments through a selected calendar year for wind speed, wind direction, DNI Constraint: measurements at 50 - 250 m	Spreadsheet of wind data available for CFD modeling obtained in collaboration with A2E and wind energy programs.	Pass	3.1.1.2.6
2.11	Wind gust measurement and modeling	Data and models of impacts of wind gusts are needed	Measurements of wind data with deviations in wind speed for CFD models	At least three measured wind gust events that can be used in CFD models	CFD modeling of transient impact of wind gusts on receiver efficiency. Include results in BP2 Q1 report	Pass	3.1.1.2.6 (Figure 9)

Milestone Number	Milestone Title	Description	Metric	Success Value	Assessment Tool	Results (Pass/Fail)	Location in Report
2.12	Particle temperature control	Control logic and demonstration of particle outlet temperature control	Deviations in particle outlet temperature from setpoint	± 2s ≤ 10 C Constraint: perturbation of receiver irradiance of ± 20% between 700 - 1000 suns at particle inlet temperature ≥ 550 C	Logic control will be presented to DOE by 5/30/20. Standard deviation of particle outlet temperature will allow assessment of particle temperature control following flux perturbation.	Pass	3.1.1.4.3 (Figure 16b)
Storage							
3.1	Insulation design for storage tanks	Work with vendors to design cost-effective insulation that enables acceptable particle outlet temperatures from the hot storage tank to the heat exchanger	Mean particle outlet temperature, Ts,out from hot storage tank after 8 hour charge, 10 hour storage, and 6 hour discharge.	95% confidence that mean Ts,out ≥ 765 °C using student's t-test. Constraint: Tambient = 20 C, wind speed = 10 mph, uniform inlet temperature distribution of Tinlet=775C-800C, bin is at steady-state cyclic operational conditions	Use of CFD or FEA models of heat loss from storage bins with consideration of convective wind losses, radiation losses from the surface, and condution through the insulation and shell.	Pass Outlet temperatures >765 °C were achievable if receiver outlet temperatures were in the range of 787-800 °C. Future work will incorporate uncertainty and variability into existing models to generate a distribution of outlet temperatures to determine the 95% confidence interval.	Section 3.1.2.3
3.2	Scaling of storage bin designs	Storage bin designs must be scalable or identified for pilot-to-commercial scales	Design meets cost, structural requirements, and particle temperature needs of the heat exchanger(s) and receiver(s).	Cost ≤ $15/kWht Structural requirements meet appropriate codes as determined by vendor Heat loss over deferred storage period meets particle temperature needs of heat exchanger(s) and receiver(s)	Vendor will use their industry-accepted modeling and assessment methods.	Partial Pass The preferred commercial design had pecific costs of ~$20/kWht. Models show that uninsulated bins can still meet particle temperature requirements. $15/kWht may be achievable using uninsulated monolithic dome construction if suitable particles can be found at <$0.75. Future work is needed to optimize insulation costs vs. collector costs as a function of heat loss.	Section 3.1.2.5
Heat Exchanger							

Milestone Number	Milestone Title	Description	Metric	Success Value	Assessment Tool	Results (Pass/Fail)	Location in Report
4.1	High-temperature plate bank bond development	Diffusion bonding and brazing practices should be developed for 800H, Haynes 230, and 740H as candidate materials for the high-temperature plate banks.	Success of a bond/braze for a given material is based on the criteria (% of parent material strength, or burst panel) required by ASME inspector.	≥ 1 material identified with suitable bond and braze properties (channel geometry influences what can be deemed successful)	Process approval from ASME inspector based on a combination of diffusion bonding test blocks and burst panels to demonstrate bond and braze strength and heated pneumatic testing.	PASS, tensile specimens for IN617 met ASME SB-168 specification for diffusion bonding manufacutring qualification.	Non-public downselect report: 3.1.3.2 (Table 14)
4.2	Evaluation of 800H corrosion with nickel enrichment	Supercritical CO2 corrosion of 800H has limited application. The nickel enrichment at the surface from the diffusion bonding process is not captured in current corrosion studies and could improve the corrosion resistance to acceptable values.	The corrosion rate constant should be measured in an autoclave furnace at 650 °C and 25 MPa for samples that have Ni enriched surfaces and as received material.	log(kp) < -15	Student's t-test with 95% confidence for calculated corrosion rate constant from three repeat measurements made at 500, 1000, and 1500 hours.	FAIL, 800H was not pursued as a material of consturction after switching to single bank design.	3.1.3.1
4.3	Heat exchanger overall heat transfer coefficient (the focus here is on bounding the design space so that studies requiring geometric parameters occuring in parallel with material development can be informed)	Identification of heat exchanger geometry and particle combinations to bound the design space that achieve an overall heat transfer coefficient suitable for commercial scale systems	Reduced order heat exchanger modeling tools used to simulate the overall heat transfer coefficient (U = Q/(A ΔTlm)).	Moving packed bed heat exchanger design space identified that can achieve > 300 W/m2-K with confidence	Probabilistic simulation of the heat exchanger performance bounding 95% confidence interval for achieving minimum overall heat transfer coefficient for each set of design variables.	PASS, geometric parameters (3mm plate spacing) leading to performance targets were identified and pursued in design and anlysis.	Non-public FY19Q1 review presentation

Milestone Number	Milestone Title	Description	Metric	Success Value	Assessment Tool	Results (Pass/Fail)	Location in Report
4.4.1	High-temperature particle flowability requirements	Identify the allowable particle flow maldistribution through heat exchanger modeling	Reduction in overall heat transfer coefficient due to flow maldistribution	Identify allowable channel velocity variance resulting in less than 10% reduction in overall heat transfer coefficient	Plot of the ratio of overall heat transfer coefficients (Umaldistribution/Uuniform) vs maximum channel velocity difference ((vmax-vmin)/vmax).	PASS, sCO2 and particle flow non-uniformity have a secondary effect of HTC	Non-public phase one continuation review: slide 78
4.4.2	High-temperature particle flowability measurements	Test particle flow in narrow vertical channels at high temperature to determine if clogging of non-uniform flow experienced.	Uniform and consistent particle flow is achieved for the channel dimensions identified in M4.3 and no clogging is observed. Measure individual channel velocities for high-temperature particle flow through visualization.	< flow maldistribution identified from M 4.1.1	Student's t-test with 95% confidence for the maximum channel velocity difference ((Vmax-vmin)/vmax).	PASS, flow maldistribution was conducted	3.1.3.3 (Table 14, 15, and 16)
4.5	Steady-state thermomechanical evaluation	The heat exchanger geometry will be modeled using CFD/FEA tools to evaluate steady state thermomechanical stresses	Heat exchanger lifetime based on typical failure modes	> 10 year operation lifetime based creep-fatigue failure mode	Determine fatigue lifetime through thermomechanical modeling to determine strain range and design curves for materials at temperature	FAIL, initial heat exchanger lifetime evaluations suggest less than 10 year operating life	3.1.3.3 (Figure 62)
4.6.1	Determine allowable sCO2 flow maldistribution	Identify the allowable sCO2 flow maldistribution through heat exchanger modeling	Reduction in overall heat transfer coefficient due to flow maldistribution	Identify allowable channel velocity variance resulting in less than 10% reduction in overall heat transfer coefficient	Plot of the ratio of overall heat transfer coefficients (Umaldistribution/Uuniform) vs maximum channel velocity difference ((vmax-vmin)/vmax).	PASS, 30% flow nonuniformity has less than 10% reduction in overall heat transfer coefficient	3.1.3.3 (Table 14, 15, and 16)
4.6.2	Evaluate sCO2 flow maldistribution	Perform CFD simulations of the new plate bank design to evaluate flow distribution in a plate bank	Flow maldistribution should be evaluated from simulated velocity distributions in individual channels.	< flow maldistribution identified from M 4.6.1	Calculate maximum velocity difference ((vmax-vmin)/vmax) the in the individual channel velocities over operational envelope.	PASS, CFD simulations predict flow non-uniformity <8% over entire operating range.	3.1.3.3 (Figure 59 and 60)

Milestone Number	Milestone Title	Description	Metric	Success Value	Assessment Tool	Results (Pass/Fail)	Location in Report
4.7	Transient thermomechanical evaluation	Perform CFD simulations of the new plate bank design to evaluate allowable heat exchanger ramp rate	Low cycle fatigue should be avoided during typical operation through keeping peak stress below yield stress (σmax/σy) for startup and load following transients.	Heat exchanger operation allows for sCO2 outlet temperature ramp rates > 15C/min during startup and changes in thermal duty of 2% of desgin point duty/min during startup	Probabilistic simulation results plotted as maximum stress vs. ramp rate indicating 95% confidence that the maximum stress is kept below the yield stress.	FAIL, simulations to identify allowable ramp rate were conducted, but did not meet probabalistic metric	Non-public phase one continuation review: slide 79-82
4.8	Construction and evaluation of prototype heat exchanger bank	A prototype heat exchanger bank that implements a modular design which eliminates the numerous nozzles and welds of the SuNLaMP design should be constructed and pressure tested.	Prototype banks (constructed from stainless steel and a material for high temperature use) evaluated through hydrotesting.	Pass	ASME BPVC hydrotesting based on the maximum allowable working temperature and pressure for stainless-steel and high-temperature banks. Potentially integrate with SuNLaMP unit for thermal performance.	PASS, prototype unit was hydrotested at VPE	3.1.3.3 (Table 17 and Figure 64)
4.9a	Heat exchanger downselection criteria	Document downselection criteria and method for heat exchanger design parameters	Report that includes downselection criteria and method for G3P3 heat exchanger	Collective agreement on downselection criteria and method from receiver developers and Technical Review Committee	Meetings and discussions with developers and TRC to identify appropriate downselection criteria for Phase 3	PASS	Heat Exchanger Design Basis Document 3.1.3 (Table 12 and 13)
4.9b	Heat exchanger final design downselect	Finial heat exchanger design downselect based on development in phases 1 & 2. This will identify the geometry and features incorporated into the >1 MWt unit for pilot plant construction.	Comparison of different design parameters to evaluate the tradeoff in heat exchanger performance, cost, manufacturability, and transient operation.	Downselect to a single set of design parameters and features to include in the final design of the moving packed-bed heat exchanger	Analytical hierarchy process and assessment from technical review committee.	FAIL	N/A

Milestone Number	Milestone Title	Description	Metric	Success Value	Assessment Tool	Results (Pass/Fail)	Location in Report
4.10	Commercial scale cost analysis and identification of heat exchanger design parameters for >1 MWt	Results from bond development, modeling, and high temperature flow testing should be integrated to determine final heat exchanger design with a technoeconomic analysis.	Technoeconomic analysis with >1 MWt prototype design parameters and materials	heat exchanger cost < $150/kWt with uncertainty of less than $50/kWt (unless higher allowable cost is identified through reduction in cost of other system components)	Uncertainty in heat exchanger cost due to performance and technoeconomic parameters for pilot plant design at 100 MW scale.	FAIL, Heat exchanger commercial scale cost exceed the target, but can still achieve system wide LCOE goal.	3.1.3.5
Particle Lift							
6.1	Particle lift design	Particle lift needs to be able to lift at least 5 kg/s at a particle temperature of at least 600 C	Particle mass flow rate capacity and operating temperature	>5 kg/s at >600 C	Quote from vendor indicating required flow rate and operating temperature Design verification from vendor	Pass	Section 3.1.4
6.2	Thermal and Electrical cost	evaluate and exercise the performance models of the lift system	Particle temperature decrease after being lifted from cold storage to top of receiver	Bulk particle temperature difference ≤10 C Constraint: Evaluation of different skip and insulation designs, velocities, and environments	Sensitivity Analysis	Pass	Section 3.1.4
Particles							
7.1	Particle selection	Selected particles must be durable and cost-effective	Attrition rate and cost, and simulated receiver efficiency; attrition is due to impact and abrasion expected during operation of G3P3	Attrition ≤ that of CARBO HSP AND Cost ≤ that of CARBO HSP ($1/kg) AND Simulated receiver efficiency ≥ 85%	Work with Tulsa U. to assess attrition rates during impact and abrasion studies. Evaluate cost from vendors of different particle materials. Evaluate receiver efficiency using existing CFD tools with new particle properties.	Pass	Section 3.1.5
System							

Milestone Number	Milestone Title	Description	Metric	Success Value	Assessment Tool	Results (Pass/Fail)	Location in Report
8.1	G3P3 structural designs	Need approved engineering drawings of G3P3 structure and assembly	Detailed engineering drawings of G3P3 structure and assembly that can withstand weight and heat of all components and seismic and wind loading	Drawings approved by EPC engineer to satisfy static loads, expected temperatures, and seismic and wind requirements according to building codes	EPC engineer will review and approve drawings	Pass	Section 3.2.2
8.2	Technoeconomic analyses	Perform technoeconomic analyses of a commercial G3P3 system	LCOE	≤ $0.06/kWh	Use systems based tool (e.g., Modelica or SAM) that has been modified to account for particle-based components and performance	Pass	Section 3.3.1 (Figure 84 and Table 22)
8.3	Quotes for G3P3 construction	Obtain quotes for G3P3 construction at Sandia	Total budget for construction and assembly of G3P3-USA at Sandia	Estimated cost is within +20%/-15% of available budget from DOE after expenditures in Phases 1 and 2	Obtain quotes from component and material vendors, EPC, and Sandia Facilities.	Pass (preliminary estimates were obtained throughout Phases 1 and 2; construction and material costs have escalated due to pandemic impacts on suply chain)	Section 3.2.1.6
8.4	Viability and appropriateness of G3P3 design	Design review of G3P3 system	Ability of G3P3 design to meet DOE metrics, market needs, and commercial scale-up.	Technical Review Committee approves G3P3 design	Tecnical Review Committee will review G3P3 design providing feedback on confidence in commercial system scale-up of concept (economics, operation, market), construction of pilot plant (within budget, relevance to commercial design), and identification of issues not addressed in milestones.	Pass	Section 3.1.1, Section 3.2.4, Section 3.2.5

APPENDIX C. G3P3 RECEIVER DOWNSELECT PROCESS

C.1. Particle Receiver Designs

C.1.1. Falling Particle Receiver

Falling particle receivers employ gravity-driven flow of particles through an open cavity. Various geometries and configurations of falling particle receivers have been considered, including free-falling and obstructed-flow designs to slow or control the flow of particles (Figure 92) [1-3, 28, 86, 87]. On-sun testing of the free-falling and obstructed-flow designs showed that temperatures over 800 °C could be achieved with thermal efficiencies achieving ~80% and above, depending on the particle temperature, mass flow rate, irradiance, and wind conditions [3].

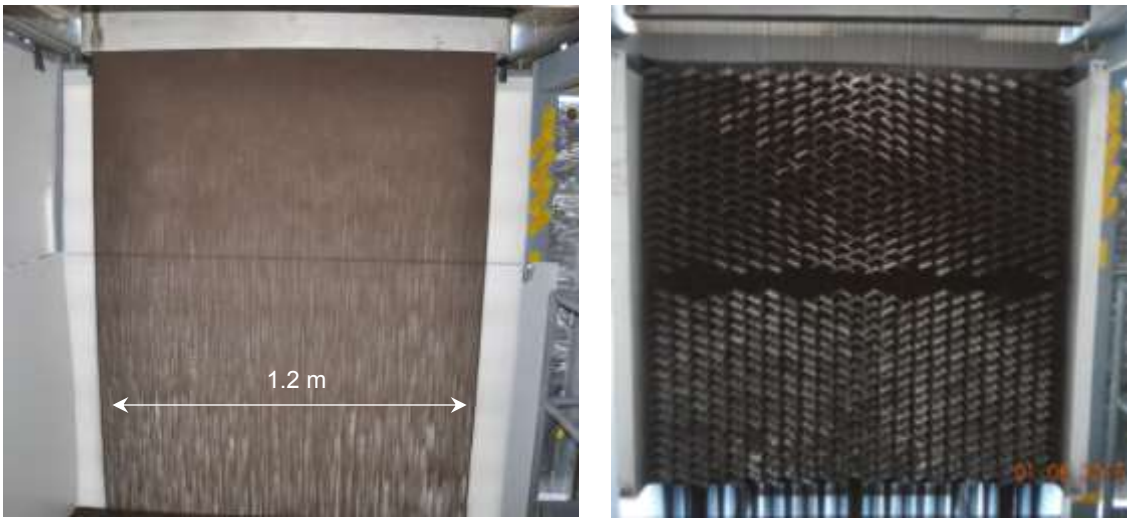

Figure 92. Free-falling (left) and obstructed-flow (right) designs for falling particle receivers (Sandia National Laboratories).

In addition, air curtains have been studied together with falling particle receivers to reduce convective heat losses from the receiver aperture [88, 89]. More recent studies have investigated the use of quartz aperture covers and multi-stage release designs to reduce particle and heat losses and increase thermal efficiencies. Advantages of falling particle receiver designs include ease of construction and operation, low maintenance, direct irradiance of the particles, and scalability to high particle mass flow rates (~100 kg/s) and larger systems (~100 MW_e). Challenges include increased convective and particle losses through the aperture relative to enclosed designs, which can lead to lower thermal efficiencies and increased particle replacement costs.

C.1.2. Centrifugal Particle Receiver

The general principle of a centrifugal receiver is the use of a rotating chamber to control the flow and residence time of particles along the walls by centrifugal force. Particles are fed into the top end of the rotating receiver, and concentrated sunlight enters through an aperture at the other end that faces the heliostat field. The centrifugal force of the rotating receiver causes the particles to move along the walls of the receiver at a controlled rate while they are irradiated by the concentrated sunlight. DLR developed a centrifugal particle receiver design and prototype (Figure 93) [6, 7, 39, 90-92]. In early tests, small bauxite

ceramic particles (~1 mm) were introduced into a rotating centrifugal receiver with different inclination angles at mass flow rates of ~3 – 10 g/s. The particles were irradiated using a 15 kW_{th} solar simulator with an irradiance ranging from ~300 – 700 kW/m^2. For a face-down receiver inclination and incident irradiance of 670 kW/m^2, Wu et al. reported a particle outlet temperature of 900 °C and a receiver efficiency of about 75% (±4%) [90]. Recent on-sun tests have confirmed the ability to achieve particle temperatures of ~900 °C. Thermal efficiencies at these higher temperatures are being determined. Advantages include control of residence time to achieve higher temperatures and potential for high efficiencies. Challenges include scaling to larger mass flow rates and systems, parasitic energy requirements, and reliability associated with a large rotating receiver system.

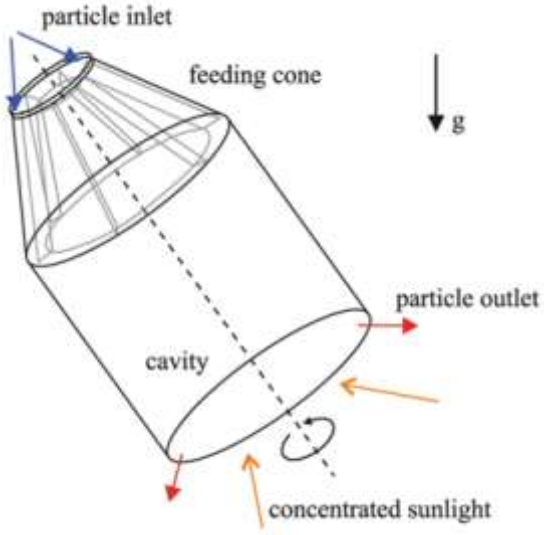

Figure 93. Schematic of a centrifugal receiver [91].

C.1.3. Fluidized Particle Receiver

Flamant et al. [8, 93, 94] proposed and demonstrated an indirect particle receiver in which the particles are forced upward through irradiated tubes by airflow, which fluidizes the particles and increases heat transfer from the tube walls to the flowing particles (Figure 94). Particle temperature increases of greater than 200 °C were recorded in a 50 cm long stainless steel AISI 304L tube with irradiances ranging from ~200 – 400 W/m^2. Suspension temperatures at the outlet of the irradiated tubed were up to 750 °C, and the wall-to-suspension heat transfer coefficient was determined to be 420 – 1100 W/m^2-K for solid mass fluxes of 10 – 45 kg/m^2-s, respectively. Thermal efficiencies were not reported. Advantages include complete containment of the particles within the tubes and the ability to control the mass flow rate of particles with the fluidization velocity. Challenges in this system include parasitic energy requirements to fluidize the particles through the receiver tubes, convective loss from the fluidizing air, attrition of the particles due to abrasion with the tube walls, erosion of the tube walls, flux limitations on the tubes, and heat losses from the tube surfaces.

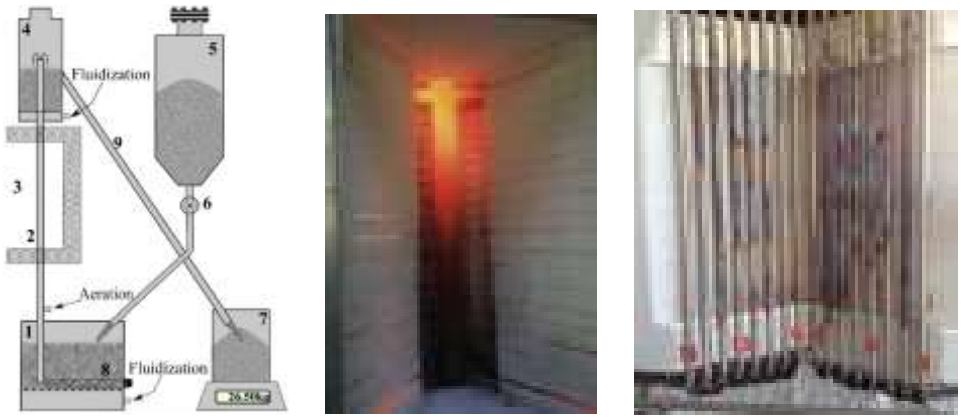

Figure 94. Schematic of the fluidized particle receiver design (left) and images of on-sun testing [93].

C.1.4. Particle Receiver Summary

Table 24 summarizes the advantages and challenges associated with the three high-temperature particle receiver designs being considered for G3P3.

Table 24. Summary of particle receiver designs.

Receiver Design	Advantages	Challenges	References
Falling	Direct irradiance of particles reduces flux limitations, scalable to large particle mass flow rates and system capacities, simple and inexpensive design	Convective heat losses, particle loss through the aperture, wear and overheating of obstructions (if present), acceleration and dispersion of particles, particle outlet temperature control	[1-3, 27, 28, 87, 88, 95]
Centrifugal	Control of particle residence time via rotational speed of receiver, direct irradiance of particles, ability to achieve high temperatures (>900°C)	Scalability to higher mass flow rates and larger systems, parasitic energy requirements, reliability associated with a large rotating receiver system	[6, 7, 90, 91]
Fluidized flow in tubes	Enhanced heat transfer from walls to particles due to fluidization, no particle loss due to containment	Parasitic energy requirements to fluidize particles, scalability to higher mass flow rates and larger systems, particle attrition/abrasion on tube walls, flux limitations on tube walls	[8, 93, 94]

C.2. Design Requirements and Criteria

Table 25 summarizes the design requirements for the G3P3 particle receiver. The thermal duty, cost, efficiency, particle outlet temperature, and particle mass flow rate are determined by the required specifications in the Funding Opportunity Announcement (FOA) of the U.S. Department of Energy (DOE) Solar Energy Technologies Office (SETO) Gen 3 pilot system.

Table 25. Design requirements for G3P3 pilot-scale particle receiver.

Target Metrics	Basis
Thermal duty: ≥1 MW_t	Thermal duty meets Gen 3 FOA goals and matches capability at NSTTF
Cost ≤ \$1M (pilot) Cost ≤ \$150/kW_t (commercial)	Cost for pilot receiver based on allowable budget from DOE (excludes lift and tower cost). Cost for commercial system based on DOE SunShot goals (includes receiver, tower, lift, and all associated components).
Thermal eff. ≥ ~80 - 85% (pilot), 85-90% (commercial) Constraint: Thermal efficiency must be met at desired particle outlet temperature below.	Recent System Advisor Model simulations show that a commercial receiver efficiency of 85-90% can still yield \$0.06/kWh_e; pilot-scale efficiency scales down with receiver size [13]
T_{out} ≥ 750 °C	Particle outlet temperature required to achieve sCO2 temperature of ≥ 700 °C at turbine inlet
$\dot{m}$ ≥ 5 kg/s	Mass flow based on required thermal duty

In addition to the quantitative metrics in Table 25, the following design criteria in Table 26 have been identified to use as a basis for evaluating and downselecting among the three particle receiver designs being studied in Phases 1 and 2 of the G3P3 project. Note that the design criteria in Table 26 can be more qualitative in nature than the design requirements in Table 25, given the inherent uncertainties of the receiver designs and performance at this early stage of development.

Table 26. Summary of design criteria for downselection of receiver design.

Design Criteria	Notes
Thermal Efficiency	≥ ~80 - 85% (pilot), 85-90% (commercial); minimize heat losses
Cost	Want cost less than \$1M (excludes lift and tower cost) for pilot scale and cost ≤ \$150/kW_t for commercial scale (includes tower, receiver, lift, and peripherals)
Reliability/Demonstration	Want long-term reliability and previous demonstration at ~1 MW_t scale of operating conditions at ~1000 suns, ~10 kg/s particle flow, and ~600 - 800 C particle temperature.
Controls	Ease and accuracy of controls for particle mass flow, particle outlet temperature (e.g., ± 25°C of setpoint temperature), and emergency procedures.
Manufacturability/assembly	Ease of manufacturing and demonstrated ability to build
Scalability	Ability to scale particle mass flow and thermal capacity to ~100 MW_t
Start-up	Want to minimize complexity and time required to start receiver operations
Parasitics	Want low power requirements, pressure drop, and heat losses
Particle Loss and Attrition	Minimize particle loss to environment and particle loss through abrasion/attrition

Design Criteria	Notes
Repair and Inspection Ease	Need easy access to inspect and repair receiver components

C.2.1. Thermal Efficiency

The thermal efficiency of the particle receiver is defined as the energy absorbed by the particles divided by the incident energy on the receiver. Energy losses that can reduce the amount of energy absorbed by the particles include solar reflective losses, thermal radiative losses, convective heat losses, and conductive losses. On-sun tests have been performed for the three categories of particle receivers being evaluated as part of G3P3 (falling, centrifugal, and fluidized). In Phases 1 and 2, the thermal efficiencies of relevant tests and simulations will be evaluated and compared among the different designs.

C.2.2. Cost

The target cost of the G3P3 receiver is less than $1M based on initial budgeting and allocations within the allowable DOE budget of $25M for construction of the entire system. This value could change as the design and cost of other G3P3 components are refined. In general, we wish to minimize the cost of the receiver while being able to achieve the design requirements in Table 25

The target cost of commercial-scale particle receiver is $\leq \$150/kW_t$, which includes the cost of the receiver and tower structure. Ho [1] provided a cost estimate of ~$\$125/kW_t$ for a 100 MW_e falling particle receiver, which includes the receiver, tower, particle lift, controls and instrumentation, spare parts, other directs, and contingency. The low cost is a result of the simplistic design of the falling particle receiver, which consists of a cavity constructed from refractory walls. Estimates of costs for the centrifugal and fluidized particle receiver designs for commercial-scale systems has not been reported. Efforts will be made in Phases 1 and 2 to perform a cost analysis of the different receiver designs.

C.2.3. Reliability/Demonstration

The long-term reliability of the receiver is an important factor to ensure continuous operation and reduce costs associated with repairs, maintenance, and lost revenue. The receiver will be exposed to high irradiances (~1000 kW/m^2) and undergo thousands of cycles over the prescribed 30-year lifetime due to start-up, shut-down, and environmental variations. Overheating of the flow obstructions and receiver walls has been reported during on-sun tests of falling particle receiver designs [2], and lessons learned from those experiences are valuable. Recent on-sun tests of the centrifugal receiver have also revealed some reliability issues that were reported in Ebert et al. [92]. Additional reliability issues and potential improvements will be reported in Phases 1 and 2 for the different receiver designs.

Testing and demonstration of each receiver design is also an important consideration for the G3P3 pilot-scale system. Receiver designs that have been demonstrated on-sun at ~1 MW_t and at the desired operating conditions are more valuable than designs that have only been tested at the bench scale or simulated with numerical models.

C.2.4. Controls

Controls for the particle receiver are necessary to maintain a desired particle outlet temperature and to ensure safe operation of the receiver. For the falling particle receiver, control of the particle mass flow rate can be performed through control of the particle feed rate into the top hopper from the lift or through control of particles flow through an aperture into the receiver via a slide gate. Automated control of the particle mass flow and outlet temperature was demonstrated in Ho et al. [29] for the falling particle receiver design. The ability to control the particle outlet temperature to

within ± 25°C of a prescribed setpoint temperature is desirable. Additional controls are required to ensure that the walls do not overheat and to ensure that there is a sufficient inventory of particles in the top hopper (about a minute) if power gets lost while concentrated sunlight is still on the receiver.

C.2.5. Manufacturability/Assembly

The manufacturability of the particle receiver is defined as the extent to which the receiver design can be manufactured with relative ease, minimum cost, and maximum reliability. If complex or expensive processes or materials are required, this would lower the manufacturability rating. If the receiver is simple to manufacture, inexpensive, and/or uses materials that do not require complex processing or assembly methods, then the manufacturability/assembly rating would be higher. Previous demonstrations of the build and manufacturing of the receiver design, or a clear tie to similar manufacturing methods or materials, that could be easily assembled at the National Solar Thermal Test Facility would also increase the manufacturability/assembly rating.

C.2.6. Scalability

Although the design requirements for the G3P3 pilot-scale system are for a ~1 MW_t thermal capacity, DOE is interested in seeing designs tested that can be scaled to larger systems (up to ~100 MW_e). So, the design intent of the particle receiver must consider the ability to accommodate very large particle mass flow rates (up to ~1,000 kg/s), control of the particle flow at those large mass flow rates, feed and discharge mechanisms, emergency operations, and cost implications.

C.2.7. Start-up

The start-up requirements of the particle receiver include the necessary ramp-up time, heating requirements, and procedures needed to begin operations and produce electricity. Start-up and heating requirements can be affected by the amount of thermal mass that is in contact with the particles in the receiver. If the particles are in contact with walls or tubes in the receiver during heating or conveyance through the receiver, those materials will require extra energy and time to be heated before the particles can achieve their desired outlet temperature. Other procedures to ensure that the receiver is operating properly and safely (e.g., particle flow controls, emergency checks) can also impact the start-up time or complexity.

C.2.8. Parasitics

Parasitics include additional power requirements to operate the receiver or peripheral equipment and instrumentation. For example, the centrifugal receiver requires power to rotate the large receiver, and the fluidized receiver required power to flow air through the receiver tubes. Trace heating, if required, would also increase parasitic power requirements. In addition, power is required to operate slide gates or other mechanisms to control the flow of particles through the receiver. Minimizing the power requirements, pressure drop, and heat losses to reduce parasitics is desired.

C.2.9. Particle Loss and Attrition

Physical loss of particles can occur by ejection through an open aperture or by abrasion and wear of the particles. In falling particle and centrifugal receivers, particles have been observed to pass through the open aperture of the receiver because of air and wind currents [3, 39]. Also, fluidized and centrifugal particle receiver designs may be subject to particle attrition from wear and friction as the particles move along the receiver tubes and walls. Particle loss can yield to increased costs due to the need for particle replacement, and the emission of fines can pose an inhalation hazard.

C.2.10. Repair and Inspection Ease

Ease of inspection and repairs will reduce operation and maintenance costs, and potential downtime and lost revenue. Receiver designs should enable inexpensive and/or easy repairs with safe access to key components. Components should be chosen and designed such that they can be replaced or repaired if they are subject to wear or failure, and suitable materials should be identified that are readily available.

C.3. Analytic Hierarchy Design Selection Process

The analytic hierarchy process (AHP) is a structured method to evaluate and select among multiple options to achieve a desired goal using weighted criteria [96]. A pairwise comparison among all the options is performed using each of the criteria, and a score is assigned based on the relative comparisons and the weightings of each criterion. The process consists of the following steps: (1) identify a goal; (2) identify criteria associated with achieving that goal and weight the criteria; (3) define alternative designs or options to achieve the desired goal; (4) for each criterion, perform pairwise comparisons of each of the design options; (5) obtain a final score for each of the design options. The mathematical formulation for determining the normalized criterion weights and scores for each design option are detailed in Saaty [96].

The goal of this work is to select a high-temperature particle receiver for G3P3. The design criteria for the particle receiver were specified in the previous section (thermal efficiency, cost, reliability/demonstration, controls, manufacturability/assembly, scalability, start-up, parasitics, particle loss/attrition, and repair/inspection ease). Three particle receiver designs are considered: (1) falling, (2) centrifugal, and (3) fluidized.

A team of researchers, stakeholders, integrators, and members of the Technical Advisory Committee will independently assign the following ratings to each pair of criteria (to weight the criteria) and to each pair of design options:

- 1/5: Extremely worse or less important
- 1/4: Significantly worse or less important
- 1/3: Moderately worse or less important
- 1/2: Slightly worse or less important
- 1: Equal or equally important
- 2: Slightly better or more important
- 3: Moderately better or more important
- 4: Significantly better or more important
- 5: Extremely better or more important

For example, if the criterion "cost" were being compared to "repair and inspection ease," and the researcher felt that cost was significantly more important than repair and inspection ease, a rating of "4" would be assigned to that pairwise comparison (see example in Table 27). This will be done for

pairwise comparisons of all the criteria, and the ratings among all the contributors will be averaged to yield a final normalized weight for each criterion.

Table 27. Criteria matrix for pairwise comparisons. Only the yellow section is filled in by the user. Example shows "Cost" was rated as significantly more important ("4") than "Repair and Inspection Ease". All other criteria were rated equally.

Criteria Ratings	Thermal Efficiency	Cost	Reliability	Controls	Manufacturability	Scalability	Start-up	Parasitics	Particle Loss and Attrition	Repair and Inspection Ease
Thermal Efficiency	1.00	1.00	1.00	1.00	1.00	1.00	1.00	1.00	1.00	1.00
Cost	1.00	1.00	1.00	1.00	1.00	1.00	1.00	1.00	1.00	4.00
Reliability	1.00	1.00	1.00	1.00	1.00	1.00	1.00	1.00	1.00	1.00
Controls	1.00	1.00	1.00	1.00	1.00	1.00	1.00	1.00	1.00	1.00
Manufacturability	1.00	1.00	1.00	1.00	1.00	1.00	1.00	1.00	1.00	1.00
Scalability	1.00	1.00	1.00	1.00	1.00	1.00	1.00	1.00	1.00	1.00
Start-up	1.00	1.00	1.00	1.00	1.00	1.00	1.00	1.00	1.00	1.00
Parasitics	1.00	1.00	1.00	1.00	1.00	1.00	1.00	1.00	1.00	1.00
Particle Loss and Attrition	1.00	1.00	1.00	1.00	1.00	1.00	1.00	1.00	1.00	1.00
Repair and Inspection Ease	1.00	0.25	1.00	1.00	1.00	1.00	1.00	1.00	1.00	1.00

After the criteria are identified and weighted, the team will perform a pairwise comparison of each design using each of the ten criteria. For example, if the centrifugal design was being compared against the fluidized design using the "cost" criterion, and the evaluator felt that the cost for the centrifugal design was significantly worse than that of the fluidized design, a pairwise rating of "1/5" or "0.2" would be assigned for this comparison (see example in Table 28).

Table 28. Sample pairwise comparison of centrifugal receiver against the fluidized receiver for the "Cost" criterion assuming that the evaluator felt that the cost of the centrifugal receiver was significantly worse than that of the fluidized receiver.

Raw Scores	Falling	Centrifugal	Fluidized
Falling	1.00	1.00	1.00
Centrifugal	1.00	1.00	0.20
Fluidized	1.00	5.00	1.00

A matrix of all pairwise ratings of the three designs will be completed by each contributor for each criterion. The average of the raw scores for each design are then multiplied by each criterion weighting to get a final weighted score for each design. Figure 95 shows an example of the weighted scores for each criterion and design if all the criteria and design comparisons were assumed equal.

In practice, the area of each design's outline in the radar chart will be different, and the design with the largest area will have the highest final weighted score.

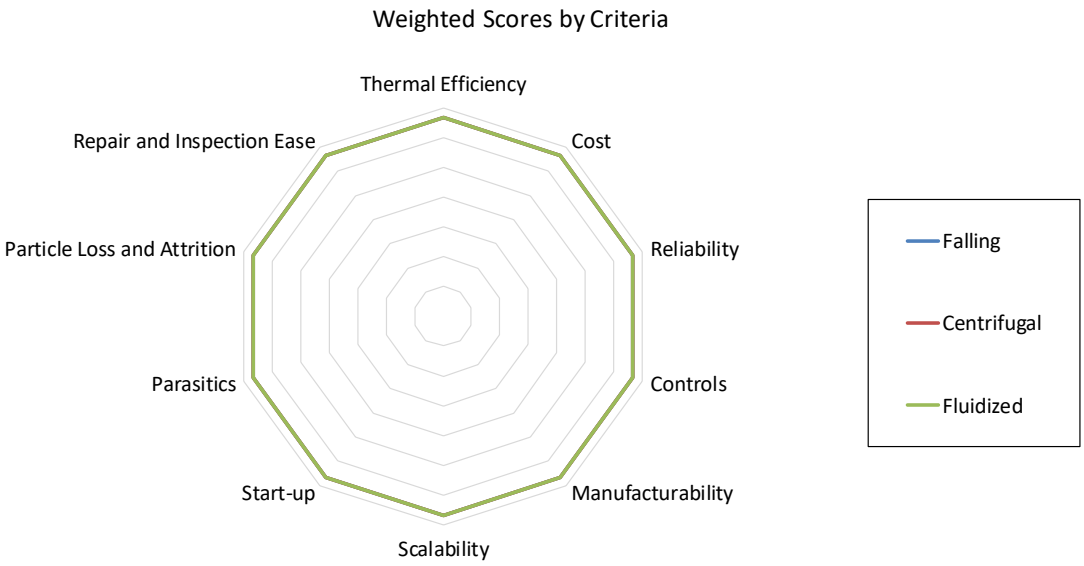

Figure 95. Weighted scores for each criterion of the three different particle receiver designs assuming equal criteria ratings.

C.3.1. AHP Evaluation by Technical Advisory Committee

EPRI convened the 14-person technical advisory committee (TAC) via webcast in mid-February to review the design basis for the G3P3 project. Engagement in the project has been very strong, and several TAC advisors followed up after the meeting with additional questions, design modification suggestions, and requests for more references on receiver designs. During the webcast Sandia also provided an overview of the spreadsheet-based analytic hierarchy process (AHP) that the TAC was asked to complete to compare the relative attributes of three particle receiver types: falling particle, centrifugal, and fluidized bed.

The AHP receiver evaluation was performed for the pilot-scale 1-MW_t G3P3 system, as well as a conceptual 100-MWe plant. The three receiver types were evaluated based on ten criteria selected by Sandia: thermal efficiency, cost, reliability, controls, manufacturability, scalability, start-up, parasitics, particle loss and attrition, and repair and inspection ease. The TAC was responsible for establishing the relative importance of the criteria through a series of pairwise comparisons before judging how well each of the receiver alternatives met each of the criteria. Spreadsheets with weighted scores for the G3P3 pilot system were received from ten TAC advisors, and results were compiled to yield a final quantitative score for each design option. Seven TAC advisors also completed AHP spreadsheets for the commercial-scale system.

Radar charts showing the relative criteria importance for the G3P3 pilot and commercial plant are presented in Figure 96. Thermal efficiency was a stronger dimension for the G3P3 pilot, whereas cost was considered more important for the commercial plant. Scalability was ranked highly for both systems, though feedback from participants revealed that there may have been confusion about how scalability is defined (e.g., for the G3P3 pilot, is scalability the ability of the technology to scale to 1 MWt size, or is it the ability to scale from 1 MWt to 100 MW?). Reliability was considered to be

more important for the commercial system, whereas particle loss and attrition was deemed to be of lesser importance at large scale. Low scores were assigned to parasitics, start-up, manufacturability, and repair and inspection ease. Controls received an intermediate score for both systems.

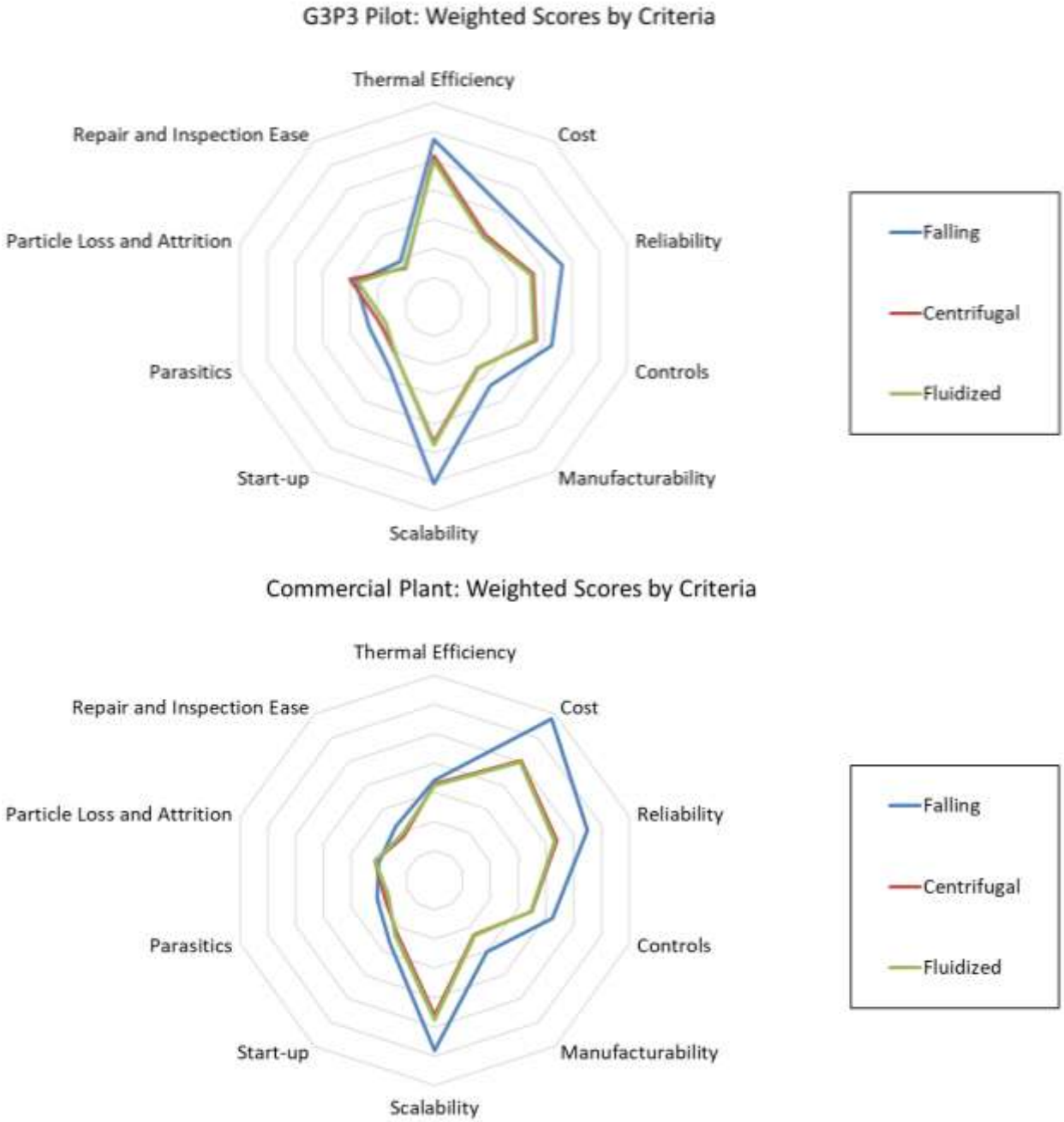

Figure 96. Weighted Scores by Criteria, G3P3 Pilot (top) and Commercial Plant (bottom).

Final weighted scores (Figure 97) indicate that the falling particle receiver—the preferred baseline design for the G3P3 particle receiver—is best able to meet the stated criteria at both pilot and commercial scales. The scores of 0.378 were identical despite slight differences in how the receiver design was perceived to meet the individual criteria. At pilot scale, the centrifugal design may be

slightly preferred over fluidized bed, whereas these designs received identical scores for a commercial-scale system.

G3P3 Pilot: Final Scores Weighted	Thermal Efficiency	Cost	Reliability	Controls	Manufacturability	Scalability	Start-up	Parasitics	Particle Loss and Attrition	Repair and Inspection Ease	**Final Weighted Score**
Falling	0.057	0.041	0.047	0.043	0.033	0.061	0.026	0.023	0.028	0.019	**0.378**
Centrifugal	0.052	0.030	0.036	0.037	0.026	0.046	0.022	0.019	0.030	0.016	**0.315**
Fluidized	0.050	0.029	0.035	0.036	0.026	0.048	0.021	0.017	0.027	0.017	**0.307**

Commercial Plant: Final Scores Weighted	Thermal Efficiency	Cost	Reliability	Controls	Manufacturability	Scalability	Start-up	Parasitics	Particle Loss and Attrition	Repair and Inspection Ease		**Final Weighted Score**
Falling	0.034	0.068	0.055	0.042	0.030	0.058	0.026	0.021	0.020	0.023		**0.378**
Centrifugal	0.033	0.050	0.044	0.035	0.023	0.046	0.022	0.018	0.022	0.018		**0.311**
Fluidized	0.032	0.050	0.043	0.035	0.023	0.048	0.023	0.017	0.022	0.019		**0.311**

Figure 97. Final Weighted Scores for Particle Receiver Designs, G3P3 Pilot (top) and Commercial Plant (bottom).

APPENDIX D. MODELICA/SOLARTHERM MODELING

ANU developed a technoeconomic analysis of a particle-based concentrating solar power (CSP) system using their Modelica-based SolarTherm model [38]. As described in Section 3.3.1, this analysis complemented the technoeconomic modeling using EES. The G3P3 project sought additional capabilities (e.g., transient simulations) available in SolarTherm that were not available in EES for future modeling and controls simulations, as well as a benchmark for comparison. Key differences between the two models are summarized below:

- ANU's SolarTherm multi-aperture model places the different apertures in series ("cascaded" configuration) vs. in parallel as modeled in EES. This brings some evident benefits, because hotter receivers can be optimised for size and flux, but it remains to be seen whether the costs and added challenges can be justified/overcome (e.g., additional chutes and hot slide gates, higher particle mass flow rates through each receiver, etc.)
- ANU used Solstice for optical modelling; the EES model used SolarPILOT
- ANU implemented optimal dispatch and TOD pricing, in addition to basic LCOE optimization with immediate dispatch.
- Cost dependencies of the tower and storage models included additional parameters in SolarTherm (e.g., tower diameter)
- Cost uncertainties of the particle lifts were not rigorously considered

The aim of the ANU study was to model the system with a sufficient level of detail for realistic estimation of the levelized cost of energy (LCOE), and then to optimize the configuration of the system for minimum LCOE. Additionally, the study aimed to examine the operation of the system in the context of varying time-of-day energy pricing, and to adapt the system design accordingly. The analysis followed the guidelines from the Gen 3 CSP Down-Selection Criteria document from DOE, with parameters taking the DOE-suggested values except where noted. The focus was on the system-level performance and optimisation, but generally *not* the estimation of component cost curves or detailed performance modelling of sub-components, which were instead generally taken to be analysis boundary conditions.

Common to all of the system configurations considered are a central receiver tower and surrounding heliostat field, free-falling particle receivers, two-tank storage of hot (800°C) and 'cold' (550°C) particles, particle lifts, a 700°C supercritical carbon dioxide (sCO_2) recompression Brayton cycle power block, a particle-sCO2 primary heat exchanger (PHX), and a control system that coordinates the system operation (Figure 98). The tower is of reinforced concrete and has a hollow cylindrical shape. The particles are assumed to be commercially-available Carbo HSP.

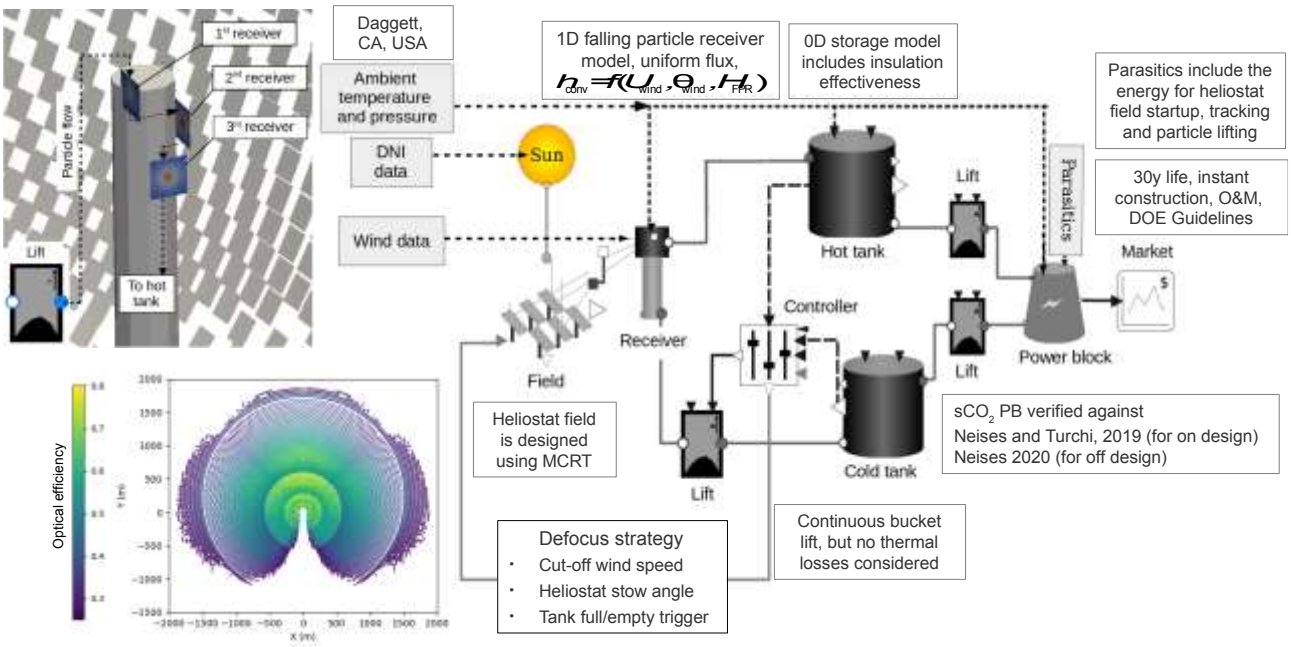

Figure 98. Conceptual overview of the G3P3 particle CSP system model developed by ANU, including its overall configuration and major components. Insets show the configuration of the three-aperture cascaded receivers, and the corresponding field layout for this same case.

The analysis considers tower-mounted (internal) storage tanks, as well as ground-mounted (external) storage tanks. In the case of internal storage, the tower itself provides the structural side-walls of the storage, and the hot tank is mounted above the PHX and power block, which in turn are mounted above the cold tank, allowing the further elimination of two particle lifts which are needed for the external storage case.

The analysis also considered single-aperture and multi-aperture configurations. In this study, the multi-aperture configuration is assumed to take the form of an in-series cascade of three receivers, with all particles passing through all three receivers in sequence, under gravity. This allows the last (lowest) receiver to be dedicated to high-temperature operation and is chosen to be the north-facing receiver that benefits from the heliostats with the highest annual optical efficiency and smallest spot size. Full details of the model implementation are provided in the report [38]. The model has been verified by comparison to a related model developed separately by Sandia and UPM and builds upon the open-source SolarTherm framework developed at ANU since 2016.

Systems optimized for lowest LCOE

Systems of each type, each with a fixed power block capacity of 100 MW_e, were optimized for lowest LCOE (Table 29). This included optimization of the heliostat field size and layout, tower size, receiver aperture dimensions, storage capacity and tank insulation thickness. The overall best configuration for minimizing LCOE was found to be a multi-aperture cascade system with external (ground-mounted) storage, which achieves an LCOE of 56.03 USD/MWh_e in a configuration with a 226 m tower, three apertures, solar multiple of 3.59 and storage capacity of 14 h. The low cost is achieved for this configuration due to a significantly shorter tower and lower total receiver aperture area compared to the other systems, despite an increase in the heliostat field area and hence cost. The smaller (and cheaper) receivers have higher spillage losses, but this is offset by lower thermal losses. This optimal configuration is quite sensitive to the tower design constraints and receiver cost and performance assumptions and should be revisited with a more detailed approach to the costing

and performance of these components. In particular, it is possible that tower-integrated storage could achieve significant further gains if a wider range of design options for the tower are considered. It should also be noted that the resulting optimized LCOE range is similar to that found using the EES model for a commercial-scale particle-based CSP plant (Figure 86).

Table 29. Optimized G3P3 system configurations, with associated performance and cost results, for each case of single-/multi-aperture and external (ground-mounted)/internal (tower-integrated) storage.

Configuration	Single-aperture		Multi-aperture		Unit
	External stor.	Internal stor.	External stor.	Internal stor.	
LCOE	**59.30**	**59.07**	**56.03**	**59.16**	**USD/MWh**
Capacity factor	80.0	79.9	82.5	82.3	%
Total capital cost	493	489	476	505	M·USD
Solar field capital cost	131	121	146	142	M·USD
Tower capital cost	68.3	83.1	45.0	81.8	M·USD
Receiver capital cost	70.2	73.4	62.7	71.7	M·USD
Annual optical efficiency	48.1	51.8	43.4	44.4	%
Ann. receiver therm. efficiency	75.3	75.4	87.3	87.1	%
Tower height	244	264	226	273	m
Tower outer diameter	31.0	36.1	25.0	35.2	m
Total heliostat area	1.54	1.43	1.71	1.67	km^2
Receiver aperture area	891	896	699	710	m^2
Solar multiple	3.53	3.53	3.59	3.65	[-]
Storage capacity	13.6	13.6	14.0	13.7	h

Sensitivity analysis

A sensitivity analysis was conducted for the case of a single-aperture system with tower-integrated storage. Using Latin hypercube sampling across plausible ranges for 23 different uncertain parameters regarding finance, performance and costs, it was found that that there is a 90% probability that the system LCOE would be below 68.34 USD/MWh_e. Using a ranked regression analysis, the LCOE was found to be most sensitive to the value of the discount rate (cost of capital, also inflation), heliostat accuracy (total optical or 'slope' error), heliostat reflectance, tower cost and power block cost, in that order. The fact that the key particle-based components do not appear high on this list suggests that even though particle technology offers large reductions in the cost of CSP and warrants development, the technical risks associated with heliostat cost and performance, and tower cost and design remain of very high importance. The sCO_2 power block is also clearly a component that is under active development, with associated risks.

This sensitivity analysis was augmented with an analysis of the contingency costs for the project. It was found that the assumed contingency cost ratio of 10%, as provided by DOE, would be sufficient, based on the considered set of uncertain cost parameters, to be sufficient to ensure a very low (0.1%) probability of capital costs being exceeded. This initial contingency analysis is optimistic, however, since it considers only a small subset of project risks. For a full-scale project, this analysis would need to be greatly expanded to consider these other factors including, in particular, the possible under-performance or failure of components such as heliostats, receiver or power block, and strategies to address those.

Peaker configurations

The single-aperture system with external (ground-mounted) storage tanks was also analyzed in a 'peaker' configuration. Here, the DOE time-of-day (TOD) pricing profile was applied, and the dispatch strategy was altered from the default 'immediate dispatch' strategy (which minimizes LCOE since energy is always dispatched if at all possible) to an 'optimal dispatch' strategy. The optimal dispatch is determined using a linear program (LP) approximation of the full system that is run hourly throughout the year using a 48-hour perfect-foresight (non-probabilistic) forecast horizon, to continuously apply a strategy that maximises the value extracted from the stored energy in the hot tank.

Taking the system configuration previously optimized for lowest LCOE, and applying the optimal dispatch strategy in place of the immediate dispatch strategy resulted in an increase of the annual average TOD factor from 1.22 to 2.06 albeit with a 22% reduction in the annual electricity output from the plant. The combined effect is an overall 30% higher total value of electricity produced annually, compared to the immediate dispatch approach.

The system design was then optimized to minimize the PPA 'bid price' (L_{bid} in the report) by varying the storage capacity, solar multiple, field layout, tower height and other variables. It is found that when the system design is varied to minimise the bid price, the optimal system becomes one with a smaller field (solar multiple 1.5), smaller storage (9 h capacity), and much shorter tower (166 m). This system is able to achieve an average TOD factor of 2.56 and a bid price of only 32.95 USD/MWhe against the TOD factor profile provided by DOE. According to Solar Dynamics, realistic TOD profiles may be even more extreme than those provided by DOE and could lead to further large design changes.

Limitations and future work

Results from this study are very encouraging for the prospects of particle-based CSP, whether for electricity production or other applications such as process heat. However, the models were relatively simple and should be refined if the concept proceeds. Tower costs and mechanical design required further attention, greater design flexibility, and mechanical analysis. Receiver thermal losses were calculated here using a 1D model that neglects lateral and through-curtain temperature variations and ignores the effect of flux nonuniformity. Multi-aperture configurations are yet to be fully optimized, and control strategies for the in-series cascade examined. The storage tank model assumes full mixing, suppressing possible thermal transients at PHX/power block. Ramping and dynamics in the power block were not considered. Cost curves, especially for the tower, were simplistic and based on limited quotation data. Power block and storage temperature ranges should be examined and optimized. PHX design parameters should be integrated with the system optimization. Particle attribution and heliostat soiling/cleaning were neglected. Although some costs and performance may worsen as detail is added, there also remain several identified areas where further gains could be achieved.

APPENDIX E. G3P3 FAILURE MODES AND EFFECTS ANALYSIS (FMEA)

Unacceptable Consequences	Any injury that requires more than basic first aid, damage to tower structure or components that causes the system to lose capability, any unanticipated and consequential chemical/material release.	11/12/2019	Added Quantitative evaluation for risk ranking purposes. (Jeremy, Rip)
Hover over heading titles for instructions for that column		11/20/2019	Reviewed with Rip, Josh, Jeremy, Carlos, Chuck, Nick, Dwight
		1/20/2020	Reviewed with full G3P3 team.
		6/18/2020	Reviewed with Facilities Project Management

Color Scale Key			
Risk Priority Index	[1-15]	[16-44]	[45-125]
Color Code	Low Risk	Moderate Risk	High Risk

Work Element Category	System or Component	Failure Mode	Hazard Effect	Consequence	Likelihood of cause [1-5]	Severity of Consequence [1-5]	Controlability Factor [1-5]	Risk Priority Index [1-125]	Engineered Controls	Administrative controls	Personal Protective Equipment (PPE)	Actions
Test Component / Work Package	Receiver / Feed Hopper	Overheating due to Slide gate failure caused by electrical failure	structural damage or deformation Falling material contamination of particle stream	Late Milestones, Impact to Budget, Failed Technical Milestones, Major Injury, Minor Injury	1	3	3	9	All electrical systems designed and built to code. Control system scrams heliostats upon detection of over-temperature. UPS power backup.	Trained heliostat operators watches receiver temperatures and can scram heliostats manually. Exclusion zone around tower during use. Cameras used for visual inspection	N/A	N/A

Work Element Category	System or Component	Failure Mode	Hazard Effect	Consequence	Likelihood of cause [1-5]	Severity of Consequence [1-5]	Controlability Factor [1-5]	Risk Priority Index [1-125]	Engineered Controls	Administrative controls	Personal Protective Equipment (PPE)	Actions
	Receiver / Feed Hopper	Overheating due to Slide gate structural failure	structural damage or deformation Falling material contamination of particle stream	Late Milestones, Impact to Budget, Failed Technical Milestones, Major Injury, Minor Injury	1	3	3	9	Thermocouple array behind curtain can detect excessive heat early and trigger scram.	High temperatures trigger alarm in control room. Trained heliostat operators watches receiver temperatures and can scram heliostats manually. Exclusion zone around tower during use. Cameras used for visual inspection	N/A	N/A
	Receiver / Feed Hopper	Overheating due to Slide gate failure caused by particles	structural damage or deformation Falling material contamination of particle stream	Loss of confidence in particle technology, Late Milestones, Impact to Budget, Failed Technical Milestones, Major Injury, Minor Injury	1	3	3	9	Thermocouple array behind curtain can detect excessive heat early and trigger scram.	High temperatures trigger alarm in control room. Trained heliostat operators watches receiver temperatures and can scram heliostats manually. Exclusion zone around tower during use. Cameras used for visual inspection	N/A	N/A
	Receiver / Feed Hopper	Overheating due to Control system measurement error of particle temperature	structural damage or deformation Falling material contamination of particle stream	Late Milestones, Impact to Budget, Failed Technical Milestones, Major Injury, Minor Injury	3	3	3	27	Thermocouple array behind curtain can detect excessive heat early and trigger scram.	High temperatures trigger alarm in control room. Trained heliostat operators watches receiver temperatures and can scram heliostats manually. Exclusion zone around tower during use. Cameras used for visual inspection	N/A	N/A

Work Element Category	System or Component	Failure Mode	Hazard Effect	Consequence	Likelihood of cause [1-5]	Severity of Consequence [1-5]	Controlability Factor [1-5]	Risk Priority Index [1-125]	Engineered Controls	Administrative controls	Personal Protective Equipment (PPE)	Actions
	Receiver / Feed Hopper	Overheating due to Cntrl sys crash	structural damage or deformation Falling material contamination of particle stream	Late Milestones, Impact to Budget, Failed Technical Milestones, Major Injury, Minor Injury	1	3	1	3	Thermocouple array behind curtain can detect excessive heat early and trigger scram.	High temperatures trigger alarm in control room. Trained heliostat operators watches receiver temperatures and can scram heliostats manually. Exclusion zone around tower during use. Cameras used for visual inspection. Safety system is separate from the control system.	N/A	N/A
	Receiver / Feed Hopper	Overheating due to Cntrl sys transient response of slide gate	structural damage or deformation Falling material contamination of particle stream	Late Milestones, Impact to Budget, Failed Technical Milestones, Major Injury, Minor Injury	3	3	3	27	Thermocouple array behind curtain can detect excessive Thermocouples early and trigger scram	Trained heliostat operators watches receiver temperatures and can scram heliostats manually. Exclusion zone around tower during use. Cameras used for visual inspection	N/A	N/A
	Receiver / Feed Hopper	Overheating due to particle curtain disruption from debris	structural damage or deformation Falling material contamination of particle stream	Late Milestones, Impact to Budget, Failed Technical Milestones, Major Injury, Minor Injury	3	3	1	9	Thermocouple array behind curtain can detect excessive Thermocouples early and trigger scram	Operator watches receiver temperatures and can scram heliostats manually.	N/A	N/A

Work Element Category	System or Component	Failure Mode	Hazard Effect	Consequence	Likelihood of cause [1-5]	Severity of Consequence [1-5]	Controlability Factor [1-5]	Risk Priority Index [1-125]	Engineered Controls	Administrative controls	Personal Protective Equipment (PPE)	Actions
	Receiver / Feed Hopper	Overheating due to particle curtain deviated flow due to wind	structural damage or deformation Falling material contamination of particle stream	Late Milestones, Impact to Budget, Failed Technical Milestones, Major Injury, Minor Injury	5	3	3	45	Receiver geometry and receiver designed to reduce particle loss. Thermocouple array behind curtain can detect excessive temperatures early and trigger scram	heliostat field shuts down during winds >25 mph Exclusion Zone prohibits personnel on Tower during test operations. Operator watches receiver temperatures and can scram heliostats manually.	N/A	N/A
	Receiver / Feed Hopper	structural failure	materials falling down	Fines and Remediations for Liability, Late Milestones, Impact to Budget, Failed Technical Milestones, Major Injury, Minor Injury	1	5	3	15	design with margin	quality control, inspections Exclusion zone around tower during operation	N/A	N/A
	Receiver / Feed Hopper	mechanical failure due to rust/deterior ation	materials falling down	Fines and Remediations for Liability, Late Milestones, Impact to Budget, Failed Technical Milestones, Major Injury, Minor Injury	3	3	1	9	weatherization of exposed components	regular inspection intervals Exclusion zone around tower during operation	N/A	N/A

Work Element Category	System or Component	Failure Mode	Hazard Effect	Consequence	Likelihood of cause [1-5]	Severity of Consequence [1-5]	Controlability Factor [1-5]	Risk Priority Index [1-125]	Engineered Controls	Administrative controls	Personal Protective Equipment (PPE)	Actions
	Receiver / Feed Hopper	mechanical failure due to abnormal particle build-up due to foreign contaminant blocking flow	materials falling down	Loss of Confidence in Particle Technology, Fines and Remediations for Liability, Late Milestones, Impact to Budget, Failed Technical Milestones, Major Injury, Minor Injury	1	5	1	5	weigh hopper sensors shut off flow and scram if discrepancies detected design of bottom hopper can withstand a blockage without structural failure of hopper (overflow vs. blowout)	Exclusion zone around tower during operation	N/A	N/A
	Receiver / Feed Hopper	mechanical failure or rupture due to abnormal particle build-up due to clumping of particles	falling material, contamination of particle stream	Loss of Confidence in Particle Technology, Fines and Remediations for Liability, Late Milestones, Impact to Budget, Failed Technical Milestones, Major Injury, Minor Injury	1	5	1	5	weigh hopper sensors shut off flow and scram if discrepancies detected design of bottom hopper can withstand a blockage without structural failure of hopper (overflow vs. blowout)	Exclusion zone around tower during operation	N/A	N/A
	Receiver / Feed Hopper	Excessive particle loss due to structural integrity of particles (fines)	EPA Violation	Reprimanded by Sandia, Loss of Confidence in Particle Technology, Minor Injury, Fines and Remediations for Neglegence, Fines and Remediations for Liability	3	1	3	9	choose particles that have high durability	test quality upon receiving	N/A	N/A

Work Element Category	System or Component	Failure Mode	Hazard Effect	Consequence	Likelihood of cause [1-5]	Severity of Consequence [1-5]	Controlability Factor [1-5]	Risk Priority Index [1-125]	Engineered Controls	Administrative controls	Personal Protective Equipment (PPE)	Actions
	Receiver / Feed Hopper	Excessive particle loss due to wind	EPA Violation	Reprimanded by Sandia, Loss of Confidence in Particle Technology, Minor Injury, Fines and Remediations for Neglegence, Fines and Remediations for Liability	5	1	3	15	Receiver geometry and receiver designed to reduce particle loss.	Don't operate during high winds	N/A	N/A
	Receiver / Feed Hopper	Hot particle overflow out of aperature due to obstruction below receiver	hot particles spill onto structure or personnel below	Structural damage or human injury	3	5	5	75	Control system monitors mass in weigh hopper and will stop particle lift and SCRAM heliostats. Safety system is independent from the supervisory control system.	Periodic inspection and maintenance of ducts and slide gates etc. Exclusion zone established during test operations.	N/A	**Add a requirement to control system to check for abnormal filling of particles within the receiver. In the event that level reaches critical level, indicating a potential clog in the receiver, shut receiver slide gate and move beam off-receiver.**
	Storage Bins	Rupture caused by weld failure	Loss of hot particles	Fire/igniting materials on module and on ground, Equipment damage and time loss due to shutdown	1	5	3	15	Tank designed to have margin to thermomechanical stress. Materials tested to margin temperatures. Partial containment from refractory layers	Inspection of welds	N/A	N/A
	Storage Bins	Rupture caused by corrosion, caused by contaminati on of steel	Loss of hot particles	Fire/igniting materials on module and on ground, Equipment damage and time loss due to shutdown	1	5	3	15	Multiple layers of wall insulation provide containment with even partial integrity of shell.	Steel is purchased from reputable supplier and inspected. Exterior is inspected for damage and contamination.	N/A	N/A

Work Element Category	System or Component	Failure Mode	Hazard Effect	Consequence	Likelihood of cause [1-5]	Severity of Consequence [1-5]	Controlability Factor [1-5]	Risk Priority Index [1-125]	Engineered Controls	Administrative controls	Personal Protective Equipment (PPE)	Actions
	Storage Bins	Rupture caused by impact due to falling objects	Loss of hot particles	Fire/igniting materials on module and on ground, Equipment damage and time loss due to shutdown	1	5	3	15	Shell is designed with steel shell and roof that will protect brittle interior materials from impact from all but tower structural steel members.	Tower construction quality plan and certification. Administrative control of all corrosive chemicals.	N/A	N/A
	Storage Bins	Blockage of outlet due to large material, due to refractory deterioratio n	Particles do not flow out of bin and bin is full of particles	Stoppage of work while bin cools and repaired manually. Cost of repairs.	3	3	3	27	Wall mesh to catch crumbling refractory and outlet grate.	Control system and heat exchanger will identify incorrect flow rate.	N/A	N/A
	Storage Bins	Blockage of outlet, caused by large foreign material entering through receiver.	Particles do not flow out of bin and bin is full of particles	Stoppage of work while bin cools and repaired manually. Cost of repairs.	3	3	1	9	Inlet slide gates will be closed while system rests., Outlet grate will prevent full blockage.	Receiver aperature door closed when not in use.	N/A	N/A
	Storage Bins	Blockage of outlet due to clumping of particles, due to moisture	Particles do not flow out of bin and bin is full of particles	Stoppage of work while bin cools and repaired manually. Cost of repairs.	1	3	3	9	Closed slide gates above storage when system is not in operation.	Door on receiver.	N/A	N/A
	Storage Bins	Blockage of outlet due to due to foreign objects	Particles do not flow out of bin and bin is full of particles	Stoppage of work while bin cools and repaired manually. Cost of repairs.	3	3	1	9	Closed slide gates above storage when system is not in operation. Screens above and below storage bin.	Door on receiver.	N/A	N/A
	Storage Bins	Failure of concrete slab/foundat ion	Hot particles and heavy concrete impact structure or ground	Stoppage of work while bin cools and repaired manually. Cost of repairs. Injury, death	3	5	3	45	Insulation design will protect concrete. Active cooling of concrete slab. Steel pan beneath concrete slab provides secondary containment.	Routine inspection of slab opening.	N/A	**High temperature concrete formulation and active cooling to be incorporated into design. Add routine inspection of slab.**

Work Element Category	System or Component	Failure Mode	Hazard Effect	Consequence	Likelihood of cause [1-5]	Severity of Consequence [1-5]	Controlability Factor [1-5]	Risk Priority Index [1-125]	Engineered Controls	Administrative controls	Personal Protective Equipment (PPE)	Actions
	Storage Bins	Egress from tank is impeded	Engulfment, entrapment, personnel in storage bin	Severe injury, loss of life	2	5	3	30	No open access to storage tank	Confined space entry permit, technical work document, multiple personnel required to be present during entry. LOTO, Hoist, air quality monitoring.	Fall Protection Harness, rescue bump cap	Completion of Confined Space Assessment and Authorization to Enter Permit Required Confined Space will be required prior to entry. To be completed upon construction completion.
	Heat Exchanger	sCO2 leak/burst into the particles, <due to corrosion> <due to thermomechanical stress> <due to erosion><due to flow maldistribution or blockage>	Shooting particles out of the hxer Cryogenic/thermal shock	Particles shot into the insulation, flow cones, human injury. Personnel could be injured by cold sCO2, thermal shock could result in heat exchanger damage which could significantly delay testing.	3	5	1	15	Housing and insulation shell around the heat exchanger, screen to block foreign material from entering heat exchanger, Materials are selected to resist corrosion, desiged to lose HX material before failure.	QL process inspects for corrosion or signs of damage. signage and barriers, exclusion zones during operation	Face Shield, Apron, Gloves	N/A
	Heat Exchanger	Particle over-temperature (on-sun) caused by particles above max are allowed into storage, caused by failure of diverter valve. <instrumentation error>	Overpressure/temperature of the hxer.	Increased sCO2 pressure, sagging/failure of the heat exchanger materials. If it goes through any over temperature, the HX must be extracted and sent for pressure testing causing full stop of work.	1	5	3	15	For pressure hazard, automated sCO2 pressure exhaust, burst disk or PRV used to relieve over pressure. For max temperature req. automated particle flow shutoff through heat exchanger. Particle temperatures are measured at the weigh hopper and after the storage bin. Slide gates automatically shut if high temperature	signage and barriers, over temperature alarm	None	Automated partice flow shutoff by closing slide gate at base of heat exchanger if temperature exceeds maximum operating temperature add vent valve thermostatic relay (limit controller)

Work Element Category	System or Component	Failure Mode	Hazard Effect	Consequence	Likelihood of cause [1-5]	Severity of Consequence [1-5]	Controlability Factor [1-5]	Risk Priority Index [1-125]	Engineered Controls	Administrative controls	Personal Protective Equipment (PPE)	Actions
									particles are detected.			
	Heat Exchanger	Foreign contamination (e.g., insulation,water)	Causes flow maldistribution	Thermomechanical stress leading to failure of the heat exchanger materials	5	3	1	15	Implement inspectable filters beneath storage, mesh liner on storage walls, door on receiver, grate on outlet of storage bin.	Receiver aperature door closed when not in use.	None	None
	Heat Exchanger	Particle over-temperature (preheater)	Overpressure/temperature of the hxer	Increased sCO2 pressure, sagging/failure of the heat exchanger materials. If it goes through any over temperature, the HX must be extracted and sent for pressure testing causing full stop of work.	1	5	1	5	For pressure hazard, automated sCO2 pressure exhaust, burst disk or PRV used to relieve over pressure. For max temperature req. automated particle flow shutoff through heat exchanger. Automatic shutdown of electric heaters using limit controller. Slide gates automatically shut if high temperature particles are detected. System is designed to shed water away from particle flow path. Clumped particles would be screened as foreign material.	signage and barriers, over temperature alarm	None	Verify additional contactors and limit controllers inventory on hand

Work Element Category	System or Component	Failure Mode	Hazard Effect	Consequence	Likelihood of cause [1-5]	Severity of Consequence [1-5]	Controlability Factor [1-5]	Risk Priority Index [1-125]	Engineered Controls	Administrative controls	Personal Protective Equipment (PPE)	Actions
	sCO2 loop	Insufficient pressure caused by leak or ambient temperature decrease	Cryogenic hazard	Slow leak of sCO2, sCO2 exposure	1	5	3	15	Leak detection system, cooling/inventroy management system	signage and barriers. TWDs	FOR ONLINE MANTAINANCE; face shield, cryogenic-rated gloves, long sleeves/pants, closed-toed shoes	Verify proper PPE on hand and Procedures established within sCO2 Assembly FMA & Operations
	sCO2 loop	Expulsion of fitting/sensor	Cryogenic hazard, impact from debris	Loss of system inventory, injury	3	3	1	9	Hose-whip style leashes and enclosed shielding to prevent components from being ejected out of sCO2 structural envelope.	signage and barriers	FOR ONLINE MANTAINANCE; face shield, cryogenic-rated gloves, long sleeves/pants, closed-toed shoes	Component Sensor leashes and shielding to be incorporated into design.
	sCO2 loop	Overpressure not controlled through another mechanism due to ambient temperature rise, PHX heating, external fire, or overfilling	Cryogenic release, loud noise	Burst disk ruptures, Loss of system inventory	3	3	1	9	Non-fragmenting burst disk, oriented down. Installed impact resistant polycarbonate around pressurized system components	signage and barriers	FOR ONLINE MANTAINANCE; face shield, cryogenic-rated gloves, long sleeves/pants, closed-toed shoes	N/A

Work Element Category	System or Component	Failure Mode	Hazard Effect	Consequence	Likelihood of cause [1-5]	Severity of Consequence [1-5]	Controlability Factor [1-5]	Risk Priority Index [1-125]	Engineered Controls	Administrative controls	Personal Protective Equipment (PPE)	Actions
	sCO2 loop	Insufficient sCO2 flow due to excessive pressure drop, high ambient temperature, or incorrect valve positions	Over Temperature Condition	ThermoMechanical Failure	1	5	1	5	Component pressure drop requirements, coooling/inventory management system design	Control system trip limits	N/A	N/A
	sCO2 loop	KAPL heater overtemperature or component failure	Overpressure/temperature of the downstream components due to component or system failure	Loss of downstream components, rupture, thermal fatigue, salt decomposition	3	1	1	3	Thermostatic limit controller to shut off 480 VAC contactor		N/A	N/A
	Particle Lift	Elevator Binding due to thermal expansion	Particles can't flow, inability to perform tests, overheating of system components if testing	Full stop of system operations, loss of time, impact to research delieverables	3	3	1	9	Support brackets allow free movement in vertical direction.	Visual monitoring of elevator height	N/A	N/A
	Particle Lift	Buckling due to thermal expansion	Structural integrity of elevator. Particles can't flow, inability to perform tests, overheating of system components if testing	Full stop of system operations, loss of time, impact to research delieverables.	3	3	1	9	Support brackets allow free movement in vertical direction.	Visual monitoring of elevator height	N/A	N/A
	Particle Lift	Backflow of particles into elevator discharge	Could cause elevator component failure, particles can't flow, inability to perform tests, overheating of system	Full stop of system operations, loss of time, impact to research delieverables.	3	3	1	9	all ducting is designed with an angle of at least 30 degrees. Load cells in feed hopper can detect if top level is exceeded and can turn lift off. Lift will shut down if motor	N/A	N/A	N/A

Work Element Category	System or Component	Failure Mode	Hazard Effect	Consequence	Likelihood of cause [1-5]	Severity of Consequence [1-5]	Controlability Factor [1-5]	Risk Priority Index [1-125]	Engineered Controls	Administrative controls	Personal Protective Equipment (PPE)	Actions
			components if testing						amperage reaches critically high level.			
	Particle Lift	Particles jam lift	Particle bed becomes densely packed or clumped at bottom of lift. Due to water or backflow of particles from upper ducting.	Full stop of system operations, loss of time, impact to research delieverables.	3	3	1	9	Lift is designed to be water tight.	All ducting is designed properly	N/A	N/A
	Particle Lift	Bucket fails mechanicall y	Bucket falls off chain	Full stop of system operations, loss of time, impact to research delieverables.	1	3	1	3	Bucket elevator is designed to be robust in high temperature environments	Annual inspection of buckets and chains.	N/A	N/A
	Particle Lift	Heat loss from lift heats structure	Structural integrity tower can be affected if members grow and cause breakage of fixtures or buckling of other members	Loss of time, inability to test, impact to cost.	1	3	1	3	Insulation on lift is designed to prevent heat transfer to tower.	Thermocouples strategically placed along walls of lift	N/A	N/A
	Ducting & Piping	Duct fails	Burst disk ruptures, Loss of system inventory, Breach of hot particles, clogged particle flow	Late Milestones, Impact to Budget, Failed Technical Milestones, Major Injury, Minor Injury	1	5	1	5	Particle flow is monitored and controlled. Ducts designed for weight of particles. Insulation provides containment. Redundant Duct supports at multiple points throughout system.	Exclusion zone around tower during operation	Hard Hats, protective clothing, steel toe boots, gloves required when working with ducts.	N/A

Work Element Category	System or Component	Failure Mode	Hazard Effect	Consequence	Likelihood of cause [1-5]	Severity of Consequence [1-5]	Controlability Factor [1-5]	Risk Priority Index [1-125]	Engineered Controls	Administrative controls	Personal Protective Equipment (PPE)	Actions
	Ducting & Piping	Junction Fixture Fails	Breach of hot particles, clogged particle flow	Late Milestones, Impact to Budget, Failed Technical Milestones, Major Injury, Minor Injury	1	5	1	5	Particle flow is monitored and controlled. Ducts designed for weight of particles. Insulation provides containment. Redundant Duct supports at multiple points throughout system.	Exclusion zone around tower during operation	Hard Hats, protective clothing, steel toe boots, gloves required when working with ducts.	N/A
	Ducting & Piping	Insulation Fails	Burn hazard	Late Milestones, Impact to Budget, Failed Technical Milestones, Major Injury, Minor Injury	1	5	1	5	Particle flow is monitored and controlled. Ducts designed for weight of particles. Insulation provides containment. Redundant Duct supports at multiple points throughout system.	Exclusion zone around tower during operation	Hard Hats, protective clothing, steel toe boots, gloves required when working with ducts.	N/A
	Electrical system (elevator motor, cooling pumps, data acquisitions, calrods/heating system, heliostat field, warning lights)	VFD fails on Lift elevator	Particle conveyance is halted	Test structure comprimised (No more particles being released, cavity overheats, loss of test data)	1	1	5	5	SCRAM for heliostats, use of thermocouples to monitor temperatures, use of BCS to monitor particle curtain, visual inspection, VFD not used to control flow	Monthly check of VFD	N/A	N/A

Work Element Category	System or Component	Failure Mode	Hazard Effect	Consequence	Likelihood of cause [1-5]	Severity of Consequence [1-5]	Controlability Factor [1-5]	Risk Priority Index [1-125]	Engineered Controls	Administrative controls	Personal Protective Equipment (PPE)	Actions
	Electrical system (elevator motor, cooling pumps, data acquisitions, calrods/heating system, heliostat field, warning lights)	Thermocouple failure	Critical control system inputs are faulty	Cavity overheating and melting components	3	1	1	3	Multiple thermocouples in close proximity	Monitor data for anomalies	N/A	N/A
	Electrical system (elevator motor, cooling pumps, data acquisitions, calrods/heating system, luker system, heliostat field, warning lights)	OLDs elevator motor fails	Particle conveyance is halted	Test structure comprimised (No more particles being released, cavity overheats, loss of test data)	1	3	3	9	SCRAM for heliostats, use of thermocouples to monitor temperatures, use of BCS to monitor particle curtain, visual inspection, VFD not used to control flow	Quarterly inspection	N/A	N/A
	Heliostats	Heliostats are intentionally or unintentionally focused on incorrect position	Overheating and structural damage	Damage to Receiver / Structure causing Program Delay and or Significant repair cost	1	3	1	3	SCRAM for heliostats, use of thermocouples to monitor temperatures	See Heliostat Field Safety Case, PHS, and FMEA	N/A	N/A
Construction / Facilities / O&M	Foundation	faulty foundation	Structural Integrity	Structure tilt, failure, collapse	1	5	3	15	built to code and requirements as supported thru the Geotechnical report	Geotechnical report assessed by Project Engineering Manager	N/A	Geotechnical Report

Work Element Category	System or Component	Failure Mode	Hazard Effect	Consequence	Likelihood of cause [1-5]	Severity of Consequence [1-5]	Controlability Factor [1-5]	Risk Priority Index [1-125]	Engineered Controls	Administrative controls	Personal Protective Equipment (PPE)	Actions
	Foundation	re-enforcing steel detail descrepencies not submitted according to Design Requirements	Structural Integrity	Structure tilt, failure, collapse	1	5	3	15	N/A	Drawings reveiwed for accuracy prior to shop submission, Site Engineer reviews implementation of Steel prior to concrete placement.	N/A	N/A
	Foundation	Concrete not as strong as specified	Structural Integrity	Re work required upon discovery, delay in project timeline added costs.	3	3	3	27	Sampling of concrete at time of placement	Reviewed by design engineer	N/A	N/A
	Structure	Structural steel detail descrepencies not submitted according to Design Requirements	Structural Integrity	Structure tilt, failure, collapse	1	5	3	15	N/A	Drawings reveiwed for accuracy prior to shop submission, Site Engineer reviews implementation of Steel prior to concrete placement.	N/A	N/A
	Structure / Tank Slab	Concrete slabs under storage bins fail	Structural Integrity	Re work required upon discovery, delay in project timeline added costs.	3	3	3	27	Sampling of concrete at time of placement	Reviewed by design engineer, site engineer, construction inspector (SNL)	N/A	Strength design safety Factors of 1.7 incorporated into design.
	Structure / Tank Slab	Concrete slab decking under storage bins fail	Structural Integrity	Structure failure, release of hot particles, injury to personnel, halt to project	3	5	3	45	**TBD - waiting for final storage bin design / drawings and requirements**	TBD	N/A	**TBD - waiting for final storage bin design / drawings and requirements**
	Structure	re-enforcing steel detail descrepencies not submitted according to Design Requirements	Structural Integrity	Structure tilt, failure, collapse	1	5	3	15	TBD	Drawings reveiwed for accuracy prior to shop submission, Site Engineer reviews implementation of Steel prior to concrete placement.	N/A	N/A

Work Element Category	System or Component	Failure Mode	Hazard Effect	Consequence	Likelihood of cause [1-5]	Severity of Consequence [1-5]	Controlability Factor [1-5]	Risk Priority Index [1-125]	Engineered Controls	Administrative controls	Personal Protective Equipment (PPE)	Actions
	Structure	Bolt / Anchor Point Failure of attachment points to components (e.g., storage bins, heat exchanger)	Structural Integrity	Structure tilt, failure, collapse	3	3	3	27	Submittal reviews of specificied Bolt strength and material characteristics	Inspection of Materials prior to assembly	N/A	N/A
	Structure Erection (Crane, skytrack)	Rigging / Lifting Failure	Structural Damage / Falling Object	Cost in damaged material, Schedule, Personnel Injury,	3	3	3	27	Lift capacity verification for lifting equipment	Crane and rigging inspections, lift plan, spotters,	N/A	Construction / Contractor Specific Safety Plan to be developed
	Structure Erection	Failure of Base or foundation area	structure topples over, structural integrity issues	Delay in schedule, rework of assembly	3	3	3	27	Temporary Shoring and Bracing	Construction Plan, Inspections, Design Reviews	N/A	Construction Plan to be developed. Required by EOR and implemented by contractor
	Structure Erection	Improper sequence of assembly	Tower improperly built, structural integrity issues	Delay in schedule, rework of assembly	1	3	1	3	N/A	Construction Plan, Inspections, Design Reviews	N/A	Construction Plan to be developed
	Structure (Jib Crane)	Crane cable hits / rubs up against steel / vertical lift	Structural Damage, Crane component damage	Loss of load, damage to crane, damage to structure, injury to personnel, additional cost to fix damage, Regulatory Violation	3	3	1	9	Design structure to allow vertical lift	Proper Crane / Lifting Equipment operation, trained personnel	N/A	Crane to be part of Construction Plan with proper Lift planning in place. Notification to FAA for use of Crane needed. To be done by Facilities / Contrator
	Structure	Falling over/collapsing - wind	Wind causing structure to fall over/collapse	End of project/loss of >1.5 million dollars/might cause site shutdown/potential human injury	3	5	1	15	Structural analysis, structural inspections (welds), Non-destructive testing (NDT)	N/A	N/A	Inspect structure for damage after winds greater than 96 MPH, weather station needed with a target on it sending alarm. TBD

Work Element Category	System or Component	Failure Mode	Hazard Effect	Consequence	Likelihood of cause [1-5]	Severity of Consequence [1-5]	Controlability Factor [1-5]	Risk Priority Index [1-125]	Engineered Controls	Administrative controls	Personal Protective Equipment (PPE)	Actions
	Structure	Falling over/collapsing - earthquake	Earthquake causing structure to fall over/collapse	End of project/loss of >1.5 million dollars/might cause site shutdown/potential human injury	1	5	3	15	Structural analysis, structural inspections (welds), Non-destructive testing (NDT)	N/A	N/A	Inspect structure after earthquakes (5.0 on Richter scale) TBD
	Structure	Lightning - fry all motors/electrical system/data	Lightning strike	Recovery possible, loss of time/money (up to hundreds of k dollars lost)	3	3	1	9	Structure will have lightning protection, site counter-poise, minimal electrical systems, some DAQ (minimum amount to be destroyed)	N/A	N/A	Structure will also be within close proximity to existing Solar Tower and unlikely to suffer a strike given adjacent height
	Structure	Human Error/Poor construction	Welds failing causing structure to fall over/collapse	End of project/loss of >1.5 million dollars/might cause site shutdown/potential human injury	3	3	1	9	Certified structural welders, welding inspections, NDT, structure fabricated to code/spec	Certified structural welders, welding inspections, NDT, structure fabricated to code/spec. QA / Inspection process	N/A	Construction and Contractor Qualification / Safety Plan to be implemented.
	Structure	Hit by aircraft - falling over/collapsing	Hit by aircraft causing structure to fall over/collapse	End of project/loss of >1.5 million dollars/might cause site shutdown/potential human injury	1	5	3	15	FAA warning light installed	Verified operational	N/A	Design requested of B&P to add Aircraft Warning Light circuitry, added in design.
	Structure	Falling over/collapsing	Over-Heating of structure/poor insulation design/insulation failure/cooling failure/lack of insulation	End of project/loss of >1.5 million dollars/might cause site shutdown/potential human injury	1	5	3	15	Thermocouples installed on structure, validated aim points for Heliostat Field, Heat Shield Cladding installed around points near the Receiver	Real-time visual inspection	N/A	N/A
	Structure	Human Error/Poor design	Excessive deflections/stresses	End of project/loss of >1.5 million dollars/might cause site shutdown/pote	1	3	3	9	N/A	Trained engineer(s) evaluating design. FMOC Project Engineering Management Review with both SNL & AF	N/A	N/A

Work Element Category	System or Component	Failure Mode	Hazard Effect	Consequence	Likelihood of cause [1-5]	Severity of Consequence [1-5]	Controlability Factor [1-5]	Risk Priority Index [1-125]	Engineered Controls	Administrative controls	Personal Protective Equipment (PPE)	Actions
				ntial human injury								
	Structure	struck by vehicle / vehicle traffic issues	Structural damage to Tower Base and Columns	Damage to Tower Columns	3	3	1	9	bollards or concrete barriers established near Tower base		N/A	N/A
	Structure	Improper Component Placement with Crane Use	Damage to Lattice Structures or Tower Columns	Unstable Tower Structure	3	3	3	27	Properly Rated Equipment for designated lifts	Crane and Rigging training / certifications for all Operators.	N/A	**Verification of training and certifications prior to deployment. FMOC PEP**
	Electrical system - Ground Excavation	Hit existing utilities, Utility Conflict,	Electrical Hazard Failure, Delay in schedule, Utility Failure	potential injury to personnel, release of water, electrical outage	3	3	2	18	Pot holing	Excavation / penetration permit process	N/A	N/A
	Welding	Equipment failure	Exposed electrical	Injury	3	3	2	18	Commercial equipment, inspections, UL listed	Skill standard, training, experience	Standard welding PPE	N/A
	Welding	Human error	Fire	Injury, equipment damage	3	1	3	9	Fire extinguisher or water present	Skill standard, training, experience, fire watch, hot work permit	Standard welding PPE	N/A
	Grinding	Equipment failure	Exposed electrical, flying particles	Injury	3	1	3	9	Commercial equipment, inspections, UL listed	Skill standard, training, experience	Eye protection, gloves, proper clothing	N/A
	Power tools	Human error	Exposed blades/bits	Injury	3	1	3	9	Commercial equipment, inspections, UL listed	Skill standard, training, experience	Eye protection, gloves, proper clothing	N/A
	Power tools	Equipment failure	Exposed electrical, flying particles	Injury, equipment damage	3	3	1	9	Commercial equipment, inspections, UL listed	Skill standard, training, experience	Eye protection, gloves, proper clothing	N/A

Work Element Category	System or Component	Failure Mode	Hazard Effect	Consequence	Likelihood of cause [1-5]	Severity of Consequence [1-5]	Controlability Factor [1-5]	Risk Priority Index [1-125]	Engineered Controls	Administrative controls	Personal Protective Equipment (PPE)	Actions
	Cranes, Forklifts	Human error, vehicle failure	struck by vehicle / vehicle traffic issues	Personal Injury, Property damage	3	3	3	27	Properly Rated Equipment for designated lifts	Properly trained and certified operators, equipment inspections and maintenance. Critical Lifts to be required thru SNL Corporate Policy	N/A	**Verification of training and certifications prior to deployment. Verification of Critical Lift Plan where and when appropriate. FMOC to provide oversight of Contractor. FMOC PEP**
	Crane on site	Off Normal event / FAA aircraft clearnace	Collision with aircraft in flight	Personal Injury, Property damage	1	3	1	3	Placement of FAA warning light on top of crane	complete FAA analysis for Crane use during construction. NSTTF has a no fly zone below 500ft	N/A	**Prior to deployment, complete FAA analysis for Crane use during construction. FMOC PEP**
								0				
								0				
Environmental & Natural Hazards	Structure	Falling over/collapsing - wind	Wind causing structure to fall over/collapse	End of project/loss of >1.5 million dollars/might cause site shutdown/potential human injury	3	5	1	15	Structural analysis, structural inspections (welds), Non-destructive testing (NDT)	N/A	N/A	Inspect structure for damage after winds greater than 96 MPH, weather station needed with a target on it sending alarm. TBD
	Structure	Falling over/collapsing - earthquake	Earthquake causing structure to fall over/collapse	End of project/loss of >1.5 million dollars/might cause site shutdown/potential human injury	1	5	3	15	Structural analysis, structural inspections (welds), Non-destructive testing (NDT)	N/A	N/A	Inspect structure after earthquakes (5.0 on Richter scale). TBD

Work Element Category	System or Component	Failure Mode	Hazard Effect	Consequence	Likelihood of cause [1-5]	Severity of Consequence [1-5]	Controlability Factor [1-5]	Risk Priority Index [1-125]	Engineered Controls	Administrative controls	Personal Protective Equipment (PPE)	Actions
	Structure	Lightning - fry all motors/electrical system/data	Lightning strike	Recovery possible, loss of time/money (up to hundreds of k dollars lost)	3	3	1	9	Structure will have lightning protection, site counter-poise, minimal electrical systems, some DAQ (minimum amount to be destroyed)	N/A	N/A	N/A
	Adverse weather - lightning	structural Failure	Exposure to lightning	Injury to personnel, damage to structures and equipment	3	1	3	9	SNL lightning warning system, ground loops, counterpoise, lightning protection on heliostat electrical system	Training, TWDs	N/A	N/A
	Wildlife pests	Wildlife in work areas	Bites, stings, dead animals	Injury or illness	3	1	3	9		Inspections, General operation TWDs, training, Staff Biologists for wildlife removal	Proper clothing	N/A
	Adverse weather - lightning	Exposure to Lightning	Exposure to lightning	Injury to personnel, damage to structures and equipment	3	1	3	9	SNL lightning warning system, ground loops, counterpoise, lightning protection on heliostat electrical system	Training, TWDs	N/A	N/A
Personnel	NSTTF personnel	Human error-unauthorized entry during testing	Exposure to concentrated sunlight, mechanical motion, high temperature surface	Injury to personnel, testing disrupted	3	3	3	27	Remote site, access controlled with fence and gates	Exclusion area (fence, gates, signs, warning lights), site voice announcement, field patrolled and monitored during testing, operations TWDs, training, experience	N/A	Review changes needed to NSTTF exclusion zones upon final design review. Incorporate exclusion zone changes into site operating TWD (Rip W)

Work Element Category	System or Component	Failure Mode	Hazard Effect	Consequence	Likelihood of cause [1-5]	Severity of Consequence [1-5]	Controlability Factor [1-5]	Risk Priority Index [1-125]	Engineered Controls	Administrative controls	Personal Protective Equipment (PPE)	Actions
	NSTTF personnel	Fatigue / Cardio Stress	Multiple trips up and down Tower stairwell due to lack of personnel / equipment elevator	Personal Injury, restriction of duty for personnel not fit to climb elevated staircase	3	3	3	27	Hoist being considered for lifting of supplies and materials to upper levels of Tower platforms	Lift process setup for bringing materials to upper levels of Tower, job planning prior to implementing tasks on upper levels of Tower	N/A	Crane Hoist being incorporated into design for lifting of supplies and materials to upper levels of Tower platforms
	Other SNL personnel (facilities)	Human error-unauthorized entry during testing	Exposure to concentrated sunlight, mechanical motion	Injury to personnel, testing disrupted	3	3	1	9	Remote site, access controlled with fence and gates	Exclusion area (fence, gates, signs, warning lights), site voice announcement, field patrolled and monitored during testing, operations	N/A	N/A
	Tour groups	Human error-unauthorized entry during testing	Exposure to concentrated sunlight, mechanical motion	Injury to personnel, testing disrupted	1	3	1	3	Remote site, access controlled with fence and gates. Tours not given of Solar Tower during on sun testing.	Exclusion area (fence, gates, signs, warning lights), site voice announcement, field patrolled and monitored during testing, operations, tours not allowed when testing is taking place, tour guides and are familiar with test operations	N/A	N/A

APPENDIX F. G3P3 COMMERCIAL SCALE-UP RISK REGISTER

Risk			Risk Analysis			Risk Monitoring and Mitigation
Category or Component	**Risk or Potential Outcome**	**Date Raised**	**Impact**	**Probability**	**Matrix Score (1 - 25)**	**Risk Mitigation**
System	Reliability over 30 years will not be demonstrated in G3P3	Feb-19	3	3	9	Two G3P3 systems (G3P3-USA and G3P3-KSA) will be operated in parallel. Together, we hope to yield thousands of hours of operation that will identify potential concerns and reliability issues Ongoing development of competing alternative designs and approaches in components and system layouts Use of commercially established components whenever possible
System	Labor Force Lacks Experience in Particle-Based CSP	Oct-20	4	3	12	Established team of researchers from multiple teams around the world have been collaborating on the development of components.
System	Commercial Investors Are Risk-Adverse to New Technologies	Oct-20	4	4	16	Modular systems with multiple towers are being evaluated to reduce the technology gap from pilot to commercial scale. Probabilistic cost models based on comprehensive plant cost studies by NREL and SBP which include labor, civil, electrical, piping, cables, equipment, water resources etc.
System	Stresses and abrasion/erosion from commercial scale system is higher than expected. Mass flow rates are 200 times greater and total particle weight in commercial systems may be on the order of 400 times greater than the G3P3 system.	Oct-18	3	2	6	Tulsa University has provided in-depth erosion testing on materials of interest including a variety of particles, refractory insulation and metals at high temperatures.

Risk			Risk Analysis			Risk Monitoring and Mitigation
Category or Component	**Risk or Potential Outcome**	**Date Raised**	**Impact**	**Probability**	**Matrix Score (1 - 25)**	**Risk Mitigation**
Receiver	Low thermal efficiency and wind impacts at 100 MWe scales	Nov-18	4	4	16	Preliminary studies have shown that hoods or nods can be implemented to mitigate wind impacts at 100 MWe scales Aperture covers using quartz-glass are likely limited to aperture sizes of a few meters Multi-cavity falling particle receiver designs (similar to Khi Solar One) are being considered to minimize aperture size and increase receiver efficiencies Scaleable multi-stage release designs being considered to reduce convective entrainment while maintaining high opacity of the particle curtain
Receiver	Particle loss through aperture	Dec-18	2	3	6	Tests and studies are being performed; preliminary results show that particle loss does not pose an inhalation or environmental hazard Methods are being pursued to reduce particle losses using multi-stage release and active airflow.

Risk			Risk Analysis			Risk Monitoring and Mitigation
Category or Component	**Risk or Potential Outcome**	**Date Raised**	**Impact**	**Probability**	**Matrix Score (1 - 25)**	**Risk Mitigation**
Receiver	Receiver and particle curtain dimensions not optimized. The width and drop distance of the receiver for a given solar field is largely determined by the optical accuracy of the heliostat system. For given optical field properties, this optimization has not been fully presented. At the 100 MW size, how much "thicker" will the particle curtain be than the 1 MW size? SNL indicated the curtain would be somewhat thicker at commercial scale which would limit transmission losses and the need for impediments to control particle drop. Clear analysis assessing this scale up consideration should be developed. This may also connect to the above control philosophy point. Transmission through the curtain damaging the back wall should be a consideration.	Mar-20	3	3	9	Lagrangian based models of the falling particle curtain in a 100 MWe receiver at anticipated mass flow rates have not shown complications from increased curtain thickness (e.g. self-shadowing). This risk is also mitigated through coupling with multistage receiver technology that increases residence time in the receiver while protecting the backwall. Successful testing of multistage technology on-sun has been performed for peak fluxes exceeding 1000 suns. Computational models demonstrate that at the highest anticipated peak heat fluxes the curtain opacity is sufficient to prevent overheating. Detailed CFD simulations have been performed at multiple scales, including the 100 MWe scale. Lessons learned from the G3P3 Phase 3 testing will be applied to improve the models and scale-up designs for a commercial system. It should be noted that the dimensions of the aperture are optimized to maximize optical efficiency while minimizing area (radiative and convective losses). This determines the width of the aperture and particle curtain. The curtain thickness will then be adjusted to yield the necessary mass flow rate. For a 1 MWt system, the particle mass flow rate is ~5 kg/s/m, which requires an slot aperture thickness of ~0.4 inches. For a 100 MWe CSP plant requiring ~550 MWt, the required mass flow rate is ~100 kg/s/m. The required slot aperture thickness is nearly 3". Hence, the transmission through the curtain at ~100 kg/s/m is expected to be low.

Risk			Risk Analysis			Risk Monitoring and Mitigation
Category or Component	**Risk or Potential Outcome**	**Date Raised**	**Impact**	**Probability**	**Matrix Score (1 - 25)**	**Risk Mitigation**
Receiver	Adverse wind impacts at 100 MWe scale are significantly worse than at tested 1 MWt scale	Mar-20	5	3	15	We completed a wind study using data from a 200 m tower and confirmed wind speed and direction models used in detailed CFD simulations. Additional wind simulations and scaling will be performed during the G3P3 Phase 3 work. Computational fluid dynamics models of candidate 100 MWe scale receivers have been developed to quantify advective and radiative losses subject to a number of different wind conditions. The implemented physical models to study receivers at this scale are the same as used at smaller scales (1 MWth) which have a considerable body of validation evidence supporting their use. Correlations that predict the thermal performance of 100 MWe receivers have been created from these simulations ensembles to inform technoeconomic models.
Receiver	Efficiency, back wall temperature, particle loss rate at the 200 MWt scale is not fully understood as a function of wind velocity, ambient temperature, mass flow rate, and particle curtain thickness.	Mar-20	5	3	15	Detailed CFD simulations have been performed at multiple scales, including the 100 MWe scale have been developed to quantify the thermal efficiency and losses for various conditions, including wind, particle mass flow rate, and incident energy. These models are used to quantify the effect of diminished performance from off-normal conditions and are leveraged in technoeconomic models of 100 MWe scale plants. Successful testing of multistage technology has demonstrated the ability to minimize back wall temperatures and increase residence time in the receiver. Lessons learned from the G3P3 Phase 3 testing will be applied to improve the models and correlations among efficiency, temperature, particle loss, wind speed, mass flow rate, and curtain thickness.

Risk			Risk Analysis			Risk Monitoring and Mitigation
Category or Component	**Risk or Potential Outcome**	**Date Raised**	**Impact**	**Probability**	**Matrix Score (1 - 25)**	**Risk Mitigation**
Receiver	Commercial cost modeling may have increased inaccuracies because tower heights must be greater for falling particle receivers and cost modeling has been informed by molten salt systems.	Mar-20	5	3	15	Particle-based tower cost models have been developed with commercial silo designers and in consultation with tower construction contractors. The models are used to augment existing molten salt tower models by SAM and SBP to account for the additional wall thicknesses, foundations, floor supports and storage bin materials as applicable
Storage	Size of storage tanks for 100 MWe system may be too big for tower integration	Oct-18	3	3	9	Consultation with silo designers and construction managers resulted in confidence that the tower-integrated system is feasible, but detailed design work is needed to fully understand logistics and costs. Storage in external bins is being developed in parallel using well-established monolithic dome construction techniques.
Storage	Heat loss may be excessive	Oct-18	3	3	9	Cyclic modeling results have begun and preliminary results show that heat-loss and temperature requirements can be met High Heat Capacities and Self-insulating properties of particles in bulk formations significantly reduce the amount of insulation required. Modeling shows heat loss is acceptable in large capacities. Phase 3 testing will provide improved understanding of thermal resistance and capacitance in refractory materials. Experimentation is being performed to understand the effects of air entrainment.

Risk			Risk Analysis			Risk Monitoring and Mitigation
Category or Component	**Risk or Potential Outcome**	**Date Raised**	**Impact**	**Probability**	**Matrix Score (1 - 25)**	**Risk Mitigation**
Storage	Cost may be excessive	Oct-18	3	3	9	Novel designs that exploit funnel flow to reduce erosion on walls have been introduced and studied that will reduce the need for expensive refractory layers. Large volume to surface-area ratio for larger systems reduces heat loss relative to smaller-scale systems; expensive insulation layers (e.g., Elmtherm) may not be needed.
Horizontal Particle Conveyance	Particle deliverance and distribution at high temperature is not feasible in all operating scenarios		3	3	9	Vendors of high-temperature particle conveyance equipment have been consulted and are participating in solutions to meet capacity and temperature requirements. Vertically integrated hot storage and heat exchanger system configurations are being designed for both tower-integrated and externally integrated systems. Cart systems are being evaluated by DLR for horizontal transporation
Heat Exchanger	Manufacturing scale-up and high cost for 100 MWe system		5	4	20	Diffusion-bonded modular banks of 32 MWt units have been designed to accommodate multi-megawatt thermal duties Alternative multi-bank and multi-heat-exchanger designs and configurations are being considered to meet cost and performance metrics

Risk			Risk Analysis			Risk Monitoring and Mitigation
Category or Component	**Risk or Potential Outcome**	**Date Raised**	**Impact**	**Probability**	**Matrix Score (1 - 25)**	**Risk Mitigation**
Heat Exchanger	Low particle-side heat-transfer coefficient		4	3	12	Detailed modeling studies and tests are being performed to increase particle-side heat-transfer coefficient and overall heat transfer performance. True-counterflow and cross-counterflow designs are being designed; recent tests on G3P3 20 kW prototype show >300 W/m2-K heat transfer coefficients Alternative fluidized bed heat exchangers are being developed that show higher heat exchange coefficients
Heat Exchanger	Low reliability and increased failure modes at commercial scale		5	3	15	Detailed modeling studies are being performed to evaluate thermomechanical stresses and how to address those in larger or modular units
Lift	Heat losses and adequate insulation associated with bucket lift	Oct-18	3	3	9	Skip hoists have been designed and evaluated for commercial-scale systems, and a leading manufacturer, FLSmidth, believes they can accommodate such a design. G3P3-KSA will test a high-temperature hoist, DLR's HiFlex project has also agreed to share cost information regarding their skip-hoist design . Duermeier is a commercial supplier of high-temperature lifts at the meter scale. They have joined an NDA with SNL to share technical experience in the development of lift designs.
Lift	Adequate particle lift rate that can handle ~2000 kg/s (~8000 tons/hour)	Oct-18	3	2	6	FLSmidth stated that they have manufactured mine hoists that can achieve these particle lift rates; insulation for high-temperature application would be needed
Risk Analysis Matrix Score: Green/Yellow/Red Threshold Values (Can be modified to fit your project)						

Risk			Risk Analysis			Risk Monitoring and Mitigation
Category or Component	**Risk or Potential Outcome**	**Date Raised**	**Impact**	**Probability**	**Matrix Score (1 - 25)**	**Risk Mitigation**
Green - maximum score	7					
Yellow - minimum score	8					
Yellow - maximum score	11					
Red - minimum score or if Impact is "5"	12					

DISTRIBUTION

Email—External

Name	Company Email Address	Company Name
Technical Library	01977	sanddocs@sandia.gov

Sandia National Laboratories

Sandia National Laboratories is a multimission laboratory managed and operated by National Technology & Engineering Solutions of Sandia LLC, a wholly owned subsidiary of Honeywell International Inc. for the U.S. Department of Energy's National Nuclear Security Administration under contract DE-NA0003525.